Plasma Physics Reports, Vol. 29, No. 11, 2003, pp. 895–954. From Fizika Plazmy, Vol. 29, No. 11, 2003, pp. 963–1030.

DUSTY PLASMA

Complex Plasmas: III. Experiments on Strong Coupling and Long-Range Correlations[1]

H. Thomas*, G. E. Morfill*, and V. N. Tsytovich**

** Max-Planck Institute fur Extraterrestrische Physik, 85740 Garching, Postfach 1312, Germany*

*** Institute for General Physics, Russian Academy of Sciences, ul. Vavilova 38, Moscow, 119991 Russia*

e-mail: thomas@mpe.mpg.de, gem@mpe.mpg.de, tsytov@tp.lpi.ac.ru, tsyto@mpe.mpg.de

Received July 10, 2002; in final form, November 26, 2002

Abstract—This paper continues a series of review papers devoted to the physics of complex plasmas, in which one of the components (dust) is in a crystalline or liquid state, while the others (electron, ions, and neutral atoms) are in a gaseous state. This review is devoted to the experimental investigations of new phenomena in complex plasmas. The experiments are explained using estimates based on the theory of elementary processes in complex plasmas, including the new phenomena considered in the previous parts of the review. The paper describes (i) the experiments on multilayer plasma crystals, including the study of their structure and phase transitions; (ii) the experiments on dust monolayer crystals; (iii) the experiments on plasma clusters formed by small number of dust grains; (iv) the experiments on dust ion-sound waves, dust acoustic waves, dust lattice waves, and dust shear waves; (v) the experiments on shock waves; (vi) the experiments on the ionization instabilities and the creation of dust voids and dust clumps; and (vii) the experiments on Mach cones excited either by fast grains or laser radiation. © *2003 MAIK "Nauka/Interperiodica".*

1. INTRODUCTION

Complex plasma, as was described in [1, 2], is a state of matter composed of dust grains, electrons, ions, and neutral atoms with one of the components (dust) being in a strongly coupled state, while the others are coupled weakly. This is possible because dust grains in plasma can have rather large charges and low temperatures. In the previous parts of this review [1, 2], we emphasized the main differences of complex plasmas as a state of matter compared to the usual state of matter and the difference between dust–dust interactions and the ordinary Coulomb and Yukawa interactions.

We showed (i) that a new feature of complex plasmas is the long-range nonscreened interaction of dust grains both of the repulsive and attractive types and that the simple screened Coulomb interaction operates in exclusive cases; (ii) that the nonlinearity in screening is large, at least for the low ion-to-electron temperature ratio encountered in present laboratory experiments; (iii) that the high plasma absorption on the grains related to the charging process (continuously operating to support the large grain charges) requires the continuous presence of ionization, which, together with the absorption on grains, changes the ground state of a complex plasma system; (iv) that the collective dust–dust interactions (where the interaction of two grains is determined by the density of all other grains) can be substantial for the dust densities used in present experiments and that the collective interaction changes the grain fields, thus creating a series of attraction minimums; and (v) that the complex plasma is an actually open system, to which the concept of free energy is, strictly speaking, inapplicable.

To estimate the role of the new processes in complex plasmas, we have given a list of the elementary processes in complex plasmas (see [2]) in such a form that they can be simply used by experimentalists to interpret the new phenomena observed. The reason for concentrating on the primary interactions and elementary processes in complex plasmas was to provide a basis for describing the most important processes that play a role in collective interactions and lead to strongly coupled and strongly correlated states and plasma condensation, which is one of the main topics of this review. Unfortunately, the theoretical understanding of the transition to a strongly correlated state of complex plasma is still poor, and it is hardly probable that the experiments in this field will provide new results in the near future. The processes listed in the previous parts of the review can only give some indication of the physics of the transition to a strongly coupled state of complex plasma. We will, therefore, use the previously given material to make some theoretical estimates, among which the most important are the estimates of collective dust–dust interactions discussed in detail in [2]. Keeping in mind that a detailed theory is still in the initial stage of development, we hope that these theoretical estimates will provide a deeper understanding of the existing observations and will determine the direction in which the theory could further be developed. Thus, we will indirectly provide some proposals for future theoretical work based on these estimates. For the phenomena for which

[1] This article was submitted by the authors in English.

theoretical models are already available, such as linear mode propagation, we will discuss the observations, compare them with the existing theoretical models, and discuss what is necessary and possible to perform in future theoretical and experimental approaches.

At present, there exist several types of experiments with crystalline structures, namely, the experiments with multilayer plasma crystals, monolayer 2D crystals, and dust clusters containing a rather small number of dust grains. In efforts to make estimates for the interpretation of these experiments, the two following general aspects of observations should be taken into account:

(i) For the plasma crystals observed, the size of the experimental installation L is usually much larger than both the ion–neutral mean free path and the ion–dust mean free path (see below). The latter inequality is expressed as $L \gg L_{cr} = \lambda_{Di}^2/aP_0$, where λ_{Di} is the ion Debye length, a is the dust size, and $P_0 = n_d Z_d/n_0$. This estimate suggests that the concept of collective dust–dust attraction (see [2]) should be used for interpreting the experimental results, rather than that of the noncollective interactions that occur when the opposite relation between the ion–dust mean free path and the installation size is satisfied.

(ii) The size of the dust clusters observed in experiments usually satisfies the opposite inequality, $L \ll L_{cr}$, and the dust grain interaction can be considered as the sum of all the possible noncollective pair dust interactions (the same as for ordinary matter with Coulomb or Yukawa interactions). The difference between the noncollective dust–dust pair interaction and Coulomb and Yukawa interactions was considered in detail in [2].

Two comments should be made concerning the particle distributions in a complex plasma when using the estimates based on the results presented in [2]:

(i) The high rate of plasma absorption on dust in the existing experiments is usually compensated for by the local ionization. Under these conditions, the thermal electron and ion distributions are not established because the necessary condition for reaching thermal distributions, $Z_d P_0 \ll 1$, is not fulfilled. One should note that the ionization process always produces nonthermal distributions and the dust charging process makes the electrons and ions nonthermal (depletes the high-energy tail of the electrons and the low-energy component of the ions). Strictly speaking, any theoretical estimate should use a kinetic description. However, such an approach is rather complicated and the full kinetic theory is still in the stage of development (only the first steps toward its development are presently being made; see below). Therefore, we use here the estimates of the elementary processes from [2] for the thermal electron and ion distribution, keeping in mind that the expressions for the parameters in those estimates contain integrals of the whole distributions of the electrons and ions and that the nonthermal part of the distributions can change the numerical results by a factor of the order of unity.

(ii) According to the existing observations and also according to the theoretical estimates of the existing kinetic theory, dust grains are usually distributed thermally. The existing theory predicts that, taking into account all new types of dust–dust interactions related to the collective effects, the dust distribution becomes thermal in a rather short time interval. This is also due to the high rate of dust–dust collisions with all collective effects included. Even for nonthermal electron and ion distributions, the existing theory (which will be discussed in the next part of the review) predicts that the distribution of the dust grains should be thermal (the dust–dust collision integral will contain only the integral over the ion and electron distributions as a common coefficient in front of the expressions, vanishing for the dust thermal distribution in the dust–dust collision integral). The experiments on plasma crystal melting (which we will discuss in detail below) also indicate that, after the melting of the crystal, the dust component has a thermal distribution. The dust–neutral collisions also thermalize the dust distribution if the neutral component is thermal. Therefore, there is good reason to assume in the estimates that the dust grains have a thermal distribution.

We will thus use the estimates based on the thermal distributions for all the complex plasma components in the form given in [2].

There are three important issues for both the theory and experiments on strong coupling in complex plasmas: (i) the physics of the complex plasma state before condensation, (ii) the physics of the strongly correlated and strongly coupled state of complex plasma after condensation, and (iii) the transition processes to the state with strong coupling and strong correlations (the phase transition).

The most complicated of these is the transition problem, which should be understood and described theoretically in a manner different from that used in studying usual matter. The condensed states—the plasma crystals and liquids—are also different from crystals and liquids in usual matter. New approaches should be used for their description. The complexity of the transition problem is related to the fact that (as opposed to ordinary matter) the concept of free energy is not always applicable to complex plasmas. Therefore, the Landau theory of phase transitions [3], which uses an expansion of the free energy with respect to the parameter of order η and associates the phase transition with the point where this parameter becomes finite is generally inapplicable for complex plasmas.

This does not mean that the parameter of order cannot be introduced in complex plasmas. Moreover, one can introduce it in a rather general way if the transition is reached from the gaseous state, which can be described in the simplest way. Let us examine a typical example. The phase transition should correspond to a

certain instability, the threshold of which can be, in principle, found in the gaseous state. We will demonstrate below that, in the gaseous state, there exists a universal instability and that, under certain conditions, one periodical mode can be excited at the threshold of this instability. The appearance of a periodicity in disturbances at the threshold can serve as an indication that the system will start to have a periodical distribution of grains or, in other words, can be regarded as the appearance of a crystalline state. Of course, it is not sufficient to do a linear analysis of such a problem, but one can at least start with such an instability as a candidate for the description of the phase transition. In the case this mode is found to be responsible for the phase transition, its amplitude in the nonlinear stage of the instability can serve as parameter of order for the system. Of course, the scheme presented here is only one of the possible scenarios for future research and, at present, there does not exist a detailed approach based on such a scenario.

Keeping in mind the many new features discussed previously, it seems that, in complex plasmas, the most important method for studying the transition to a strongly correlated state and the formation of a condensed state is the investigation of the pair correlations as a function of the parameter of order. We will, therefore, concentrate on the problems of the change in the pair correlation function during the transition stage and in the condensed phase of complex plasmas. The value of the parameter of order at which long-range correlations appear should correspond to the phase transition condition. Such an approach is obviously more sophisticated than the Landau approach, but it can also be used under the conditions where the concept of free energy is not applicable. We will not go here into the details of this problem and note only the existing difficulties and one way they could be resolved. In the next part of the review, we will give a more detailed description of such an approach. It is desirable that the new theory includes the possibility of using the scale invariance approach to find the universal indexes for fluctuations at the critical point.

Note that the term "strong coupling" does not really express the meaning of the state to which complex plasma can condensate. In ordinary matter, the transition to the crystalline or liquid state is indeed related to the strong coupling at which the electrostatic energy substantially exceeds the kinetic energy of the interacting grains. The basic requirements for producing liquid and crystalline states under laboratory conditions were discussed in [1, 2]. Obviously, there exist many possible parameters on which, in particular, the attraction forces depend (such as the grain size, the parameter P, the intergrain distance, etc.). One of our most important results is the experimental measurements of the coupling constant Γ_{cr} for the transition, which depends on the dust charge, dust temperature, intergrain distance, and dust shielding. To reach the transition, Γ should exceed the critical value Γ_{cr}, for which different theoretical approaches give somewhat different values. In experiments, Γ_{cr}, as well as its dependence on different parameters, is measured. Usually, the Γ_{cr} value should be large enough for the transition to occur. To obtain such large values of Γ, we need to have high grain charges (i.e., large electron and low ion temperatures and a large dust size) and small kinetic grain temperatures. In most cases, the experimentally obtained Γ_{cr} does not correspond to the value given by the one-component plasma (OCP) approach (see [1, 2]).

In ordinary matter, strong coupling leads to strong correlations, namely to the appearance of long-range correlations (long-scale order in crystals and short-scale order in liquids). In complex plasma, the relation between the strong coupling and long-range correlations is not obvious. For example, long-range correlations can be related to dust attraction when the kinetic energy of a dust grain is not too large (of the order of the attraction potential well). Then, under conditions where the long-range correlations are present, we will deal not with strong interaction but with middle-range interaction. Thus, strictly speaking, for condensation to appear, it is required only that the long-range correlations start to form. The level of interdust interaction corresponding to the appearance of strong correlations should be the subject of both theoretical and experimental work. As in [1, 2], we can also introduce the parameter Γ, which, under the conditions where the transition to a strongly correlated state occurs, can be large. However, since the physics of transition is different from the physics of transitions in ordinary matter or in the system of Yukawa interacting grains, this parameter can be determined by physical effects other than those in ordinary matter. Therefore, the intergrain distance entering into this parameter and the ratio of the intergrain distance to the screening length could be not the only parameters determining the phase transition.

After these introductory comments, we will now turn to the description of the experimental results and perform some estimates, using the description of the elementary processes in complex plasmas given in [2]. These theoretical estimates can serve only as a first approximation of the problem, and a detailed theory is still waiting to be developed. We postpone the discussions of the existing theoretical approaches, correlation effects, and other collective effects to the next part of the review, in which we will consider the present achievements and the outlook for future theoretical research. In the next part of the review, we will also discuss the value of Γ_{cr} found in several theoretical models and make some comments on the applicability of the existing models to real complex plasma experiments. Here, we mainly focus on the experimental results on pair correlation functions and the values of Γ_{cr} that demonstrate the presence of long-range correlations after the transition.

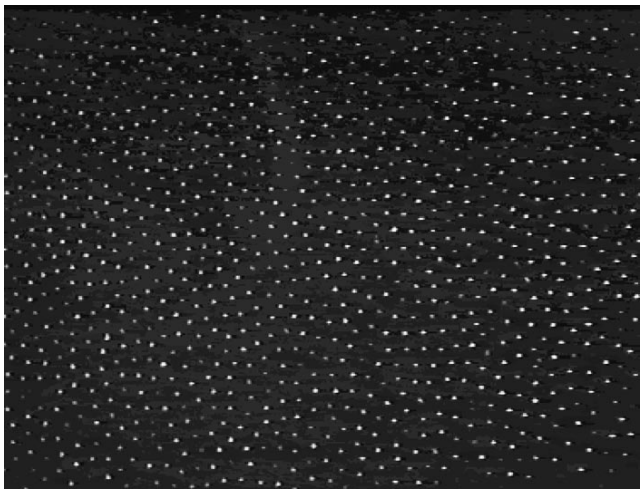

Fig. 1. Distribution of dust grains in a plasma crystal obtained in an RF discharge plasma [4].

2. PLASMA CRYSTALS

2.1. Crystalline Structures Observed under Different Conditions

Plasma crystals[2] and long-range correlations in complex plasmas were observed under quite different experimental conditions—different temperatures, charge component densities, gas pressures, and dust sizes. In addition, the dc floating-potential electric fields of the walls and other types of forces are important in establishing the dust force balance and the formation of plasma crystals. Therefore, the main questions are the following: What do experiments performed under quite different experimental conditions have in common? Are the values of parameter Γ of the same order of magnitude or they are quite different in different experiments? Is the parameter P_0, which determines collective dust interaction, of the same order in different experiments, or its value is quite different in different experiments? Is the ratio of the dust size to the screening length different? How important is the ionization power? Not all of these parameters are available from the experimental data, but some estimates can be made using the estimates of the elementary processes in complex plasmas [1, 2].

Observations of plasma crystals under quite different experimental conditions have certain advantages for a deeper understanding of the physics related to the observed plasma condensation. We start with listing some of the observations and then describe in more detail the particular case of the radio-frequency (RF) discharge plasmas that are most often used in experiments.

There are several types of plasma devices that provide the conditions for the observation of long-range correlations in complex plasmas. There are RF plasmas [4–7], low-power dc plasmas [8], high-pressure combustion plasmas [9], inductive plasmas [10], and radioactive plasmas [9]. All these plasmas have been used successfully in the generation of strongly coupled or long-range correlated complex plasma states [11–15]. Most of the existing experiments were devoted to RF plasmas and also to dc plasmas. These experiments produced the largest amount of information and will be, therefore, described in more detail.

Here, we start with an illustration of how different were the conditions at which plasma crystals were observed. In RF discharges (see Fig. 1), the grain size ranged from 3 to 10 μm, the krypton gas pressure was in the range 1–2 Torr, the ionization was homogeneous and produced by an RF field, ion density was 5×10^8 cm^{-3}, the dust averaged spacing was 260 μm, the dust charge was $Z_d \approx 10^4$, and the dust density was $n_d = (1–2) \times 10^4$ cm^{-3}. The electric field in the plasma sheath was 50–100 V/cm and could support rather heavy dust grains against the pull of gravity. The parameter Γ in this case was 10^4 (much larger than the OCP critical value).

In dc glow discharge plasmas (Fig. 2) [8], the configuration of the electric field in striations was three-dimensional. Apart from the field along the discharge, the floating-potential field of the cylindrical wall was important; on average, the field in striations was 10 V/cm (much lower than for RF plasmas near the electrodes). The ionization was supported by a dc current of several amperes, and the pressure ranged from 0.1 to 1 Torr. The grain charge was as high as $Z_d \approx 10^6$, and the size of the grains ranged from 2 to 63 μm. Nevertheless, the intergrain distance in the crystalline state was 300–400 μm (similar to that in RF discharges), the grain density was 10^4 cm^{-3}, and $\Gamma \sim 160–850$ (as compared to $(2–10) \times 10^4$ in RF discharges). Although the electric field in the stratum, as well as the value of the ion drift velocity caused by the electric field, was inhomogeneous, the intergrain distance in the crystalline state was almost constant. In both mentioned types of experiments, the ion-to-electron temperature ratio was very small, $\tau \approx (1–2) \times 10^{-2}$.

In a high-density atmospheric-pressure plasma in which the ion-to-electron temperature ratio was of the order of unity [16] (see Fig. 3), a regular structure was observed in the boundary region between the combustion plasma and its condensation region. In this case, the dust density was 10^6–10^7 cm^{-3}, and the temperature was in the range 1900–2000 K. No external electric field was applied. The parameter was $\Gamma \approx 0.5–18$, the electron density was $(0.3–3) \times 10^{10}$ cm^{-3}, and the dust charge was $Z_d \approx 500–700$.

Another experiment involving the observation of dust structures at atmospheric pressure was performed for a nuclear excited plasma where the source of ionization was the radioactivity of nuclei with a source local-

[2] This term is widely used by experimentalists to denote the crystals formed by dust grains in a plasma.

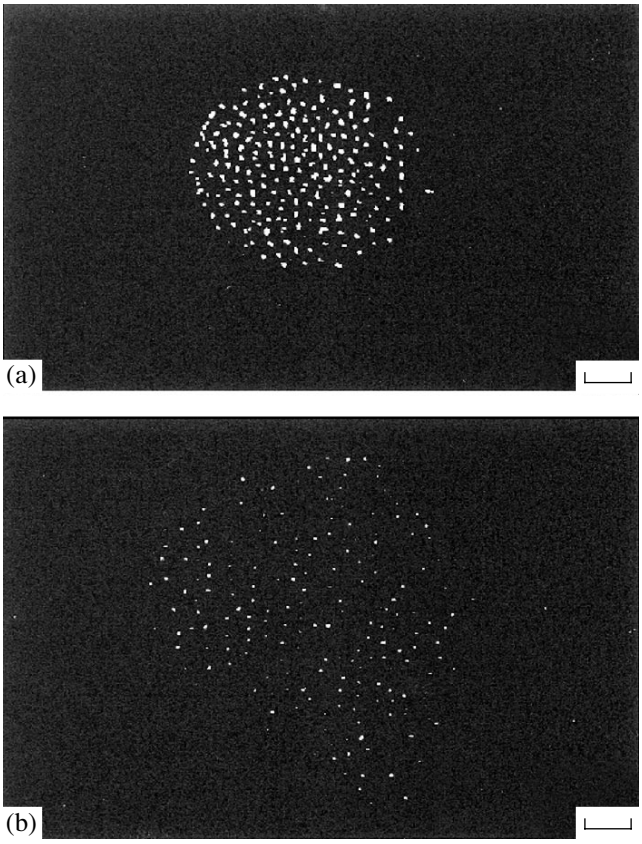

Fig. 2. Typical distributions of dust grains in a plasma crystal obtained in striations of a dc discharge plasma at a current of 1 mA and pressure 0.2 Torr [8]: (a) distribution in the horizontal plane and (b) distribution in the vertical plane. The bars correspond to 1 mm.

ized in space and with large fluctuations of the densities of the ionized electrons and ions as functions of the distance from the source. The grains had the size 1.8–4.8 μm, the grain charge was about $Z_d \approx 10^3$, and Γ was about 30, while the spacing between the grains was again of the order of that in all previously mentioned experiments (about 200 μm).

In glow discharges, structures with the simultaneous presence of the crystalline, liquid, and gaseous states were also observed (see Fig. 4).

Thus, under different experimental conditions, the measured values of the parameter Γ differ substantially and can even be of the order of or less than unity. Nevertheless, the value of the parameter P_0 in all experiments was of the order of unity. This should be taken into account in theoretical models that are used to explain the results of observations. Here, we mention only that the use of the collective dust–dust interactions (including long-range attraction and repulsion), which were described in detail in [2], is able to explain qualitatively the difference in the values of Γ observed in different experiments. We will return to this problem in the next part of the review.

Fig. 3. Regular structure observed in the boundary region between the combustion plasma and its condensation region [9].

Let us now describe in more detail the experiments in RF discharge plasmas.

2.2. Observational Techniques

The physical situation is the simplest in RF discharge plasmas, since the crystals are formed in the electric field of the plasma sheath, where the only important forces in the vertical direction are the force of gravity, the electric force of the sheath, and the drag force of the ions accelerated towards the wall by the electric field of the sheath. These are external forces in the absence of dust, and they can be, in principle, measured. The presence of dust can substantially alter them; when this happens, the interdust interaction forces can be important. These effects are of interest in investigations of crystal formation.

The suspension of dust grains against the pull of gravity is realized either electrostatically in the sheath or by neutral gas drag. The latter, of course, is much more difficult to control.

In RF plasmas, the electron temperature is usually ~2 eV, the ion temperature is mostly much lower (by a factor of about 100). The grain kinetic temperature is governed by collisions with neutral gas particles, which are usually at room temperature (in the case of combustion plasmas, the gas temperature may be, of course, substantially higher).

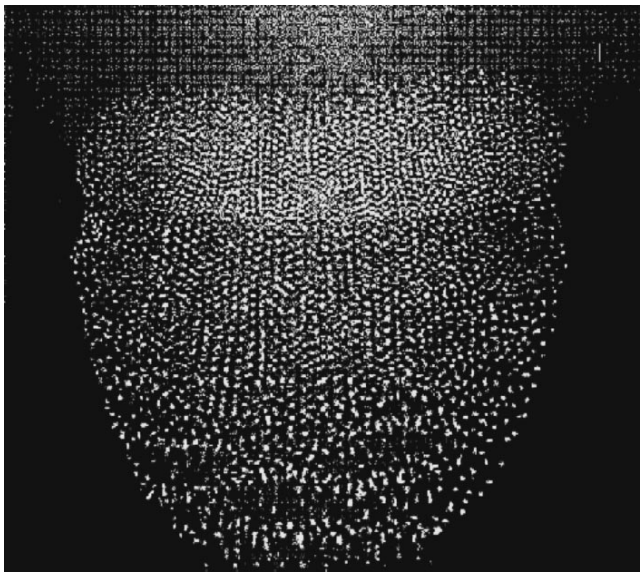

Fig. 4. Structure with the simultaneous presence of crystal, liquid, and gaseous states, observed in a glow discharge [9].

The optical detection system used to locate dust grains is similar in all the systems employed so far. It is shown in Fig. 5 for an RF device as a representative case [11].

The principle is straightforward. The grains are illuminated by a narrow sheet of laser light (e.g., a He–Ne laser) with a thickness of 100 μm and are detected via scattered light using a CCD camera. The optics used to produce the sheet of laser light can vary; commonly, however, this is a combination of cylindrical lenses and reflection mirrors. The thickness of the sheet is smaller than the two lattice plane separations, which makes it possible to pick out a single lattice plain. This system works very well, as shown in the figures above. The laser sheet can be arranged horizontally and viewed from the top, or vertically and viewed from the side, or both. In general, the frame speed of CCD cameras of about 50 Hz is sufficient for most of the processes investigated so far. The reason for this is the slowing-down of the processes due to the large mass (and, thus, inertia) of the dust grains (of course, this does not apply to pure ion or electron modes). The so-called "dust-plasma frequency,"

$$\omega_{pd} = \sqrt{\frac{4\pi n_d Q_d^2}{m_d}}, \tag{1}$$

is much lower than the ion plasma frequency ω_{pi}, since the grain masses are usually 100 billion times larger than the ion mass

$$\frac{\omega_{pd}}{\omega_{pi}} = \left(\frac{n_d Z_d^2 m_i}{n_i m_d}\right)^{1/2} = \left(P Z_d \frac{m_i}{m_d}\right)^{1/2}. \tag{2}$$

In an extreme case, where the electron density is low ($n_i \gg n_e$) and $P \approx 1$, we obtain

$$\frac{\omega_{pd}}{\omega_{pi}} \approx \left(Z_d \frac{m_i}{m_d}\right)^{1/2}, \tag{3}$$

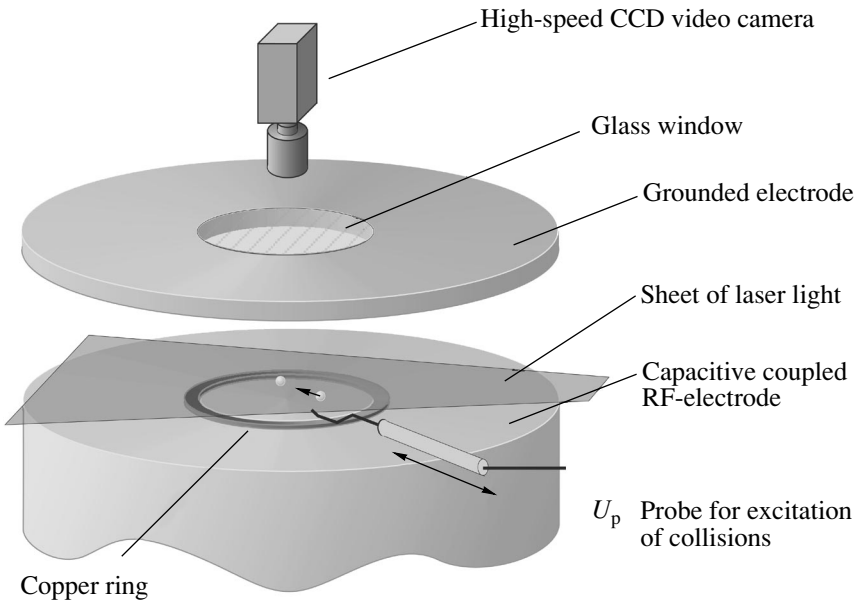

Fig. 5. Schematic of an optical detection system used to locate dust grains (as an example, the system used in an RF device is shown) [11].

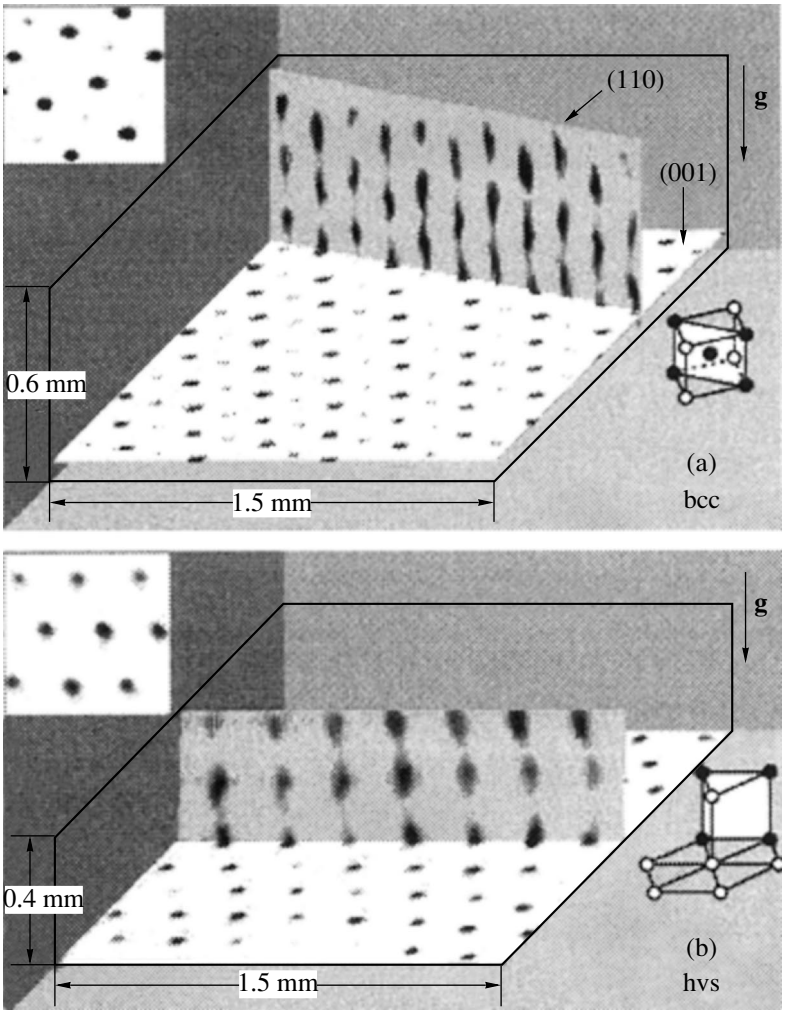

Fig. 6. Images of (a) body centered cubic (bcc) and (b) hexagonal vertically stacked (hvs) systems in a 3D plasma crystal formed by 9.4-μm-diameter polymer spheres in a krypton discharge at a pressure of 1.4 Torr [17]. In each image, one horizontal plane and one vertical cross section are shown; the insets show the vertical plane viewed from above. The data present a stack of the horizontal planar images resolved by selective illumination by a 90-μm-thick swept ribbon laser beam. The grain images appear to be longer in the vertical direction due to the infinite thickness of the laser beam.

which is 10^{-4} or less under typical experimental conditions. Since the ion plasma frequency in a typical RF plasma (under the conditions used for complex plasma investigations) is ≈1 MHz, we see that, up to the dust plasma frequency, the processes are readily observable using conventional CCD cameras. For more detailed applications, cameras with a much higher frame rate are available too.

By scanning through the system, it is possible to study the full 3D structure. This technique has been successfully employed in experiments on plasma crystals [4–7, 10–15]; however, it is still too slow for 3D observations of phase transitions. Hence, one of the main research goals—the 3D investigation of critical processes (such as melting or sublimation) at the kinetic level and the comparison of the experimental results with the macroscopic properties of complex plasma—has not yet been reached. Two-dimensional investigations of the melting transitions have already been made and will be discussed later.

2.3. Crystal Structure

Most experiments have resulted in the observation of dust grains arranged in a simple hexagonal structure where the grains are arranged horizontally on a triangular lattice with one grain above another vertically. The early investigation in [3] reported the simultaneous coexistence of the body-centered cubic (bcc) and face-centered cubic (fcc) crystalline structures under certain experimental conditions. These results are based on the visual observation of various lattice planes coming into view while adjusting the microscope focus.

The first determination of the 3D structure of plasma crystals with the use of separate horizontal and vertical laser sheets was performed in [5] (see Fig. 6). These results were obtained in 1.4-Torr krypton plasmas formed by applying a 13.56-MHz RF voltage with a power of 2.3 W with nearly monodisperse (9.4 ± 0.3 μm) spherical polymer dust grains injected into the discharged volume. The measured electron temperature was 8 eV, while the electron density varied from 3.2×10^8 to 1.8×10^9 cm^{-3}. The bcc and hexagonal vertical stacked (hvs) structures (no fcc structures) were observed. These structures can coexist under certain conditions; under other conditions, the entire volume is occupied by either bcc or hvs structures. The free energy of different types of structures is different, and the possibility of their coexistence is apparently related to the inapplicability of the concept of free energy to complex plasmas. The latter is also confirmed by the observations of hvs structures. The parameters important for estimating the possible physical reason for the vertical stacking are the size of the dust cloud, which was 2 mm, and the average intergrain spacing in the horizontal direction, which was 195 ± 1 μm. These investigations [17] suggested that the plasma crystal structure can often be an hvs structure; this is an unexpected state for ordinary crystals, since the minimum free energy principle suggests that fcc or bcc structures should be formed in ordinary crystals. This is confirmed by molecular dynamic simulations [17, 18]. The observations imply that an additional energy source is required to keep the plasma crystal in the hvs state (which is an excited state for thermal systems). On the other hand, this is what can be expected for complex plasmas. We emphasized earlier that complex plasmas are open systems, and it is not surprising that, in open systems, the crystal structure in the ground state is different from ordinary matter. There should always exist energy source in complex plasmas. It can be identified as the energy flux of plasma ions in the sheath, resulting in anisotropic screening [19–29], or as an energy source due to ionization, as discussed before for the homogeneous ground state of complex plasmas. In fact, the two energy sources have the same origin, since the ion flow appears in the sheath due to the constant volume ionization maintained by the RF power. Thus, one can regard the basic state as that discussed in [2]; one must, however, account for the inhomogeneous conditions related to the wall sheath. Here, we will assess which of the two possible anisotropy effects are important: the anisotropy due to the single-grain wake-field effect or the anisotropy due to the collective wake-field [2]. Obviously, a crystal is formed by many grains. By the term single-grain effect, we mean that the interactions of many grains can be considered as a sum of the pair interactions of each grain with all others. In this case, the assessments can be made by considering a single grain (or, more exactly, the interaction of a pair of isolated grains) and then summing up the result obtained over many grains. Note that, in this case, the flow produces a drag force, anisotropic screening, and an induced component dipole (in addition to the electrostatic charge monopole field of the grain itself) due to the concentration of ion charge behind the grain in the direction of the ion flow. With two grains, the interaction becomes much more complicated.

In the case of collective effects, even two-grain interaction depends on the average dust density in the system and the dust–dust interaction becomes collective (as was demonstrated in [2]). Both the collective [29] and the noncollective [20–29] wake-field interactions lead to an anisotropy that is higher in the collective case than in the noncollective case.

Let us consider in more detail why in the noncollective case the dust–dust interactions can be different along the direction of the ion flow and perpendicular to this direction. The noncollective case corresponds to a dust cloud of small size: $L < L_{cr}$, where L_{cr} is the size at which noncollective pair interactions are substituted with collective interactions. For most of the experiments discussed above, this criterion is not fulfilled, while it is fulfilled for the dust clusters discussed below. Nevertheless, it is reasonable to discuss the conditions under which the interactions can be regarded as the sum of pair dust interactions and the concept of nearest neighbors can be introduced (at least for not long-range interactions). Generally, the interaction of two dust grains is mediated by the complete plasma response and is affected by nonlinear effects. If a grain is not isolated, the nearest neighbors interact in six different ways. Denoting the grains by p and the screening cloud by s, we obtain the following interactions: p_1p_2, s_1s_2, p_1s_1, p_2s_2, p_1s_2, and p_2s_1. Also, the neighboring grains partially shield one another from the collisions with ions and neutrals with the net effect of either a noncollective or a collective force. All these forces can play a role in the formation of a crystalline structure or small-size clusters.

The situation becomes even more complicated if the ion flow is supersonic or even subsonic, when the drift velocity is close to the speed of sound. The perturbation of the flow (and the associated potential) by the "upstream" grain can then be readily communicated to the "downstream" grain, but not vice versa, provided that the information is transferred by ion-acoustic wave (for the supersonic case) or Landau damping (for the subsonic case). Hence, there is a fundamental asymmetry in a complex plasma system with ion drift, which is ultimately caused by gravity. The reason for this is that the grains require the sheath electric field determined by $m_d f = Q_d E$ for suspension (levitation in the gravity field). The same electric field causes the ion flow toward the lower electrode and, hence, provides the source of energy and the openness of the system. The situation is further complicated by large dust grains making the responses nonlinear. In this case, the linear ion dielectric constant can be used only at rather large

distances from the grains (larger than the ion Debye length or even larger than the electron Debye length).

For the noncollective case, the numerical results for the interaction of two grains in the presence of an ion flow [28] confirm the presence of asymmetry and the formation of a positive ion charge behind the grain, which can serve as a potential well for another grain. This mechanism was checked experimentally in [24] for the interaction of two grains. The main question for the interpretation of experiments is: Are these types of interactions relevant in the formation of a crystal or should other interactions (such as collective attraction) be substituted for the wake interactions? The collective wake also produces an asymmetry; however, this effect is weaker and can produce only the alignment of grains along the ion flow, while the other (collective) effects produce the main potential well forming the crystal. Certainly, the presence of a crystalline structure perpendicular to the flow cannot be explained by this asymmetry. Thus, the use of the attraction forces seems to be necessary for the explanation of the effects observed.

For our estimates, we will use the relations for the elementary physical processes in complex plasmas [2]. Assuming that the ion temperature corresponds to the room temperature ($T_i = 0.025$ eV), the ion Debye length is ~35 μm. A criterion for the collective interaction to operate is that the size of the dust cloud L be larger than $L_{cr} = \lambda_{Di}^2/aP_0$. From the data of [17], we can assume $P_0 = n_d Z_d/n_i \approx 0.3$ and $\lambda_{Di} \approx 35$ μm. Thus, we obtain $L_{cr} \approx 0.43$ mm, whereas the size of the dust cloud was ~2 mm, which means that the collective interactions were dominant. However, the ion temperature in the existing experiments is not well known; hence, if we assume to be larger, it could be that the conditions of [17] were on the border between the collective and noncollective cases. (At least they are closer to the collective case than to the noncollective one.) In [17], the estimates were made using the noncollective case. For both cases, the anisotropy needed for an hvs structure to exist is predicted.

Our estimates of the noncollective interaction do not yield an intergrain distance in the plane perpendicular to the flow, which agrees with observations. In the noncollective case, it should be larger than the electron Debye length $\lambda_{Di} \approx 450$ μm, whereas the observations give ≈200 μm, which is about half as much as that estimated by the noncollective effects. The discrepancy is not large; nevertheless, the electron temperature and the electron density are well measured, and to stretch the parameters in order to reduce the Debye length twice is not easy. For the collective case, the simplest is to estimate the effect in both extreme cases: when the collective parameter $\eta_{coll} = a^2 P_0^2 z_0^2 \alpha_{dr}\alpha_{ch}/(1+z_0)\lambda_{Di}^2\tau$ (see [2, 30]) is small and when it is large. In the case $\eta_{coll} \gg 1$, the grain–grain interaction is determined by collective effects and the intergrain distance should be on the order of $\lambda_{De}/\sqrt{P_0} \approx 800$ μm, while the observed spacing is ≈200 μm. In the opposite case, $\eta_{coll} \ll 1$, the collective effects do not change the screening but are still dominant in the dust–dust attraction; hence, the intergrain distance should be ≈160 μm, i.e., less than that observed. An estimate of the η_{coll} for the data of this experiment is $\eta_{coll} = 0.615$ (for the dimensionless charge in Xe plasma $z_0 \approx 2.5$ and for $\tau \approx 0.006$); i.e., it corresponds to an intermediate case.

Both estimates for the collective and noncollective cases are rough, since they do not take into account the nonlinearities that could be of importance.

The alignment in the presence of an ion flow is not observed in some experiments. An example of this is the observation of the crystal structure under gravity conditions in the sheath in the presence of an ion flow [26]. The experiments were performed in a symmetrically driven directly coupled RF discharge in argon at a pressure of 0.47 mbar (see Fig. 7). The 3D structure was determined by scanning a vertical laser beam horizontally across the system and recording the position of each grain with a CCD camera in x, y, and z. The diameter of dust grains was 3.375 ± 0.102 μm. The scanning speed of the laser beam (and the CCD camera) was 0.30 mm/s. The total scan took 18.3 s. The experiment showed that the plasma crystal is very stable at these conditions.

Due to the finite width of the laser beam, the dust grains are typically seen on 15 consecutive video images. This is the reason why, in the horizontal image, the grains are apparently elongated. The actual grain position is located at the center of the elongated light trace.

Grains with a size of 3.7 μm were injected into an argon plasma at a pressure of 0.47 μbar. The size of the dust cloud was about 3 cm. The total number of grains was 2×10^4, which corresponded to the average density 2×10^3 cm^{-3} and $P_0 \approx 0.04$–0.05. The critical length was $L_{cr} \approx 0.7$ cm, which was substantially smaller than the size of the dust cloud. Thus, in this case, collective interaction should be dominant. However, due to the small value of P_0, the collective parameter is small, $\eta_{coll} \approx 10^{-3}$; hence, in the perpendicular direction, where the influence of the ion flow is small, the intergrain distance estimated from collective attraction is $\approx \lambda_{Di}\ln(1/\eta_{coll}) \approx 242$ μm. The observed intergrain distances are presented in Fig. 8 [26].

In [26], the noncollective interaction was estimated in the model of the shielded Debye potential. In this case, one should keep in mind that $\lambda_{Di} \approx 35$ μm, while $\lambda_{De} \approx 350$ μm. With allowance for the ion flow, which makes the shielding equal to or larger than the electron Debye length, the value of the latter is somewhat larger than that observed. Gravity influences the structure since, with an increase in the vertical distance z, the spacing between grains increases. In the framework of the model of collective attraction, this could be related to the decrease in the ion density in the sheath region

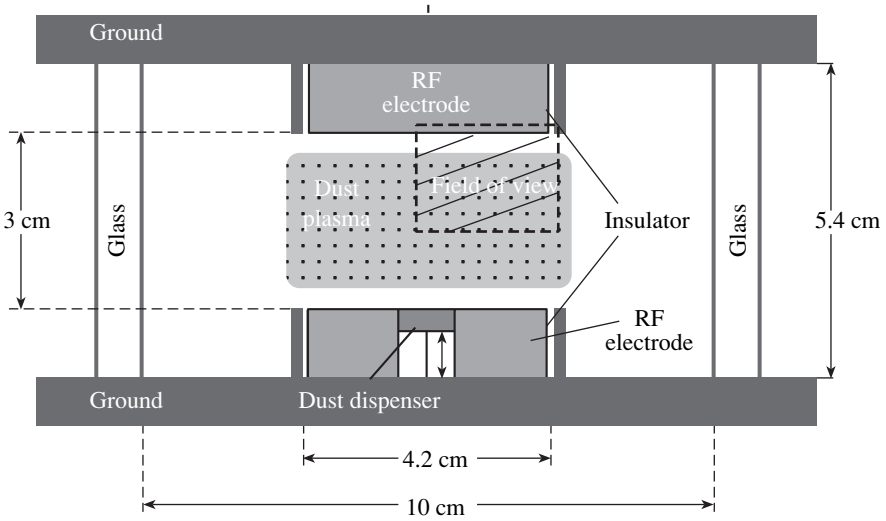

Fig. 7. Schematic of a symmetrical plane-parallel reactor installed in a glass cylinder [26]. A piston covered by a 20-μm wire mesh operates as a dust dispenser. The piston is inserted in the center of the lower electrode. Monodisperse polymer grains 14.9 μm in diameter are injected into the plasma by a remote command. The pressure of the working gas (krypton) is 0.4 mbar. The RF power can be varied. The grains are illuminated by a vertically arranged ribbon laser beam with a thickness of about 100 μm and are imaged using a CCD video camera. Both the camera and laser can be moved horizontally to obtain a 3D image of the plasma cloud. The field of view covers roughly one-fourth of the cylindrically symmetric plasma column. A similar device was used in microgravity experiments carried out both in parabolic flights and onboard the International Space Station (the description of these experiments and the corresponding references are given in Section 6).

with increasing height. Estimates show [26] that gravity can operate as an additional pressure produced by the upper layers. This effect could explain the change of separation between the planes, but not inside the planes. In contrast to the ion density, the electron density in the sheath decreases with height; therefore, the presence of an ion flow in the noncollective model cannot be responsible for such dependences of the grain separation in the plane. Besides this, the ion flow seems not to influence the crystal structure much and is not able to produce an alignment in the vertical direction as in [17]. This is illustrated by Figs. 9 and 10 [26].

The fcc and hexagonal closely packed (hcp) lattices are shown to coexist in the crystal, while the bcc structure and vertically aligned structure were not detected. The absence of alignment in the observed lattice structure indicates that the effect of an ion flow on the intergrain interaction is weak. This could be due to the fact that the alignment is determined by the collective wake interaction, which is proportional to the square of the dust size a^2 (the area of the dust surface) and the square of the dust charge (another a^2). In the experiments in [26], as compared to the experiments in [17], the dust size was 3.2 times smaller, which decreased the collective wake effect by two orders of magnitude.

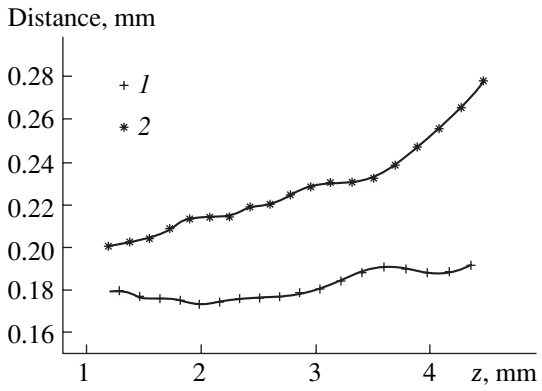

Fig. 8. (*1*) Vertical distance Δ_t between the horizontal planes and (*2*) the mean intergrain distance $\Delta_{x,y}$ in each plane as functions of the vertical position z [26].

An important characteristic of the plasma crystalline state is the binary correlation function defined by the relation

$$g(\mathbf{r}) = \langle \delta n_d(\mathbf{R}) \delta n_d(\mathbf{R} + \mathbf{r}) \rangle. \quad (4)$$

This correlation function gives the probability of finding two grains at a distance determined by the vector **r**. Another correlation function $g(r)$ can be introduced that describes the probability of finding two grains at the absolute value of distance r independently of the angle between the grains (independently of the direction of the vector **r**). This correlation function $g(r)$ describes the radial (pair) density distribution and measures the translational order in the structure. For an ideal crystal at zero temperature, $g(r)$ is a series of δ functions whose positions and heights can be determined from the grain separations in a perfect lattice. Another type of correlation function is the so-called bound orientational function g_6 defined in terms of the nearest neighbor bound angle of the lattice. In a perfect

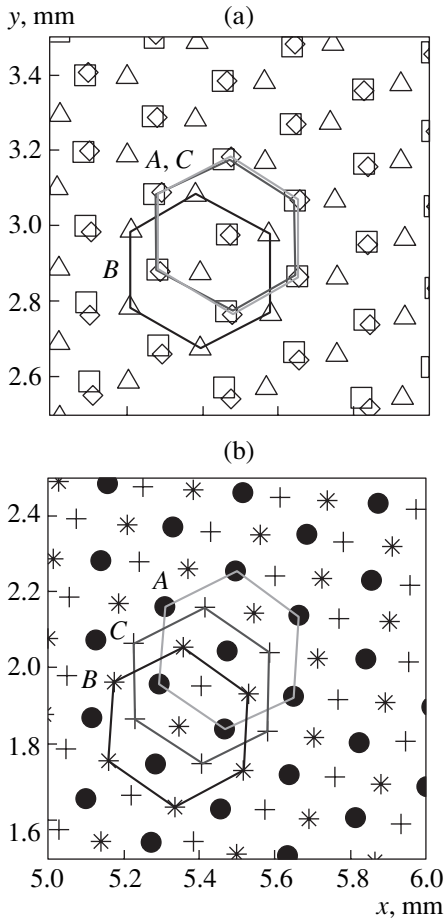

Fig. 9. Top view of three superimposed crystal layers near the bottom of the crystal: (a) the fourth (squares), fifth (triangles), and the sixth (circles) layers (counted from the bottom) form a hcp structure; (b) the first (closed circles), second (asterisks), and third (crosses) form either a fcc or bcc structure with the (111) plane parallel to the electrodes [26].

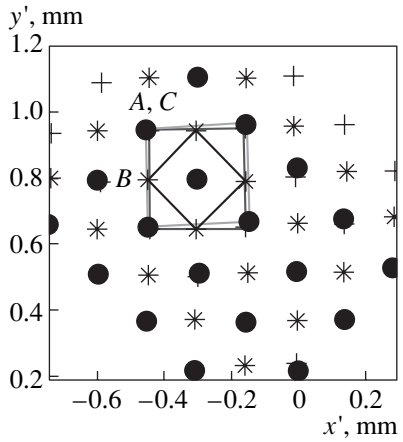

Fig. 10. Determination of the lattice type seen in Fig. 9. The region is shown with an undefined lattice type (fcc or bcc) that is rotated from the (111) plane (x, y) to the (001) plane (x', y'). It is seen that the grains with the first (closed circles), second (asterisks), and third (crosses) planes form an fcc lattice [26].

hexagonal lattice, all bounds should have the same angle modulo $\pi/3$ with respect to an arbitrary axis. For a perfect hexagonal crystal at zero temperature, g_6 is a constant equal to unity, while for other phases, it decays with r. It is accepted for ordinary matter that, in the crystalline phase, $g(r) \propto r^{-\eta(T)}$, $\eta(T) < 1/3$, and $g_6 =$ const, while in the liquid state, both correlation functions decay with distance exponentially, with a factor in the exponent which characterizes the degree of the translational and orientational order.

From the early (basically two-dimensional) measurements in [27], it was possible to calculate the 2D pair correlation function $g(r)$ in a given horizontal plane. One such result is shown in Fig. 11, which shows the normalized pair correlation function versus the normalized distance.

To fit the measurements, it was assumed that the δ functions are Gaussians attenuated by an overall envelope:

$$g(r) = g_0 \exp(-r/\xi). \quad (5)$$

In Fig. 11, the triangles show the measured values of the pair correlation function, while the solid line shows their least squares fit. The locations of the peaks expected for a perfect hexagonal lattice are indicated by the vertical lines, whose lengths correspond to the relative heights of the peaks. The fit yields the mean intergrain spacing $\Delta = 270$ μm, $\eta = 0.059$, and the Debye–Waller factor $b = 0.013$ (see below).

The decay of the translational order can be expressed as an exponential decay factor $\exp(-\eta\Delta)$. Here, Δ is the mean grain separation and $1/\eta$ is the correlation decay length. The transition between the ordered ($\eta\Delta \ll 1$) and disordered ($\eta\Delta \gg 1$) states occurs at $\eta\Delta \approx 1$ [27]. In the example shown in Fig. 11, $\eta\Delta \approx 1.6 \times 10^{-3}$, which signifies a high degree of order. The Debye–Waller factor b is 0.013. The measured correlation function g_6 is presented in Fig. 12. Fitting $g_6(r)$ by an exponentially decaying function $\propto\exp(-r/\xi_6)$ yields the scale length $\xi_6 = (1.4 \pm 0.1)\Delta$, while fitting by a power-law function $\propto r^{-\eta}$ leads to the coefficient $\eta = 1.05 \pm 0.05$ as displayed in Fig. 12.

The pair correlation functions were measured in [26]. Figure 13 clearly shows the presence of both the fcc and hcp phases, but not the bcc phase. This observation is not surprising because of the openness of the system and the fact that the results of simulations predicting a bcc lattice structure are inapplicable for sufficiently large values of Γ. The detailed investigation shows that both the fcc and the hcp crystalline structures occur in different regions (domains) of the plasma crystal separated by some unidentified intermediate structure [30].

Figure 14 shows the result of the first observations of a bcc lattice [5]. The 3D structure was measured using a revolving mirror to sweep the sheet of laser

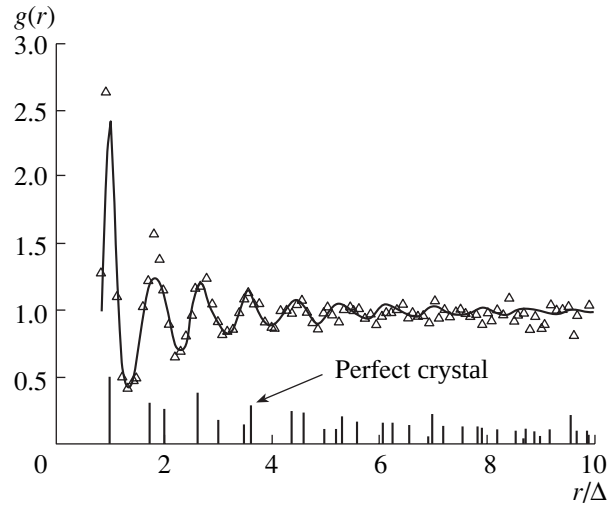

Fig. 11. Pair correlation function g normalized to the average surface density of the grains (1200 cm^{-2}) vs. normalized distance r/Δ [27]. The experimental results are shown by the symbols, while the solid curve shows the best fit correlation function. The segments of vertical lines on the abscissa show the correct positions and relative heights of the correlation peaks in a perfect crystal. The mean intergrain spacing and the correlation length yielded by the fit are $\Delta = 290$ μm and $\xi = 2\Delta$, respectively.

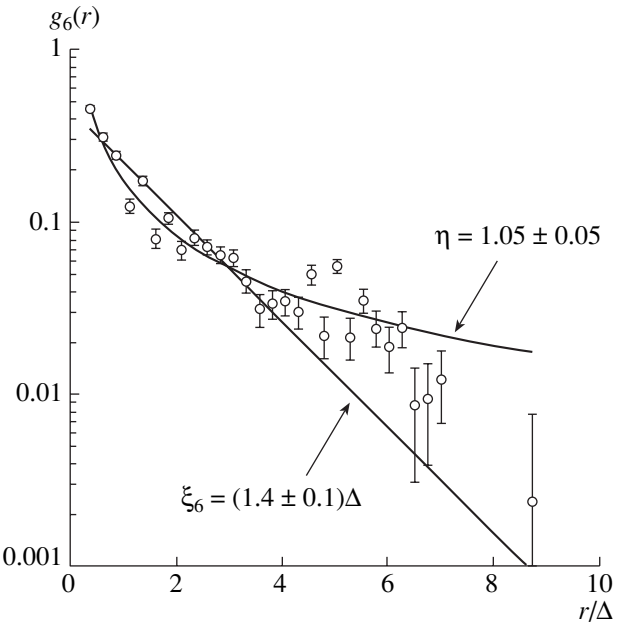

Fig. 12. Bond angle correlation function g_6 vs. normalized distance r/Δ [27]. The experimental results are shown by the symbols. The solid curves show the exponential and power-law fits, ξ_6 and η, respectively.

light across the system and, thus, to consecutively illuminate different lattice planes.

The largest 3D plasma crystal observed in the laboratory so far has 19 vertical planes and about 40 horizontal planes [27]. By normal crystal standards, this is still quite small; the system contains only about 3×10^4 grains. Nevertheless, it marks major progress in this field.

At the end of this description, we list the major characteristics of the observed plasma crystals with the hvs lattice structure.

Wigner–Seitz cell (2D): (2D), $A_S = \frac{\sqrt{3}}{2}\Delta^2 \approx 3.5 \times 10^{-4}$ cm^{-2}.

Wigner–Seitz radius (2D): (2D), $r_S = \left(\frac{\sqrt{3}}{2}\right)^{1/2}\Delta \approx 0.019$ cm.

Wigner–Seitz cell (3D): (3D), $V_S = \frac{\sqrt{3}}{2}\Delta^3 \approx 6.9 \times 10^{-6}$ cm^{-3}.

Wigner–Seitz radius (3D): (3D), $r_S = \left(\frac{9}{8\pi\sqrt{3}}\right)^{1/3}\Delta \approx 9 \times 10^{-3}$ cm.

Separation of the lattice planes: $d = \frac{\sqrt{3}}{2}\Delta \approx 0.017$ cm.

Ion Debye length: $\lambda_{Di} \approx 0.0035$ cm.

Electron Debye length: $\lambda_{De} \approx 0.03$ cm.

Lattice wave speed: $v_L = \sqrt{\alpha^*\Delta/m_d} \approx 5$ cm/s (definition of α^* see below).

Debye frequency: $\nu_D = v_L/\pi\Delta \approx 80$ s^{-1}.

Gruneisen constant: $\gamma = (\Delta/c_L)dc_L/d\Delta$.

Compressibility: $\beta = \delta r_S^2/T$.

Of course, for other lattice structures, the geometry and, hence, the characteristic parameters will be slightly different.

More sophisticated experiments can be carried out as the understanding of these newly discovered plasma states grows and the advanced technology for their investigation is being developed [9, 11, 27, 30–32].

Let us emphasize the main unusual aspects in the physics of complex plasma condensation and the existing understanding of the observations of plasma crystal formation.

(i) Strong coupling in usual matter can be achieved due to the presence of chemical bindings. For small particle kinetic energy, these bindings can result in long-range interactions and the formation of usual crystals. In the absence of molecular attraction, free-boundary crystals are difficult (and may be impossible) to create in usual matter.

(ii) In complex plasmas, the molecular binding is negligible and collective and noncollective attraction can serve as mechanisms for the formation of plasma crystals. The criterion that the kinetic grain energy is

small as compared to the Coulomb interaction energy is insufficient to provide crystal formation. Numerical simulations using periodic boundary conditions seems to be inadequate for complex plasmas. A free-boundary Coulomb system without attraction is always unstable and cannot be in the crystalline state; however, in complex plasmas, free-boundary crystals can be created.

(iii) Most of the experiments in which plasma crystals were observed correspond to the case of collective attraction where the interaction with remote grains influences the interaction between neighbor grains, which is quite unusual.

(iv) The openness of complex plasma systems introduces a fundamentally new physics in which the collective plasma flux, which provides both the attraction between each pair of grains and the self-confinement of a system with a collective flux, plays a major role. The coexistence of different crystalline structures can be explained by the presence of external sources providing a flow of energy into the system.

(v) It is quite probable that plasma crystals, when not confined externally, are limited in their size.

(vi) The free energy concept used in the ordinary crystal problem often does not operate in complex plasmas, due to the openness of the system.

We should make some remarks in connection with these statements.

The first point is that most of the processes discussed in the previous parts of this review [1, 2] and related to the openness of the system can play a significant role in the formation of a plasma crystal. However, we were able to give here only a rough estimate using the described elementary processes in complex plasmas. Detailed theoretical models are still waiting to be developed in order to make a final conclusion on the role of the attraction forces in complex plasmas. Future experiments are also necessary in which many important parameters can be varied, such as the grain size (to make the crystal formation independent of the grain weight, the grains should be hollow), the ion temperature, and the parameter P_0. The only conclusion that is generally clear is that the ground state should be determined experimentally and can be different for different plasma sources. In this sense, the observed structures correspond to the ground state for the particular sources used in particular experiments.

The second point is the observed inhomogeneity of plasma crystal structures. The volume of a crystal actually scanned is shown schematically in Fig. 15. Only about one-half of the cylindrical system was actually measured. The approximate location of the observed fcc and hcp zones is marked. There is some tendency for the fcc structure to be located in the central region of the system, whereas the hcp structure is at the periphery. This points to a radial variation (albeit a subtle one) in the crystal ordering parameters. Presumably, there are radial pressure gradients in addition to the observed vertical gradients; i.e., the crystal is inhomogeneous.

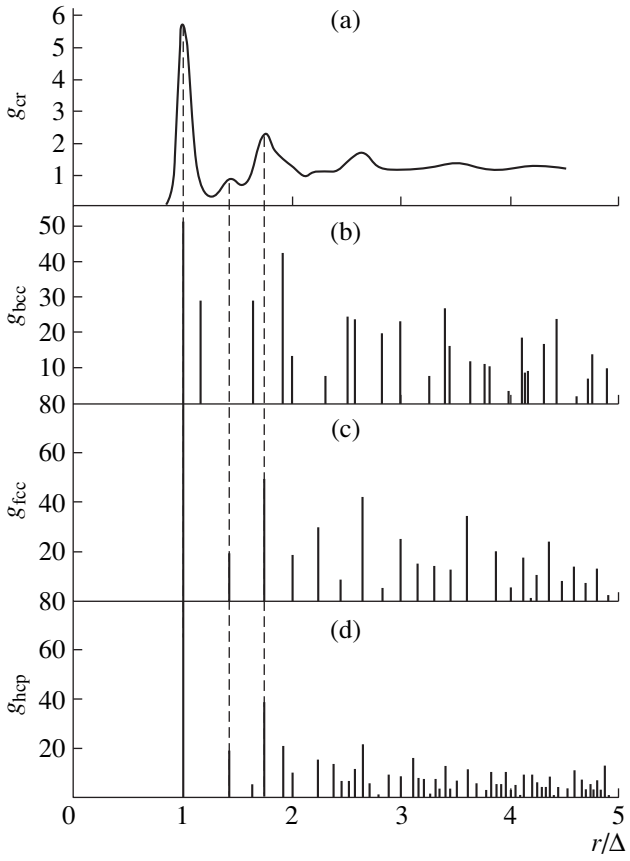

Fig. 13. (a) 3D correlation function $g_{cr}(r)$ averaged over the viewing field, and the correlation functions for a perfect lattice types: (b) bcc, (c) fcc, and (d) hcp [26].

This is not surprising, since the state preceding the crystal has the general properties to form an inhomogeneous state (see Section 4.4, devoted to the structurization and instabilities of complex systems). Also, the forces between dust grains can be different because of the different values of the drift velocity at the center and the periphery (note that in the case where gravity plays an important role, the change in the drift velocity can result in a state with different plasma parameters). The ratio of the intergrain forces to the vertical bulk forces are different at the center and at the periphery. The bulk forces are always needed to suspend the grains by electrostatic fields (the drag force acts at the lower plate sheath in the same direction as gravity). In the horizontal direction, the balance of the bulk field does not play a significant role or is much smaller if the drag and electric fields are not strictly vertical. This seems to be significant enough to influence rather subtle energy differences between fcc, hcp, and bcc lattices. In other words, the center and the periphery could be in different external source conditions. The questions naturally arise as to whether this inhomogeneity will increase with increasing the crystal size and whether a very large plasma crystal can be created. This point has not yet been investigated experimentally. If the size of the

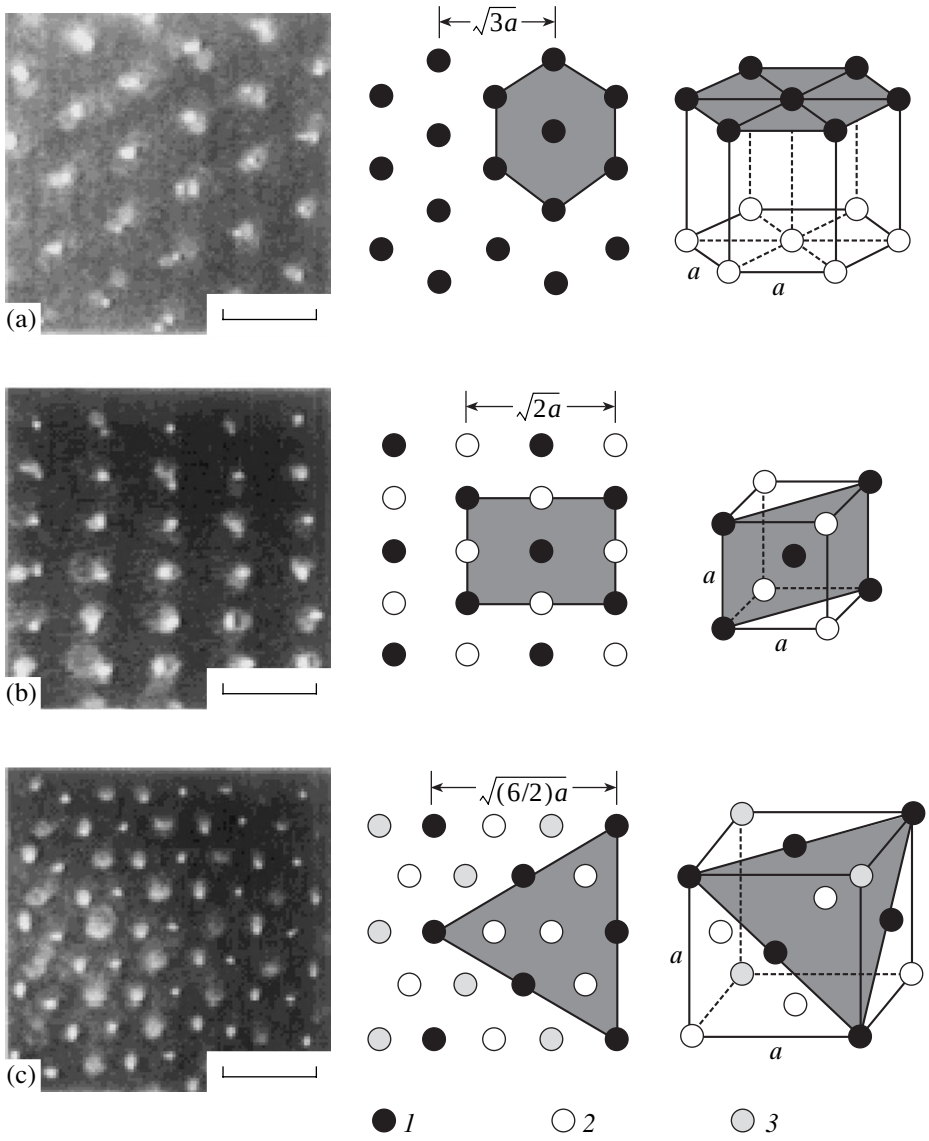

Fig. 14. Microphotographs and sketches of different crystalline structures: (a) hvs, (b) bcc, and (c) fcc [5]. The central column corresponds to the structures observed in the microphotographs. The shaded area in the sketches is normal to the optical axis. The bars correspond to 200 μm. The circles show the grains located in the (*1*) first, (*2*) second, and (*3*) third layers.

plasma crystal is universally limited, the situation will be different from ordinary matter, in which there are no obvious limitations on the crystal size (although an increase in crystal defects can limit the maximum possible size). Obviously, this is an experimental problem, which is, however, also of general physical interest, since solving this problem will allow one to answer the question of whether there are general physical processes that restrict the existence of large-size plasma crystals.

Let us discuss the topics that are of interest for future research and that can be formulated now by using the results of the existing experiments:

(i) It is important to investigate the transition regions between different lattice structures on the microscopic (the kinetic) level, the geometry of the structural transition, its stability and dynamics, and its responses to several types of small vibrational perturbations (e.g., to answer the question as to whether 3D annealing is possible).

(ii) It of important to investigate how the change of the global energy supply can change the type of the crystal structure (possibilities include altering the rate of gas cooling or the RF power). Is it possible that, by changing the energy supply, the region occupied by one type of lattice will grow, and finally only one type of structure will be present. In this case, it would be of interest to study how the growth of crystals occurs.

(iii) It was established that the observed lattice structure should be considered as a ground state of a

crystal in an open system and that this structure depends strongly on the energy sources. The question is, how the crystal structure will depend on the ground state of the complex plasma system.

(iv) Is it possible to determine time scales for the propagation of, for instance, fcc/hcp transition fronts, and to investigate how such propagation depends on the external experimental parameters determining the energy supply to the system.

(v) A very interesting research topic is the investigation of "force-free" crystals under microgravity conditions. The microgravity excludes the gravity field from the bulk balance equation and does not need the electric field to support the grains against gravity. Thus, in the balance equation, only one term will be absent, namely, the gravity term. Therefore, no electric field is needed, but the force-free conditions require also that the other two terms, namely, the drag force and the electric field force, be absent. This means that the grains should also be far away from the walls. However, any experiments in microgravity conditions will include walls of the chamber. The first microgravity experiments, which were only recently performed, will be discussed at the end of this part of the review. They show the simultaneous presence not only of the plasma crystal discussed above, but also of the void structures and convection structures discussed below.

(vi) It would be of interest to find the conditions under which the grains that start to form the crystal are far away from the walls and far from any other electric fields, which will cause the ion drift and the ion drag forces. In this case, the complete force-free conditions will be reached. The main requirement is that the gravity, electric field, and drag force have a weak influence on the intergrain interactions. Somehow, the grains should be confined in this region by some forces, and the question is whether these forces will alter the interaction. Thus, the problem is not so simple; however, from the physical standpoint, it seems to be solvable. The physics lie in the presence of a collective flux created by all the grains forming a crystal. This flux can create, in principle, a sufficient ram pressure to confine the system. This will be a *natural self-confinement*. A crystal of this kind should be called a free-boundary crystal. It would be of interest to investigate whether free-boundary plasma crystals can be created and what type of crystalline structures they will have.

(vii) It is very important to investigate experimentally the details of the dynamics of the crystalline state on the kinetic level.

Note finally that comprehensive experimental investigations of a recently discovered new plasma state, such as plasma crystals, also benefit other related research, as has often happened in the past.

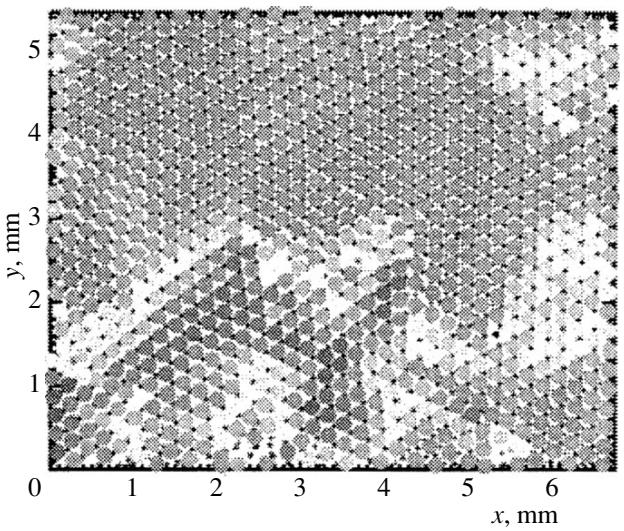

Fig. 15. Coexistence of fcc (dark) and hcp (light) lattices in the middle of a plasma crystal (from the eighth to tenth horizontal layers) [26].

2.4. Dislocations and Defects in Plasma Crystals

The crystalline plasma states exhibit crystal defects and dislocations in a way similar to that which their better known "normal" crystalline counterparts in ordinary matter do. We mentioned this in the previous chapter, in connection with the transition from the fcc crystalline structure to the hpc structure (see Fig. 15).

A self-consistent 3D analysis of crystal defects remains to be done; however, there is a large amount of available experimental data on 2D- and 2.5D-dimensional plasma crystals (see, e.g., [11, 26, 30]).

In 2D crystals, in which lattice planes are usually horizontal, the well-known hexagonal structures dominate. The lattice defects involve a local breakup of this hexagonal structure, the most common (and simplest) defect being the "7/5 defect," in which two interlocking cells represent a septagon and a pentagon.

Such lattice defects occur at the ends of the so-called "lattice line." Other lattice defects involving only two cells are possible in principle (e.g., 6/4 defects), but they are not favored in terms of energy (when speaking about energetic favoring in an open system, we mean the total energy spent on the formation of a dislocation, including the external energy; for instance, the ionization source energy). In this sense, defects involving three interlocking cells (e.g., 7/5/7 or 5/7/5 defects) are more probable.

So far, no systematic investigations of the energetics of defects have been performed. These should be very precise investigations that include measurements of the vibrational energy of the grains in defect cells, the measurements of the change in the defect cells, and the measurements of the energy supplied from an external source, as compared to its mean value without defects. It has been noted that the grains in defects tend to be

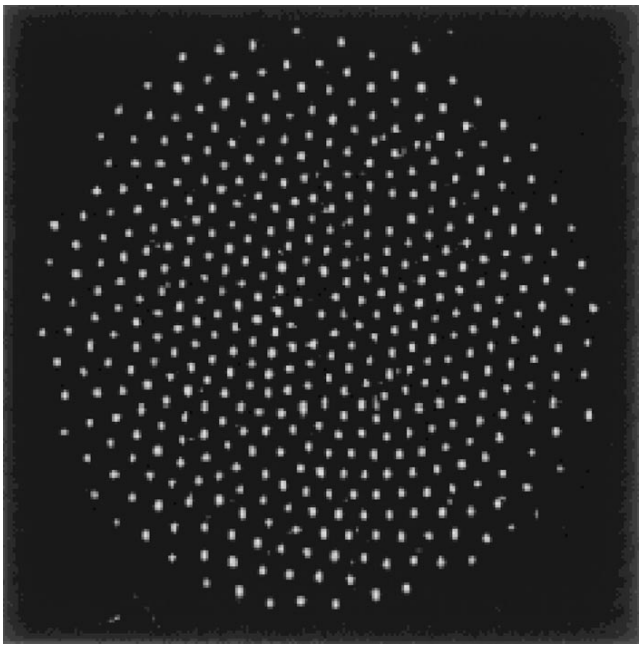

Fig. 16. An example of 14-mm-diameter single-layer plasma crystal formed in a parabolic well above the lower electrode [36]. The total number of grains is 434, the power deposited in the plasma is 4 W, the pressure is 100 mTorr, and $a = 0.5$ μm.

more excited (in terms of their vibrational energy) than on average in the crystal, which could be an indication that the external energy supply at the location of the defects might be larger. Local defects can probably be created by a local change of external energy supply, such as a local change of ionization. Such experiments have not been performed so far. Also, the energy states of the observed lattice defects have not yet been computed or measured.

The first, rather promising step in this direction is the investigation of the deformation energy of small systems involving small numbers of grains. The technique, which was employed for the first time in [33], is to "push" individual grains through radiation pressure using a laser beam and to determine the conditions at which slippage occurs, i.e., the system no longer rotates as a solid body. The measurements show that a small system containing magic numbers (12, 19, …) of grains has a greater binding energy than the others. The reason lies in the sixfold symmetry. This latter point will be discussed later in connection with "ordering rules" [34]. The question as to how this ordering can be influenced by the change in the external source was not investigated, but it is clear that this problem can be more relevant for a set of several separated small systems that do not form together a crystal, or small systems coexisting against a homogeneous background of a "sea" of other (smaller or larger) dust grains forming or not forming a strongly correlated state. It is clear, however, that this problem, namely, the microscopic study of defects at the kinetic level, including the defect migration and annealing using periodic changes in the energy source (e.g., using a chopping laser sheet [35]), is a very promising field for future research. The application of the results obtained to systems in ordinary matter may be beneficial for other fields of science. This may be of particular relevance for surface physics involving monolayers (see below about monolayer plasma crystal). In addition, the 3D nature of the observed dislocations, i.e., the length of the dislocation lines and their (probably fractal) structure, has not been investigated so far. Here, we have to await the planned microgravity experiments (low-stress or "force-free" experiments), whilst systems experiencing comparatively high gravitational stresses can be investigated quite soon.

2.5. Monolayer Plasma Crystals

There are two studies that can be performed using complex plasma monolayers. First, there are the studies of isolated monolayers, suspended electrostatically against the force of gravity. Most of the present monolayer experiments are of this type. They include wave propagation and dispersion analysis, melting and sublimation experiments, and crystal defect studies.

Second, there are the studies of attached monolayers (e.g., those consisting of smaller grains) located at the top of another monolayer (of larger grains), or at the top of a system containing several lattice planes (of larger grains), or a system of larger grains in an uncorrelated state. Experiments of the second type have not been reported in the literature so far, but promise to be very interesting from the standpoint of basic physics.

At present, the formation of a monolayer crystal requires grains in a very narrow mass range because of the vertical force balance dictated by the presence of gravity. In addition, the equipotential horizontal planes of the levitating field should be significantly extended in order to produce large systems. RF and inductive discharges appear to be best suited for the latter requirement, and the experiments reported on monolayer investigations utilize such plasma devices [36, 37]. Figure 16 shows the structure of a monolayer crystal observed in [36].

Monolayers possess a number of specific features:

(i) Wake fields generated by the ions accelerated in the sheath do not play any significant role in grain interactions. In particular, if the ion flow is supersonic, information about the ion focusing in the wake below the grain cannot propagate upstream or in the perpendicular plane.

(ii) Parasitic charge depletion is not important, since the supply of electrons and ions comes from the top or bottom (i.e., in the direction perpendicular to the plane of the monolayer). This means that the grain charge should not vary systematically (e.g., in large 3D systems, one might expect a reduced value of the charge at

the center of the system). The reduction of the charges due to their mutual interaction in the plane survives, but this is a part of the dust–dust interactions resulting in a strongly correlated state.

(iii) In the case of a monolayer located on the same equipotential surface, the plasma parameters of relevance, e.g., the Debye length, the temperatures of ions and electrons, the ion flow velocity, etc., should be the same everywhere. Of course, this homogeneity depends on the quality of the plasma chamber design.

(iv) A dust grain monolayer will not modify the electron and ion components of the plasma as much as a system containing many layers. Hence, these species may to a large extent be treated separately. In particular, this means that the sheath models calculated without the presence of dust grains retain their usefulness to a significant extent.

(v) Monolayers are easy to manipulate in a controlled way, e.g., using lasers. In particular, this is due to the lack of interactions with neighboring dust layers, as well as to the smaller total mass of dust grains involved.

All this makes monolayers particularly interesting from the point of view of their application for controlled deposition. From the standpoint of basic physics, active experiments, e.g., experiments on waves, shocks, shear flows, etc. (see below) are of particular interest.

In the first deposition experiments, a monolayer crystalline structure of melanin-formaldehyde grains was formed in suspension and was then deposited on the substrate by simply turning the plasma source off. In this case, the deposition accuracy is about 15 μm.

Let us consider the problem of the constancy of the grain charge in a monolayer. There is a simple experimental test for this. We have already referred to the equilibrium condition for the levitation of charged grains in the electrostatic field of the sheath and the drag force field of the ion flow in the sheath, particularly in connection with the determination of the form of the shielded potential around the grains used in collision experiments. One of the earliest techniques for determining the grain charge was to excite vertical oscillations [37]. The method is as follows. Assuming, as in [37], that the drag force is small, we obtain for the equilibrium position x_0 of a grain

$$m_d g = QE(x_0). \tag{6}$$

For small deviations from x_0, we may expand the electric field in powers of $x - x_0$:

$$E = E(x_0) + \frac{\partial E}{\partial x}(x - x_0) + \ldots, \tag{7}$$

where the higher order terms are ignored and the derivative $\partial E/\partial x$ is assumed to be constant. If the grain charge Q is constant, then the electric and gravitational forces form a parabolic potential well,

$$V = \frac{1}{2}Q\frac{\partial E}{\partial x}(x - x_0)^2, \tag{8}$$

which has a resonance frequency

$$\omega_0 = \left(\frac{Q}{m_d}\frac{\partial E}{\partial x}\right)^{1/2}. \tag{9}$$

Modulation of the lower electrode potential with variable frequency ω excites the forced harmonic oscillations of the suspended grains. The damping of these oscillations is caused by friction with a neutral gas. Having measured ω_0, one can then either use the sheath model to determine $\partial E/\partial x$ at x_0 or measure the ion density and relate it to the field gradient via Poisson's equation. In either case, one can obtain the Q value [38]. In the sheath, the drag force contributes to a degree comparable to that of the electric field force. Indeed, using the expression for the drag force and assuming as earlier that the dust grain charge is constant, we find that the oscillations will be determined by an effective potential in such a manner that, in expression (8), the derivative $\partial E_{\text{eff}}/\partial x$ should be substituted for $\partial E/\partial x$, where (this expression is obtained here for the first time by using the results of [2])

$$\frac{\partial E_{\text{eff}}}{\partial x} = \frac{\partial E}{\partial x} + \frac{2\tau n_i(z_0)e}{n_e(z_0)z_0\lambda_{Di}^2}\left(\frac{1}{M(z_0)}\right)^2 \times\left(\ln\Lambda - \frac{M(z_0)^2}{4z_0^2}\right)\frac{\partial M}{\partial x} - \frac{\tau e}{z_0\lambda_{Di}^2 M(z_0)^2} \times\left(\ln\Lambda + \frac{M(z_0)^2}{2z_0} + \frac{M(z_0)^4}{4z_0^2}\right)\frac{\partial}{\partial x}\frac{n_i(z_0)}{n_e(z_0)}, \tag{10}$$

where $M(z_0)$ is the local Mach number of the ion flow in the sheath, which is known to be on the order of unity (note that, for monolayers, the dust changes the structure of the sheath insignificantly). We also note that, in expression (10), the notation of [1, 2] is used and that $z_0 = -Qe/T_e a$ is the dimensionless dust charge at the position x_0. We give this analytic expression for determining the equilibrium position of a grain with the drag force included in order to show that ignoring the drag force (as was done in [39]) is, strictly speaking, incorrect because, by the order of magnitude, the drag force makes the same contribution to the frequency as the electric field force. Indeed, roughly estimating the electric field in the sheath as the ratio of the wall potential to the sheath distance gives $E \approx T_e/e\lambda_{De}$. The coefficient by the drag force is of the same order of magnitude in the case where the characteristic inhomogeneity scale of the Mach number and the ion-to-electron density ratio in the sheet is on the order of the inhomogeneity scale of the electric field. Up to now, this effect has not been taken into account, but the changes introduced by the drag force in the estimate of the charge Q yield a factor on the order of unity. Keeping in mind that when-

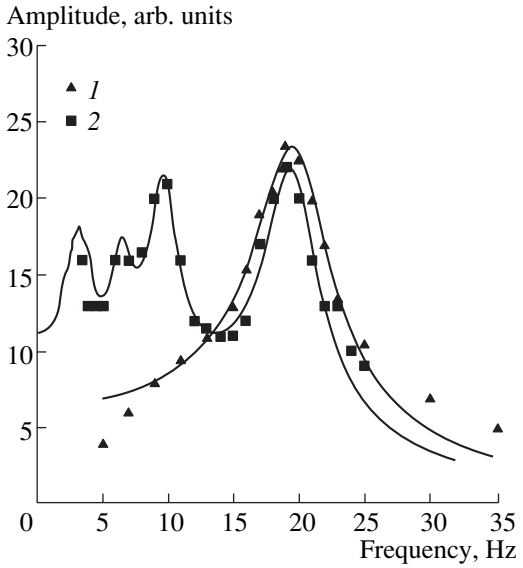

Fig. 17. Measured resonance curves of dust grains obtained by (*1*) the sinusoidal modulation of the electrode voltage and (*2*) pulse-periodic laser excitation at a pressure of 20 Pa [40]. The solid lines are the least squares fits of the response functions.

ever we use one model of the sheath or another, there is always an amount of uncertainty involved, the estimate of the absolute value of Q cannot be made more accurate than in [39]. In the future, the role of the drag force should be investigated in more detail. The further discussions deal with relative effects and do not depend on the absolute value of the measured dust charge.

Experiments have shown that the vertical resonance frequency ω_0 is practically the same for a single grain, a chain of grains, and a monolayer [40]. All the particles oscillate up and down at the same phase; hence, the longitudinal coupling effects are small (if the amplitudes and phases were exactly the same, the horizontal coupling would not be affected at all). An example of the resonance curve obtained in [40] is shown in Fig. 17.

This observation supports our statements about the specific features of monolayers. It also implies that any systematic charge variations across a homogeneous monolayer are small; otherwise, the resonance frequency would be position sensitive. We will return to monolayers later when discussing wave propagation and the instabilities in them.

2.6. Complex Plasma Clusters—Small Systems with Ordering Rules

In complex plasmas, as in ordinary matter, one of the most interesting questions in homogeneous nucleation is the transition from a molecule (an ordinary molecule in ordinary matter or a molecule formed by two grains in a complex system [41]) to a cluster of molecules (ordinary clusters [42–44] or clusters of either grain molecules or individual grains in complex plasma [45]) to a solid or crystalline state. In a cluster or molecules, binary interactions between the small finite numbers of components dominate the physics (and also the chemistry), whereas the collective and surface effects dominate in solids. Of course, "small" volumes of complex plasmas are not analogous to small volumes in ordinary matter, and the physics of transition from Coulomb clusters to plasma crystals in complex plasmas possesses a number of specific features. We have here one of the rare possibilities to observe this transition at the kinetic level, to measure the binary binding energy and its dependence on the source parameters (for instance, ionization intensity), to determine the relationships between this energy and the shear modules, the global modes of cluster oscillations, the compressibility, elasticity, etc. In addition, the interaction forces between grains in small clusters are usually the noncollective binary interactions, including long-range attraction and repulsion. These interactions are more complicated than the screened Coulomb interactions or hard-sphere interactions, which play a dominant role in ordinary matter. Interactions in complex plasma clusters can be determined directly from experiments. The problem with applying these results to clusters with a large number of particles is that the forces determined from experiments with small clusters differ from those for big clusters or plasma crystals, since the collective effects alter these interactions as was discussed in [2]. Thus, the interactions in small monolayer clusters can differ from the interactions in volume crystals. In monolayer crystals in the plasma sheath, cluster formation occurs in the direction perpendicular to the ion flow. Nevertheless, the ion flow can modify the attraction potential well inside the plane of a monolayer. In general, the problem of a continuous transition from small dust clusters including a small number of grains to 3D or 2D crystals including many grains is a separate field of research with its own problems, even when the interaction between the particles is a simple Coulomb or Yukawa interaction [42–46] as in ordinary matter.

The investigation of clusters formed in ordinary matter is a wide field of research. These clusters are usually confined in special traps. In the case of ordinary particles, their interaction is a simple Coulomb interaction, and such clusters are called Coulomb clusters. 3D ion Coulomb clusters were observed in Paul and Penning traps [47, 48] and 2D clusters formed by electrons were found in liquid helium [49] and colloidal suspensions [50]. Liquid colloidal suspensions are not suitable for investigating the dynamic processes in clusters because of the large overdamping due to the interaction with electrolyte.

In complex plasmas, not only the new types of interactions are important, but the dust–neutral collisions as well. The latter can alter the properties of the clusters in two aspects. First, they can damp the dust motion, causing some of the cluster configurations that are unstable

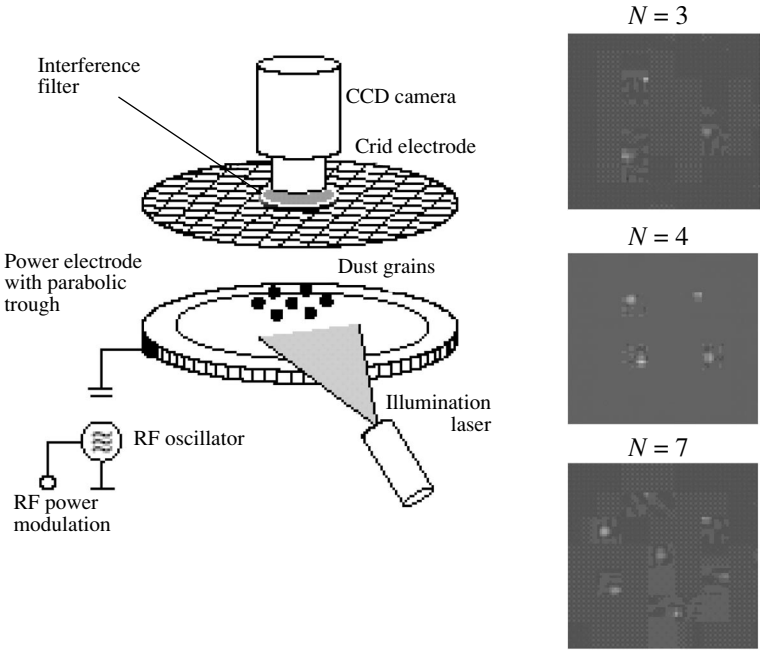

Fig. 18. A schematic of the experimental setup and images of the equilibrium clusters consisting of three, four, and seven grains [44].

in the absence of dust–neutral collisions to be stable in the presence of dust–neutral collisions. Second, they may cause the damping of the cluster eigenmodes, which, however, is much weaker than that in colloids. The frequencies of the cluster modes are directly related to the form of the interdust interaction potential and, therefore, can be used to determine the potential of dust–dust interaction in complex plasmas. The point is that the number of grains in the clusters is not large and, therefore, the collective effects in dust–dust interaction may be unimportant. In this case, one can expect that the pair dust–dust interaction will not depend on the average density of other dust grains, and one can apply the model that takes into account all pair interactions of every dust grain with every other dust grains.

The conclusion that there are attraction shadow forces present between two grains opens up the new possibility of forming dust molecules that was first mentioned in [41], in which it was recognized that this can create in the future a new area of research such as superchemistry, where the attraction between grains can result in more complex molecules and, finally, clusters. However, noncollective attraction is not the only type of new interaction in complex plasmas. The others are nonlinearity in shielding and the forces related the bombardment of dust grains by neutral particles and their attachment to the grains (see [2]).

Purely Coulomb 2D systems of grains that interact via the Coulomb potential and are confined in the plane of a monolayer by the external parabolic potential were investigated theoretically in [45]. It was found that, at a low kinetic energy, the clusters have a shell structure and that the increase in the kinetic energy leads to the instability related to the appearance of intershell rotation. A further increase in the number of grains in the shell, as well as an increase in their kinetic energy, results in an increase in the intershell diffusion and, finally, the formation of a Wigner lattice. The case corresponding to the Yukawa interaction (i.e., screened Coulomb interaction) was not investigated in such detail, and the problem of interaction with the potential corresponding to the dust–dust interaction in complex plasma was not investigated at all.

Recently, a general theory was developed for the case of 2D clusters in which the interaction between components is described by arbitrary forces, while the system is confined in the plane by an external parabolic potential well [51]. This allows one to analyze the experimental data for arbitrarily charged or uncharged grains in clusters that have both attraction and repulsion interactions and makes it possible to experimentally evaluate the type of interdust forces by analyzing the global modes of the clusters, their stability, and the frequencies of the global oscillations. This theory can be applied to complex plasma clusters and opens up the unique possibility of investigating the binary dust–dust interaction in complex systems in the future.

The collective effects and collective attraction can appear in a case where these clusters have as a background a homogeneous complex plasma (with the grain sizes different from those of the dust grains in the cluster). It is hoped we will be able in the future to extend such research to the 3D case (mainly by performing microgravity experiments [52]) and, probably, to create a general 3D theory (at present, this seems to be a rather

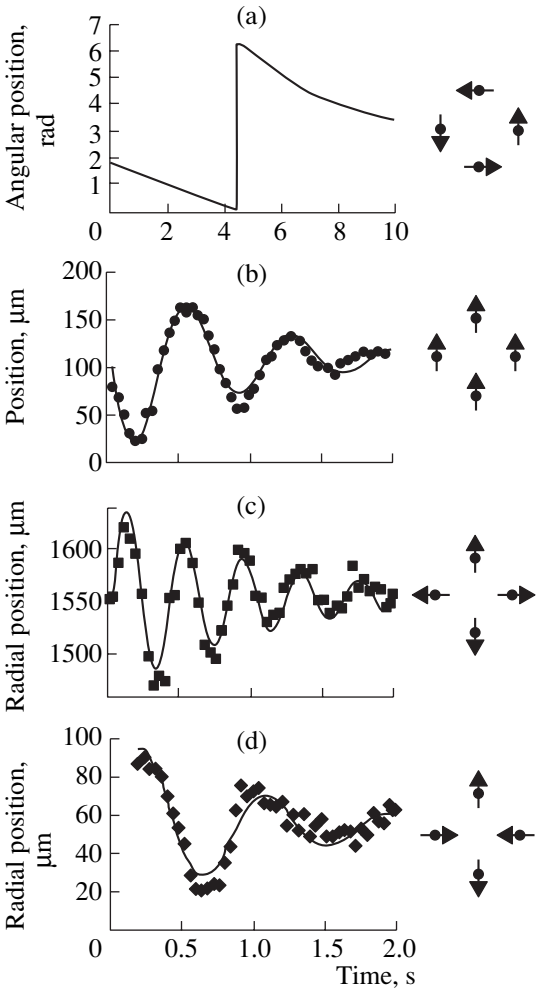

Fig. 19. Normal modes of a cluster consisting of four grains: (a) rotation around the center of the potential well, (b) center-of-mass motion, (c) breathing mode, and (d) antisymmetric mode [44]. The symbols show the results of measurements of damped oscillations, and the solid lines are the best fits to the experimental data.

complicated task, but the initial efforts have already been started).

2D clusters in complex plasmas were experimentally observed only in a few experiments [42–44]. Today, 2D monolayer clusters have been investigated and compared with the results of the screened potential model. In [43], damped cluster modes were observed for small numbers of grains. A scheme of the experiment and the observed damped oscillations are shown in Figs. 18 and 19.

Figure 20 shows the results of estimating the parameter $K = \Delta/\lambda_D$ for the Debye screened model. Shown are the normalized frequencies versus the intergrain distance in units of the screening length for clusters consisting of $N = 4$ (on the left) and $N = 7$ (on the right) grains.

It appears that, for different clusters, different values of K fit the experimental results. This is most pronounced for antisymmetric cluster modes for which the observed parameter K is rather large. One conclusion that can be drawn from this result is that the screened Coulomb potential, as well as the Yukawa potential, does not fit the observations. This is not surprising because, as was shown in [2], the interactions in complex plasmas are more complicated than those described by the screened Coulomb potential; in particular, the attraction potential and the nonscreened repulsion potential cannot be ignored.

It was found that, in 2D systems, the subsequent cluster shells have magic numbers of grains [10], as in the Mendeleev Periodic Table of Elements. For 2D dusty clusters, these numbers can differ from those for Coulomb clusters. Figures 21 and 22 [42] illustrate structures with different sets of magic numbers observed in clusters with different total numbers of dust grains N. In Fig. 22, the difference between the configurations of dust clusters and Coulomb clusters is clearly seen.

Figure 23 [46] shows the "ordering rule" according to which 2D plasma clusters are built up. Shown is the number of grains in the respective shells and the ordering into magic numbers, which is caused by the energetics (including those of external sources) of the structures produced.

These magic numbers resemble the Mendeleev Table rules in ordinary chemistry [53], and we can say that they are as important in the superchemistry of plasma clusters as Mendeleev rules are in ordinary matter.

In [46], a comparison was made between the measured plasma cluster structures and hard-sphere configurations (both are located in a quadratic external potential well). The difference was obvious and probably reflected the effect of the long-range nonscreened potential or the presence of the attraction forces.

Calculations of the molecular dynamics in these 2D systems [13] result in configurations similar to those observed, including the slight compression of the central region of the plasma cluster. Preferably, one should also use for comparison the general theory in [51], first identifying the different types of interactions between the grains by measuring the global cluster oscillations or the equilibrium conditions. The more sophisticated codes needed for complex plasma simulations should also be developed. It is unlikely, however, that the simple molecular dynamic simulations of fixed-charge grains with a fixed screening length (without account taken of the screening nonlinearities), with collective attraction ignored, and, consequently, with a given coupling potential, will be sufficient to model and to understand 3D plasma clusters.

Figure 24 [42] presents the first measurements of the stability of 2D plasma clusters. The criteria of stability were also given in the general theory [51]. These criteria, however, can contradict the experimental results, because, in the experiments, the shear was induced using laser light pressure and also because the general theory (without dust–neutral damping included) pre-

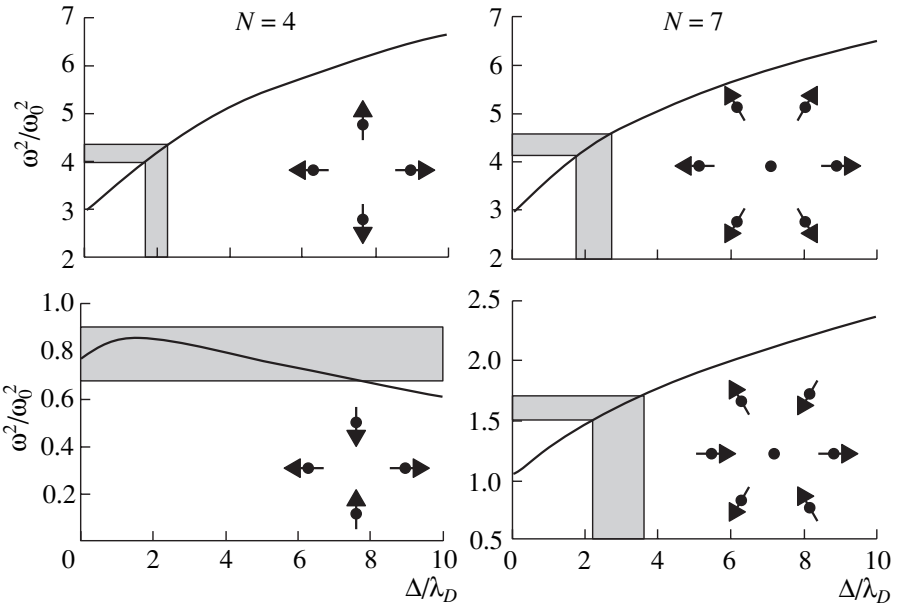

Fig. 20. Estimation of the parameter $K = \Delta/\lambda_D$ for the screened Debye model: normalized frequencies of the breathing mode (on the top) and the antisymmetric mode (on the bottom) vs. intergrain distance in units of the screening length for clusters consisting of four (on the left) and seven (on the right) grains [44]. The shaded area corresponds to the measured frequency values.

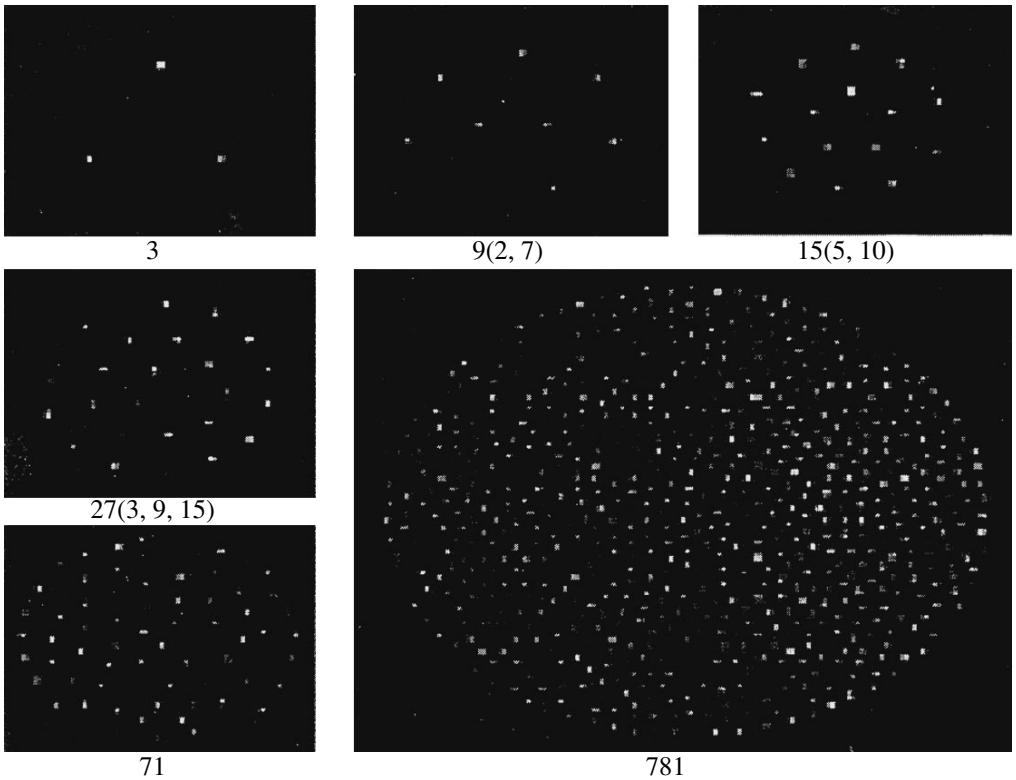

Fig. 21. Microphotographs of typical cluster structures at different numbers of grains N (the structures are shown on different spatial scales) [42]. The characteristic intergrain spacing is 0.3–0.7 mm.

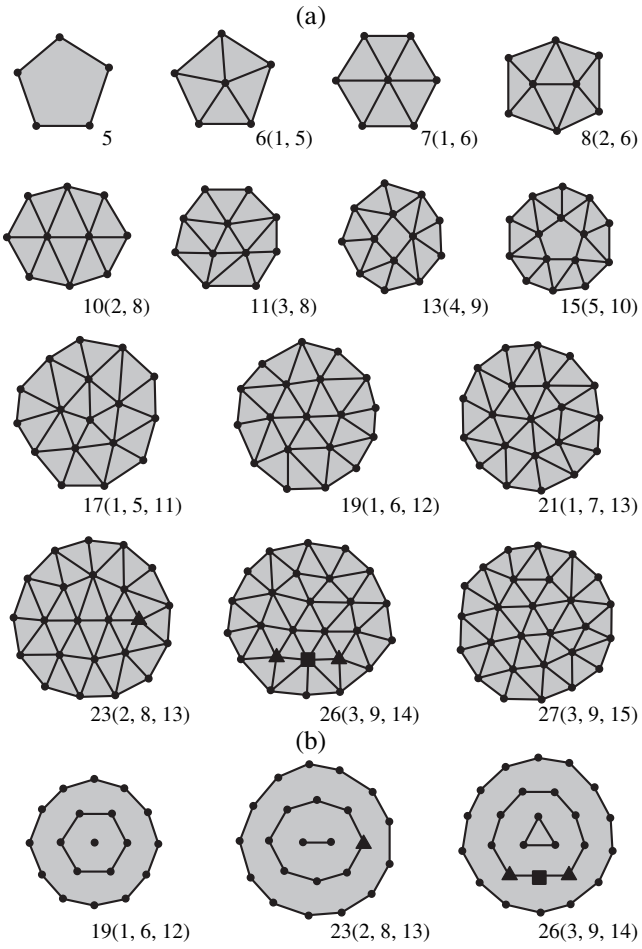

Fig. 22. (a) Typical cluster configurations observed at different numbers of grains N and (b) three different structures obtained in 2D simulations for the unshielded Coulomb repulsion in a circular parabolic potential well [43]. The triangular lattices are plotted to illustrate the deviation from the central symmetry. The small triangles and squares in a few images show the fivefold and sevenfold dislocation defects, respectively.

dicts [51] the instability of any clusters with $N > 6$. The instability observed during the transition from the $N = 19$ to $N = 20$ structure is related to the rotation of the inner shell with respect to the outer shell.

It is easy to see that configurations with a hexagonal structure, which are the preferred from the energy standpoint, are more difficult to dislodge than configurations that are already in an elevated energy state. Moving onto larger systems, the point to note is that the geometry of the confining force (cylindrical in this case) begins to assert itself more and more. One way to quantify this is to calculate the rms deviation Δr of n outermost grains from the best fit circle (of radius r_0):

$$\Delta r = \frac{1}{n}\left(\sum_{i=1}^{n}(r_i - r_0)\right)^{1/2}. \qquad (11)$$

The study of plasma clusters (both two- and three-dimensional) promises to be a very interesting field, one which has only just begun. Apart from the current investigations into homogeneous clusters, work should proceed in the investigation of clusters of grains with one size in a homogeneous "sea" of grains with another (probably lower) size to measure the role of the collective attraction produced in complex plasmas, as well as in the investigation of binary mixtures (clusters with grains of different size), inhomogeneous clusters, and the influence of the confining potential (in the plane of a 2D cluster) on the cluster structure.

Purely Coulomb clusters (without plasma) have been produced in Paul traps with supercooled Mg^+ ions [47, 48]. These structures are a result of the pure Coulomb interactions between the ions and the external coupling potential. Such structures can probably be described by the OCP model.

Returning to complex plasmas, we note that the better we understand such systems as plasma clusters (which can be observed at the kinetic level), the better we will be able to understand other systems and utilize them.

3. PHASE TRANSITIONS IN PLASMA CRYSTALS

3.1. General Description of Phase Transitions in Complex Plasmas

It is well known that ordinary matter can be in the solid, liquid, and gaseous states. Analogous transitions are possible in complex plasmas; however, the physics of such transitions can be quite different. In usual matter, these states are characterized by macroscopic state variables (e.g., the pressure P and temperature T for gases), which can be considered as the appropriate integrals of the kinetic particle properties. One of the most fascinating problems is the understanding of the transitions between the states (in particular, the melting transitions) at the kinetic level. In ordinary matter, observations at the kinetic level (i.e., the observations of individual atoms or molecules) are generally impossible; hence, in ordinary matter, a direct comparison of kinetic theory and experiments is ruled out.

As was already noted above, this is not the case for plasma crystals. Here, one component (the most massive and energetically dominant) can be observed at the kinetic level with sufficiently high time and spatial resolutions, so that kinetic theory and experiments are, for the first time, on a roughly equal footing. Unfortunately, due to the openness of complex plasmas, the theory of such transitions is still waiting to be formulated (some theoretical approaches using the Van der Waals equation in complex plasmas will be given in the next part of the review). Of course, we can do this (in principle) for the few special plasma crystal systems for which external energy sources are known and well analyzed both experimentally and theoretically.

Nevertheless, the accessible ranges of physically different systems is quite broad. We can investigate

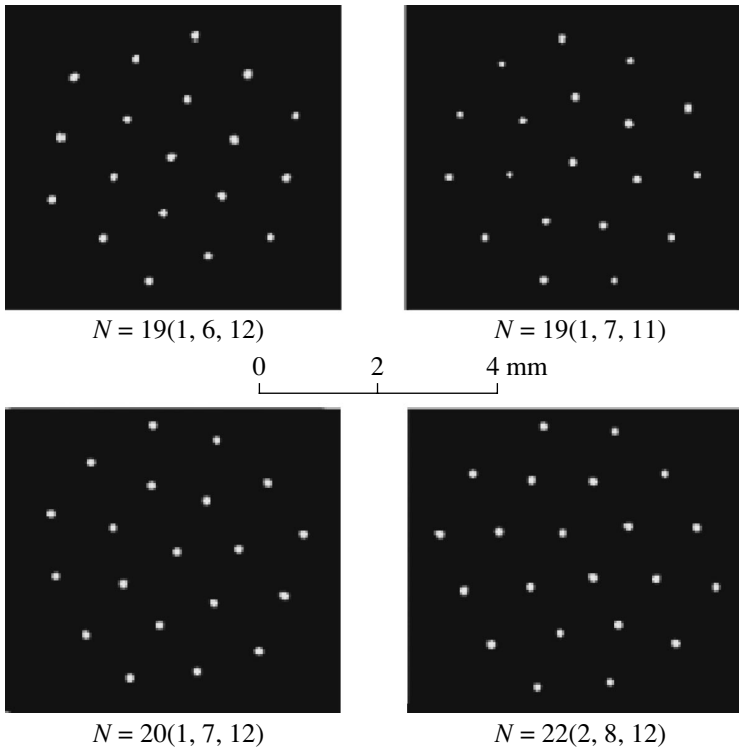

Fig. 23. CCD camera snapshots of clusters in the plasma sheath (*N* is the number of grains in the cluster) [46].

homogeneous (glassy) systems with several sorts of dust grains, or anisotropic systems consisting of microrods (with additional rotational degrees of freedom). We can, in principle, investigate a broad range of parameters (Γ, K, P_0, a/λ_{Di}, etc.) in both stressed (in the presence of gravity) and stress-free (under microgravity conditions) systems. Of course, such experiments are quite demanding and the level of sophistication in the data analysis is quite high, too. It is not surprising, therefore, that so far only four experiments have been performed [53–56]. All three experiments were carried out with at most 10 horizontal lattice planes, and all of them were restricted to 2D diagnostics. This implies that grains leaving or entering a particular horizontal lattice plane could be observed, but the broader 3D picture is still unknown.

3.2. Phenomenological Description of Phase Transitions in Complex Plasmas

Whilst in [53] great emphasis was placed, in particular, on the migration of lattice defects during the preliminary stages of the melting transition, the other research concentrated more on the phenomenology of the transition: the changes in the 2D correlation function (translational order) and the variations in the temperature (velocity distribution), orientational order, self-diffusion, and viscosity of dust grains [57] (see Fig. 25).

The melting transition can be initiated and controlled by lowering the gas pressure in the plasma

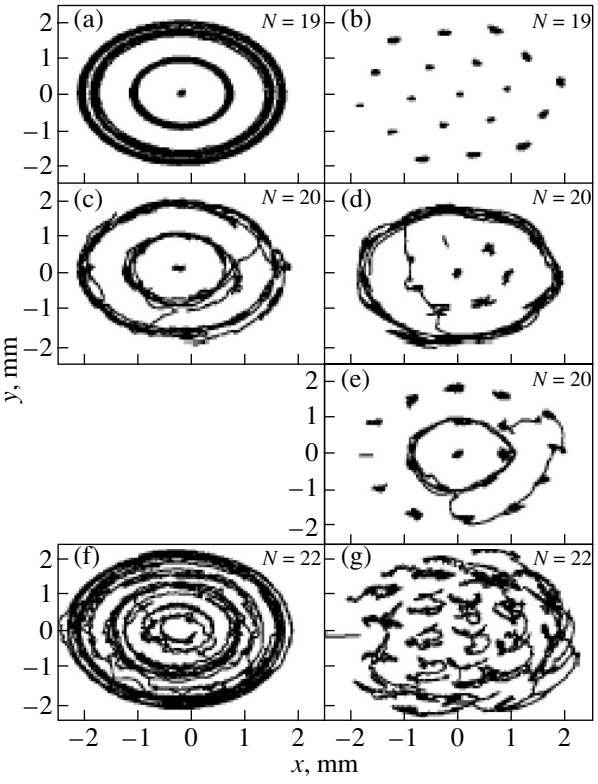

Fig. 24. Dust grain trajectories over 220 s for clusters consisting of (a) 19, (c) 20, and (f) 22 grains without laser excitation. Plots (b), (d), (e), and (g) show the trajectories corrected for cluster rotation [43].

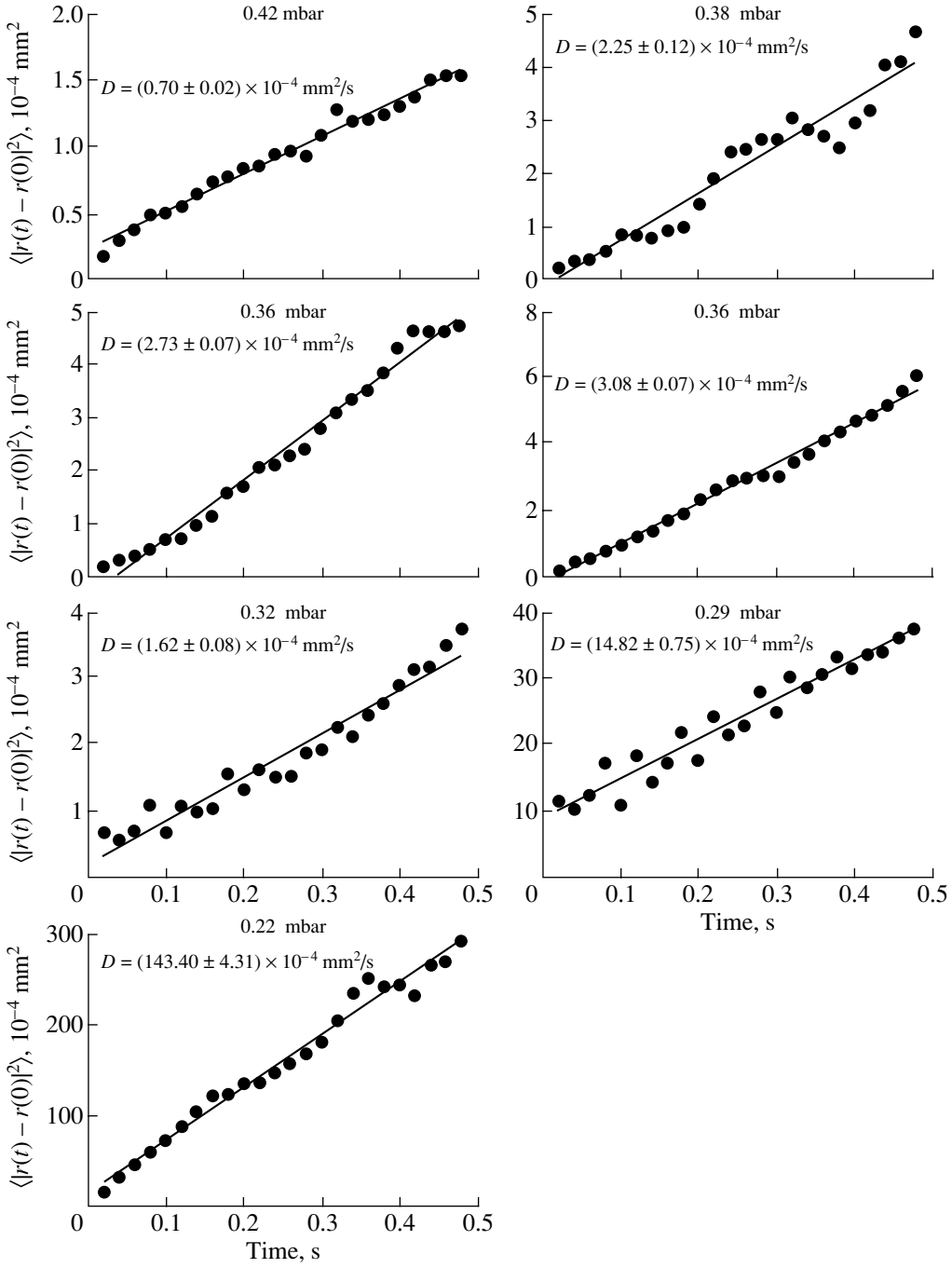

Fig. 25. Measurements of grain self-diffusion during the melting of a plasma crystal at different pressures [57].

chamber. This has several consequences. First, it reduces the friction damping of the grains; second, it increases the collisional mean free path of ions and electrons; and finally, it lowers the plasma ion and electron densities and increases the sheath width. All these processes act in a complicated way to decrease the coupling parameter Γ and to initiate melting.

The transition from the crystalline to the liquid state is accompanied by an increase in the vibrational excitation of grains at the lattice defects, followed by defect migration (see Fig. 26).

This behavior is expected from the studies of classical annealing and is confirmed at a microscopic level for complex systems. Next, grain migrations across horizontal lattice planes become more frequent. Whether this is a response to a structural realignment in the vertical direction is still unknown. Of interest is the asymmetric response to the vertical grain migration.

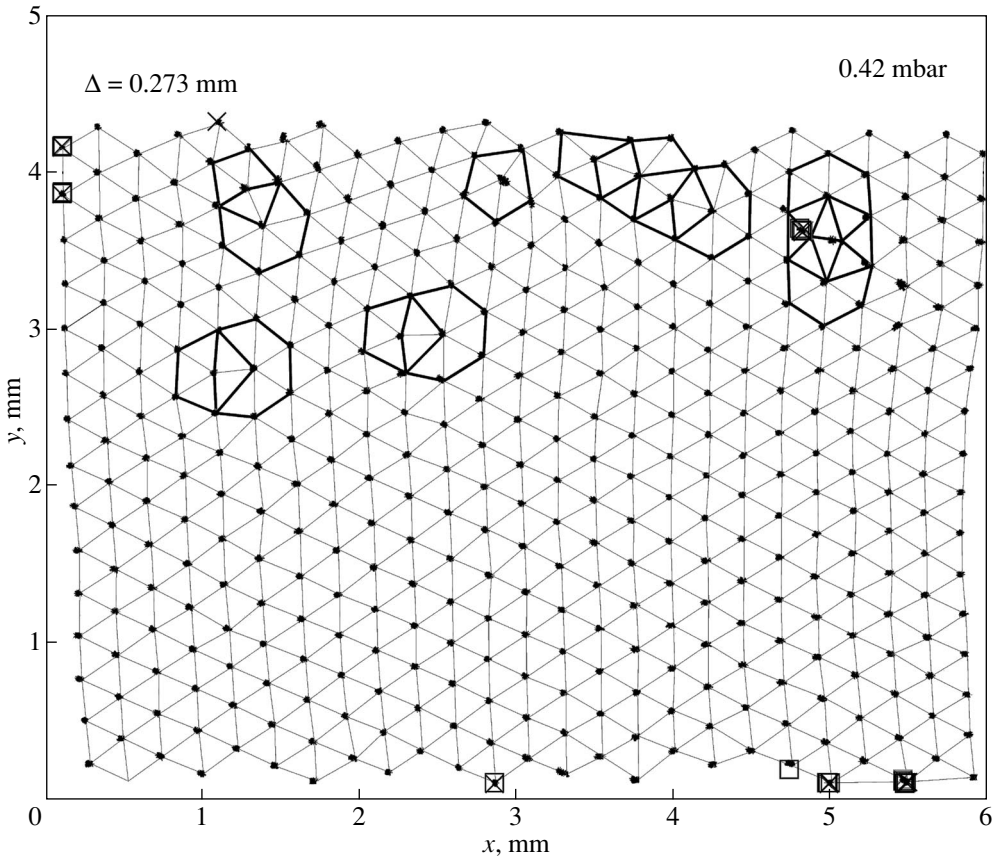

Fig. 26. Appearance of crystal defects [56].

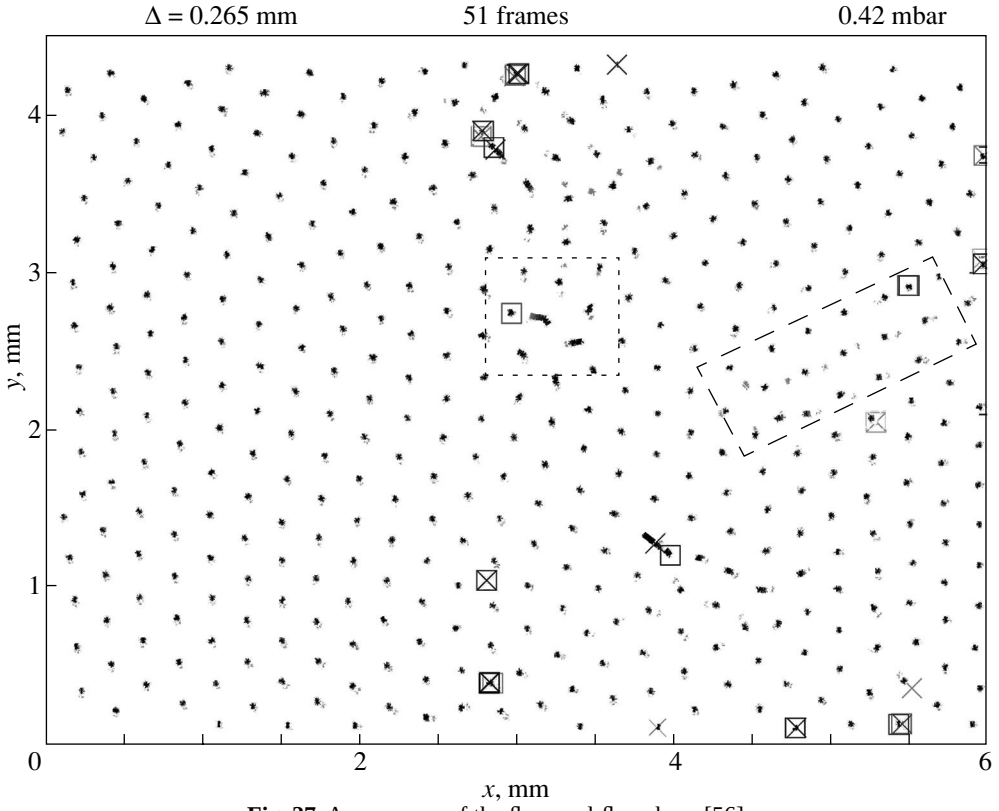

Fig. 27. Appearance of the flow-and-floe phase [56].

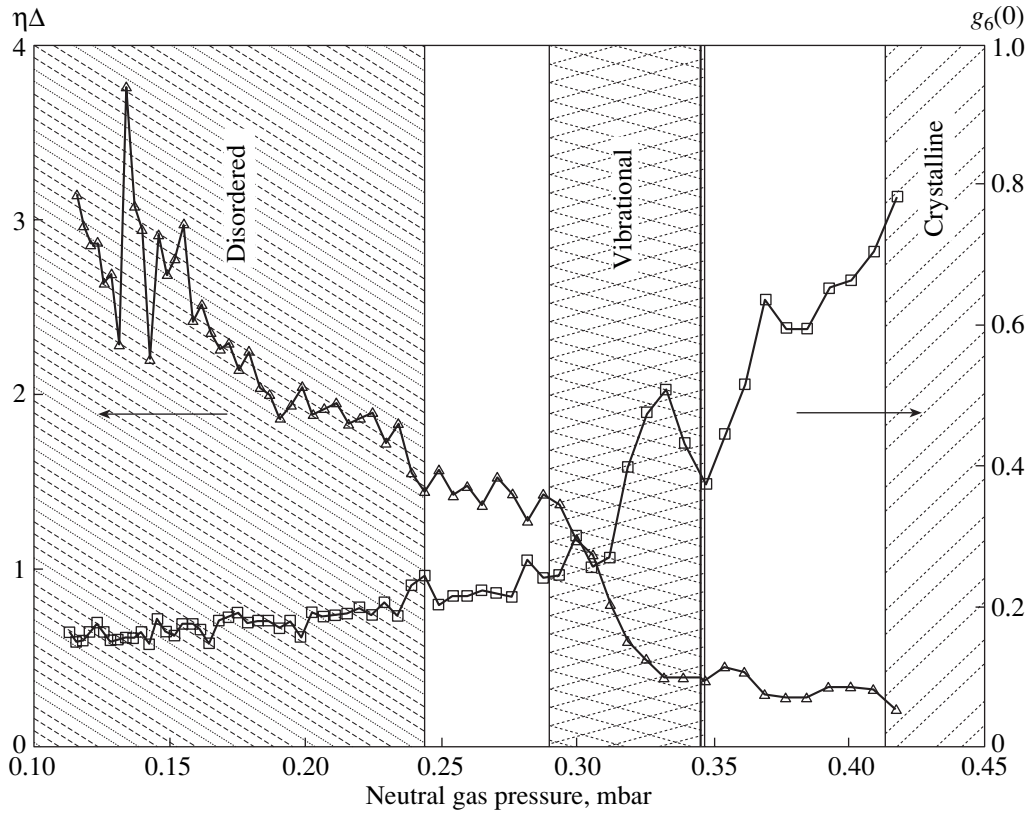

Fig. 28. Evolution of the transitional order parameter ηΔ (triangles) and the orientational order parameter $g_6(0)$ (squares) during the phase transitions caused by varying the neutral gas pressure [57]. The domains corresponding to the crystalline state ($p \geq 0.42$ mbar), the vibrational phase ($p \approx 0.32$ mbar), and the disordered state ($p \leq 0.245$ mbar) are hatched. The intermediate flow-and-floe phase occurs at $p \approx 0.36$ mbar.

When a grain *enters* a horizontal lattice plane, it naturally leads to a displacement of its nearest neighbors (see Fig. 27). Observations show that, in this case, only the grains in adjacent cells are involved. This adjustment might be expected to proceed at the propagation speed of the dust lattice wave; however, it is found to be about two orders of magnitude slower.

When a grain *leaves* a horizontal lattice plane, again a readjustment of the nearest neighbors takes place. In contrast to the symmetric displacement of the nearest neighbors (which is observed when a grain is added to the lattice), a disappearing grain produces a direct flow along a given lattice string, which may extend over many (up to 10) neighboring cells (see Fig. 27).

Thus, there is a fundamental asymmetry in the readjustment of grains in a given horizontal lattice to the addition or loss of a grain.

Next, it was found that parts of the system started to "flow." Although it is not yet confirmed experimentally, the conception is that these flow regions could look like miniconvection cells involving two or three horizontal lattices. At the same time, other regions retained quite stable crystalline domains of varying size (typically, 10 to 50 Wigner–Seitz cells in one lattice plane). This structure is reminiscent of a classical first-order phase transition, e.g., water and ice, where liquid and solid phases coexist. It was named the "flow-and-floe" phase. Its appearance is related to certain neutral gas pressure and is shown in Fig. 28 together with other phase states (see below).

It was natural to expect that this melting process would simply proceed as follows: the "floes" should get smaller until the entire system becomes liquid. However, the expected development did not happen. Instead of liquefying further, the complex plasma acquired a new (and unexpected) intermediate state. Starting in a few locations that were not obviously associated with lattice defects (this evidence is in part circumstantial and not 100% certain, since only one lattice plane was observed and information about neighboring planes and their defects is lacking), individual grains began to vibrate with substantial amplitudes up to about 10% of the initial lattice separation (see Figs. 29, 30). The associated increase in the kinetic energy was a factor of 10 or more.

Subsequently, as the melting transition proceeded further, more grains started to vibrate and the vibration amplitudes increased. This stage of the phase transition had the appearance of a classical Lindermann picture, with the grains vibrating in their lattice sites around their equilibrium positions. The vibration amplitude

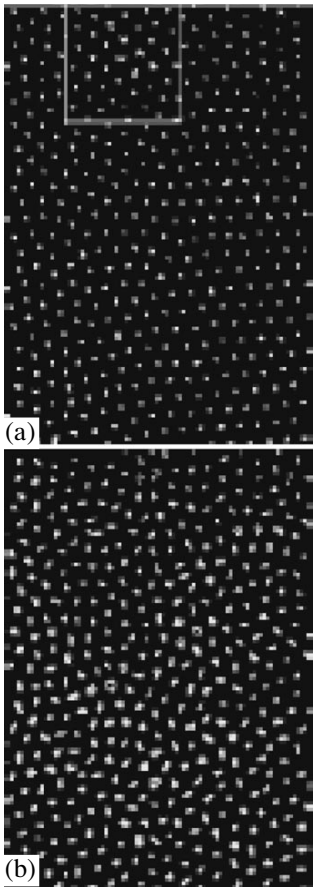

Fig. 29. Images (each presenting two consecutive video frames overlaid) corresponding to the beginning (a) and the end (b) of the vibrational phase (pressures of 0.32 and 0.29 mbar, respectively) [56]. In the marked window in image (a), the vibrations are first observed; they then spread throughout the crystal.

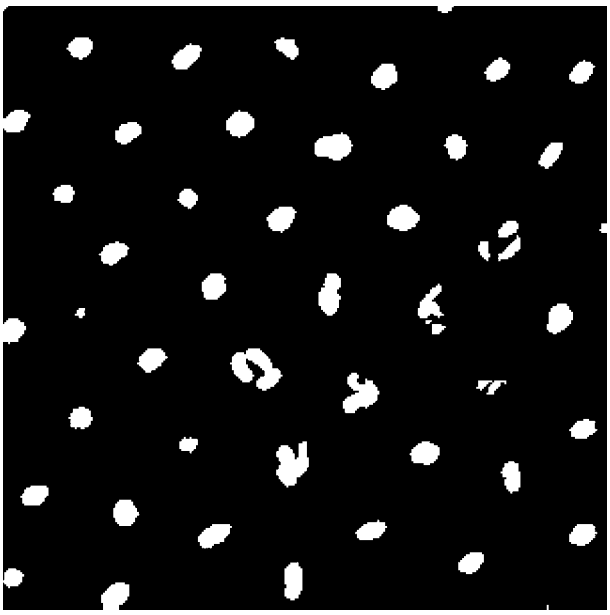

Fig. 30. Side view of a plasma crystal in the vibrational state. The figure illustrates that the grain vibrations are essentially isotropic [58]. At the bottom of the crystal, melting is seen to start.

increases until the system eventually passes to a disordered (fluid or gaseous) state (see Figs. 30–32).

From the top view (Fig. 30), we can see the basic crystal-like structure, in which some grains oscillate with substantial amplitudes along circular, oval, or linear trajectories and some appear not to vibrate. This could be due to the projection effect, as shown in the side view (Fig. 31). A cursory "head count" of the different orientations of vibration planes shows that the vibration is essentially isotropic, which means that either the energization process is not directional or there is a process that rapidly randomizes the grains. Observations of the individual grains show that the vibrational orientation is conserved over a few vibration periods until the directional information is lost.

Note that, in the vibrational state, the orientational order is more pronounced than in the flow-and-floe state. This will be discussed in greater detail later. In the disordered state, the grains move very fast, with a kinetic energy far exceeding 1 eV. Consequently, the grain trajectories are visible as "lines" in individual video frames (see Fig. 31). Also clearly seen are sudden "kinks" in the grain trajectories, probably caused by Coulomb collisions. In principle, the statistics of such collisions could be used for diagnostic purposes, but this has not been attempted so far.

3.3. Translational and Orientational Orders in Phase Transitions in Complex Plasmas

The standard techniques for quantifying crystalline structures are the determination of translational and orientational orders [58].

For the former, one usually employs the radial pair correlation function $g(r)$, fitted to the appropriate lattice structure (in our case, hexagonal), normalized to the mean lattice separation Δ, and broadened by the so-called Debye–Waller factor. This factor accounts, in particular, for thermal broadening, but one should expect that the broadening in the case of a plasma crystal will not be thermal. Since the correlations generally decrease with increasing distance r, the decay of the translational order can be expressed through the exponential decay factor $\exp(-\eta\Delta)$, where Δ is the lattice separation and η^{-1} is the correlation decay length. Clearly, the smaller $\eta\Delta$, the greater the translational order. The transition from the ordered ($\eta\Delta \ll 1$) to disordered ($\eta\Delta \gg 1$) state occurs at $\eta\Delta \sim 1$ [11, 27].

For the orientational order, the bond orientational correlation function $g_6(r)$ is usually taken. This is defined in terms of the nearest neighbor bond angles and, in our case, measures the sixfold symmetry in the structure [59]. Only the nearest neighbors were used in

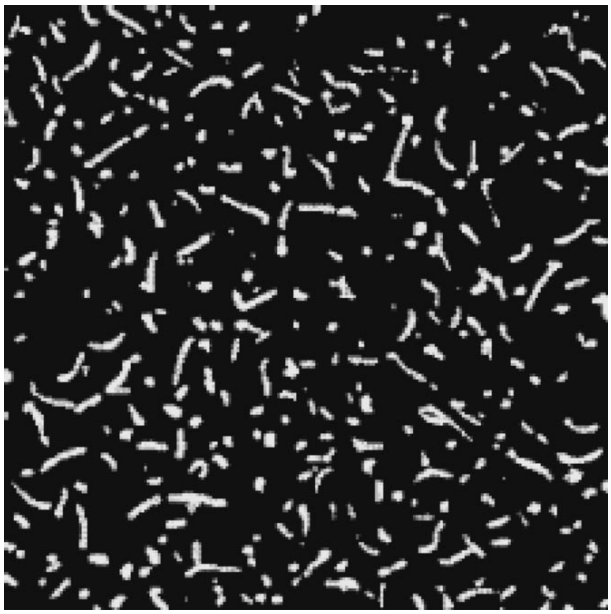

Fig. 31. Beginning of the disordered state (p = 0.13 mbar) [55, 56]. The image was taken with an exposure time of 0.02 s. The area shown is 3.9×4.1 mm^2.

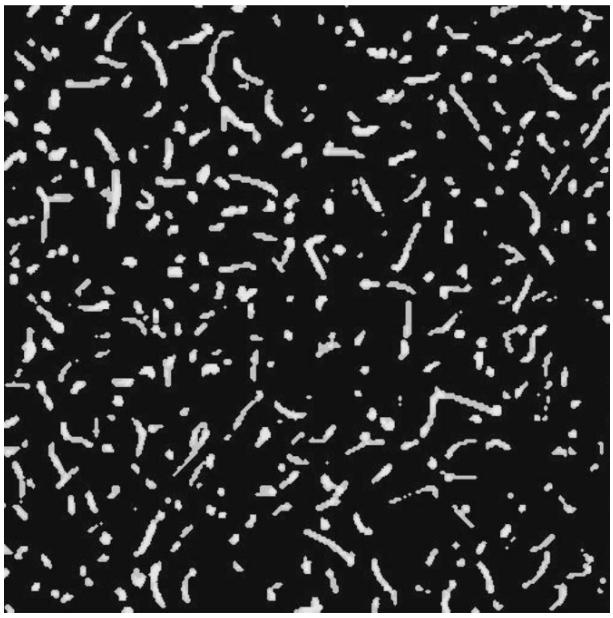

Fig. 32. Grain motion in the disordered state [57].

[59] to evaluate $g_6(0)$ by averaging over all the grains. Hence, in [59], only the very local orientational order was determined. Clearly, in a crystal, this parameter is most sensitive to dislocations, e.g., if there appears a pentagon or septagonal structure instead of the usual hexagonal structure. However, it is also sensitive to statistical variations in grain positions as a result of fluctuations of the grain charge and plasma parameters or other collective variations (note that the averaging of the grains positions over time was not performed in [59]). The higher orientational order corresponds to the larger value of $g_6(r)$, the maximum being equal to unity.

The translational and orientational order parameters are plotted in Fig. 28 as functions of the gas pressure [60], which was used as a control parameter in studying the phase transition. The crystalline, vibrational, and disordered states are hatched. The flow-and-floe state occurs in the intermediate region between the crystalline and vibrational states. It develops more or less continuously from the fully crystalline state to the mainly crystalline state with migrating defects and, then to crystalline islands in viscous liquid until the vibrational state is reached.

It is interesting to note that the onset of the vibrational state is indicated in both ordering parameters by a return to a more ordered structure.

3.4. Dust Grain Temperature in Phase Transitions in Complex Plasmas

Since the dust component of the complex plasma can be visualized with a high time resolution at the kinetic level, it is possible to measure the velocity distribution function of dust grains directly. This distribution function can then be compared, for instance, with a Maxwell distribution, or one may take moments to identify the flow velocities, etc. According to a visual inspection, there are indeed stages during the phase transition when the directed flows occurred. A suitable analysis had to be made to quantify these flows. Figure 33 shows the unidirectional velocity distribution function $f_d(v_x)$, which is compared with the best Maxwellian fit (solid line) at different neutral gas pressures [56]. The correlation function measured during the phase transition is shown in Fig. 34 [57].

The results of [53–61] can be formulated as follows:

(i) In the crystalline state ($p \geq 0.42$ mbar), the grains have a Maxwellian velocity distribution with a temperature of 0.036 eV (slightly above room temperature). The system is clearly in equilibrium (some kind of thermodynamics can probably be used to describe this state, although the concept of free energy is inapplicable).

(ii) In the flow-and-floe state ($p \approx 0.36$ mbar), the velocity distribution of grains is still well described by a Maxwellian distribution with a temperature of 0.037 eV and is close (within the allowable errors) to that in the crystalline state.

(iii) In the vibrational state ($p \approx 0.32$ mbar), there is clear evidence for bi- or multi-Maxwellian distributions. The best fit with a single temperature of 0.073 eV is clearly inadequate. A bi-Maxwellian fit with 60% of the grains at 0.04 eV and 40% at 0.9 eV is much better. This indicates that, at this stage, many grains have made the transition to the vibrational dynamics.

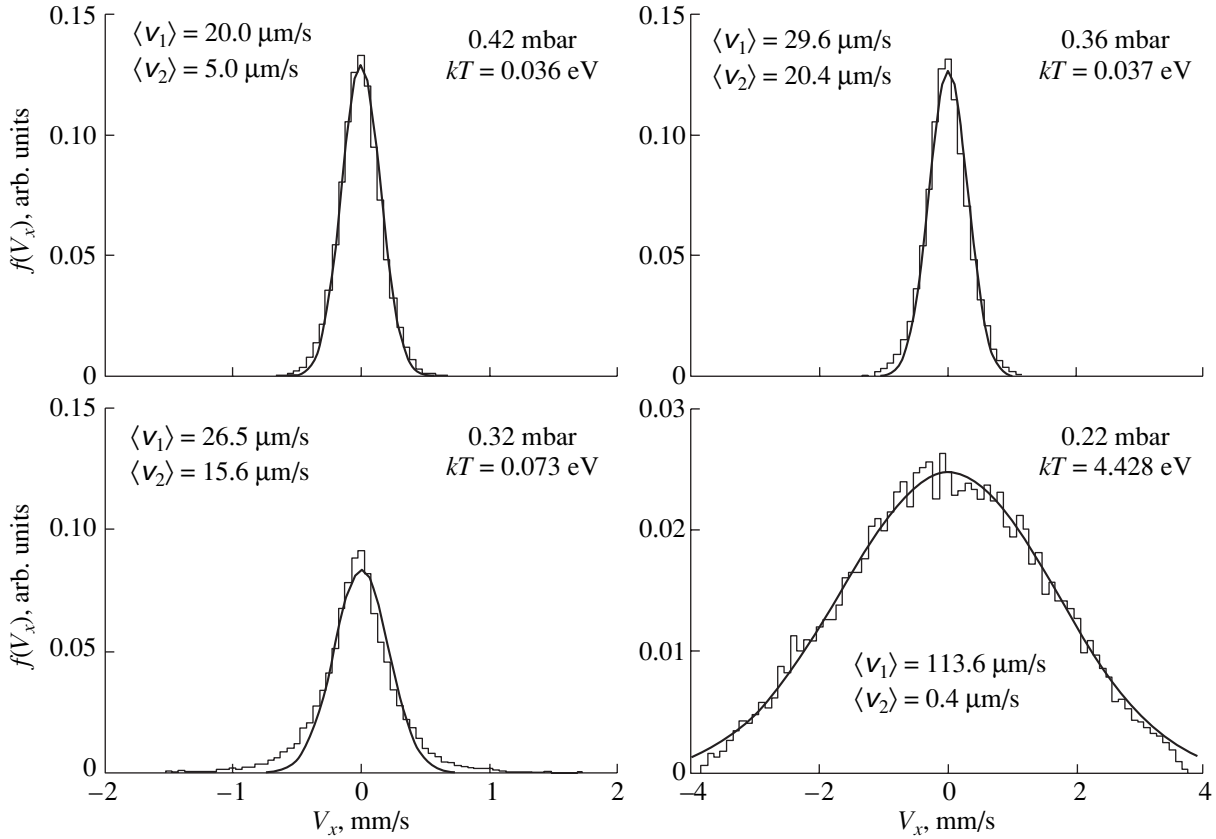

Fig. 33. Change of the dust grain distribution over v_x with pressure on the course of crystal melting [56]. The solid curves show Maxwellian fits with the dust temperature T; $\langle v_1 \rangle$ and $\langle v_2 \rangle$ are the chaotic and regular drift velocities, respectively.

(iv) In the disordered state ($p \le 0.245$ mbar), the distribution function is again almost Maxwellian with a temperature of 4.43 eV. This is more than two orders of magnitude higher than the equilibrium value observed in the crystalline state. Considering only gas friction (Epstein drag; see [2]), this implies that, in order to maintain the grain temperature at this level, a power ≈3.0 eV/s per grain has to be provided. This means that an external power of few watts is required to maintain the plasma. Thus, the external energy source plays an important role in the transition. We mention also that the kinetic theory predicts that, in the gaseous state, the complex plasma can rapidly reach a thermal equilibrium [62, 63] and that the grain distribution can be thermal (the thermal distribution satisfies the dust–dust collision integral for all attraction interactions included). Thus, there is some theoretical basis for the grain distribution to quickly reach the thermal distribution, at least in the disordered state (there is no theoretical predictions for other states in phase transitions).

As was mentioned earlier, the ion and electron distributions are usually not thermal, which can cause the existence of directed dust flows in the intermediate regimes of phase transitions. Such flows can occur, for instance, during the annealing of lattice defects, but they also manifested themselves (in a much more dominant way) during the flow-and-floe phase.

4. WAVES AND INSTABILITIES IN CRYSTALLINE AND DISORDERED STATES OF COMPLEX PLASMAS

4.1. Change of the Dispersion Relations in Complex Plasmas

Complex plasmas, as a new state of matter, should have new waves and instabilities due to the openness of the system, the large rate of dissipation of plasma particles on grains, and the presence of external sources. In the first approximation, these waves and instabilities can be described by linear responses and linear dispersion relations and can then be treated nonlinearly by using nonlinear responses. To find these responses, it is necessary to specify the external sources, since the responses are different for different sources. The linear and the nonlinear waves in complex plasmas have been the subject of experimental investigations. We start with the simplest disordered gaseous state of complex plasmas, where it is simpler to qualitatively formulate how the presence of the dust component changes the modes, and when these changes are substantial. From the physical standpoint, one can estimate the ranges of

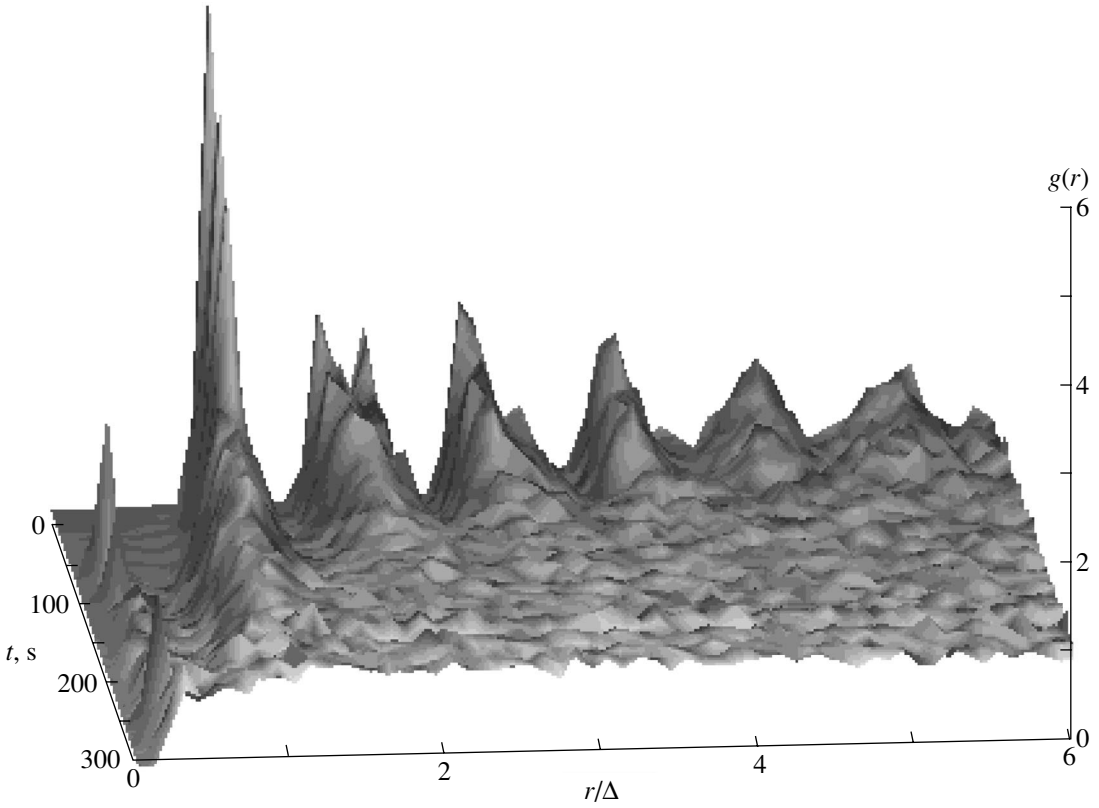

Fig. 34. Evolution of the pair correlation function $g(r)$ during melting caused by varying the gas pressure [57].

wavenumbers and frequencies in which linear modes in a complex plasma will change. This estimate will be the same for all kinds of external sources, although the dispersion relation depends on the source. Indeed, the frequencies at which the changes are big should be less than either the charging frequency $\nu_{ch} \approx v_{Ti}a/\lambda_{Di}^2$ or the frequency of collisional friction of the plasma particles on dust grains $\nu_{ch}P_0$ (see [2]). The latter is of the same order of magnitude as the charging frequency if P_0 is on the order of unity. The wavenumber domain where the changes occur should correspond to wavenumbers less than ν_{ch}/v_{Ti} or $\nu_{ch}/v_{Ti}P_0$. This is a very broad range in the (ω, k) plane, where all low-frequency responses are usually located. This is because the charging frequency is only a factor of a/λ_{Di} less than the ion plasma frequency. All the classical theory of waves and instabilities in ordinary plasmas written in textbooks (see, e.g., the monograph by Mikhailovskii [64]) should be revised in this range of the wavenumbers and frequencies. Although the work on renewing this "table" of the waves and instabilities has not yet been completed, it is clear in general that all the so-called negative energy waves (among them are all beam modes and drift waves) will be much more unstable in complex plasma than in ordinary plasma. The reason for this is that, for negative energy waves to grow, it is necessary to have the dissipation of the disturbances, and the complex plasma provides a very efficient mechanism of dissipation via charging and the friction on grains. Without going into details, we will mention, for instance, that the investigations of drift waves [65] show that, in complex plasma, both the threshold of the drift instability decreases and its growth rate increases. The same is true of the beam instabilities, i.e., instabilities related to the propagation of the electron and the ion beams in plasmas. What is most important is not only that the known waves and instabilities change but also that new modes and instabilities appear. Thus, in the liquid and the gaseous states of complex plasmas, dust acoustic waves (DAWs) exist. The theoretical investigation of the latter was started with a modification of the known results [64] for a multicomponent plasma in which dust is simply one of the heavy components [66–70]. However, such an approach is not appropriate, as can be seen from the discussion of the elementary processes in complex plasmas [2] (see also a detailed discussion of this problem in [71, 72]). The relevant experiments will be considered later in the context of a description of DAWs with allowance for charging processes, as well as descriptions of dust ion sound waves (DISWs), which are the low-frequency branch of the usual ion-sound waves in plasma [73]; gravitation-like electrostatic instability (GLEI) [74], which is related to the noncollective dust attraction and is similar to the gravitational instability in usual gravitating systems; and

structurization instability (SI) [74], which is related to the collective dust attraction and describes the clumping of a complex plasma in dust-containing structures and dust-free regions (dust voids). Recently, another type of wave has also been discussed, namely, dust Coulomb waves (DCWs) in a system of strongly interacting grains. These modes are the most important new waves in the disordered state. In the plasma crystalline state, new wave phenomena include dust lattice waves (DLWs) [75] and dust shear waves (DSWs) [76, 77]. These are peculiar only to strongly coupled crystalline systems and are absent in the liquid or the gaseous states. These waves may be excited in 1D "string" systems, 2D planar lattices, and 3D crystals. Their solid analogs are the crystal sound and shear waves.

Under the Earth's gravitational conditions, we have to bear in mind that there is a fundamental asymmetry for dust grains located in the plasma sheath. This asymmetry is caused by the ion flow, although, as was noted above, this effect is smeared out (not completely) by collective charging effects. This causes some anisotropy in the interaction among the grains. We recall that experiments exist which illustrate that there is a close coupling between vertically aligned grains, such that, when the upper grain is shifted, the interaction is clearly observed, while the coupling is absent when the lower one is shifted. However, these observations were performed for two interacting grains. In the presence of many grains, this effect is smeared, but some asymmetry survives. For these reasons, our main attention will be focused on monolayer systems and horizontal interactions.

For simplicity, we will first consider the gaseous state and will find simple linear relations from the forces acting on the electrons, ions, and grains, adding to the force balance equations the terms with the time derivative $\partial/\partial t$ and then linearizing the system as was done in [2] (see also [72]). The applicability of such an approach is justified by the fact that we are dealing here with low-frequency and long-wavelength perturbations, and the electron and ion distributions are assumed to be thermal. As was discussed earlier, the latter is not a good assumption; however, the full kinetic treatment of the new modes is still waiting to be performed, and this assumption will allow us at least to illustrate the main features of these modes by introducing the temperatures $T_{e,i,d}$ as certain averaged particle energies. Another simplification is the assumption that the long-wavelength perturbations are quasineutral; in this case, we do not need to solve Poisson's equation.

4.2. Experiments on Dust Ion-Sound Waves

DISWs, which are an analogue of ordinary ion-sound waves in the absence of dust, are substantially modified by the presence of the dust component. The wave as linear perturbation can exist only against some ground state, which, in the absence of dust, requires only the charge balance, while in the presence of dust, it requires also the power balance for frequencies lower than the frequencies of charging and dust–ion collisions, and for wavelengths longer than those corresponding to these frequencies. For $\tau = T_i/T_e \ll 1$, the frequency related to the scattering of ions on dust grains is a factor of $\ln\Lambda/\tau$ higher than the charging frequency (where $\ln\Lambda$ is the Coulomb logarithm modified with allowance for collective effects and large-angle scattering). In experiments, this frequency is on the order of 10^7 s^{-1}, which corresponds to a time scale on the order of 0.1 μs. The charging frequency is on the order of 2×10^5 s^{-1}, and the corresponding time scale is on the order of 5 μs. The ions are absorbed on the latter time scale; however, in experiments, the external source is kept constant at time scales much longer than those related to both charging or ion–dust scattering. Therefore, one can assume that the power balance is kept in the entire range of DISW frequencies. Although the frequency related to dust–ion collisions does not determine the power balance, it should enter into the dispersion relation, somewhat modifying it at high frequencies. As was demonstrated in [2], the power balance in the basic state has two consequences: (i) the basic state is governed by a single parameter P_0 (which determines the electron-to-ion density ratio and the dust charge z_0 for a given dust size and given values of τ and ion mass) and (ii) the perturbations of the basic state (including those related to DISWs) are highly dissipative.

The linear dispersion relation for DISWs is easy to obtain using the linearized expressions written in [2]. They describe the perturbations of the balance of the basic state; the perturbations of the ion momentum balance with allowance for the change of the dust drag, dust thermal pressure, ion inertia, and electric field; and the adiabatic perturbations of the electron density. The calculations are rather simple [72], and the exact derivation of the dielectric constant with the use of the results given in [2] is straightforward. Here, we start with presenting some simple estimates. For high frequencies, only the contribution of dust in the charge balance equation of the ground state is important and the electron-to-ion density ratio entering the dispersion relation is equal to $1 - P_0$. Thus, we obtain

$$\omega_{\mathrm{DISW}} = kV_{\mathrm{DISW}}, \quad V_{\mathrm{DISW}} = \sqrt{\frac{T_e}{m_i(1-P_0)}}. \qquad (12)$$

Note that the charging frequency is much less than the ion–dust collision frequency and, in the case where the frequency of the wave is larger than the ion–dust collision frequency ν_{id}, the variation of charges in a DISW can be ignored in first approximation. Since $\nu_{id} \approx P_0 z_0 v_{Ti} a/\lambda_{Di}^2$ (see [2]), we find that expressions (12) are valid only if $k\lambda_{De} \gg P_0 z_0 a/\tau\lambda_{Di}$. The exact condition

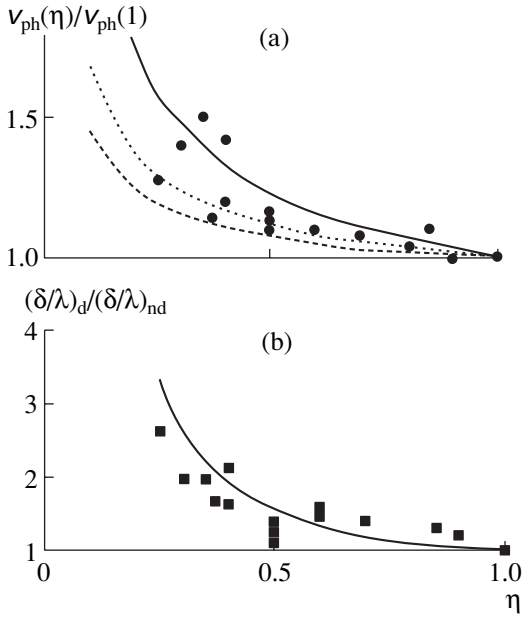

Fig. 35. (a) Phase velocity and (b) spatial damping rate (squares) of DISWs vs. parameter $\eta = 1 - P_0$ [80]. The solid curves in plot (a) are the results of calculations by the fluid theory with allowance for the drift along the magnetic field for three values of the drift velocity: (*1*) 0, (*2*) c_s, and (*3*) $2c_s$ (where c_s is the ion acoustic speed). The solid curve in plot (b) is obtained by taking into account the Landau damping only.

found in [72] determines only the numerical coefficient in this inequality, which reads

$$k\lambda_{De} \gg P_0 z_0 \ln\Lambda \frac{1}{3\sqrt{2\pi}} \frac{a}{\lambda_{Di}\tau}. \qquad (13)$$

Under the conditions of the experiments in which the conversion to the plasma crystalline state was observed, $a/\lambda_{Di} \approx 1/10$, $\tau = 0.02$, and $\ln\Lambda \approx 3$. In this case, the right-hand side of inequality (13) is larger than unity, while the linear relation between the wave frequency and the wavenumber is valid only for $k\lambda_{De} \ll 1$. Thus, the range where expressions (12) are valid is absent. This result is important because the nonlinear steepening of the waves and the formation of a shock wave is possible only for an approximately linear relation between the frequency and the wavenumber. The question is whether the linear relation (with the only change of the DISW phase velocity) can survive in the case opposite to inequality (13). As was found in [72], such a linear relation does not survive and the dispersion relation in this case describes a purely damped perturbation with a damping rate close to the frequency of ion–dust collisions ν_{id}:

$$\mathrm{Im}\,\omega = -P_0 z_0 \ln\Lambda\, v_{Ti} \frac{a}{3\sqrt{2\pi}\lambda_{Di}^2\tau}. \qquad (14)$$

Thus, the linear dispersion occurs only for rather small a/λ_{Di} values or small P_0. Special experiments need to be performed to satisfy condition (13). There are several experiments in which DISW shocks and DISW linear waves were observed [78, 79]. We mention that, in [79], the ratio a/λ_{Di} was in the range 3×10^{-3} to 10^{-2} and the effect of damping described by Eq. (14) was not large. However, in [69, 80], λ_{Di} varied from 30 μm to 1 cm, while the dust size varied from 1 to 10 μm. The ratio a/λ_{Di} could be on the order of 0.3; however, no investigations were made on the dependence of the damping rate on the dust size, which is predicted by Eq. (14).

Let us discuss this point in more detail for the experimental conditions of [80]. In [80], experiments were carried out in a *Q*-machine dusty plasma device with almost equal electron and ion temperatures ($T_e \approx T_i \approx$ 0.2 eV) and plasma densities in the range from 10^5 to 10^{10} cm^{-3}. Dust grains fell with velocities of about 30 cm/s, which is smaller than the estimated DISW velocity, therefore, the dust motion was unimportant. For equal temperatures, the Landau damping should be large; however, an important point is that the DISW phase velocity can be larger than the ion thermal velocity, due to the factor $1 - P_0$ in the denominator of the second expression in (12). Thus, the presence of dust can substantially reduce the Landau damping if P_0 approaches unity. In [80], the dependences of the phase velocity and spatial damping of DISWs on the parameter $\eta = 1 - P_0$ were determined (see Fig. 35).

The authors of [80] suggest that the main damping mechanism is the Landau damping, which depends crucially on the phase velocity of the waves. Under conditions where the ion and electron temperatures are equal, the DISW dispersion relation should include the ion pressure term. In this case, in the expression for the DISW phase velocity, instead of the factor $1/\sqrt{1-P_0}$ (see (12)), there should be the factor

$$\begin{aligned} \mathrm{Re}\,F &= \sqrt{(1 + (1 - P_0))/2} \\ &= \sqrt{(1 - P_0/2)/(1 - P_0)} \end{aligned} \qquad (15a)$$

and the relative change of the spatial Landau damping is described by the additional factor

$$\mathrm{Im}\,F = \exp\left(\frac{P_0}{1 - P_0}\right)\left(\frac{1 - P_0}{1 - P_0/2}\right)^{3/2}. \qquad (15b)$$

Figure 36 shows these factors as functions of the parameter $1 - P_0$. Qualitatively, they correspond to the experimental data shown in Fig. 35. For a more detailed comparison with the experimental curves, it is necessary to take into account the damping due to ion–dust collisions given by Eq. (14) and to investigate the dependence of dumping on the dust size. The damping (14) does not allow the wave to propagate if its wavenumber is less than that determined by inequality (13).

This effect depends strongly on the ratio a/λ_{Di} and the wavelength. It can manifest itself under the experimental conditions of [80]; however, no information about the observation of the cutoff or the absence of waves with wavenumbers less than those determined by the inequality that is the opposite of inequality (13) is presented in [80]. In the future, not only the threshold for the existence of DISWs but also the damping caused by ion–dust collisions in the range of the parameters where the DISW exist should be examined experimentally. For this purpose, it is more suitable to use complex plasmas with $\tau \ll 1$ (this condition is often met in complex plasma experiments). For the future experiments, we give the corrections for both the real and imaginary parts of the DISW frequency, which determine, respectively, the phase velocity and damping of DISWs in the range where these waves exist and are weakly damped. We mention that the Landau damping of DISWs is usually small if $\tau \ll 1$; the exception are experiments carried out in *Q* machines [81], in which the Landau damping on ions is of importance due to the low phase velocity of the waves for equal ion and electron temperatures. The Landau damping on electrons is usually small due to the large ion-to-electron mass ratio m_i/m_e for the gases with heavy ions often used in low-temperature experiments. Under conditions where the damping is small, the effects due to the damping caused by charging and ion–dust collisions, and the effect due to the Landau damping, make an additive contribution to the frequency. Therefore, we give here only the corrections to the phase velocity due to charging and ion–dust collisions in the range of weakly damped DISWs by using the general dispersion relation found in [72] in the limit $\tau \ll 1$:

$$\frac{\omega_{\mathrm{DISW}}^2 T_e(1-P_0)}{m_i k^2} = 1 - \Delta_{\mathrm{DISW}};$$
$$\Delta_{\mathrm{DISW}} = \frac{P_0^2 \alpha_{\mathrm{dr}}^2 z_0^2 (1-P_0) a^2}{2\tau k^2 \lambda_{Di}^4} + k^2 \lambda_{De}^2. \quad (16)$$

These dispersion corrections are small: the first term is small in view of condition (13) for the existence of DISWs, and the second term is small because the wavelength should be longer than the electron Debye length in order for the deviations from quasineutrality to be small. However, the first term, which is inversely proportional to k^2, can compete with the second term, which is proportional to k^2, and this can be checked experimentally. The charging effect changes the damping slightly [72]:

$$\mathrm{Im}\,\omega_{\mathrm{DISW}} = -\frac{P_0}{2\sqrt{2}} \frac{v_{Ti} a}{\lambda_{Di}^2} \left[\frac{\alpha_{\mathrm{dr}} z_0}{\tau} + \frac{2\alpha_{\mathrm{ch}}}{1-P_0} \Delta_{\mathrm{DISW}} \right]. \quad (17)$$

When the dusty plasma is perturbed by a large disturbance and the dispersion of DISWs is linear (the frequency is proportional to the wavenumber), the steepening of the profile of the perturbation and formation of a shock is usually expected. To form the shock, the damping should be small. In the experiments performed in the Q-machine device with equal electron and ion temperatures [78], this condition can be satisfied only for large values of P_0. In the experiments of [81], which were performed in a device similar to that of [80], the steepening of a disturbance created by launching a rectangular voltage pulse to the plasma grid was observed for $P_0 \geq 0.75$. The plasma density was lower than 10^7 cm^{-3}, and the plasma Debye length was 0.3 cm. Therefore, the ratio a/λ_D was small (on the order of 10^{-3}) and the wavelength at which the ion–dust collisions become important was about 10 m (larger than the device size), while the steepening was observed at distances of 30–40 cm. It can be seen from Fig. 37 that, without dust, the applied pulse spreads as the distance from the grid increases, while in the presence of dust, the steepening of the pulse and the shock formation is observed at $P_0 \approx 0.75$. Obviously, the thickness of the shock front (see Fig. 38), which is about 40 cm, cannot be explained by the dissipation due to either charging or ion–dust collisions (according to the list of the elementary process in complex plasma [2], it should be on the order of $\lambda_d^2/a \approx 5$ m) and can be explained only by the Landau damping of ion-sound perturbation on ions. The dust only increases the phase velocity of the wave and leads to steepening of its profile, but the dust still cannot be the main cause of dissipation in the shock.

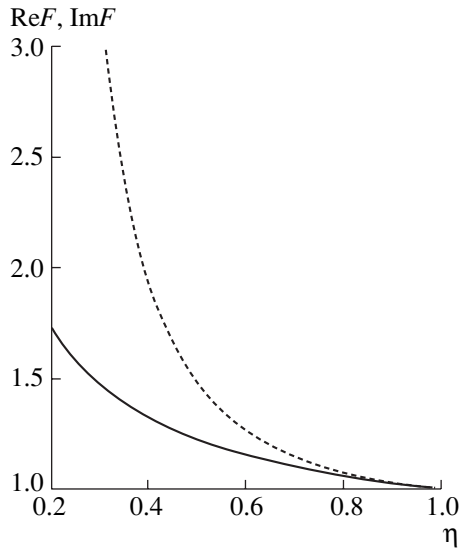

Fig. 36. Functions ReF (solid curve) and ImF (dashed curve) vs. parameter $\eta = 1 - P_0$ [see Eqs. (15a), (15b)].

In experiments of [79, 81, 82], linear DISWs, DISW solitons, and DISW shocks were observed in a low-temperature plasma under conditions close to those for the plasma crystal formation, but still not at such low

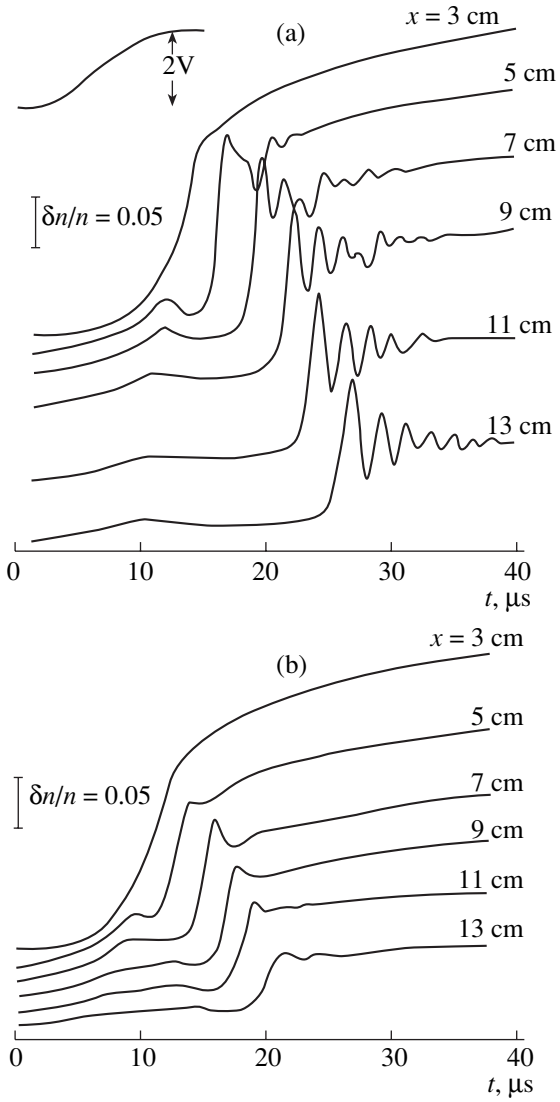

Fig. 37. Observation of the appearance of an oscillatory structure after the steepening of the wave profile for n_d = (a) 0 and (b) 5×10^4 cm^{-3} ($\lambda_D = 0.06$ cm, $\omega_{pd} = 3 \times 10^5$ s^{-1}) [81].

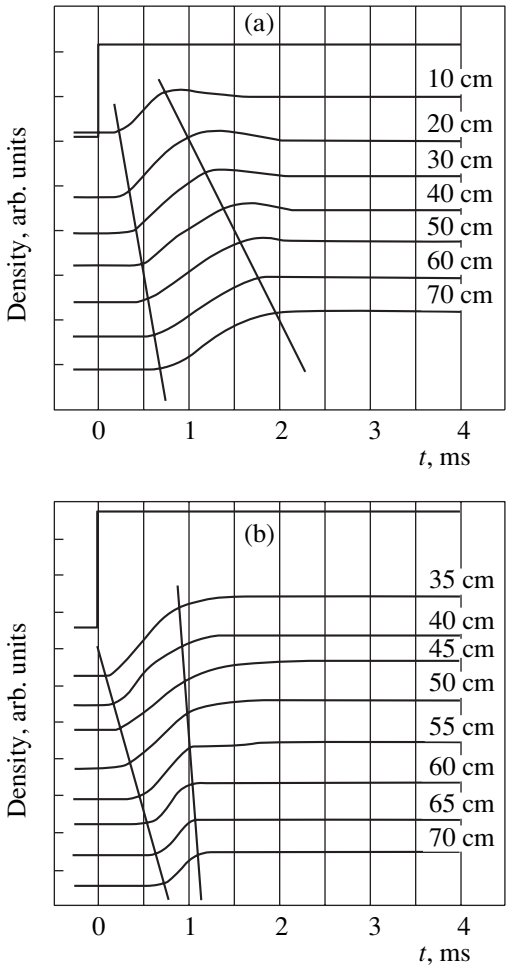

Fig. 38. Variations in the plasma density at different distances from the grid (a) in the absence of dust and (b) in the presence of dust with $P_0 \approx 0.75$ [80]. The horizontal segments of the curves correspond to uppermost values of n at different z. The top square wave is the pulse applied to the grid. The dashed lines mark the advancement of the leading and the trailing edges of the pulses. In plot (a), the dashed lines diverge, indicating that the pulse front spreads out, whereas in plot (b), the lines converge, indicating the steepening of the pulse front.

values of τ as in plasma crystal experiments. First, we consider the experimental conditions and the data obtained, and then give some estimates using the table of elementary processes in complex plasma [2] and discuss how the theory can be formulated.

The experiments were performed in a double-plasma device. The electron temperature was about 1–1.5 eV, and the ion temperature was about 0.1 eV, which corresponds to $\tau \approx 0.1$. The electron density was in the range $10^8 < n_e < 10^9$ cm^{-3}, and the ion Debye length was in the range 90–230 μm. The dust size was about 9 μm. For the Ar gas used, this corresponds to $z_0 \approx 3.2$. The parameter P_0 varied from 0.3 to 0.4. Under these conditions, inequality (13), which determines the range of the existence of DISWs, takes the form $k\lambda_{De} = k/k_e >$ 0.1. It is this range of wavenumbers that was investigated experimentally in [79–82]. This is not surprising because, in the other ranges, the DISWs should not exist. The gas pressure was about 10^{-4} Torr, and the mean free path for collisions with neutral atoms was about 300 cm, which was larger than the discharge tube length. Thus, the only important collisions were the ion–dust collisions. The experiments are able, in principle, to check the theoretical values of the frequency of ion–dust collisions. The mean free path for ion dust collisions λ_{id} can be estimated from Eq. (14) as $v_{Ti}/2\mathrm{Im}\,\omega \approx \lambda_{Di}^2 3\tau\sqrt{\pi}/\sqrt{2}aP_0 z_0 \ln\Lambda \approx$ 2500–500 μm for P_0 = 0.1–0.4, which is 20 times less than that claimed by these experiments (see [81]). This estimate

is important because the hydrodynamic concepts for ion–dust collisions (such as ion viscosity) can be used only for $\lambda \gg \lambda_{id}$. At $n_i \approx 10^8$ cm^{-3}, the wavelength of the observed waves varied from $0.6\lambda_{id}\sqrt{(1-P_0)/\tau} \approx 227$–420 μm to the values five times larger (1135–2100 μm) as the parameter P_0 varied in the range $0.1 < P_0 < 0.4$. For the densities $n_i \approx 10^9$ cm^{-3}, the corresponding wavelengths are shorter by a factor of 3.3. Using both the theoretical and the experimental estimates of the mean free path for ion–dust collisions, we find that it is much larger than the wavelength, and the concept of viscosity cannot be used in analyzing the observations (as was done in [81]). We mention that the estimate of the mean free path equal to 1.2 cm, which is needed to fit the experimental results, was obtained by adding the viscosity term. Under the conditions where the wavelength is much less than the mean free path, the viscosity should be considered to be zero. The observations of the linear dispersion [81] should be compared with the linear dispersion curves in which the viscosity is ignored. Such a comparison shows that the theoretical estimates agree qualitatively with the dependences obtained experimentally. The experimental results are shown in Fig. 39, where $k = k_r + ik_i$. The authors claim that the damping in the absence of dust is not related to the Landau damping. We note, however, that it is the experimental data that are of importance, rather than their comparison with the linear theory that includes viscosity.

In the nonlinear case, the DISWs convert into solitons [82] and shock waves [81]. In comparing the experimental results with the theoretical predictions, one should use an appropriate nonlinear description. The simplest description is based on the Korteweg–de Vries (KdV) equation in dusty plasma [81] under the assumption that the nonlinearity is weak. The usual expression for the nonlinear term in the KdV equation is $\propto\phi\partial\phi/\partial x$. In complex plasmas, the coefficient in front of the nonlinear term depends on P_0 and τ, as well as on the phase velocity, which is determined by the linear part of the equation. It is clear that, under conditions where the ground state of the complex plasma is determined by the balance of ionization and absorption on dust, a new nonlinear term will appear from the perturbations in the ion continuity equation, containing the nonlinearity of the type $n\partial u/\partial x$ and $u\partial n/\partial x$, which can be converted into the $\phi\partial\phi/\partial x$ nonlinearity by using the linear relations between n, u, and ϕ. Thus, in complex plasmas, the numerical factor by the nonlinear term in the KdV equation should be different from that in the usual KdV equation used in [81] to interpret the experimental data. In the future, the observations should be analyzed using this more appropriate theoretical model.

Here, we mention the main qualitative results of the observations [82] and their qualitative interpretation:

(i) The Mach number M as at a fixed soliton height decreases with increasing dust density. This can be explained as follows. Since, in the usual KdV equation, the soliton height is proportional to $(M-1)v_s$ and since, in presence of dust, $v_s \propto 1/\sqrt{1-P_0}$, the value of M should be proportional to the height times $\sqrt{1-P_0}$ and, thus, should decrease with increasing P_0.

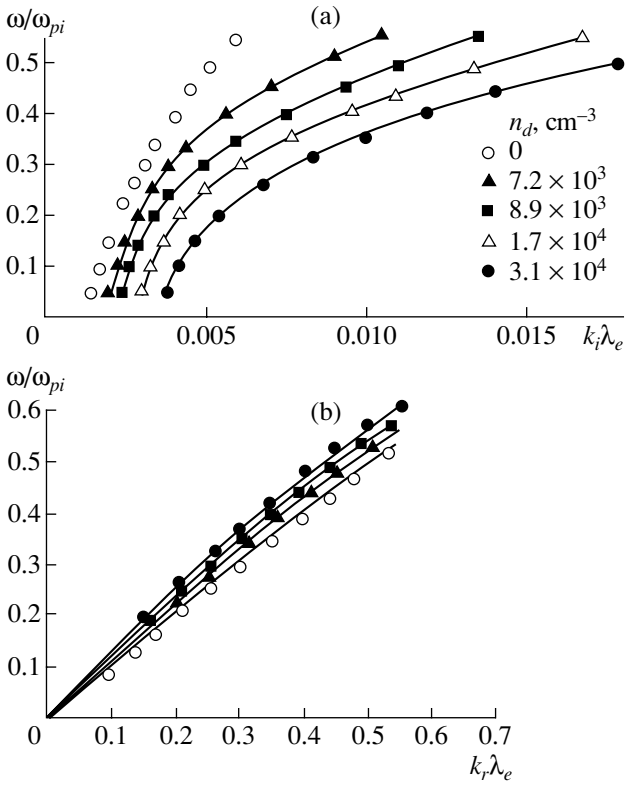

Fig. 39. (a) Measured values of the imaginary part of the DISW wavenumber vs. frequency ω for different dust densities n_d. The solid curves show theoretical estimates obtained with allowance for ion–dust collisions using the corresponding fitting parameters for each curve. (b) Measurements of the dispersion relation for DISWs. The solid curves (from bottom to top) are the theoretical results obtained for $\eta = 1 - P = 0.27$, 0.1, 0.063, and 0.052, respectively [81].

(ii) The width of the soliton increases with increasing dust density. This can be understood from the known dependence of the width of a KdV soliton on its height, namely, from the fact that the soliton width is inversely proportional to the square root of the height. Since the soliton height decreases with increasing dust density, its width should increase.

(iii) The damping of solitons is approximately proportional to the dust density. This can be explained by the fact that the damping is produced by ion–dust collisions whose frequency is proportional to P_0.

Thus, the experimental results are qualitatively understood, while the detailed comparison with the theory appropriate for complex plasmas is still the subject of future investigations. A similar statement can be made for the shock wave structures observed in [81].

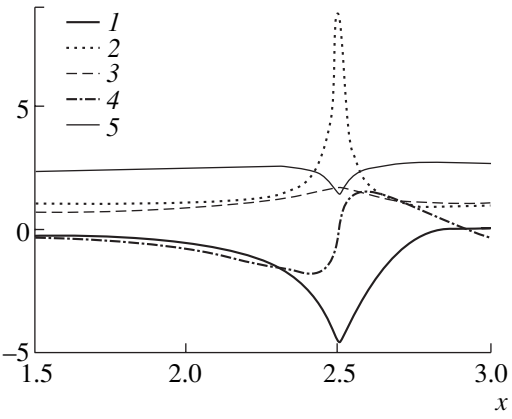

Fig. 40. Strongly nonlinear dissipative structure showing the necessity of applying an external electric field to support a DISW shock wave [83]. The curves are obtained by numerically solving the hydrodynamic balance equations for a structure propagating with a constant velocity u_0 in the absence of an external electric field. The profiles are shown of (*1*) the normalized ion drift velocity $u = u_i/\sqrt{2}v_{Ti}$, (*2*) the ion density $n = n_i/n_0$, (*3*) the electron density $n_e = n_e/n_0$, (*4*) the self-generated electric field $E = eE\lambda_{Di}^2/aT_e$, and (*5*) the dust charge $z = Z_d e^2/aT_e$, where n_0 is the ion density in the absence of a wave, λ_{Di} is the ion Debye length, T_e is the electron temperature, and a is the grain radius. The Mach number is $M = -u_0/\sqrt{2T_i/T_e} = 1$ (the wave propagates from right to left; the curves are drawn in the reference frame moving with the wave).

Some general remarks should be made in connection with these observations.

(i) It is obvious that the use of devices with a higher (as compared to the plasma crystal experiments) ion temperature (up to $\tau \approx 0.1$) was an important feature of the experiments on DISW waves and shocks. The higher ion temperature is related to the lower pressure of neutral atoms, which cannot equalize their temperature with ions. The high ion temperature leads to the existence of a range of wavenumbers where DISWs are not heavily damped. Thus, these experiments are not dealing with the usual low-temperature plasmas in which the pressure is 3–4 orders of magnitude higher and $\tau \approx 0.01$–0.02. Under such conditions, one can hope to observe DISWs only for rather small dust sizes, $a/\lambda_{Di} \leq 10^{-3}$, at which the dust grain charges are not so big and the plasma condensation does not occur.

(ii) The above experiments allow the direct measurements of the ion–dust collision frequency; however, under conditions close to plasma condensation, the frequency of these collisions can differ from that in the low-density limit.

(iii) Although linear DISWs cannot exist when condition (13) is violated, strong nonlinear perturbations can exist and propagate. In this case, nonlinear structures excited and supported by external sources can also exist even when the frequency of ion–dust collisions is high. Such strongly dissipative structures require a separate experimental study. From the theoretical point of view, the nonlinear set of equations for these structures can easily be formulated by taking nonlinearities into account exactly (not only weak nonlinearities as in the above KdV approach). For this purpose, one can assume that the nonlinear wave propagates with a constant velocity determined by the Mach number M. In this case, the equations can be converted into 1D equations, which can be solved numerically. These equations are the equation of ion motion and the ion continuity equation, including variations in the dust charge but assuming that the dust is at rest. These equations were written in [2], where no assumptions on the weakness of the nonlinearities was made. An example of a strong dissipative structure obtained in this way is presented in Fig. 40, which demonstrates a quite unusual distribution of the parameters and electric fields in such a structure [83]. The structure propagates from right to the left with a Mach number of $M = 3$. At the far left from the front, the complex plasma is assumed to be unperturbed, and the usual force balance for the ground state is valid. The ion density in the structure is much enhanced, and the ion dust collision frequency is somewhat decreased because the charge of dust grains is decreased, but the dissipation (per unit length) is highly increased because of the enhanced ion density in the structure.

(iv) In general, ion-sound shock waves as steady-state nonlinear steplike structures with different values of the ion drift velocity on both sides of the shock front cannot exist in complex plasmas. Indeed, in the case of nonmoving dust (which is the case of ion-sound perturbations), the ion motion is stopped by the ion–dust collisions and the ion drift velocity cannot be constant behind the shock even when it is zero in front of the shock. This means that such structures, if observed, should be either supported externally (for example, by some external electric field behind the shock) or they should be nonstationary.

(v) Different theoretical approaches used to describe DISWs (except that used in [72]) do not take into account the power balance in the ground state (see [2]). To take into account the power balance is the only way to determine the state against which the linear perturbation develops. The homogeneous power balance, which is the simplest to analyze, defines completely the basic state by a single parameter P_0. This allows less flexibility in choosing the complex plasma parameters and makes the consideration quite general. The simplest way to obtain the general dispersion relation for DISWs in such a formulation of the problem is to use the force balance equations, the continuity equations, and the charging equation, as well as the linearized expressions for ion and electron densities in Poisson's equation. Simple algebra then leads directly to the dielectric function, which should be used for the description of DISWs. We will here give this expression, from which

one can easily obtain all the approximate dispersion relations and the damping of DISWs used above in our discussion:

$$\epsilon_{\mathbf{k},\omega} = 1 + \frac{\tau}{k^2\lambda_{Di}^2}\left\{\left(1 - P_0 + \frac{\alpha_{ch}P_0}{(1+z_0)\alpha_{ch} - i\omega}\right) + \left(1 + \frac{\alpha_{ch}P_0}{(1+z_0)\alpha_{ch} - i\omega}\right) \times \left[1 - \frac{\alpha_{ch}a^2P_0(\alpha_{ch}z_0 - i\omega)(\alpha_{dr}P_0z_0 - 2i\tau\omega)}{((1+z_0)\alpha_{ch} - i\omega)k^2\lambda_{Di}^4}\right] \times \left[\tau + \frac{a^2}{k^2\lambda_{Di}^4}\left(\frac{P_0\alpha_{ch}(z_0\alpha_{ch} - i\omega)}{(1+z_0)\alpha_{ch} - i\omega} - i\omega\right) \times (\alpha_{dr}P_0z_0 - 2i\tau\omega)\right]^{-1}\right\}, \quad (18)$$

where $\omega = \omega^{ac}\lambda_{Di}^2/a\sqrt{2}v_{Ti}$ is the dimensionless frequency and ω^{ac} is the actual frequency.

4.3. Dust Acoustic Waves

The first attempt to describe dust acoustic waves was made in [66, 67] using the known theory of waves in multicomponent plasma (see also [68–70]) in which dust serves as one of the heavy components. Such waves in a usual multi-ion plasma have long been known [64] and were investigated in detail both experimentally and theoretically. The difference between the approaches of [67] and [64] is only in the mass of heavy ions (i.e., the dust grain mass), since the dust component is extremely heavy as compared to the ions in usual plasma. However, as was already mentioned, all the waves in complex plasma change completely in the low-frequency and small-wavenumber range. These changes were not taken into account in [64, 66–70], and an attempt to take them into account was made in [71, 72, 84, 85]. The charging process as a damping mechanism of DAWs was considered for the first time in [85], but the ion–dust collisions were not included. The first kinetic description of DAWs was performed in [71], where the external source maintaining the complex plasma was considered to be independent of the plasma parameters. The full hydrodynamic description with a source proportional to the electron density was formulated in [72]. In that paper, it was shown that both the real frequency and the damping of DAW in a complex plasma is quite different from those in a usual multicomponent plasma (a similar result, but without the inclusion of, ion–dust collisions was obtained in [85]). In particular, the DAW frequency $\omega_{DAW} = kV_{DAW}$ (where V_{DAW} is the DAW phase velocity) obtained in [71, 72, 84] depends strongly on the parameter P_0, and coincides approximately with the expression given in the multicomponent approach only at large wavenumbers and in the limit $P_0 \longrightarrow 0$, i.e., when the dust is almost absent. In [71], by a kinetic consideration, it was also found that, in the low-frequency range $\omega \ll \nu_{ch}P_0$, the damping rate of DAWs can be estimated as $\mathrm{Im}\,\omega \sim k^2V_{DAW}^2/\nu_{ch}P_0$, which is very similar to the damping rate of acoustic waves in ordinary neutral gas, $\mathrm{Im}\,\omega \sim k^2V_{DAW}^2/\nu$.

Here, we will not consider in detail the kinetic description of DAWs [71], since such a description also needs a generalization for the case of a source depending on the plasma parameters. Instead, we will give an extremely simple description of DAWs using the results of [2] (here, we follow [72]). Contrary to [71], where the external source was assumed to be independent of the plasma parameters, we will use the ground state with a source proportional to the electron density. Such a model is more adequate in describing the experimental conditions corresponding to ionization by an RF field. In this case, we can use static expressions for the low-frequency electron and ion responses obtained in [2], which substantially simplifies all the results [72]. We will also assume that the power balance in the ground state is satisfied, which is necessary in any formulation of the linear theory. In some cases, the discharge chamber walls, where the ionized component can recombine, can make a significant contribution to this power balance. This can happen only if the size of the system is less than the mean free path for plasma absorption on dust grains, λ_{Di}^2/aP_0 (see [2]). Since the opposite is valid for most of the experiments in complex plasmas, we will assume the presence of the power balance in the ground state between ionization and absorption on dust (the dispersion of DAW without such a balance was obtained in [86, 87] and differs from that discussed in [72]).

The frequency of DAWs is much less than both the charging frequency and the frequency of ion–dust collisions. The phase velocity of DAWs is much less than the ion and electron thermal velocities, but is much larger than the dust thermal velocity. The speed of these waves (due to the large dust charges $Z_d \gg 1$) is always larger than $\sqrt{T_i/m_d}$, which is close to the dust thermal velocity if the ion temperature is close to the dust temperature. The only expression that we need to describe DAWs is the response of the dust. The dust response is determined only by the dust inertia, the dust pressure, and the Epstein drag force on neutral atoms [2]. The linearization of these equations and simple algebra gives the dielectric constant that describes DAWs. This dispersion relation is quite different from that used in the first considerations of acoustic waves in the framework of the multicomponent plasma approach (henceforth, these waves will be referred to as multicomponent acoustic waves (MCAWs)).

We will give the expression for the dielectric constant at the end of this section and start here with emphasizing the difference of the dispersion of DAWs for real complex plasmas from the dispersion of MCAWs in a multicomponent plasma. In a complex plasma, perturbations caused by a DAW inevitably lead to variations in the dust charges, which turn out to be different in different parts of the wave. The DAW dispersion is also related to the disbalance of the ground state by the DAW perturbations. The latter affects the DAW in such a way that the linear dispersion of DAWs (i.e., the linear dependence of the wave frequency of the wave number) is valid only for large wavenumbers satisfying the inequality

$$k^2\lambda_{Di}^2 \gg P_0^2\alpha_{\rm dr}\alpha_{\rm ch}\frac{a^2}{\lambda_{Di}^2\tau}. \quad (19)$$

It is important to note that criterion (19) depends on the product of the charging and drag coefficients. Therefore, the simultaneous presence of charging and drag is crucial for calculating responses in complex plasma (remind that $\alpha_{\rm dr}\alpha_{\rm ch} \approx \ln\Lambda/3\pi$ [2]). When condition (19) is valid, the dispersion relation for DAWs has the form

$$\omega_{\rm DAW} = kv_{\rm DAW}, \quad (20)$$

with

$$v_{\rm DAW}^2 = \frac{P_0Z_dT_i}{m_d}\frac{1+z_0}{1+z_0+P_0+\tau(1+z_0-P_0z_0)}. \quad (21)$$

If one simply (without any justification) ignores the dust charge variations, one gets the expression obtained in the multicomponent model:

$$\omega_{\rm MCAW} = kv_{\rm MCAW}, \quad (22)$$

where

$$v_{\rm MCAW}^2 = \frac{P_0Z_dT_i}{m_d(1+\tau(1-P_0))}. \quad (23)$$

Although $v_{\rm MCAW}$ substantially differs from $v_{\rm DAW}$, in the first experiments on DAWs [88], the comparison was made with Eq. (23). Note that, in most of the experiments, P_0 was on the order of unity, in which case the difference between expressions (21) and (23) is rather large. In the limit $\tau \ll 1$, we obtain

$$v_{\rm DAW}^2 \approx \frac{P_0Z_dT_i}{m_d}\frac{1+z_0}{1+z_0+P_0}; \quad v_{\rm MCAW}^2 \approx \frac{P_0Z_dT_i}{m_d}. \quad (24)$$

For expressions (24) to be valid, it is necessary that, besides restriction (19), the inequality $k \ll \lambda_D^{-1} \approx \lambda_{Di}^{-1}$ be satisfied. The latter inequality is violated when the wave frequency reaches the dust plasma frequency

$$\omega_{pd} = \sqrt{\frac{4\pi Z_d^2 n_d e^2}{m_d}} = \sqrt{\frac{P_0Z_dT_i}{m_d\lambda_{Di}^2}}. \quad (25)$$

Thus, linear relation (20) for DAWs can exist only for sufficiently small dust size grains,

$$\frac{a^2}{\lambda_{Di}^2} \ll \tau. \quad (26)$$

The deviations from the linear dependence occur due to both the deviations from quasineutrality and the disturbances of the ground state, which result in corrections that are small by virtue of inequality (19):

$$\omega^2 \approx \omega_{\rm DAW}^2\left(1+\frac{\alpha_{\rm dr}\alpha_{\rm ch}P_0z_0(1+P_0)a^2}{k^2\lambda_{Di}^4\tau}-k^2\lambda_{Di}^2\right). \quad (27)$$

Let us briefly discuss the damping of DAWs. Note that, for a system externally driven at a frequency ω, the wave frequency is real and the wavenumber is complex, $k = k_r + ik_i$. The wavelength is related to k_r, and the damping (or growth) is related to k_i. The dispersion equation can be solved for k^2 as a function of ω^2. When the damping is small, it is characterized by $k_i/k_r \approx \gamma/\omega$.

When analyzing the damping of DAWs, it is necessary to take into account the following circumstances:

(i) The presence of the large factor $Z_d \gg 1$ in the expression for the DAW phase velocity makes it much larger than the dust thermal speed $v_{Td} = \sqrt{T_d/m_d}$. Thus, the Landau damping on dust grains, which is proportional to $\exp(-v_{\rm DAW}^2/2v_{Td}^2) \approx \exp(-P_0^2Z_d^2T_i/2T_d)$, is usually negligible. For example, under typical experimental conditions ($a \approx 3$ μm, $\tau \approx 0.02$), the DAW speed is $V_{\rm DAW} \approx$ 1–2 cm/s, while the dust thermal speed at room temperature is 3×10^{-4} cm/s (i.e., it is four orders of magnitude lower).

(ii) Landau damping on ions (which is much stronger than that on electrons) is on the relative order of $\omega_{\rm DAW}/kv_{Ti} \approx v_{\rm DAW}/v_{Ti} = \sqrt{Z_dP_0m_i/m_d}$ and is also very small, due to the large dust-to-ion mass ratio.

(iii) The two effects related to the charging processes contribute to damping. One of them is directly related to the charging, which is modified by the change of the ground state, while the other is related with the dissipation due to both the disbalance of the ground state and dust–neutral collisions. The first effect is on the relative order of $\omega_{\rm DAW}/\nu_{\rm ch} \ll \omega_{pd}/\nu_{\rm ch} \ll 1$, while the second effect is due to the mutual influence of drag and charging and is proportional to the product of the charging and the drag coefficients. An important point is that, in the range of existence of DAWs, the latter effect is related only to a small correction to dispersion relation (27) (the second term in parentheses, which is always small in the considered range of the linear DAW dispersion) and is proportional to the small factor on the order of $\omega_{\rm DAW}/\nu_{\rm ch}$, which is less than $\omega_{pd}/\nu_{\rm ch} \approx \sqrt{m_iZ_dP_0/m_d}(\lambda_{Di}/a) \ll 1$ (see [2]). Note again that the difference between these two damping mechanisms is

that the first one is proportional only to the charging coefficient, while the second one is proportional to both the charging and drag coefficients. Both of these mechanisms become of the same order of magnitude at the lowest possible frequency in the range of existence of DAWs (see (19)).

(iv) The damping of DAW can be related to collisions with neutral atoms. This mechanism seems to be most important in experiments. Nevertheless, the corresponding ratio $k_i/k_r \approx \nu_{nd}/2\omega_{\mathrm{DAW}}$ is also small if $k \ll k_n = \nu_{dn}/v_{\mathrm{DAW}}$. For typical experimental conditions and a pressure of several tenths of a millibar, this corresponds to wavelengths of $\lambda_n = 2\pi/k_n \approx (1\text{–}6) \times 10^{-2}$ cm, while the wavelength is usually equal to fractions of a centimeter.

We will, therefore, focus our attention on the general expression for the real part of the DAW frequency (27), which also takes into account the dust charge variations and the deviation of the DAW dispersion from the linear law.

The first observations of DAWs in laboratory dusty plasmas were reported shortly after the discovery of plasma crystals [89]. Since then, such observations have been reported in many experiments [89–92]. Clearly, one of the important tasks for the future is the investigation of instabilities leading to the excitation of these waves.

Figure 41 shows schematically the glow discharge device used in [89–92], while Fig. 42 shows the results of observations of compressional DAWs in a dc discharge plasma. The peaks and rarefactions of the dust grain density are easily recognized. In these experiments, the ion density was $n_i \approx (4\text{–}8) \times 10^8$ cm^{-3}, the ion temperature was 0.03–0.1 eV, and the electron temperature was 2.5 eV, which corresponded to $\tau \approx 0.013$–0.043 and $\lambda_{Di} \approx 360$–640 μm. Since the dust size was 0.7 μm, the ratio of the dust size to the Debye length was $a/\lambda_{Di} \approx (1\text{–}2) \times 10^{-3}$ and condition (26) was satisfied. The measured wavelengths were in the range 5–15 cm^{-1}, which corresponded to $k\lambda_{Di} \approx 0.1$–$0.3$. The working gas was nitrogen; in this case, for the given values of the dust size and electron temperature, we have $z_0 \approx 2$, $Z_d \approx 2 \times 10^3$, and $n_d \approx 10^5$ cm^{-3}, which means that $P_0 \approx 0.3$–0.5. For these parameters, the second term in parentheses in dispersion relation (27) is approximately 0.1 for the lowest measured wavenumber $k \approx 5$ cm^{-1}, while the third term is 0.01. Thus, the dispersion is related to the second term. This can be seen from the experimentally measured dispersion relation presented in Fig. 43.

The open circles in Fig. 43 correspond to the experimentally measured values, while the curve corresponds to the MCAW dispersion described by Eq. (22). It can be seen from Eq. (24) that the DAW phase velocity should have a lower value and the straight line corresponding to the theoretical prediction should go higher than that in the figure. For $z_0 = 2$ and $P_0 \approx 0.5$, the decrease in the phase velocity is only 8%, but it fits the observations better and suggests directly that the dispersion is determined by the second term in parentheses in Eq. (27); i.e., it is the opposite of the usual dispersion of sound waves in plasma. It would, of course, be desirable to take more precise measurements in the future to check all the new features of DAWs.

Experiments in which waves were excited externally (either by applying a sinusoidally varying potential to a wire located in the discharge chamber or by chopped laser light pressure) were first reported in [92]. These experiments initiated a highly successful and growing research technology employing so-called "active manipulation." We will not describe these experiments in detail here, but will instead refer to them in the following sections in the context of DLWs and DSWs.

Let us note here the main important points related to the DAW experiments:

(i) Investigations of DAW dispersion can serve as an efficient method for determining the parameters of complex plasmas. Generally, this includes the investigation of the DAW damping. The results of [2] allow one to find directly and in the simplest way the dielectric response functions, which include all the dispersion and damping effects

$$\epsilon_{\mathbf{k},\omega} = 1 + \frac{\tau}{a^2k^2}\frac{1}{(\tau + P_0k_{\mathrm{drch}}^2/k^2)}\left\{1 + \frac{P_0\alpha_{\mathrm{ch}}}{\alpha_{\mathrm{ch}}(1+z_0) - i\omega} + \tau\left(1 - \frac{P_0(\alpha_{\mathrm{ch}}z_0 - i\omega)}{\alpha_{\mathrm{ch}}(1+z_0) - i\omega}\right)\right.$$
$$\left. - \frac{P_0^2k_{\mathrm{drch}}^2}{k^2} + \frac{P_0k^2(\tau + k_{\mathrm{drch}}^2(P_0 - \tau)/k^2)(\tau + \alpha_{\mathrm{dr}}\alpha_{\mathrm{ch}}P_0z_0(1+P_0)/k^2)}{[(\tau_dk^2 - \omega(\omega + i\nu_{nd})\tau/\mu)(\tau + P_0k_{\mathrm{drch}}^2/k^2) - P_0z_0\alpha_{\mathrm{ch}}\alpha_{\mathrm{dr}}\tau]}\right\}, \quad (28)$$

where

$$k_{\mathrm{drch}}^2 = \alpha_{\mathrm{dr}}\alpha_{\mathrm{ch}}P_0z_0\frac{\alpha_{\mathrm{ch}}z_0 - i\omega}{\alpha_{\mathrm{ch}}(1+z_0) - i\omega}, \quad (29)$$

Here, $\omega = \omega^{\mathrm{ac}}\lambda_{Di}^2/a\sqrt{2}v_{Ti}$ is the frequency normalized to the charging frequency, $k = k^{\mathrm{ac}}\lambda_{Di}^2/a$ is the wavenumber times the charging length, $\mu = Z_dm_i/2m_d$, and $\tau_d = T_d/T_eZ_d$.

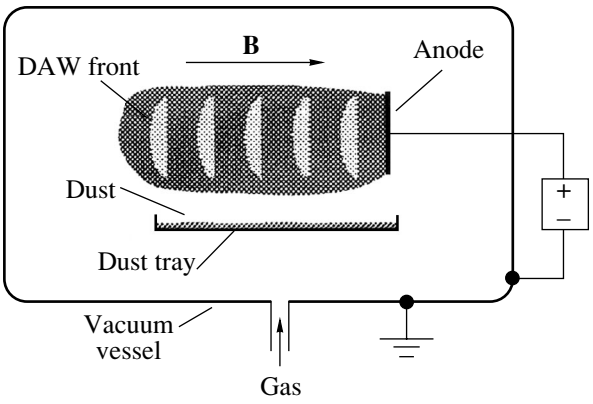

Fig. 41. Schematic of the glow discharge device used to trap negatively charged dust grains [89].

(ii) The real part of Eq. (29) completely describes the DAW dispersion (which was only approximately described by relation (27)) and takes into account exactly the dispersion related to the change of the balance in the ground state.

(iii) The imaginary part in the second and third terms in braces describes the effect of damping caused by charging [84], but in contrast to [84], generalizes this effect by taking into account the dispersion produced by the change of the ground state. In [92], this damping was named "Tromso damping."

(iv) In Eq. (28), the damping related to both the charging and the drag effect enters only into the dispersion terms proportional to $1/k^2$ and is determined by the product of the charging and drag coefficient (this means that, in the absence of one of these effects, both the dispersion and the damping related to the change of the background state disappear). The damping described by these terms can be named a "creation damping" (term used in [92]), meaning that the plasma particles, which are continuously absorbed by dust grains, should be replaced by some "new" ions injected in the discharge volume. The exact formulation of this effect can be made only if one initially starts with a formulation of

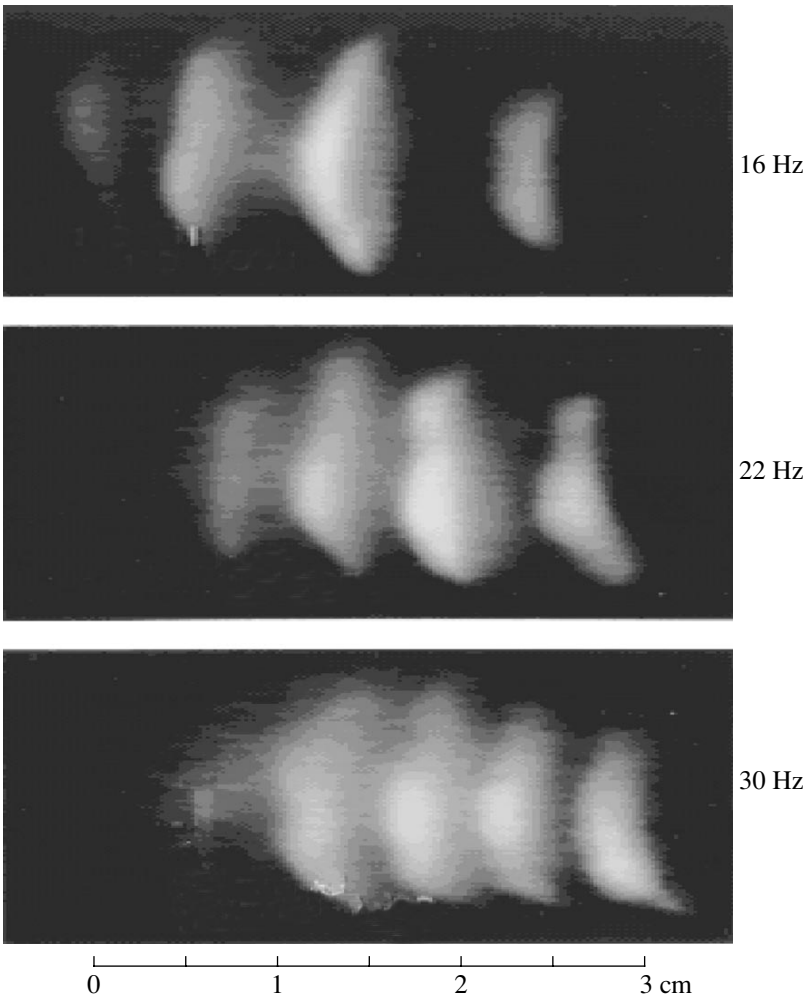

Fig. 42. Compressional DAWs in a dc discharge plasma (several dust acoustic fronts are shown) [89].

the basic state by using the power and particle balance equations as we have done here. Thus, expression (28) serves as an explicit and exact mathematical formulation of the "creation damping" mentioned in [92].

(v) The most important effect introduced by the basic state variations and "creation damping" is that DAWs do not exist (or are strongly damped) for small wavenumbers satisfying the inequality opposite to inequality (19). Expression (29) can be used to find the precise value of the critical wavenumber. The impossibility of the existence of low-frequency DAWs should be checked in future experiments.

4.4. Universal Instabilities in Complex Plasmas: Structurization, Gravitation-Like, and Crystallization Instabilities

In ordinary plasmas, instabilities appear in the presence of some nonequilibrium distributions such as the anisotropy of particle distributions, the inhomogeneity of the system, etc. A specific feature of complex plasmas is that instabilities can develop in the absence of such nonequilibrium distributions. The source of these is the energy and particle supply in the ground state. In this sense, they are universal instabilities (UIs) of complex plasma. The physical reason for the appearance of the instability is the possibility of attraction for like-charged grains in complex plasma. When the growth rate is large enough, only the ions are involved in these instabilities, and the dust grains are not able to follow the development of the instability because of their large mass. When the growth rate is sufficiently small, the dust grains can follow the development of the instability (the electrons are always adiabatic). In some sense, this is similar to two types of waves in dusty plasma: DISWs (in which the dust motion is not included) and DAWs (in which the dust motion is included).

The physics of such instabilities is related to the charging and friction (ion friction is described by the drag coefficient). The perturbations arising in the course of these instabilities are almost quasineutral. Assume, for example, that due to fluctuations, the ion density in a particular region of space becomes larger than in other regions. The electron density is then also increased in this region and the ionization rate becomes larger, more ion–electron pairs are produced in this region, and the ion density increases further. The effect that does not allow the ions to escape freely from the region with an enhanced ion density is the friction of ions on the dust grains. This friction allows the ions to leave the region with an enhanced ion density, with a finite velocity determined by friction. Thus, for a sufficiently large size of the region with an enhanced ion density, the escape of ions from this region cannot balance the increase in the ion density due to ionization; this results in the onset of instability. To estimate the critical length or the critical wavenumber at which the instability starts to develop, we notice that, in any dissipative system, resistance creates an electric field.

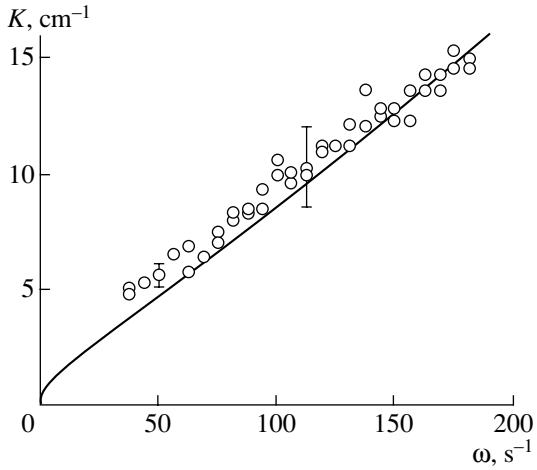

Fig. 43. Measured dispersion relation for DAWs [89–93].

Hence, the ion flux, being resisted by dust, creates an electric field which can be estimated using the results of [2]. In dimensionless units, this field will be on the order of $E \approx -\alpha_{dr} P_0 u z_0$. On other hand, the presence of the electric field creates an electron density gradient (due to the adiabatic behavior of electrons, we have $dn_e/dx \approx -E \approx \alpha_{dr} P_0 u z_0$). The ion flux is proportional to the electron density, $du/dx \approx \alpha_{ch} P_0 n_e$ (the coefficient in front of n_e is taken from the condition of the balance of the ionization and absorption on dust grains in the ground state, and we ignore for a moment the absorption of the ion flux on dust grains). Since the dimensionless length is in units of the charging length λ_{ch}, we find from here a simple estimate for the characteristic length L_{cr} at which instability starts to develop: $(\lambda_{ch}/L_{cr})^2 \approx \alpha_{dr}\alpha_{ch} P_0^2 z_0$ (we recall that $\lambda_{ch} \approx \lambda_{Di}^2/a$). This estimate shows that, the effect is indeed determined by the product of the charging and drag coefficients. This estimate is rough because it ignores the absorption of the ion flux on the dust grains, assuming that it is just of the same order of magnitude as the change in the ion density due to ionization. Direct calculations using dielectric functions (28) give

$$k_{cr}^2 \lambda_{ch}^2 = \alpha_{dr}\alpha_{ch} P_0^3 \frac{z_0^2}{1 + z_0 + P_0}. \qquad (30)$$

The instability has a property similar to the gravitational instability because the collective ion attraction (see [2]) results in the enhancement of the ion density, and the collective attraction force is proportional to $\alpha_{dr}\alpha_{ch}$, which determines the threshold of the instability. For $P_0 \longrightarrow 0$, the critical wavenumber decreases as $P_0^{3/2}$, i.e., much faster than in the case of the previous rough estimate. The character of the instability depends on whether or not the time is sufficient for dust to react. When the instability is fast enough, the correspondent

growth rate has a maximum at $k = 0$, i.e., at the largest possible size in the system, similarly to the gravitational instability. The growth rate γ in this case was first found in [75], and for $P_0 \ll 1$, it is described by the simple expression

$$\frac{\gamma}{\nu_{Ti}\sqrt{2}a/\lambda_{Di}^2} = \alpha_{ch}P_0^2\frac{z_0}{1+z_0}. \quad (31)$$

Recall that the expression in the denominator of the left-hand side of Eq. (31) is on the order of the charging frequency and that $\alpha_{ch} = 1/2\sqrt{\pi}$. In the opposite case ($P_0 \longrightarrow 1$), the factor $1 + z_0$ on the right-hand side of Eq. (31) can be omitted.

In the case of slow instability, when the dust grains are able to be driven by the instability, they are removed from the region of enhanced ion density by the ion drag force, thus forming a dust rarefaction. The complex plasmas are then divided into dust clumps and dust depletions. The dispersion relation for this case can be found from expression (24) for the dielectric permittivity in the limit opposite to inequality (19), which determines the range in which DAWs can exist [72]:

$$\frac{\omega^2}{2\nu_{Ti}^2a^2/\lambda_{Di}^4} = \frac{Z_dm_i}{2m_d\tau}\frac{\alpha_{ch}\alpha_{dr}z_0P_0^2(1+P_0)(1+z_0)}{[1+P_0+z_0-\alpha_{ch}\alpha_{dr}P_0^3z_0^2/k^2\lambda_{ch}^2]}. \quad (32)$$

In this case, the maximum growth rate corresponds to the wavenumber close to k_{cr} (see (30)).

Both types of instabilities are substituting the DAW and DISWs in the range of small wavenumbers (smaller than the critical value k_{cr}) and can be classified as structurization instabilities (SIs) [75]. Therefore, we can conclude that the formation of structures is one of the main properties of complex plasmas. There is no direct way to stabilize these instabilities by the ion pressure or the ion friction on neutral gas. Indeed, the instability appearing as a continuation of the DISWs to the range of small wavenumbers is created by the drag force. Therefore, adding friction on neutrals will even increase the growth rate of the instability. The ion pressure effect is proportional to k^2; thus, the SI survives in the limit $k \longrightarrow 0$, where the growth rate is maximal. The same is true for the instability that is the continuation of the DAW branch. An analysis of dispersion relations (18) and (28) (neglecting the dust pressure effects and the dust–neutral collisions) confirms this statement.

For the UI or SI, the critical wavenumber determined by expression (30) depends substantially on P_0. Note that, in several experiments, the value of P_0 was specially made close to unity. In this case, the growth rate of the instability is rather large and the main question concerns the critical wavenumber determined by expression (30). In the existing experiments on DISWs and DAWs, this critical wavenumber was not reached. However, it is not difficult to reach it for other dust sizes and other Debye lengths. Indeed, for the typical parameters of the plasma crystal experiments ($a/\lambda_{Di} \approx 0.1$, $P_0 = 0.6$, $z_0 = 3$, and $\ln\Lambda = 3$), we have $k_{cr}/\lambda_{Di} = 0.037$ and, for $\lambda_{Di} = 36$ μm, we find $k_{cr} \approx 9$ cm^{-1}, which is inside the range of wavenumbers usually measured in the existing experiments. Thus, the UI can be observed at these and smaller wavenumbers. Under usual experimental conditions ($\tau \ll 1$), there exist a range of wavenumbers between that determined by expression (19) (at which DAWs and DISWs start to be strongly damped) and the critical wavenumber determined by expression (30). This range can be also covered in future experiments. The continuation of the DISW branch to this range can be easily obtained from Eq. (18) and the continuation of the DAW branch can be easily obtained from Eq. (28). In the former case, we obtain a pure damped mode with a frequency determined by ion diffusion due to ion–dust collisions, $\omega \propto -ik^2/\nu_{id}$, and, in the latter case, we obtain a weakly damped mode related to charging:

$$\omega^2 = \omega_{pd}^2\alpha_{ch}\alpha_{dr}z_0P_0(1+P_0)\left(\frac{a^2}{\lambda_{Di}^2\tau}\right). \quad (33)$$

When condition (26) is satisfied, the frequency of this mode is smaller than the dust plasma frequency. The frequency of mode (33) can easily be made in the range of experimentally measured frequencies if the dust size is sufficiently large. Thus, both the UI and new dust modes could be the subject of future investigation. These modes can be excluded either by choosing the size of the system L to be less than that determined by the critical wavenumber or by some nonlinear stabilization. For the former case, we have

$$L \ll 1/k_{cr} \approx \frac{\lambda_{Di}^2(\sqrt{(1+P_0+z_0)})}{aP_0^{3/2}z_0\sqrt{\alpha_{ch}\alpha_{dr}}}. \quad (34)$$

This condition, nevertheless, does not completely exclude the existence of instability. Indeed, condition (34) can be compared with the condition at which the noncollective attraction dominates (see [2]),

$$L \ll \lambda_{Di}^2/aP_0, \quad (35)$$

which was obtained from the physical considerations that the size of the system should be less than the mean free path for the ion absorption on the grains. Therefore, one may expect that condition (34) expresses more exactly condition (35), which was obtained from simple physical considerations. Thus, under condition (34), the noncollective attraction is dominant and the attraction force is proportional to $1/r^2$, as is the case of gravitation attraction. As is well known, the latter

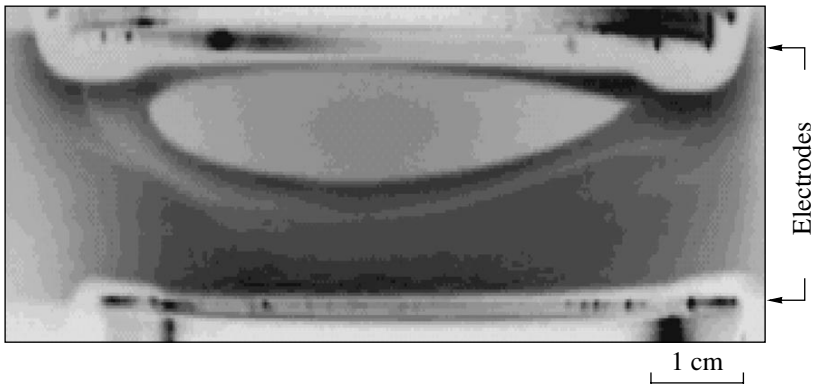

Fig. 44. Void structure observed experimentally in [95].

creates gravitational instability, which is described by the relation

$$\omega^2 = k^2 v_s^2 - 4\pi G n m, \qquad (36)$$

where v_s is the sound speed and G is the gravitational constant. Thus, one can assume that, in complex plasmas, the gravitation-like electrostatic instability (GLEI) due to the noncollective dust attraction can develop. We can estimate the growth rate of this instability by putting in Eq. (36) $v_{\mathrm{DAW}}^2 \approx \lambda_{Di}^2 \omega_{pd}^2$ instead of v_s^2, the expression

$$G_{\mathrm{eff}} m_d = \eta_{\mathrm{attr}} Z_d^2 e^2 a^2 / (m_d \lambda_{Di}^2)$$

instead of G (see [2]), and $n_d m_d$ instead of nm. We obtain $k_{\mathrm{cr}} \approx \sqrt{\eta_{\mathrm{attr}}} a/\lambda_{Di}^2$, which corresponds to the characteristic size at which the noncollective attraction starts to operate. This size in complex plasma is analogous to the Jeans length in gravitating systems. The GLEI was first considered in [74], and the detailed numerical results where dispersion (similar to that of DAWs) is taken into account were obtained in [93]. The self-contraction of small dust clouds described by this instability has not yet been investigated experimentally, but the self-contraction was observed numerically in simulations of the formation of dust clouds with only noncollective attraction included [94]. The final stage observed numerically was a free-boundary plasma cluster, which means that the plasma crystal can form not only when the collective attraction between dust grains is dominant but also when the noncollective attraction is operating.

The nonlinear stage of UI and GLEI depends on such parameters as the ionization rate, the dust pressure, and the neutral gas pressure. One possibility is that the dust rarefaction grow until the full separation of dust-containing regions (dust clumps or dust structures) and regions where the dust is completely absent (dust voids). Another possibility is that, in the nonlinear stage, only the fastest growing mode dominates and either filamentary structures or plasma crystals are formed. The void structures were first observed in [95, 96], and the nonlinear theory of them was considered in [97–99]. When voids develop, the quasineutrality condition can be violated in the nonlinear stage close to the void surface, which gives rise to an additional ion flux toward the dust condensation. Figure 44 presents the dust void structure obtained experimentally in [95] under the Earth's gravity conditions. The gravity force in those experiments was small because rather small dust grains ($a \approx 0.3$ μm) were used. The void was 100% free from dust and had very sharp edges with an abrupt jump of the dust density at the boundary. This phenomenon was predicted theoretically in [100, 101]. An important point in the void creation is that the drag force on dust grains in the vicinity of the void surface mainly acts on the first dust layer and shifts it stronger than the subsequent layers, where the drag force is depleted due to the absorption on dust. This creates large dust density gradients, and the edges of the void should be rather sharp [102]. This is what was observed in experiments where the voids were discovered for the first time [95], as well as in experiments carried out under microgravity conditions [96] (see Fig. 45).

The sharp void edges and sharp dust density jump appear while all other complex plasma parameters (such as the electron and the ion densities and the ion flux velocity) are continuous. Such a boundary presents a new type of discontinuity in complex plasmas. Recall that, in DISW shocks, the dust density is continuous while the other parameters change at the shock front. A moving void can be considered as a kind of DAW shock, but the real dust shock corresponds to the case where all the other plasma parameters behind the shock front relax to the new values (this relaxation length describes the thickness of a DAW shock).

The theoretical description of voids [97–99] is based on elementary processes described in [2], including all the nonlinear processes. The size of the void can be determined from the continuity of the electric field and the dust grain charge at the boundary of the void. This gives not only the size of the void as a function of

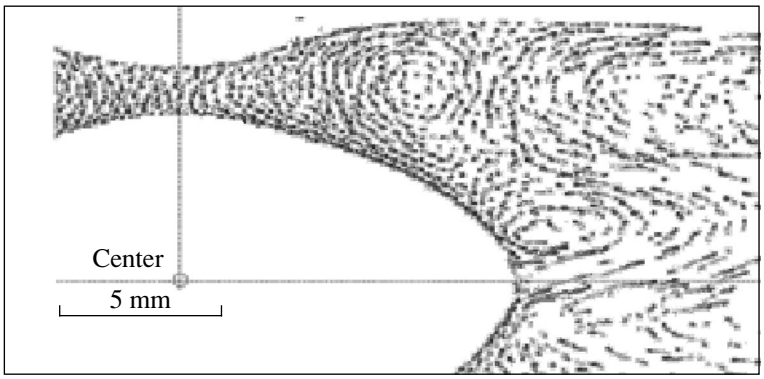

Fig. 45. Cross-sectional view through a dust plasma condensation formed under microgravity conditions in the experiment [96]. The power introduced in the plasma is 0.045 W. The figure is obtained by superimposing 150 video frames with a total exposure of 3.0 s. The dust cloud is rotationally symmetric about the chamber axis and contains 10^6 dust grains with a mean separation of 300 μm. In the center of the chamber, there is a spherical dust void, which contains no grains.

the degree of ionization, the ion and electron densities at the void surface, and the dust charge at the surface, but also the value of the jump of the dust density and the ion drift velocity at the surface of the void. Two cases were examined, namely, the case where the size of the void was less than the ion–neutral collision mean free path [97] and the case where the size of the void was larger than the ion–neutral collision mean free paths [98]. In the latter case, the theory predicts that the size of the void should increase with increasing the degree of ionization, which agrees with observations.

Dust voids not only exist as separate structures, but also surround the dust clumps. The formation of voids is usually accompanied by dust clumping. In the plane geometry, this corresponds to the dust layer formation observed in [103]. The ion flux created outside the structure can compress it. If the UI develops to its nonlinear stage, it can create dust clumps that self-confine dust grains inside the structure. It was proved in [100, 102] that the boundary between the dust-containing region and the void is nevertheless continuous, but is always relatively sharp as compared to the size of the void and the size of the dust clump if $T_d \ll T_e Z_d$, which is the case of most experiments with complex plasmas. This unusual conclusion follows directly from the force balance equation with the use of Poisson's equation. Thus, one can say that it is a direct consequence of the electrostatic balance in a complex plasma. One can imagine (although the whole temporal evolution of the complex plasma starting from the onset of instability up to its nonlinear stage was not fully analyzed) that the result of the development of UI can be a complete structurization of the complex plasma, i.e., its division into dust structures and voids. Therefore, in [75], this instability was classified as a structurization instability. The characteristic size of the structures and voids is determined by the critical wavenumber (30); i.e., for P_0 on the order of unity, it is on the order of the charging length (more exactly, it is on the order of the charging length divided by $P_0^{3/2}$). We emphasize this point because, after melting of a crystal, the complex plasma should convert itself into this structurized state or, before crystallization, the complex plasma should be in a structurized state. The voids also appear in the plasma sheath near the wall [104]. In microgravity experiments, it is necessary to form inside the chamber a structure surrounded by a void and a wall (preferably of spherical geometry). The theoretical possibility of the existence of such a nonlinear structure was investigated in [105], where the conditions of its existence, as well as the number of the maximum possible confined dust grains, were found. In [105], restrictions were found according to which, in order to avoid the void formation in the center of the chamber, the ionization rate should be less than a certain critical value, the ion and electron densities should be in certain ranges, etc. It was also found that, for the ion–neutral mean free paths usually encountered in experiments, the total number of dust grains cannot exceed of several millions. The question as to whether a dust structure or a dust void will form is one of the most important to be resolved in microgravity experiments on dust crystal formation. Figure 46 schematically shows the combinations of dust structures and dust voids investigated so far.

In dust-containing regions, dust convection was observed, which seems to be a general phenomenon for most of the possible combinations of voids and structures. In [106], the linear stage of dust convection was explained by the convection instability in which the dust mainly takes part, while the perturbations of other plasma components (electrons and ions) are small. This phenomenon of dust convection is new because it differs from the usual convection in gases in that the dust charging processes play an important role in the formation of convection cells.

There is also another possibility for the nonlinear stage of the UI, namely that, in the nonlinear stage, the

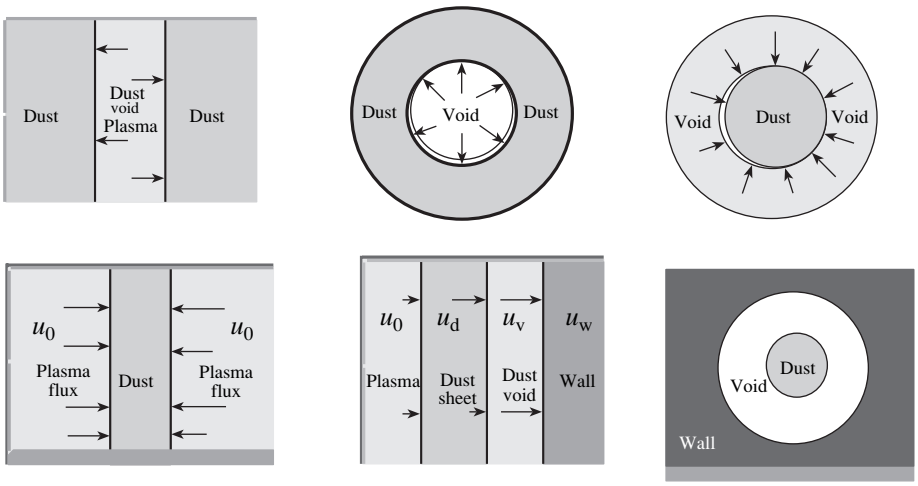

Fig. 46. Examples of structures containing dust clumps and voids that were investigated numerically by solving the exact hydrodynamic balance equations [101, 102, 105].

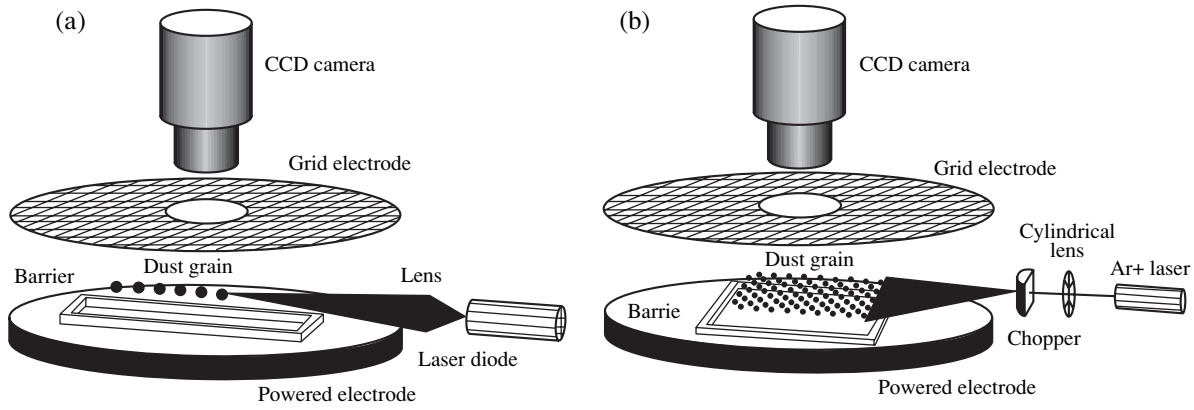

Fig. 47. Sketch of an apparatus for the excitation of longitudinal DLWs by a laser pulse in (a) a linear chain and (b) a monolayer plasma crystal [111].

perturbation converts into a single sinusoidal mode. One could expect that it can lead directly to the crystal formation because the periodic distribution of dust grains corresponds to a crystalline structure. Indeed, such a possibility exists because the growth rate tends to infinity as $k \longrightarrow k_{cr}$, which can lead to the excitation of a single mode with k close to k_{cr}. However, this is not guaranteed because, in the nonlinear stage, either a broad spectrum will be created leading to the void structure formation or a single mode will dominate. Both cases are well known in nonlinear physics. In fact, the growth rate determined by Eq. (32) cannot be infinite because it is restricted by the inertia of the charging process. Nevertheless, the growth rate will be maximum at k close to k_{cr}, which means that, in the linear stage, almost a single mode can be excited. The maximum growth rate can be found from Eq. (32) if one takes into account the inertia of dust charging and substitutes in Eq. (32) $1 + z_0 - i\omega/\alpha_{ch}$ for $1 + z_0$. It is easy to find that dust–neutral collisions cannot stabilize this instability. Indeed, for $\omega \ll \nu_{dn}$, one should substitute in (28) $\omega(\omega + i\nu_{dn})$ for ω^2. In this case, for $k < k_{cr}$, we get the dissipative instability. As was shown in [72], the only effect that can stabilize the instability is the dust pressure. It is found in [72] that the instability is stabilized if

$$\frac{T_d}{Z_d T_e} > \frac{2(1 + z_0 + P_0)}{\sqrt{3}\alpha_{ch}\alpha_{dr}P_0^3 z_0^2} \times (\alpha_{ch}\alpha_{dr}P_0^2(1 + P_0)(1 + z_0))^{2/3}\left(\frac{Z_d m_i}{2m_d\tau}\right)^{2/3}. \quad (37)$$

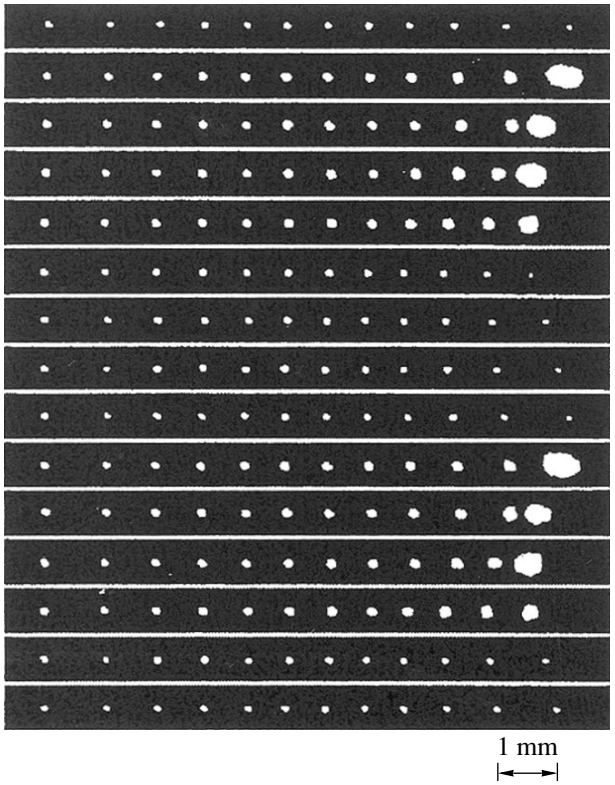

Fig. 48. Excitation of waves in a linear chain: a series of 15 snapshots taken at 100 ms intervals [110].

By assuming that the charging and drag coefficients and z_0 are on the order of unity, we get the dependence of the critical temperature on the parameters of the system:

$$T_{d,\mathrm{cr}} \approx T_i \frac{Z_d^{4/3}}{\tau^{4/3} P_0^{5/3}} \left(\frac{m_i}{m_d}\right)^{2/3}. \quad (38)$$

By using the data that are usually found in the existing experiments ($\tau = 0.02$, $Z_d = 10^3$, $P_0 \approx 1$, and $m_d/m_i \approx 10^{10}$), we found from Eq. (38) that $T_d > T_i$. Keeping in mind the roughness of this estimate, we can conclude that the criterion obtained agrees with the results of experiments in which phase transitions were observed.

Several points should be mentioned in connection with the problems raised in this section:

(i) The dust cluster self-contraction is a general phenomenon and can occur both for large and small dust clouds. In the first case, the collective dust attraction can be responsible for the UI formation of dust clusters, while in the second case, the noncollective attraction can be responsible for the GLEI formation of dust clusters.

(ii) When investigating the phenomenon of crystallization in complex plasma, one cannot avoid the initial structurization that can cause the appearance of crystal defects.

(iii) It is unlikely that monocrystals with sizes larger than the initial structure size can be created in microgravity experiments. In this case, it is more probable that these crystals will be polycrystals (a mixture of small crystals).

(iv) A theoretical concept can be further developed according to which the crystal formation is a result of the excitations of a single-mode UI. In this case, the amplitude of this nonlinear wave can be regarded as a parameter of order and the scale invariance approach can be used.

(v) More detailed investigations (both experimental and theoretical) of the thresholds and nonlinear evolution of UI can provide the desired information to resolve the dilemma concerning the crystal or void–clump structure formation.

(vi) There is a wide field for future investigations of the phenomenon of dust convection.

4.5. Dust Lattice Waves

When dust grains are packed into a crystal lattice (plasma crystal), their direct Coulomb or collective interactions dominate and DLWs can propagate in complex plasma. These waves are in a sense a continuation of DAWs less disturbed by dissipation, as compared to the waves in a gaseous state. The dispersion relation for DLWs can easily be derived following the classical "linear chain" model [107, 108]. For simplicity, only nearest neighbor interactions and neutral gas friction will be taken into account. Of course, the dust–dust interactions are much more complicated (see [2]), especially if one takes into account long-range collective interactions. However, even for these interactions, the subsequent potential energy minimums are smaller than the first, and we can assume that only the nearest grains make the main contribution. The Yukawa potential (or the Debye screened potential) is an oversimplification, and we will use it here only as an illustration. Assuming that the neutrals are at rest, we derive the force acting on the *n*th grain in the chain. We define the grain's deviation as δ_n and introduce the quantity $x_n \equiv \delta_n/\Delta$, where Δ is the mean lattice spacing. Then, in limit of $x_n \ll 1$, we find

$$m_d \Delta \frac{d^2}{dt^2} x_n = \alpha(x_{n-1} - 2x_n + x_{n+1}) - \nu_{nd} m_d \Delta \frac{d}{dt} x_n, \quad (39)$$

where the coupling constant α is determined by the interaction potential of two grains. In particular, assuming for simplicity that the grain charge is constant and the grains interact through a screened Coulomb potential ($V = (Q^2/r)\exp(-r/\lambda_D)$), we have

$$\alpha \equiv \frac{Q^2}{\Delta^2} \exp(-K)[(1+K)^2 + 1], \quad (40)$$

where $K \equiv \Delta/\lambda_D$. If we take some other type of interactions listed in [2], we will obtain a similar expression, but with another coupling constant. Making use of Bloch's condition, i.e., the fact that, in a regularly spaced array of particles the distance of a particle from the origin position $\mathbf{r}_0$ is determined in the zero approximation by the lattice vector $\mathbf{l} = n\mathbf{\Delta}$ ($\mathbf{r}_n = \mathbf{r}_0 + n\mathbf{\Delta}$), we get $x_n = \exp(i\mathbf{k}\cdot\mathbf{l})x_0$, where $\mathbf{k}$ is a given wave vector. In an infinite lattice, the origin position is arbitrary; hence, we can take the position of the nth grain as the origin. We will also assume that the wave vector is directed along the chain. Then, we get $x_{n-1} = x_0\exp(-ik\Delta)$, $x_n = x_0$, $x_{n+1} = x_0\exp(+ik\Delta)$, and Eq. (39) takes the form

$$m_d\Delta\frac{d^2}{dt^2}x_0 = -2\alpha x_0(1-\cos(k\Delta)) - m_d\nu_{nd}\Delta\frac{d}{dt}x_0. \quad (41)$$

From here, we obtain the dispersion relation

$$\omega^2 - \beta^2\sin^2\left(\frac{k\Delta}{2}\right) + i\omega\nu_{nd} = 0, \quad (42)$$

where $\beta^2 = 4\alpha/m_d\Delta$. We mentioned earlier that for an externally driven system, the frequency ω is real and the wavenumber k has a real and an imaginary component. Hence, in order to compare the "active manipulation" experiment (see below) with the theory, we have to derive the spatial damping rate of the wave as it propagates through the crystal. From Eq. (42), we get

$$k\Delta = 2\arcsin\left[\frac{\omega^2 + i\omega\nu_{nd}}{\beta^2}\right]^{1/2}, \quad (43)$$

where $k = k_r + ik_i$. For small k values, the spatial damping rate is given by

$$k_i^2 = \frac{2\omega^2}{\beta^2\Delta^2}\left[-1 + \sqrt{1+\left(\frac{\nu_{nd}}{\omega}\right)^2}\right]. \quad (44)$$

In the high-frequency limit ($\nu_{nd}/\omega \ll 1$), this expression reduces to $k_i\Delta = \nu_{nd}/\beta$, i.e., to a constant (frequency-independent) spatial damping. In the low-frequency limit ($\nu_{nd}/\omega \gg 1$), we get $k_i\Delta = \sqrt{2\nu_{nd}\omega}/\beta$; i.e., the spatial damping rate is proportional to the square root of the frequency.

Long-wavelength DLWs, such that $k\Delta \ll 1$ (but, at the same time, $\omega \gg \nu_{nd}$) are weakly dissipative and possess linear dispersion ($\omega \propto k$). The phase velocity of these waves is equal to

$$V_{\mathrm{DLW}} = \sqrt{\frac{\alpha\Delta}{m_d}}. \quad (45)$$

Here, the product $\alpha\Delta$ plays a role of the effective temperature (or effective energy) determining the wave phase velocity. Generalizing the above consideration to a 2D lattice (monolayer) and taking into account more than just the nearest neighbors, we arrive at the following equation of motion:

$$m_d\Delta\frac{d^2}{dt^2}\delta x_{jl} = \sum_{m=-\infty}^{\infty}\sum_{n=-\infty}^{\infty}\{K_{mn}^{jl}(\delta x_{jl} - \delta x_{mn})\} - m_d\nu_{nd}\frac{d}{dt}\delta x_{jl}, \quad (46)$$

where the wave is taken to propagate in the x direction and δx_{jl} are the displacements of a grain jl, which is normally located at the lattice site with the unperturbed positions $x_{jl,0}$ and $y_{jl,0}$. The coupling between the grain mn and the grain jl is described by the operator K_{mn}^{jl}, which, in the case of the screened Coulomb potential, is equal to

$$K_{mn}^{jl} \equiv \frac{Q^2}{\Delta^4}\exp\left(-\frac{r}{\lambda_D}\right) \times\left\{(x_{jl,0} - x_{mn,0})^2\left(3 + 3\frac{r}{\lambda_D} + \frac{r^2}{\lambda_D^2}\right) - r^2\left(1 + \frac{r}{\lambda_D}\right)\right\}, \quad (47)$$

with r being the distance between the grain mn and the grain jl. Representing the solution in the form $\delta x_{jl} \propto \exp[i(kx_{jl,0} - \omega t)]$, we obtain the dispersion relation

$$\omega^2 - \frac{4}{m_d}\sum_{m=1}^{N_m}\sum_{n=-N_n}^{N_n}K_{mn}^{00}\sin^2\left(\frac{k\Delta x_{mn,0}}{2}\right) - i\omega\nu_{nd} = 0. \quad (48)$$

The result for the linear chain can be recovered by setting $N_n = 0$ in Eq. (48).

The measurements of periodical perturbations propagating in plasma crystals have been performed by a few research groups using different techniques. Such perturbations are simple to produce experimentally by using a sinusoidal voltage applied to a wire located in the plasma near the plasma crystal [109]. A disadvantage of this method is that the perturbing potential also modifies the ion and electron flows, which, in turn, may influence the dynamics of the plasma crystal; i.e., the system becomes too complicated. From the experimental standpoint, the perturbations introduced by using the light pressure of a laser beam [110] are preferable.

Figure 47 shows a schematic of the experimental setup intended to investigate linear chains and monolayer plasma crystals [111]. The experiments were performed in a plane-parallel RF discharge (f = 13.56 MHz). The diameter of the lower electrode was 170 mm. The upper electrode was a grounded grid. The two electrodes were separated by a 65-mm gap. The working gas was helium at a pressure in the range of 10–100 Pa. A light inert gas was chosen in order to reduce the frictional damping as much as possible and, thus, to allow the dust lattice waves to propagate. The discharge power was in the range of 5–10 W. The grains

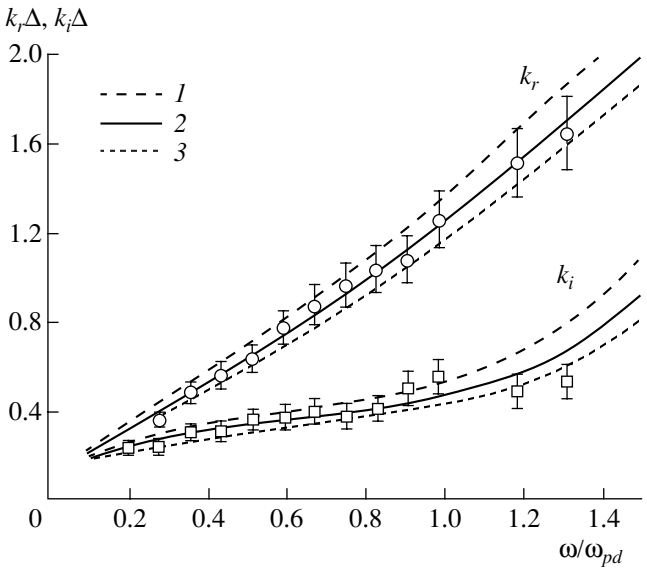

Fig. 49. Measured dispersion relations for a chain of dust grains [111]. A comparison with the theory takes into account only the screened Coulomb potential and does not take into account any other forces; that is why the theoretical curves are given for three values of the fitting parameter in the screened Coulomb potential: K = (*1*) 0.7, (*2*) 1.1, and (*3*) 1.5 (Δ is the intergrain spacing).

were monodisperse melamine formaldehyde grains 9.47 μm in diameter. The diameter variations were a few percent. The grains in a linear chain were pushed periodically at a given frequency using the radiation of a laser diode focused on the end grain. Since the grains in this device could only be pushed (not pulled), a confining box potential was produced using an elevated barrier on the lower electrode. The inner dimensions of the barrier were 90×20 mm, and the height was 4 mm, which was comparable to the characteristic length of the sheath. This barrier allowed the grains to relax back when the radiation force was switched off.

The measurement results for a linear chain are depicted in Fig. 48 [110] as a series of fifteen snapshots taken with 100 ms intervals. The displacement of the grains in the right part of the chain is clearly seen, as well as the increased brightness of the end grain during the illumination phase, when the laser diode is switched on. It can also be seen that the damping is substantial (due to friction by the neutral gas). Using these data, it is possible to determine both the real part of the wavenumber k_r and the spatial damping rate k_i as functions of the frequency and, thereby, to obtain the dispersion relation. The measured dispersion curves are shown in Fig. 49, in which the theoretical curves [111] calculated for different shielding parameters $K = \Delta/\lambda_D$ are also depicted. The best fit is obtained for $K = 1.1 \pm 0.4$.

The results obtained for a monolayer plasma crystal are shown in Fig. 50 [111]. It can be seen that the fitting of the experimental results by the theoretically predicted 2D dispersion relation for Yukawa interactions yields a shielding parameter of $K = 0.8 \pm 0.4$, which is somewhat less than in the case of a linear chain.

DLWs with a wavelength much larger than the intergrain distance can be described by KdV equation [112], in which the DLW phase velocity, the linear dispersion term, and the nonlinear term are functions of the coupling constant, which is related to the interaction potential of two neighboring grains. Nonlinear soliton waves are known to be standard solutions of the KdV equation. Indeed, in [112], solitons were observed experimentally with an amplitude inversely proportional to the square of the soliton width, as it should be according to the KdV description. An advantage of the experimental investigation of DLW solitons is the possibility of determining the type of interaction between strongly

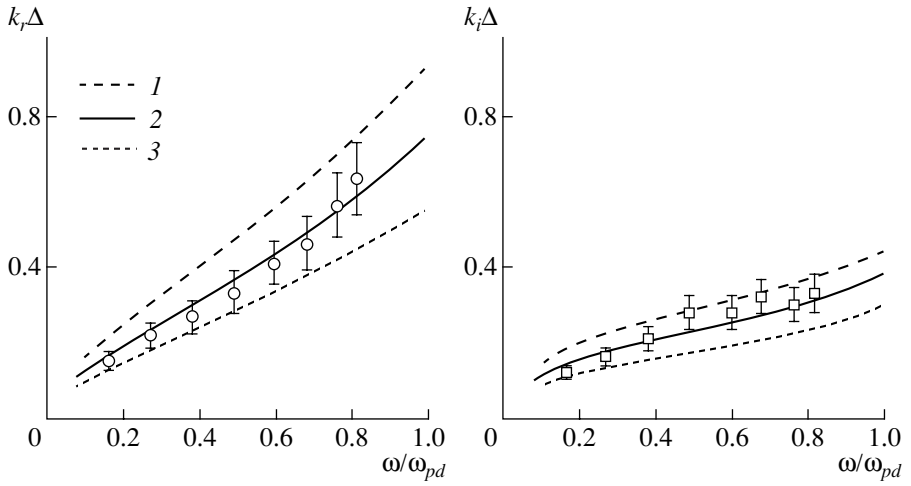

Fig. 50. Measured dispersion of longitudinal DLWs in a monolayer crystal [111]. The solid curves show the results of calculations with allowance for the screened Coulomb potential for three values of the fitting parameter: K = (*1*) 1.2, (*2*) 0.8, and (*3*) 0.4.

coupled grains in complex plasmas. This possibility has not yet been used. Up to now, only the screened Coulomb interaction has been used and no attempts were made to fit the experimental results by using the theoretical curves with other types of interaction, although it is obvious that the screened Coulomb potential is not proper for describing collective and nonlinear interactions, as well as the charging processes.

No theoretical efforts have been made so far to describe DLWs with allowance for interactions other than the screened Coulomb interaction, although there are no principal difficulties for doing this, since taking these interactions into account in the dispersion relation and in nonlinearities will change only the DLW phase velocity in such a way that it will depend only on the value of the potential interaction and its derivatives. At present, only a comparison with the screened Coulomb potential has been performed, and the value of the parameter K was extracted from the experimental data. An important question is whether other interactions and the nonlinearity in screening might significantly affect the theoretical predictions. The experimental results of [107, 111] mean that both the experiments are compatible for shielding parameters in the range $0.7 \le K \le 1.2$. It seems also that K is in fact smaller for monolayers. The physical arguments for this can be the following:

(i) In the plane perpendicular to the ion flow, all the grains should have the same charge. The removal of plasma particles (ions and electrons) is unlikely to play an important role in monolayers under this geometry, since the supply from the main plasma is plentiful and each grain is directly accessible to the ion flow. This means that the charge modification by this effect is of minor importance and, hence, the charges of all the grains should be the same, provided that the plasma conditions (i.e., the pressure, RF power, etc.) and the ion drift velocity are kept constant.

(ii) Introducing a larger number of grains into a fixed-geometry potential well does change such an important parameter as the dust pressure. This suggests that, in the equilibrium state, the system with a larger number of grains will be more compressed, since the ram pressure produced by the plasma flux increases with an increase in the number of grains. Bearing this in mind, it is quite reasonable to conclude that a more tightly packed 2D system should exhibit a systematically smaller K value than a loose 1D chain. Some support is given to this from the fact that, in equilibrium linear chains (without a lattice wave excited), the spacing between grains at the end of the chain [111] is often larger than in the (more compressed) central region.

(iii) This effect can also take place if the plasma is inhomogeneous and the screening length varies in an appropriate way. Such an inhomogeneity can be produced by the chain itself and is related to its self-contraction.

(iv) At present, we can only estimate the role of other forces between the grains that may be responsible for changing DLWs. Note that, in the analysis, we cannot directly refer to the dust collision experiments that show that the interaction corresponds to screening Debye potential [113], because in [113] the ratio a/λ_D was 10^{-4}, whereas in the experiments of [111], which we are discussing here, this ratio was $a/\lambda_{Di} \sim 0.3$. On the other hand, the noncollective attraction is proportional to $(a/\lambda_{Di})^2$. Since, in collision experiments [113], the screening length was close the electron Debye length λ_{De}, which is approximately seven times larger than λ_{Di}, we have for the experimental conditions of [113] the estimate $(a/\lambda_{Di})^2 \approx 5 \times 10^{-3}$. This estimate shows that, in [111], the attraction forces are expected to be 20 times larger than in [113]. In [111], the attraction forces should occur at distances close to the electron Debye length, which is close to the intergrain distance under the given conditions. One cannot therefore exclude the possible role of these forces in the difference observed in [111] between the values of K for a 1D chain and a monolayer. On other hand, one should keep in mind that the experiments with 1D chains and monolayers, as well as the collision experiment [113], were performed in the sheath in presence of an ion flow, when the anisotropy in screening can play an important role.

(v) Strictly speaking, expressions for the collective attraction forces [2] cannot be directly applied to 1D chains and monolayers, because these expressions were derived for the 3D case. The theoretical analysis of the collective attraction for the 1D and 2D cases still is waiting to be performed. Certainly, from what we know from the 3D case, the collective attraction is much stronger than the noncollective one and, therefore, it may be very important for the observed compression of 1D and 2D dusty structures. From the physical standpoint, we can expect that the collective effects in attraction will be larger in the 2D case than in the 1D case (i.e., the K value should be less in the 2D case than in the 1D case). This is qualitatively what is observed, but quantitative estimates of this phenomenon are still absent.

We emphasize once again that the performing of 3D experiments seems to be very important. A topological transition from 1D and 2D structures to 3D structures depends on the compressibility of the plasma crystal, i.e., on the strength of the intergrain forces. In this case, the attraction forces (specially the collective attraction forces) should play the most important role. The self-confinement effects, which are related to the collective flux, and the effects of self-organization and structurization, should be more pronounced in 3D systems. A systematic investigation of the dependence of K on the number of the grains in the confining well, including the above-mentioned topological transitions, will probably shed some light on the basic self-organization processes in static equilibrium open systems.

4.6. Stimulated Plasma Crystal Sublimation

An improvement of the radiation-pressure active manipulation technique is to "guide" the grains in a controlled way using two lasers. This makes the active control independent of the geometry of the potential field and the characteristic relaxation time scales. Such improved control can be used, for instance, to extend the frequency range to the crystal Debye frequency. Theoretically, at that frequency (corresponding to the dust acoustic wavelength equal to twice the grain separation, $\lambda = 2\Delta$), the propagation of information becomes impossible (at least for acoustic modes). This result can immediately be seen from Eq. (42) and is well known in crystal physics. However, it is possibile that the energy may be converted to other wave modes or that the crystal may be destroyed due to parametric instabilities or other nonlinear effects. To observe this at the kinetic level in a model system is clearly one of the most exciting topics for future research.

Preliminary experiments on wave excitation in a dusty plasma by applying an ac voltage to a wire were reported in [112]. However, as was mentioned above, the interactions are very complicated and, accordingly, the experiments are very difficult to interpret. For this reason, we restrict ourselves to the presentation of the observations at this stage, which is only a heuristic attempt at interpretation. The grain motion in the horizontal plane is initially just noticeable (practically thermal). As the frequency increases from 34 to 35 Hz, one of the grains acquires at some point a large horizontal momentum. Its energy is in excess of 3 eV, which is three orders of magnitude higher than in the previous video image, taken at 0.02 s earlier. This grain then plunges through the crystal and disrupts it, leading to complete sublimation in a time scale of 0.1 s. Of course, this disruption is not possible through the dissipation of the initial energy of a single grain. Each of the sublimed (disordered) grains has an energy in excess of 10 eV; therefore, the single "trigger" grain merely liberates the energy stored in the system. There are two kinds of stored energy: the energy of vertical oscillations and the potential (electrostatic) energy. Note that the crystal is moving up and down as a solid body with a relatively large amplitude of about 500 μm and the stored energy amounts to about 20 eV per grain. Thus, the disruption of the crystal by a single grain liberates this energy and thermalizes it.

The following questions therefore arise:

(i) What leads to the "breakout" of the trigger grain from the crystal?

(ii) Is it a purely statistical effect and is there always only one grain that starts the process?

(iii) Is there a systematic change in the crystal structure that facilitates the process?

(iv) Which processes are responsible for the collective crystal vibrations and what are their stability criteria?

To answer these (and many others) questions, much more research needs to be done.

Regarding possible systematic changes in the crystal structure just prior to the sublimation transition, an intriguing observation has been made. The grain separations are initially almost the same (except for the edge, as was noted earlier). As the wave frequency is slowly increased to the critical value at which sublimation sets in, it was noted in [112, 114] that the structure of the crystal undergoes a systematic change so that short separations alternate with long ones. This corresponds to a compressional (sound) wave with the wavelength $\lambda = 2\Delta$ (twice the lattice separation). Although this can be, in principle, an accidental coincidence, this is nevertheless sufficiently intriguing to follow up with a systematic investigation.

At 44 Hz, recrystallization is observed. Hence, the width of the sublimation resonance is ~9 Hz.

4.7. Dust Shear Waves

An ordinary plasma does not support shear waves. However, in plasma crystals, there should exist so-called dust shear waves (DSW). Indeed, such waves have recently been observed experimentally [114, 115]. As was noted above, a specific feature of such experiments (which is related to the necessity of the electrostatic suspension of dust grains against the action of gravity) is their fundamental asymmetry, which can substantially affect the wave propagation. Let us briefly discuss the conditions of these experiments:

(i) In RF discharges, the dust grains are suspended in horizontal layers and the supporting electrostatic field of the sheath is directed downward (towards the lower electrode). The ion flow is also directed downward. Electrostatic focusing by the negatively charged grains leads to an enhanced ion density in the wake generated below the grain (although, as was mentioned above, the collisional or collisionless dissipative processes somewhat smear out this wake). The system "grain + wake" may be thought as a vertically aligned asymmetric "charge + dipole" system. In the presence of many grains, due to a change in dust interactions, the picture changes substantially and, generally speaking, cannot be regarded as a collection of charge + dipole components. Nevertheless, for simplicity, we will speak below about the dipole component, which leads to asymmetric nonlinear collective screening.

(ii) In considering horizontally propagating DLWs, we ignored the dipole component (although we applied the argument that the presence of the ion flow substantially changes the screening in the horizontal direction). When the waves are excited with laser light pressure, the wake just follows the disturbed grain. If the waves are excited electrostatically using a wire, then the negatively charged grains and their positively charged wakes are accelerated in the opposite directions, which leads to additional complexity.

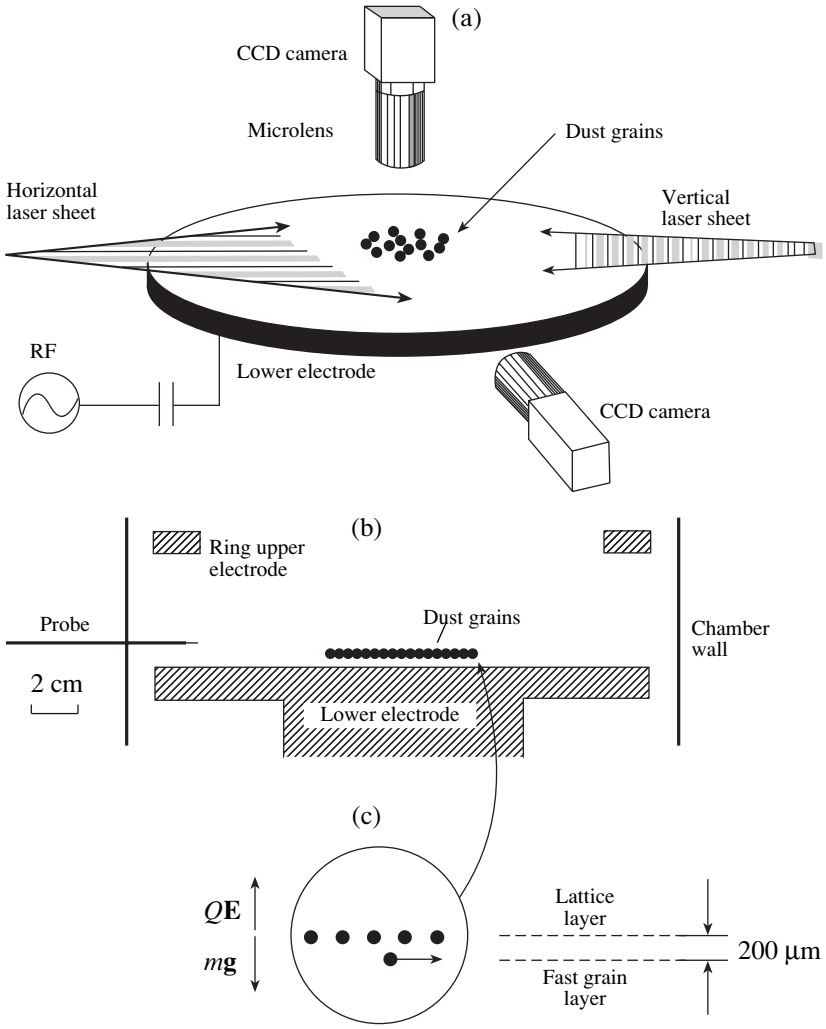

Fig. 51. (a) Sketch of an apparatus used to measure DSWs, (b) the cross-sectional view of the electrode system, and (c) a monolayer plasma crystal formed of negatively charged grains levitating above the lower electrode (between the crystal and the electrode, there are a few fast grains moving in the horizontal plane) [117].

(iii) When horizontally polarized DSWs are excited with laser light pressure, we may assume that the wake interaction is marginal. However, in the case of vertically polarized DSWs (the second type of DSWs, which can be called "bending waves" because they bend the monolayers out of its original plane), the interaction with the wakes cannot be ignored if the amplitudes are sufficiently large.

(iv) In dc discharges, it is possible to produce long vertical strings of grains suspended in the electrostatic field of striations. In this case, the ion wake is again located below the grains; however, the dipoles are now aligned with the grain strings. As a result, only one type of DSWs exists, which, however, differs from the shear waves discussed above. There can be an asymmetry for waves propagating downward and upward, since the wake is located downstream from its grain.

(v) DLWs will also be modified by the aligned dipoles. To investigate the influence of the wake in such a system, it is necessary to perform special experiments.

(vi) A scenario with dipoles is a very rough picture for strongly screened and strongly coupled systems. The full description of all the modes, including DSWs, requires considering the linear perturbations of a nonlinear stationary initial state, finding the dielectric tensor $\epsilon_{i,j,\omega,\mathbf{k}}$, and solving the corresponding dispersion relation [116]. This approach has not been used so far.

Figure 51 shows a schematic of the experimental device, and while Fig. 52 presents the results of the first observations of DSWs [117] (see also [118]).

Due to the small amplitude of the laser field exciting the shear waves, many data sets have to be superposed to extract the systematic grain motion from the random thermal noise. So great care is to be taken, both with the

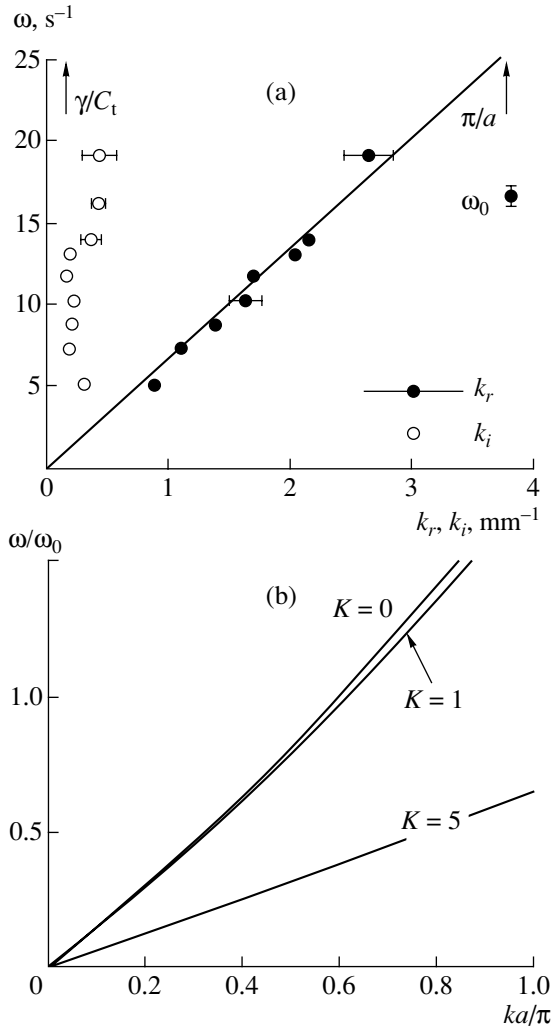

Fig. 52. Dispersion relation for DSWs [117]: (a) experimentally measured values of k_r (closed circles) and k_i (open circles) (the solid line indicates the sound speed) and (b) theoretical curves calculated for the screened Coulomb potential at three values of the fitting parameter K.

measurements and the data analysis. The verification of the existence of these very slowly propagating DSWs is quite exciting (note that the measurements were performed for horizontally polarized DSWs mentioned above), since this technique can in principle be improved to investigate bending waves, as well as waves in a system with aligned dipoles.

The theoretical dispersion relation was derived in [116, 119]. Considering only "nearest neighbor" interactions in a linear chain, the transverse mode dispersion relation reads [116]

$$\omega(\omega + i\nu_{nd}) = \omega_s^2 + \frac{1}{\pi}\omega_{pd}^2 \exp(-K)\sin^2\left(\frac{k\Delta}{2}\right), \quad (49)$$

where

$$\omega_{pd}^2 = \frac{4\pi Q^2 n_d}{m_d} = \frac{4\pi Q^2}{\Delta^3}. \quad (50)$$

Equation (49) is similar to the dispersion relation for DLWs. The main difference is the term ω_s^2, which merely reflects the normal mode oscillations in the confining potential (e.g., for a single undamped grain, we have $\omega = \omega_s$).

A comparison of the observations [115] with the theory [116] showed, however, that using the shielding parameter K as a fitting parameter does not allow one to achieve a satisfactory agreement between theory and experiment.

In conclusion of this section, we note the following:

(i) Generally, it is impossible to cover all the aspects of wave propagation, mode coupling, stability criteria, damping, specific effects related to nonlinearities in screening, charge variations, dust–dust interactions, and other effects specific for complex plasmas. Although the literature here is already very large, no systematic consideration has yet been performed for either the linear or the nonlinear dispersion. Consequently, we are only able to summarize some results and refer the reader to original references from where research can be continued.

(ii) It should be noted that there are many theoretical works in which the relations known for multicomponent plasma are simply "transferred" to a dusty plasma, merely changing the notation for heavy ions to be the dust component. This is irrelevant for complex plasmas because the charging processes and the absorption of electrons and ions by dust substantially change the dispersion relation in a very broad range of frequencies ($\omega < \omega_{pi} a/\lambda_{Di} P$) and wavenumbers ($k < \lambda_{Di}^2 P/a$). In fact, it is this range of frequencies and wavenumbers that is of interest for the existing experiments. On the other hand, the dispersion relation in this low-frequency and long-wavelength range also depends on the external source (for instance, on the type of the ionization source used). There are only a few papers that adequately take into account the effect of the source on the dispersion relation.

(iii) It was shown in [120] that, under certain conditions, charge fluctuations can lead to the excitation of lattice oscillations. However, there is still no experimental confirmations of this effect.

(iv) Apart from these phenomena, there are a number of other publications devoted to the propagation, scattering, and damping of waves in dusty plasmas. In particular, the effect of the concentration of nonlinear electron and ion polarization charges around the grains has been addressed. In this context, the local enhancement of the ion density in a Debye sphere around a negatively charged dust grain may be of particular importance.

(v) Another interesting physical phenomenon that has been discussed in connection with the grain oscillations in RF discharge plasmas is the existence of resonance frequencies, which can be used to probe the sheath (or determine the grain charge) and to study coupled systems, parametric instabilities, charge delay effects, etc., in dusty plasmas. We do not give here the references to the corresponding papers in which these problems were only touched upon, since comprehensive consideration still remains a great problem for future research.

(vi) From expressions (18) and (28) for the dielectric constant, it is clear that the interaction between two grains depends strongly on the parameters P_0, k_{cr}, and τ, as well as on the charging and drag coefficients and the distance between the grains. Estimates show that the distance at which the dielectric constant changes substantially is on the order of the distance between the grains in the crystalline state. Of course, expressions (18) and (28) were derived for a gaseous state, but all the processes that were taken into account in deriving these expressions (such as charging and the ion drag) are also present in the crystalline state. These processes will substantially modify the potential of interaction between the grains and, accordingly, both the DLW and DSW dispersions (as they modified the DAW dispersion). Therefore, it is obvious that the screened Coulomb potential used in deriving the dispersion relations for these waves can serve only as a rough and preliminary estimate.

(vii) Clearly, in order to achieve an adequate theoretical description of linear waves and instabilities in complex plasmas, comprehensive investigations must be performed with allowance for all elementary processes described in [2], with special emphasis on collective dust–dust interactions.

5. MACH CONES IN COMPLEX PLASMAS

5.1. Mach Cones: General Remarks

It is well known that mach cones are excited in any material by objects moving faster than the phase velocity of the waves in the system. For charged particles in ordinary matter, this corresponds to the Cherenkov emission of waves by particles [121]. It was first proposed in [122, 123] to use Mach cones for diagnosing the dusty plasma parameters, in particular, to determine the parameters of Saturn's rings by observations of Mach cones created in dusty plasmas by a big boulder moving in the ring. At present, Mach cones are regarded as a possible diagnostic tool in thin-film deposition technology [124] and other technological applications of dusty plasmas [117, 125–127].

Mach cones can be considered as a composition of linear waves if their source is not strong, or as a nonlinear wave (or even a shock wave) if the source is strong. If a large grain moves through a uniform complex plasma that is in the gaseous state, a DAW is excited. Simple kinematics then gives the known relation for the Mach cone angle

$$\cos^2\theta = \sin^2\mu = \frac{v_{DAW}^2}{v^2}, \tag{51}$$

where v is the velocity of the fast grain, θ is the angle between $\mathbf{v}$ and the wave vector $\mathbf{k}$ of the emitted wave, and μ is the angle between the Mach cone front and the grain velocity. Of course, the velocity of the fast grain should be larger than the DAW speed to satisfy relation (51). The Mach cone is simply described by the kinematics of emission, but the intensity of emission depends on the interaction of the fast grain with the complex plasma. There are several complications in the Mach cone effect for complex plasmas, as compared to the standard Cherenkov emission of waves that create Mach cones in ordinary matter:

(i) The first is related to the intensity of the waves emitted. As we already emphasized, close to the grain, the field is nonlinear (and for a large grain this nonlinearity is even more important). The linear mechanism for the excitation of DAWs operates only if the contribution from nonlinear excitation is small at distances on the order of the wavelength of the emitted wave. The general consideration of this kind should be made, first, for the case of weak nonlinearities, which requires a knowledge of the first-order nonlinear responses. At least, one hopes that it can provide a criterion showing where the results of the linear approximation can be used. Nevertheless, some information can be obtained using the standard linear approach in deriving the distribution of the intensity of the emitted waves over wavenumbers or the wavelengths. In the linear approximation, the power I emitted by a charge $Z_d e$ moving in an infinite (with a size much larger than the wavelength of the emitted waves) complex plasma with dielectric constant (28) is

$$I = \frac{Z_d^2 e^2 v_{DAW}^2}{v}\int_{k_{cr}} F(k)k\,dk\left(1-\frac{k_{cr}^2}{k^2}\right)^2, \tag{52}$$

$$F(k) = \frac{1+\dfrac{a^2}{\tau k^2\lambda_{Di}^4}\alpha_{dr}\alpha_{ch}z_0P_0(1+P_0)}{1+\dfrac{P_0(k_{drch}(0))^2a^2}{\tau k^2\lambda_{Di}^4}}\left[\frac{1+z_0}{1+P_0+z_0}\right], \tag{53}$$

where $k_{drch}(0)$ is the value of k_{drch} at $\omega = 0$ [see relations (29)]. In Eqs. (52) and (53), we ignored the dust–neutral friction and considered $k \ll 1/\lambda_{Di}$ (i.e., $\omega \ll \omega_{pd}$). The critical wavenumber k_{cr} is given by expression (30). As was pointed out above, the waves with $k < k_{cr}$ do not exist and they are not emitted. The largest emission intensity corresponds to the largest k (the shortest

wavelengths), which is on the order of λ_{Di}^{-1}. Expressions (52) and (53) serve only as an illustration because, for short wavelengths, the nonlinearities certainly play a role.

(ii) The dispersion of the waves can result in the Mach cone broadening, since waves with different wavelengths are emitted at different angles. For example, expression (51) is valid only for $k^2 \gg k_{\text{drch}}^2 P_0/\tau$, while in the opposite limit and for $k \gg k_{\text{cr}}$, we get from Eq. (29)

$$\cos^2\theta = \frac{v_{\text{DAW}}^2}{v^2}\frac{\alpha_{\text{dr}}\alpha_{\text{ch}}P_0(1+P_0)a^2}{k^2\lambda_{Di}^4\tau}. \qquad (54)$$

A strong dispersion of Mach cone directions can be recognized in this case.

(iii) It is known that Mach cones are excited in a media if the source (here, a fast grain) is moving in the channel with a size less than the emitted wavelength [121]. The fast grain creates the channel itself, but can collect other grains when moving through the system. As a result, its size and charge increase [124] and the Mach cones become "dynamic Mach cones" (DMC), which can also be used for diagnostic purposes. Note that, if the size of the channel is less than the emitted wavelength, the Mach cone is the same as in the absence of a channel [121].

(iv) It is also well known that Mach cones can be excited not only by a source moving inside the medium, but also by a source moving close to the surface of the medium if the distance between the source and the surface is less than the wavelength of the excited waves [121]. As the distance between the fast grain and the surface increases, the waves with a wavelength larger than this distance are only excited. This can serve also as a powerful diagnostic method for the measurement of the spectra of the waves emitted because, in the plasma sheath, the distance of the fast grain from the surface is usually determined by its mass (the heavier grains move below the surface at larger distances from the surface due to the balance of the gravity and electric forces). Mach cone measurements in complex plasmas can also serve as an efficient mechanism for the diagnostics of the plasma crystalline state and its transitions. In this case, Mach cones can be excited by a fast grain moving below the crystal with a velocity larger than the phase velocity of DAW, DLW, or DSW.

(v) The restrictions on the maximum possible wavelength of DLWs and DSWs still need to be investigated in a way similar to that described above for DAWs. An important point of research is to find how close to the crystal surface the grain should move to excite the Mach cone. The answer will allow one to determine the maximum wavelength of DLWs or DSWs. At present, there is still no theory of these waves with all necessary effects included (as it is for DAWs). Thus, there is a wide field for experimental investigations.

(vi) As was shown in [2], specific conditions appear in the plasma sheath because the ion flow can change the drag coefficient and create a collective wake. Under these conditions, the dispersion relations and the Mach cones can differ from those considered above in the case of a screened Coulomb potential.

(vii) The determination of the maximum possible wavelength of the emitted wave in monolayer crystals is more complicated because, in this case, the description of the collective dielectric response and its dependence on the surface density of grains differs from those obtained for 3D distributions of grains. The collective attraction also changes in this case. The measurements of the maximum distance at which the Mach cone is excited when a fast grain is moving close to the crystal surface is thus of special interest for estimating the forces acting between the grains.

(viii) Another important point is the possibility of exciting Mach cones close to the surface of a void. The presence of voids with sharp boundaries was demonstrated experimentally. In this case, the grain size is not limited by the conditions to have a large grain charge, as it is in the case of plasma condensation (remember that the grain charge is approximately proportional to the grain size).

5.2. Observation of DLW Mach Cones

Mach cones excited in a monolayer plasma crystal by a fast charge moving below the dust layer were observed experimentally in [117, 125]. The crystal was located in an RF discharge with an electron temperature of $\approx$1 eV and ion density of $n_i \approx (1\text{–}5) \times 10^9$ cm^{-3}. The grain size was 8.9 and 4.8 μm. The working gas was Xe, Kr, or Ar. The grain separation in the crystal was about 400 μm. Fast dust grains moved below the plane of the crystal at a distance of 200 μm from its surface with a speed of 30–60 mm/s and formed the second dust layer below the one already existing. A grain moving with a velocity exceeding the speed of DLWs and DSWs excited the DLW and DSW Mach cones. The crystal was located at a relative large distance from the electrode (about 8 mm), which is much larger than the electron Debye length. The value of ion drift velocity at the position of the crystal was not measured. The dust charges were about $Z_d \approx 10^4$. The Mach cones were identified on the grain speed map and on the grain density map (see Fig. 53).

The fast grain usually excites two cones: the first is a compression wave and the second (which follows the first one) is a rarefaction wave. Figure 54 shows the values of the acoustic velocity derived from the Mach cone condition (51).

In the experiments of [117], it was observed that the Mach cones corresponded to the shocks excited in the crystals. The Mach cone can serve as a diagnostic method for determining the parameters of a crystal by

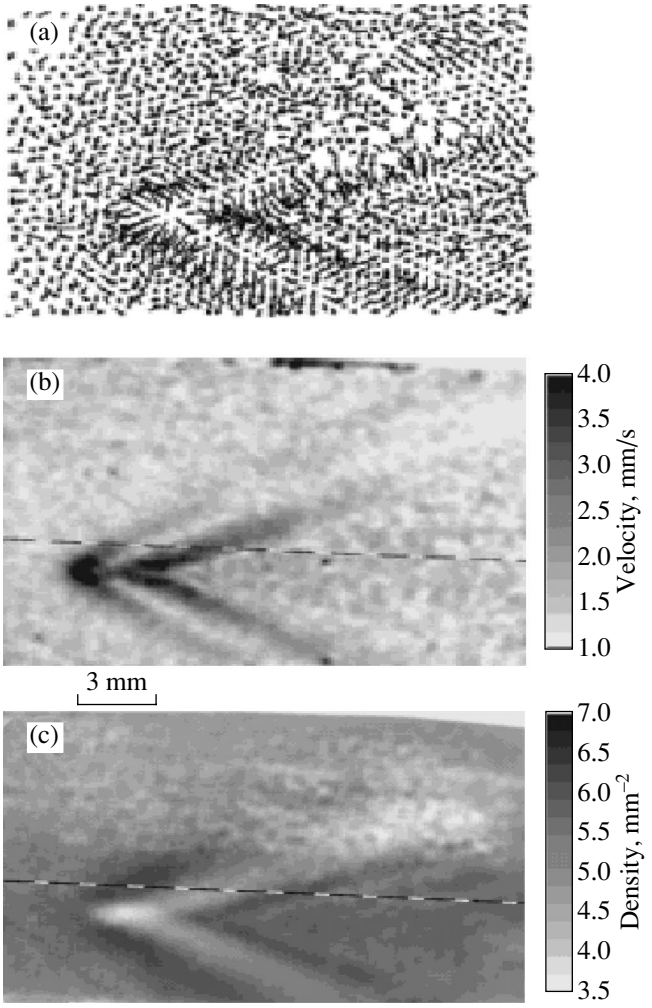

Fig. 53. Mach cones in a dusty plasma with 8.8-μm grains (a krypton discharge, the input power is 100 W) [125]. A supersonic grain moves from right to left: the grain velocity vector map derived from the grain positions in two consecutive frames (a) and the gray scale maps of the grain velocity (b) and number density (c), obtained by averaging over 20 frames.

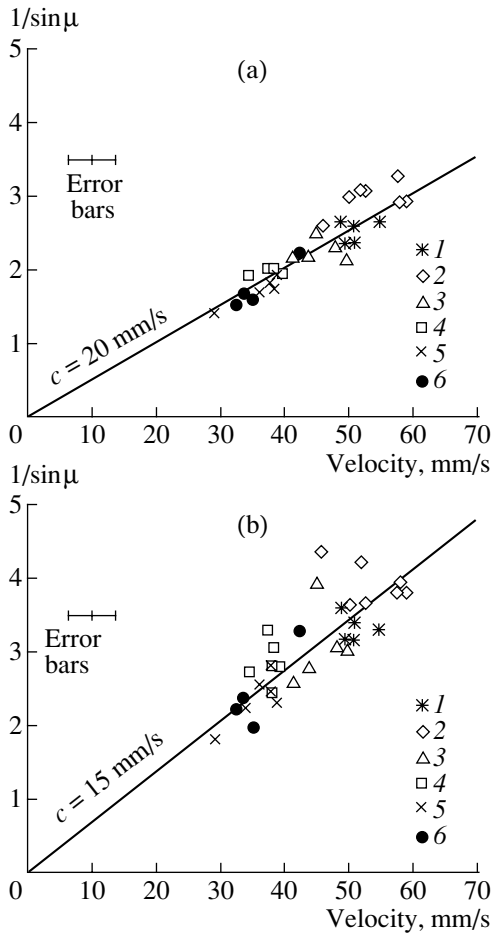

Fig. 54. Mach number (1/sinμ) vs. supersonic grain velocity determined for (a) the first and (b) the second cone at different discharge conditions: (*1*) Ar, 50 W; (*2*) Ar, 100 W; (*3*) Kr, 50 W; (*4*) Kr, 100 W; (*5*) Xe, 50 W; and (*6*) Xe, 100 W [117]. The grain size is 8.9 μm. The straight lines correspond to the averaging over all the experimental points. The acoustic velocity is the same for all the discharge conditions.

adjusting the results to the theoretical model (in [117], it was the Yukawa model). This method allows one to determine two parameters: the charge and the ratio of the intergrain distance to the screening length. Usually, one also needs to take into account other forces (see [2]).

In the experiments of [126], using a similar device, the Mach cones were excited by a laser beam whose focus moved with a supersonic velocity. The action of the laser beam on the grains in a monolayer crystal was due to the radiation pressure of the focused beam. A multiple Mach cone structure was observed with at least three distinct Mach cones (see Fig. 55).

The Mach angle relation (51) was satisfied in a wide range of Mach numbers for both the first and the second cones. The sound speed measured from the first Mach angle was found to increase with the dust number density (Fig. 56). A comparison of the results obtained with the theory of DLWs with the use of two interaction parameters in the Yukawa model allowed one to determine the screening length and the dust charge.

In conclusion of this section, we make the following remarks:

(i) Mach cones are an effective diagnostic method for studying dust crystals, especially when using a more refined theoretical model.

(ii) The determination of the distributions of the emission intensity over wavelengths is still an open experimental task for future investigations.

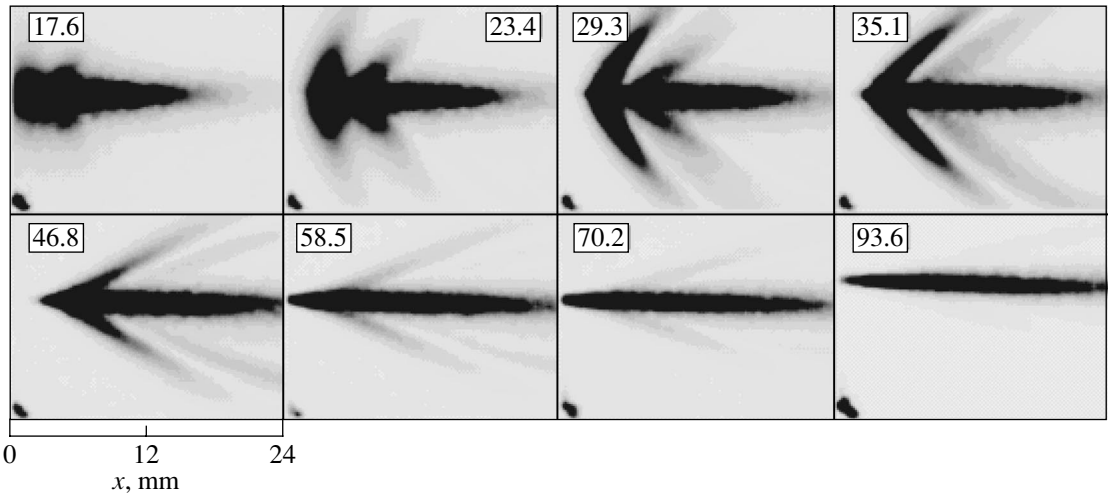

Fig. 55. Gray scale maps of the grain velocity $v = |\mathbf{v}|$ for different speeds of the laser spot **V** [126]. The darker regions correspond to higher grain velocities (black corresponds to ≈4 mm/s). The numbers in the boxes indicate the speed of the laser spot in mm/s. The dark spot in the lower left corner is an artifact and is unrelated to the Mach cones.

6. PLASMA CRYSTALS OBSERVED IN MICROGRAVITY EXPERIMENTS

Two types of microgravity experiments have been performed. One type was performed in parabolic flights [128] with only 30-s time available for microgravity to exist, and the other type was performed onboard a space station (the PKE-Nefedov experiments [129, 130]). In both cases, very complicated dust structures were observed, including dust voids, dust convection, and regions with plasma crystals. Plasma crystals in the microgravity experiments were first observed in the PKE-Nefedov experiments onboard the space station [129, 130]. The crystal was embedded in liquid or gaseous component of the complex plasma system containing a large dust void and several dust vortices [129, 130] (see Fig. 57).

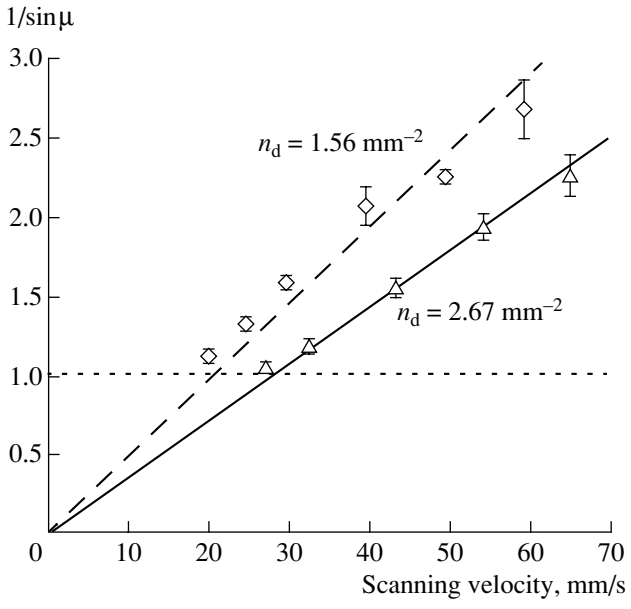

Fig. 56. Measurements of the sound speed as a function of the grain number density [126]. The solid and dashed lines correspond to different regions of the same lattice in the same discharge. A higher number density corresponds to a higher sound speed.

In Fig. 58, the part of the system where the crystal was observed is marked by a square [130]. The grains were 6.9 μm in size, and the pressure was between 0.1 and 1 mbar. The crystal was observed not in the center but at the wall side, which suggests the presence of an ion drift that diminishes the drag and the charging coefficients. The value of P_0 was rather low (about 0.1), which corresponds to small η_{coll} values and large Γ_{cr} values. From the theory based on the Van der Waals approach, it follows that the latter is about 10^4, whereas the observed value is about 3×10^4. Note that, in dust crystals formed in microgravity experiments onboard the space station, regions with bbc, fcc, and hcp crystal lattices were simultaneously observed.

Two conclusions can be made from these observations:

(i) The observation of the simultaneous presence of not only bcc and fcc structures, but also hcp structures (which are not favorable thermodynamically because of their larger free energy) is surprising only at first glance. In ground-based experiments, a similar anomaly was also observed (and this point was discussed above in detail). However, in ground-based experiments, this anomaly can be attributed to gravity, which provides additional stress energy. Looking now at the microgravity system, one has the impression that the appearance of energetically unfavorable crystal structures could be a general phenomenon of complex plasmas. This is what could be indeed expected in open sys-

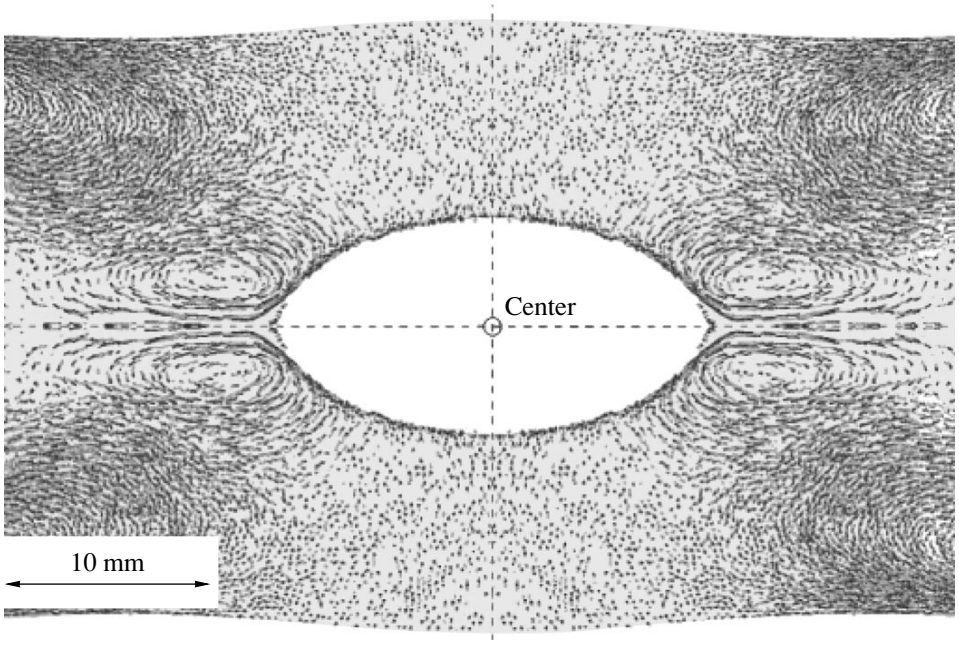

Fig. 57. Complicated dusty structure and grain motion observed in PKE-Nefedov experiments [129, 130].

tems, which are favorable for self-organization (all living things are also energetically unfavorable). As was emphasized many times above, the energy flux through the system always exists in complex plasmas, and the concept of free energy does not operate. Observations [129] give further experimental support to the last statement. Hence, in this case, the principles of self-organization [131] should be used.

(ii) The experiments support the general statement that the complex plasmas are universally unstable against the appearance of various structures. Thus, in experiments of [129, 130], plasma crystals, dust voids, and dust vortices were simultaneously observed.

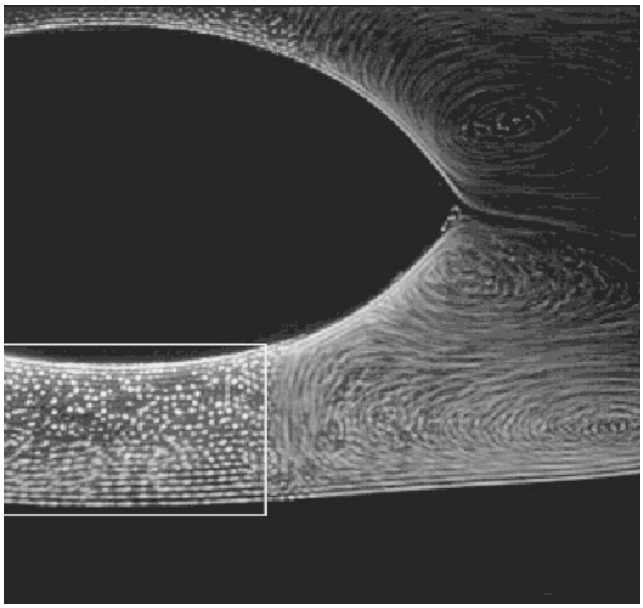

Fig. 58. Plasma crystal observed in PKE-Nefedov experiments [130]. In the region marked by the rectangle, a crystalline structure is observed.

7. CONCLUSIONS

It is certain that the experiments are ahead of the theory in the general description of this new state of matter (in both numerical simulations and kinetic description). Nevertheless, even in the framework of the existing simplified approach, many assessments can be easily made, such as taking into account various forces in the wave description, the construction of the theory of the equilibrium stability and the oscillations of clusters with arbitrary forces, the general description of the modes in complex plasmas in an external magnetic field, the molecular-dynamics numerical simulations with allowance for the real forces encountered in complex plasmas, etc. The general breakthrough in this area already exists, but a final complete description that can be used in experiments is still unavailable. It will be the subject of intense research in the near future. The experiments already performed should be repeated as soon as a better understanding of the processes becomes available. The future theoretical description can be formulated at present, but this is only one half of the theoretical problem, since a complete theoretical

description will take a great deal of time. It is clear that the experiments also will be done in a number of different directions, especially those that have industrial applications and are designed to resolve new general physical problems. Hopefully, the future theory will be compatible with the coming new experiments and explain in detail their exciting observations.

ACKNOWLEDGMENTS

One of the authors (V.N. Tsytovich) appreciates the hospitality shown during his stay in Garching at Max Planck Institute for Extraterrestrial Physics, when this review was begun. The authors are grateful to A.S. Sakharov for carefully preparing the manuscript for publication and his valuable remarks concerning the physical aspects of the material presented.

REFERENCES

1. V. N. Tsytovich, G. E. Morfill, and H. Tomas, Fiz. Plazmy **28**, 675 (2002) [Plasma Phys. Rep. **28**, 623 (2002)].
2. G. E. Morfill, V. N. Tsytovich, and H. Tomas, Fiz. Plazmy **29**, 3 (2003) [Plasma Phys. Rep. **29**, 1 (2003)].
3. L. D. Landau and E. M. Lifshitz, *Statistical Physics* (Nauka, Moscow, 1976; Pergamon, Oxford, 1980).
4. H. Thomas, G. E. Morfill, V. Demmel, and J. Goree, Phys. Rev. Lett. **73**, 652 (1994).
5. J. H. Chu and I. Lin, Physica A **205**, 183 (1994).
6. A. Melzer, T. Trottenberg, and A. Piel, Phys. Lett. A **191**, 301 (1994).
7. Y. Hayashi and K. Tachibana, Jpn. J. Appl. Phys. **33**, 804 (1994).
8. V. E. Fortov, A. P. Nefedov, O. F. Petrov, *et al.*, Phys. Lett. A **219**, 89 (1996); V. E. Fortov, A. P. Nefedov, V. M. Torchinsky, *et al.*, Phys. Lett. A **229**, 317 (1997).
9. V. E. Fortov, V. I. Molotkov, A. P. Nefedov, and O. F. Petrov, Phys. Plasmas **6**, 1759 (1999).
10. V. E. Fortov, A. P. Nefedov, V. Sinel'shchikov, *et al.*, Phys. Lett. A **267**, 179 (2000).
11. G. E. Morfill, H. Thomas, U. Konopka, and M. Zuzic, Phys. Plasmas **6**, 1769 (1999).
12. V. E. Fortov, V. I. Molotkov, A. P. Nefedov, and O. F. Petrov, Phys. Plasmas **6**, 1759 (1999).
13. V. E. Fortov, A. P. Nefedov, V. I. Vladimirov, *et al.*, Phys. Lett. A **258**, 305 (1999).
14. O. S. Vaulina, A. P. Nefedov, O. F. Petrov, and V. E. Fortov, Zh. Éksp. Teor. Fiz. **118**, 351 (2000) [JETP **91**, 307 (2000)].
15. A. P. Nefedov, O. F. Petrov, and V. E. Fortov, Usp. Fiz. Nauk **167**, 1215 (1997) [Phys. Usp. **40**, 1163 (1997)].
16. V. E. Fortov, A. P. Nefedov, O. F. Petrov, *et al.*, Phys. Rev. E **54**, 2236 (1996).
17. J. B. Pieper, J. Goree, and R. A. Quinn, Phys. Rev. E **54**, 5636 (1996).
18. Ya. K. Khodataev, R. Bingham, V. P. Tarakanov, *et al.*, Phys. Scr. **89**, 95 (2001).
19. S. V. Vladimirov and M. Nambu, Phys. Rev. E **52**, 2172 (1995).
20. S. V. Vladimirov and O. Ishihara, Phys. Plasmas **3**, 444 (1996).
21. I. Lapenta, Phys. Plasmas **6**, 1442 (1999).
22. I. Lapenta, Phys. Rev. E **62**, 1175 (2000).
23. M. Lampe, G. Joyce, and R. Ganguli, Phys. Scr. **89**, 106 (2001).
24. V. A. Schweigert, A. Melzer, and A. Piel, J. Phys. IV **10**, 421 (2000).
25. A. Melzer, V. A. Schweigert, and A. Piel, Phys. Scr. **61**, 494 (2000).
26. M. Zuzic, A. V. Ivlev, J. Goree, *et al.*, Phys. Rev. Lett. **85**, 4064 (2000).
27. R. Quinn, C. Cui, J. Goree, *et al.*, Phys. Rev. E **53**, 2049 (1996).
28. F. Melanso and J. Goree, J. Vac. Sci. Techol. A **14**, 511 (1996).
29. R. Kompaneetz and V. Tsytovich, Contrib. Plasma Phys. (in press).
30. U. Konopka, G. E. Morfill, and L. Ratke, Phys. Rev. Lett. **84**, 891 (2000).
31. H. Schollmeyer, A. Melzer, A. Homann, and A. Piel, Phys. Plasmas **6**, 2693 (1999).
32. U. Konopka, G. E. Morfill, H. Thomas, and L. Ratke, AIP Conf. Proc. **446**, 53 (1998).
33. A. Homann, A. Melzer, and A. Piel, Phys. Lett. A **223**, 389 (1996).
34. A. Homann, A. Melzer, S. Peters, and A. Piel, Phys. Rev. E **56**, 7138 (1997).
35. M. Klindworth, A. Melzer, A. Piel, and V. A. Schweigert, Phys. Rev. B **61**, 8404 (2000).
36. H. Totsuji, Phys. Plasmas **8**, 1856 (2001); H. Schollmeyer, A. Melzer, A. Homann, and A. Piel, Phys. Plasmas **6**, 2693 (1999).
37. G. Hebner, M. Riley, D. Johnson, *et al.*, Phys. Rev. Lett. **87**, 235001 (2001).
38. H. Schollmeyer, A. Melzer, A. Homann, and A. Piel, Phys. Plasmas **6**, 2693 (1999).
39. A. V. Ivlev, U. Konopka, and G. E. Morfill, Phys. Rev. E **62**, 2739 (2000).
40. A. Holman, A. Melzer, and A. Piel, Phys. Rev. E **59**, 3835 (1999).
41. V. N. Tsytovich, Ya. K. Khodataev, and R. Bingham, Comments Plasma Phys. Control. Fusion **17**, 249 (1996).
42. M. Klindworth, A. Melzer, A. Piel, and V. A. Schweigert, Phys. Rev. B **61**, 8404 (2000).
43. A. Melzer, M. Klindworth, and A. Piel, Phys. Rev. Lett. **87**, 115002 (2001).
44. Juan Wen-Tau, Z.-H. Huang, J.-W. Hsu, *et al.*, Phys. Rev. E **58**, R6947 (1998).
45. V. A. Schweigert and F. Peeters, Phys. Rev. B **51**, 7700 (1995).
46. J. Goree, D. Samsonov, Z. Ma, *et al.*, in *Proceedings of the 2nd International Conference on Physics of Dusty Plasmas, Hakone, 1999*, Ed. by Y. Nakamura (Elsevier, Amsterdam, 2000), p. 92.

47. D. Wineland, C. Bergquist, M. Wayne, *et al.*, Phys. Rev. Lett. **59**, 2935 (1987).
48. F. Diedrich, E. Peik, J. Chen, *et al.*, Phys. Rev. Lett. **59**, 2931 (1987).
49. P. Leiderer, W. Ebner, and V. Shikin, Surf. Sci. **113**, 405 (1982).
50. S. Neser, T. Palberg, C. Blechinger, and P. Leiderer, Prog. Colloid Polym. Sci. **104**, 194 (1997).
51. Sh. Amiranashvili, N. Gusein-zade, and V. Tsytovich, Phys. Rev. E **64**, 016407 (2001).
52. *International Microgravity Plasma Facility* (Max-Plank Institute of Extraterrestrial Physics, Garching, 2000).
53. G. E. Morfill and H. Thomas, J. Vac. Sci. Technol. A **14**, 490 (1996).
54. H. Schollmeyer, A. Melzer, A. Homann, and A. Piel, Phys. Plasmas **6**, 2693 (1999).
55. H. Thomas and G. E. Morfill, J. Vac. Sci. Technol. A **14**, 2501 (1996).
56. H. Thomas and G. E. Morfill, Nature **379**, 806 (1996).
57. G. E. Morfill, H. Thomas, U. Konopka, and M. Zuzic, Phys. Plasmas **6**, 1769 (1999).
58. G. E. Morfill, H. Thomas, U. Konopka, *et al.*, AIP Conf. Proc. **446**, 184 (1998).
59. I. V. Schweigert, V. A. Schweigert, A. Melzer, and A. Piel, Phys. Rev. E **62**, 1238 (2000).
60. G. P. Hoffmann and H. Lowen, J. Phys.: Condens. Matter **12**, 7359 (2000).
61. A. Piel and A. Melzer, Plasma Phys. Controlled Fusion **44**, 1 (2002).
62. V. Thystovich and U. de Angelis, Phys. Plasmas **6**, 1093 (1999).
63. V. Tsystovich and U. de Angelis, Phys. Plasmas **8**, 1141 (2001).
64. A. B. Mikhailovskii, *Theory of Plasma Instabilities* (Atomizdat, Moscow, 1971; Consultants Bureau, New York, 1974).
65. S. Benkadda, P. Gabai, V. N. Tsytovich, and A. Verga, Phys. Rev. E **53**, 2717 (1996).
66. N. Rao, P. Shukla, and M. Yu, Planet. Space Sci. **38**, 543 (1990).
67. P. Shukla and V. P. Silin, Physica Scr. **45**, 508 (1992).
68. M. Rosenberg, J. Vac. Sci. Technol. A **14**, 631 (1996).
69. M. Rosenberg, Planet. Space Sci. **41**, 229 (1993).
70. M. Rosenberg and V. W. Chow, Planet. Space Sci. **46**, 103 (1998).
71. V. N. Tsytovich, U. de Angelis, and R. Bingham, Phys. Plasmas **9**, 1079 (2002).
72. V. N. Tsytovich and K. Watanabe, Preprint No. NIFS-720 (National Inst. for Fusion Science, Toki, 2002); Contrib. Plasma Phys. **43**, 51 (2003).
73. V. N. Tsytovich, *Lectures on Nonlinear Plasma Kinetics* (Springer, Helderberg, 1995).
74. V. N. Tsytovich, U. de Angelis, R. Bingham, and D. Resendes, Phys. Plasmas **4**, 3882 (1997).
75. G. E. Morfill and V. N. Tsytovich, Fiz. Plazmy **26**, 727 (2000) [Plasma Phys. Rep. **26**, 682 (2000)].
76. F. Melanso, Phys. Plasmas **3**, 3890 (1996).
77. X. Wang, A. Bhattachrjee, and S. Hu, Phys. Rev. Lett. **86**, 6026 (2001).
78. Q.-Z. Luo, N. D'Angelo, and R. L. Merlino, Phys. Plasmas **6**, 3455 (1999).
79. Y. Nakamura and H. Bailung, in *Proceedings of the Workshop on Physics of Dusty Plasmas, Iowa City, 2001*.
80. R. Merlino, A. Barcan, C. Thompson, and N. D'Angelo, Plasma Phys. Controlled Fusion **39**, 421 (1997).
81. Y. Nakamura, H. Bailung, and P. Shukla, Phys. Rev. Lett. **83**, 1602 (1999).
82. Y. Nakamura and A. Sarma, Phys. Plasmas **8**, 3921 (2001).
83. V. N. Tsytovich, in *Proceedings of the International Conference on Physics of Dusty Plasmas (ICPDP-2002), Durban, 2002.*
84. F. Melandso, T. K. Aslaksen, and O. Havnes, J. Geophys. Res. **98**, 13315 (1993).
85. V. N. Tsytovich and O. Havnes, Comm. Plasma Phys. Control. Fusion **18**, 267 (1993).
86. A. V. Ivlev and G. E. Morfill, Phys. Plasmas **7**, 1094 (2000).
87. K. Ostrikov, S. Vladimirov, M. Yu, and G. E. Morfill, Phys. Rev. E **61**, 4315 (2000).
88. A. Barkan, R. L. Merlino, and N. D'Angelo, Phys. Plasmas **2**, 3563 (1995).
89. R. L. Merlino, A. Barkan, C. Thompson, and N. D'Angelo, Phys. Plasmas **5**, 1607 (1998).
90. C. Thompson, A. Barkan, N. D'Angelo, and R. L. Merlino, Phys. Plasmas **4**, 2331 (1997).
91. R. L. Merlino, A. Barkan, C. Thompson, and N. D'Angelo, Plasma Phys. Controlled Fusion **39**, 421 (1997).
92. N. D'Angelo, Planet. Space Sci. **42**, 507 (1994).
93. V. N. Tsytovich and D. Rezendes, Fiz. Plazmy **24**, 71 (1998) [Plasma Phys. Rep. **24**, 65 (1998)].
94. Ya. K. Khodataev, V. P. Tarakanov, R. Bingham, *et al.*, Phys. Scr. **89**, 127 (2001).
95. D. Samsonov and J. Goree, Phys. Rev. E **59**, 1047 (1999).
96. G. E. Morfill, H. Thomas, U. Konopka, *et al.*, Phys. Rev. Lett. **83**, 1598 (1999).
97. J. Goree, G. E. Morfill, V. N. Tsytovich, and S. V. Vladimirov, Phys. Rev. E **59**, 7055 (1999).
98. V. N. Tsytovich, S. V. Vladimirov, G. E. Morfill, and J. Goree, Phys. Rev. E **63**, 056609 (2001).
99. V. N. Tsytovich, Phys. Scr. **89**, 26 (2001).
100. V. N. Tsytovich, Comments Mod. Phys. **1**, 1 (2000).
101. V. N. Tsytovich, Fiz. Plazmy **26**, 712 (2000) [Plasma Phys. Rep. **26**, 668 (2000)].
102. V. N. Tsytovich, in *Proceedings of the 2nd International Conference on Physics of Dusty Plasmas, Hakone, 1999*, Ed. by Y. Nakamura (Elsevier, Amsterdam, 2000), p. 99.
103. H. Thomas, in *Proceedings of the International Conference on Physics of Dusty Plasmas (ICPDP-2002), Durban, 2002.*
104. S. Benkadda, S. V. Vladimirov, and V. N. Tsytovich, Phys. Rev. E **60**, 4708 (1999).

105. G. E. Morfill and V. N. Tsytovich, Phys. Plasmas **9**, 4 (2002).
106. A. Boushoule, G. E. Morfill, and V. N. Tsytovich, Comments Mod. Phys. **1**, 131 (1999).
107. Y. Nakamura, H. Bailung, and P. Shukla, Phys. Rev. Lett. **83**, 1602 (1999).
108. F. Melanso, Phys. Plasmas **3**, 3890 (1996).
109. E. Tomme, B. Annaratone, and J. Allen, Plasma Sources Sci. Technol. **9**, 87 (2000).
110. A. Homann, A. Melzer, S. Peters, and A. Piel, Phys. Rev. E **56**, 7138 (1997).
111. A. Piel, A. Homann, and A. Melzer, Plasma Phys. Controlled Fusion **41**, Suppl. 3A, A453 (1999).
112. D. Samsonov, A. V. Ivlev, R. Quinn, and G. E. Morfill, Phys. Plasmas (in press).
113. U. Konopka, L. Ratke, and H. Thomas, Phys. Rev. Lett. **79**, 1269 (1997).
114. M. Zuzic, H. Thomas, and G. E. Morfill, J. Vac. Sci. Technol. A **14**, 496 (1996).
115. S. Nunomura, D. Samsonov, and J. Goree, Phys. Rev. Lett. **84**, 5141 (2000).
116. A. V. Ivlev and G. E. Morfill, Phys. Plasmas **7**, 1094 (2000).
117. D. Samsonov, J. Goree, H. Thomas, and G. E. Morfill, Phys. Rev. E **61**, 5557 (2000).
118. A. Melzer, M. Klindworth, and A. Piel, Phys. Rev. Lett. **87**, 115002 (2001).
119. V. Nosenko, J. Goree, Z. Ma, and A. Piel, Phys. Rev. Lett. **88**, 135001 (2002).
120. F. Peters and X. Wo, Phys. Rev. A **35**, 3109 (1987).
121. V. L. Ginzburg and V. N. Tsytovich, *Transition Radiation and Transition Scattering* (Higler, Bristol, 1992).
122. O. Havnes, T. Aslaksen, T. Hartquiat, *et al.*, J. Geophys. Res. **100**, 1731 (1995).
123. G. E. Morfill, O. Havnes, and C. Goertz, J. Geophys. Res. **98**, 11285 (1993).
124. O. Havnes, F. Li, T. Hartquist, *et al.*, Planet. Space Sci. **49**, 223 (2001).
125. D. Samsonov, J. Goree, Z. Ma, *et al.*, Phys. Rev. Lett. **83**, 3649 (1999).
126. A. Melzer, S. Nunomura, D. Samsonov, *et al.*, Phys. Rev. E **62**, 4162 (2000).
127. O. Havness, T. Hatrquist, A. Bratti, *et al.*, Phys. Rev. E **65**, 045403 (2002).
128. M. Zuzic, A. V. Ivlev, J. Goree, *et al.*, Phys. Rev. Lett. **85**, 4064 (2000).
129. A. P. Nevedov, G. E. Morfill, H. Thomas, *et al.*, Phys. Rev. Lett. (in press).
130. A. Nefedov, G. Morfill, V. Fortov, *et al.*, New J. Phys. **5**, 33/1 (2003).
131. A. Hasegawa, Adv. Phys. **34**, 1 (1985).

Plasma Physics Reports, Vol. 29, No. 11, 2003, pp. 955–970. Translated from Fizika Plazmy, Vol. 29, No. 11, 2003, pp. 1031–1046.

TURBULENCE AND CHAOS

Diffusion Equations and Turbulent Transport

O. G. Bakunin

Russian Research Centre Kurchatov Institute, pl. Kurchatova 1, Moscow, 123182 Russia

Received December 26, 2002; in final form, May 12, 2003

Abstract—Diffusion equations are considered that differ substantially in structure from classical ones. A description of diffusion under strongly nonequilibrium conditions in a highly turbulent plasma requires the use of equations that take into account memory effects and the nonlocal nature of transport. Different methods are developed for constructing such equations, ranging from those in the quasilinear approximation to those with fractional derivatives. It is emphasized that the theoretical concepts underlying the equations proposed are common for a very wide variety of specific physical problems. The ways of applying theoretical probabilistic ideas are demonstrated. © *2003 MAIK "Nauka/Interperiodica".*

1. INTRODUCTION

The equations describing diffusion phenomena are among the key tools for investigating transport processes in plasmas. The ever-increasing complexity of the problems requires the development of more and more elaborate and diverse diffusion models. The relation between heat conduction and random-walk processes was established as early as the beginning of the 20th century [1–6]. In the first stage of research in this field, the main problem was that of calculating the diffusion coefficient (thermal conductivity). Investigation of turbulent diffusion in an atmosphere led to new equations that differ substantially in structure from the classical diffusion equation [7–9]. It was revealed that transport processes in turbulent plasmas are nondiffusive in nature. New forms of equations describing transport processes have constantly been sought since the first studies on quasilinear theory [10–11]. The description of diffusion under strongly nonequilibrium conditions in a highly turbulent plasma required the use of equations that take into account memory effects and the nonlocal nature of transport processes [12–19].

The objective of this paper is to consider different methods for constructing such equations, ranging from those in the quasilinear approximation to those with fractional derivatives. The topics to be discussed include the telegraph equation, the Levy–Khintchine distribution, and the Kohlrausch slow relaxation law. Use will be made of some important notions belonging to the theoretical probabilistic analysis: the return probability, the self-intersection probability, and the probability of staying in a trap. The issues addressed in the paper can be conditionally divided into four groups:

(i) the quasilinear approximation and renormalization,

(ii) the Markov equations and nonlocality,

(iii) memory effects in diffusion problems, and

(iv) correlations and the role of returns.

This formal division is based on which analysis method dominates each of the groups. However, it is impossible to draw a rigid distinction between these groups. The material will be presented in a physically precise way and will be exemplified by reference to the description of turbulent diffusion. For brevity, many interesting points had to be omitted because the scientific problem under discussion has a hundred year history of research. Despite a host of works on the problem, it is still far from being completely resolved. Various aspects of the subject have been elucidated in a number of brilliant monographs and reviews [12–19].

2. QUASILINEAR APPROXIMATION

The great importance of the quasilinear approximation was stressed in the Introduction. Quasilinear equations were first considered in [10, 11] in connection with the problem of describing diffusion in phase space due to the interaction between waves and particles. For our purposes, it is sufficient to consider only some of the ideas advanced in the cited papers, namely, those associated with the averaging of the quasilinear equations [20–22].

We consider the continuity equation for the density of a passive scalar characterizing an incompressible flow:

$$\frac{\partial n}{\partial t} + v\frac{\partial n}{\partial x} = 0, \tag{1}$$

where $n(x, t)$ is the spatial density of the passive scalar and $v(t)$ is the random velocity field. We use the method of averaging over the ensemble of realizations for Eq. (1), assuming that the density field can be represented as a sum of the mean density $n_0(x, t) = \langle n \rangle$ and the fluctuation component $n_1 = n - \langle n \rangle$,

$$n = n_0 + n_1. \tag{2}$$

1063-780X/03/2911-0955$24.00

We also set $\langle n_1 \rangle$ and $v = v_0 + v_1$, where v_0 = const and $\langle v_1 \rangle = 0$. As a result, after simple manipulations (which are frequently used in the literature [20–22]), we arrive at the following two equations:

$$\frac{\partial n_0}{\partial t} + v_0 \frac{\partial n_0}{\partial x} + \left\langle v_1 \frac{\partial n_1}{\partial x} \right\rangle = 0; \quad (3)$$

$$\frac{\partial n_1}{\partial t} + v_0 \frac{\partial n_1}{\partial x} + v_1 \frac{\partial n_0}{\partial x} + v_1 \frac{\partial n_1}{\partial x} - \left\langle v_1 \frac{\partial n_1}{\partial x} \right\rangle = 0. \quad (4)$$

We assume that the fluctuations n_1 and v_1 are as small as δ in comparison with the mean density n_0 and retain the terms on the order of δ^2 in Eqs. (3) and (4). The quasilinear character of the approximation indicates that, in Eq. (3) for n_0, we keep the nonlinear term on the order of δ^2 but, in Eq. (4) for n_1, we keep only the terms that are of the first order in δ. At this point, such assumptions and transformations are justified because, on the one hand, we wish to see how the equation for n_0 changes when fluctuations are taken into account and, on the other, we wish to obtain a solvable equation for n_1. As a result, the transformations put Eq. (4) for n_1 into the form

$$\frac{\partial n_1}{\partial t} + v_0 \frac{\partial n_1}{\partial x} = -v_1 \frac{\partial n_0}{\partial x}. \quad (5)$$

We solve Eq. (5) by the method of Green's functions. We consider Eq. (5) as a first-order linear hyperbolic equation with the source term $I(x, t) = -v_1 \frac{\partial n_0}{\partial x}$, where the derivative $\frac{\partial n_0}{\partial x}$ is the parameter of the equation. We also supplement the equation with the uniform initial condition $n_1(x, 0) = 0$. Then, we consider the equation for the Green's function G:

$$\frac{\partial G}{\partial t} + v_0 \frac{\partial G}{\partial x} = \delta(x - x_1)\delta(t - t_1). \quad (6)$$

It is easy to solve this equation by applying the Laplace transformation in the time t and the Fourier transformation in the spatial coordinate x:

$$\tilde{\tilde{G}}_{k,s} = \frac{\exp(-t_1 s)}{s + ikv_0} \exp(ikx). \quad (7)$$

Here and below, the tilde marks the Fourier- or Laplace-transformed quantities. The solution has a simple physical meaning: it describes perturbation propagating along the characteristic $z = x - v_0(t - t_1)$:

$$G(x, t, x_1, t_1) = \delta(x - x_1 - v_0(t - t_1))h(t - t_1), \quad (8)$$

where we have used the notation $h(t)$ for the Heaviside function. The sought solution $n_1(x, t)$ has the form

$$n_1(x, t) = -\int_0^t v_1(t_1) \frac{\partial n_0(z, t)}{\partial z} dt_1. \quad (9)$$

We substitute this expression for n_1 into Eq. (3) and perform simple manipulations [20–22] to obtain

$$\frac{\partial n_0}{\partial t} + v_0 \frac{\partial n_0}{\partial x} = \int_0^t \langle v_1(t) v_1(t_1) \rangle \frac{\partial^2 n_0(z, t_1)}{\partial z \partial x} dt_1. \quad (10)$$

The integral nature of Eq. (10) reflects the Lagrangian character of the relationships between the derivatives of $n_0(x, t)$. In this respect, the continuity equation at hand is quite different from the fundamentally local continuity equation. The characteristic that appeared in our analysis relates the derivatives at different times. The left-hand side of Eq. (10) contains the partial derivatives with respect to x and t. On the right-hand side, we sum the values of the derivative $\frac{\partial^2 n_0}{\partial x^2}$ calculated along the characteristic with a weighting factor C, which is the autocorrelation function of velocity,

$$C(t, t_1) = \langle v_1(t) v_1(t_1) \rangle. \quad (11)$$

It is because of the wide variety of correlation effects that there exist a large number of models for describing different aspects of random-walk processes. In the case of a steady-state random process, the function $C(t, t_1) \approx C(t - t_1)$ in the equation under analysis plays the role of the memory function. It is the function $C(\tau)$ that will be used in further analysis. The particular form of the equation is governed by the choice of the memory function $C(\tau)$. In the following three sections, we will consider three different situations in each of which the nonlocal equation assumes its familiar form.

3. THE CASE OF SHORT-RANGE CORRELATIONS

In the simplest physically meaningful case, Eq. (10) reduces to the classical diffusion equation

$$\frac{\partial n_0}{\partial t} + v_0 \frac{\partial n_0}{\partial x} = D \frac{\partial^2 n_0(x, t)}{\partial x^2}. \quad (12)$$

This is possible only if the main contribution to the integral on the right-hand side of Eq. (10) comes from a short interval $(t - t_0, t)$ such that $t_0 \ll t$. The quantity t_0 can be estimated as

$$t_0 \approx \frac{1}{C(0)} \int_0^\infty C(t) dt. \quad (13)$$

If the second derivative changes insignificantly over the short interval, we obtain

$$\int_0^t \langle v(t) v(t_1) \rangle \frac{\partial^2 n_0(z, t)}{\partial z \partial x} dt_1 \approx \frac{\partial^2 n_0(x, t)}{\partial x^2} \int_{t - t_0}^t C(t - t_1) dt_1. \quad (14)$$

In fact, we are assuming that the correlations are short-range. Thus, in this approximation, we arrive at the familiar Kubo–Green formula for the diffusion of a passive impurity [5]:

$$D = \int_0^\infty C(\tau)d\tau = \int_0^\infty \langle v(0)v(t)\rangle dt. \quad (15)$$

In terms of the δ correlations [2],

$$C(t-t_1) \approx C_0\tau\delta(t-t_1), \quad (16)$$

which are often used in theoretical analysis, the local representation for quasilinear equation (10) takes the form

$$\frac{\partial n_0}{\partial t} + v_0\frac{\partial n_0}{\partial x} = C_0\tau\frac{\partial^2 n_0(x,t)}{\partial x^2}, \quad (17)$$

where the diffusion coefficient is estimated from the formula $D = C_0\tau \approx V^2\tau$. This result corresponds to the expected diffusion effect, which arises when the perturbation field is taken into account.

4. THE CASE OF LONG-RANGE CORRELATIONS

In the case of long-range correlations such that $C \approx$ const for $t_1 \gg 0$, Eq. (10) can be reduced to

$$\frac{\partial n_0}{\partial t} + v_0\frac{\partial n_0}{\partial x} = C_0\int_0^t \frac{\partial^2 n_0(z,t_1)}{\partial z\partial x}dt_1. \quad (18)$$

In turn, this equation can be further simplified by using the properties of the characteristic z. Differentiating Eq. (18) with respect to x gives

$$\frac{\partial^2 n_0}{\partial t\partial x} + v_0\frac{\partial^2 n_0}{\partial x^2} = C_0\int_0^t \frac{\partial^3 n_0(z,t_1)}{\partial x^3}dt_1. \quad (19)$$

Differentiating Eq. (18) with respect to t gives

$$\frac{\partial^2 n_0}{\partial t^2} + v_0\frac{\partial^2 n_0}{\partial x\partial t} = C_0\frac{\partial^2 n_0}{\partial x^2} - v_0\int_0^t \frac{\partial^3 n_0(z,t_1)}{\partial x^3}dt_1. \quad (20)$$

Eliminating the integral in Eqs. (19) and (20) yields

$$\frac{\partial^2 n_0}{\partial t^2} + 2v_0\frac{\partial^2 n_0}{\partial x\partial t} + (v_0^2 - C_0)\frac{\partial^2 n_0}{\partial x^2} = 0. \quad (21)$$

This equation differs markedly from the classical diffusion equation. For $C_0 > 0$, it is a hyperbolic equation, possessing the corresponding properties. Thus, a complete solution to this equation can be represented as a superposition of two initial distributions $n_0(x, 0)$ moving at different velocities. As is well known, the fact that hyperbolic equations have characteristics opens up new possibilities for describing nonlocal effects. It should be noted, however, that, from the mathematical point of view, the above passage from a parabolic to a hyperbolic equation is incorrect. The Cauchy problems for these two types of equation are radically different. Nevertheless, interest in such passages can be traced back to Hadamard. In the case at hand, we can draw an analogy with the Hadamard hyperbolic equation

$$-\frac{\partial n_0}{\partial t} + \varepsilon\frac{\partial^2 n_0}{\partial x\partial t} + \frac{\partial^2 n_0}{\partial x^2} = 0. \quad (22)$$

For $\varepsilon \longrightarrow 0$, this equation reduces to the classical diffusion equation. According to Hadamard's ideas [2], any parabolic problem can be considered as a limiting case of the corresponding hyperbolic problem. However, in the case at hand, the analogy between Eq. (21) and the telegraph equation

$$\frac{\partial n}{\partial t} + \tau\frac{\partial^2 n}{\partial t^2} = D\frac{\partial^2 n}{\partial x^2} \quad (23)$$

has the deepest physical meaning. The telegraph equation was one of the first so-called nondiffusion equations that were applied to describe the turbulent transport of passive impurities.

5. TELEGRAPH EQUATION

In the theory of random processes [2, 6], one of the most widely used correlation functions is an exponential one:

$$C(t) = C_0\exp\left(-\frac{t}{\tau}\right).$$

This choice is quite natural because it is in this form that the correlation function is used in the Langevin model of random-walk processes. With the help of this exponential function, we can transform integral equation (10) into a partial differential equation. To do this, we set

$$C(t, t_1) = C(t-t_1). \quad (24)$$

Differentiating Eq. (10) with respect to x gives

$$\frac{\partial^2 n_0}{\partial t\partial x} + v_0\frac{\partial^2 n_0}{\partial x^2} = \int_0^t C(t-t_1)\frac{\partial^3 n_0(z,t_1)}{\partial x^3}dt_1. \quad (25)$$

Differentiating Eq. (10) with respect to t gives

$$\frac{\partial^2 n_0}{\partial t^2} + v_0\frac{\partial^2 n_0}{\partial t\partial x} = C_0\frac{\partial^2 n_0}{\partial x^2} - \frac{1}{t_0}\int_0^t C(t-t_1)\frac{\partial^2 n(z,t_1)}{\partial x^2}dt_1 - v_0\int_0^t C(t-t_1)\frac{\partial^3 n_0(z,t_1)}{\partial x^3}dt_1.$$

Eliminating the integral in these two equations yields

$$\frac{\partial n_0}{\partial t} + v_0\frac{\partial n_0}{\partial x} + t_0\left[\frac{\partial^2 n_0}{\partial t^2} + 2v_0\frac{\partial^2 n_0}{\partial x\partial t} + (v_0^2 - C_0)\frac{\partial^2 n_0}{\partial x^2}\right] = 0. \quad (26)$$

In accordance with the hyperbolic nature of the problem, we introduce the new variables

$$\xi = t, \quad \eta = x - vt \quad (27)$$

to obtain

$$\frac{\partial n_0}{\partial \xi} + t_0\frac{\partial^2 n}{\partial \xi^2} = C_0 t_0\frac{\partial^2 n_0}{\partial \eta^2}, \quad (28)$$

where $\sqrt{C_0}$ is the propagation velocity of the perturbations. This is actually the telegraph equation (22) in a frame of reference related to coordinates (27).

Davydov [8] was the first to apply the telegraph equation to turbulent diffusion. His idea was to describe rapid transport processes by including additional partial derivatives in the classical diffusion equation. This problem turned out to be particularly important in connection with the investigations of turbulent diffusion that were carried out in 1926 by Richardson [7], who revealed that the laws of atmospheric diffusion differ significantly from the classical law:

$$R^2 \propto t^3 \gg t \quad \text{or} \quad D \approx \frac{R^2}{t} \propto R^{4/3}. \quad (29)$$

The studies by Richardson undoubtedly opened up an entirely new area of study and made a significant impact on the further development of the theory of transport processes. At this point, it should be noted that scaling (29) refers to the relative diffusion of Lagrangian particles, or actually to their evolution averaged over the ensemble of realizations. This feature of Richardson's diffusion model was widely discussed in the literature [7].

Davydov used the following phenomenological set of equations for the particle density $n(x, t)$:

$$\frac{\partial n}{\partial t} + \frac{\partial q}{\partial x} = 0; \quad \frac{\partial q}{\partial t} = \frac{q_0 - q}{\tau}, \quad (30)$$

where $q_0 = -D\dfrac{\partial n}{\partial x}$.

Formal manipulations with this set of equations yield telegraph equation (23). He suggested using Eq. (23) to take into account the finite particle velocity v during the molecular diffusion. The classical parabolic diffusion equation follows from telegraph equation (23) in the limit

$$\tau \longrightarrow 0; \quad D \approx v^2\tau \longrightarrow \text{const}. \quad (31)$$

The physical meaning of the representation proposed by Davydov for the particle flux q can be easily clarified by writing the formal solution

$$q = \int_0^t q_0 \exp(-(t - t'))\frac{dt'}{\tau}. \quad (32)$$

Obviously, such an expression for the particle flux takes into account memory effects. After Davydov, this formula was generalized in many studies in such a way as to replace the exponential function by an arbitrary memory function $M(t - t')$:

$$q = \int_0^t q_0 M(t - t')\frac{dt'}{\tau}, \quad (33)$$

in which case the general diffusion equation becomes

$$\frac{\partial n(x, t)}{\partial t} = \int_0^t D\frac{\partial^2 n(x, t')}{\partial x^2}M(t - t')\frac{dt'}{\tau}. \quad (34)$$

Later, the telegraph equation in form (34) was often applied to describe turbulent diffusion [9, 23–26].

6. DIFFUSION APPROXIMATION FOR CORRELATION EFFECTS

The obvious drawback of the quasilinear theory is that the nonlinear term in the equation for n_0 is retained, while the nonlinear terms in the equation for n_1 are omitted. There are a large number of papers whose authors try to refine the quasilinear approximation. A detailed analysis of such papers was carried out in [15, 22]. The most interesting papers in this area were written by Dupree [27–29], who conceived the idea of diffusive spreading of the particle trajectories, which is physically close to the assumption made by Corrsin [30]. In fact, the equation for n_1 is linear and hyperbolic; therefore, it keeps the Lagrangian character of the correlations. This opens up the possibility of describing the omitted correlation effects—the combination $v\dfrac{\partial n_1}{\partial x} - \left\langle v\dfrac{\partial n_1}{\partial x}\right\rangle$ in Eq. (4)—by supplementing the equation for perturbations with the additional diffusion term $D\dfrac{\partial^2 n_1}{\partial x^2}$.

In this context, it is expedient to present some of the results obtained by Kadomtsev and Pogutse [31] on anomalous electron transport in a magnetic field. They considered a three-dimensional problem of transport in a strong constant field $\mathbf{B}(0, 0, B_0)$ pointing along the z direction in the presence of a weak random field $\mathbf{B}'(B_x, B_y, 0)$. As usual, the quasilinear representation is valid only when the diffusion-related displacement in the transverse direction is much smaller than the transverse correlation length. Kadomtsev and Pogutse also consid-

ered the opposite case. They introduced the continuity equation for the density of the magnetic field lines,

$$\frac{\partial n_b}{\partial z} + \mathbf{b}\nabla n_b(\mathbf{r}_\perp, z) = 0, \quad \mathbf{b} = \frac{\mathbf{B}'}{B_0} \approx \mathbf{b}_0, \tag{35}$$

and represented n_b as a sum of the mean density $n_0 = \langle n_b \rangle$ and the fluctuation component n_1,

$$n_b = n_0 + n_1.$$

The problem as formulated is close to problem (3) and (4) of the quasilinear diffusion of a passive scalar. In fact, the authors of [31] wrote the equation for n_0 in traditional form:

$$\frac{\partial n_0}{\partial z} + \nabla \langle \mathbf{b} n_1 \rangle = 0. \tag{36}$$

However, in the equation for n_1, they replaced the second-order terms (which were omitted in earlier studies) by a diffusion term. In essence, they followed Dupree's ideas and related the discarded correlation effects with the diffusive spreading of the trajectories:

$$\frac{\partial n_1}{\partial z} - D_F \nabla_\perp^2 n_1 = -\mathbf{b}\nabla n_0. \tag{37}$$

Thus, they kept the equations linear but passed from a hyperbolic equation of form (5) to parabolic equation (37). Applying the mathematical apparatus of Green's functions to Eq. (37), we obtain

$$\frac{\partial G}{\partial z} - D_F \nabla_\perp^2 G = \delta(\mathbf{r} - \mathbf{r}'). \tag{38}$$

Kadomtsev and Pogutse derived the following equation for n_0:

$$\frac{\partial n_0}{\partial z} = D_F \nabla_\perp^2 n_0, \tag{39}$$

with

$$D_F = \frac{1}{2}\int \frac{b^2(\mathbf{k})}{ik_z + k_\perp^2 D_F} d\mathbf{k},$$
$$b^2(\mathbf{k}) = \frac{1}{(2\pi)^2}\int \langle b(0)b(r)\rangle \exp(-i\mathbf{k}\mathbf{r}) d\mathbf{r}. \tag{40}$$

For $\Delta k_z > k_\perp^2 D_F$, they got the quasilinear expression [20–22]

$$D_F = \frac{\pi}{2}\int d\mathbf{k} b^2(\mathbf{k})\delta(k_z) \propto b_0^2 \Delta_z, \tag{41}$$

where Δ_z is the longitudinal correlation length.

In the case of strong correlations ($\Delta k_z < k_\perp^2 D_F$), they arrived at the following result, which is similar to that obtained by Howells [32]:

$$D_F^2 = \frac{1}{2}\int \frac{b^2(\mathbf{k})}{k_\perp^2} d\mathbf{k}. \tag{42}$$

This results of Kadomtsev and Pogutse once again showed, on the one hand, that it is important to take into account the correlation effects that are ignored in the quasilinear approach and, on the other, that these correlation effects are closely related to the problem of how different spatial scales should be treated in turbulent transport theory.

In the context of the problem considered in [31], we should mention the well-known papers by Rechester and Rosenbluth [33, 34], who raised the question of incorporating the effect of divergence of the neighboring magnetic field lines in the problem of anomalous electron heat conduction. Those papers, together with [31], have played a very important role in developing the modern theory of transport in a stochastic magnetic field.

7. BASIC EQUATION FOR MARKOVIAN PROCESSES

It has been shown above that a host of different effects has gone unstudied in the theory based on the classical diffusion equation. On the other hand, very many phenomenological assumptions were made in order to refine the diffusion equation. Consequently, sophisticated transport models should be constructed based on the fundamental ideas of transport processes. These ideas are provided by the theoretical probabilistic approach to the problems of random-walk processes. For our purposes, the most important method for deriving equations is that of constructing a functional equation for the probability density (a chain equation). As early as 1905, Albert Einstein obtained a functional equation for the particle density solely on the basis of the general ideas about the process of random walk [1]:

$$n(x, t+\tau) = \int_{-\infty}^{+\infty} W(\Delta) n(x-\Delta, t) d\Delta, \tag{43}$$

where $W(\Delta)$ is the density of the probability of undergoing a jump Δ. This fundamentally nonlocal equation can be made local by reducing it to a diffusion equation. Assuming that the time scale τ is short and the jump Δ is small, Einstein arrived at the classical diffusion equation. In this way, he used the expansions

$$n(x, t+\tau) = n(x, t) + \frac{\partial n}{\partial t}\tau + \ldots, \tag{44}$$

$$n(x+\Delta, t) = n(x, t) + \frac{\partial n}{\partial x}\Delta + \frac{\Delta^2}{2}\frac{\partial^2 n}{\partial x^2} + \ldots. \tag{45}$$

Simple calculations yield

$$n + \frac{\partial n}{\partial t}\tau = n\int_{-\infty}^{+\infty} W(\Delta)d\Delta + \frac{\partial n}{\partial x}\int_{-\infty}^{+\infty} W(\Delta)\Delta d\Delta + \frac{\partial^2 n}{\partial x^2}\int_{-\infty}^{+\infty} W(\Delta)\frac{\Delta^2}{2} + \ldots. \quad (46)$$

Assuming that the function W is symmetric,

$$W(\Delta) = W(-\Delta) \quad (47)$$

and specifying the normalization condition,

$$\int_{-\infty}^{+\infty} W(\Delta)d\Delta = 1, \quad (48)$$

we obtain the equation

$$\frac{\partial n}{\partial t} = D\frac{\partial^2 n}{\partial x^2}, \quad D = \frac{1}{\tau}\int_{-\infty}^{+\infty} W(\Delta)\frac{\Delta^2}{2}d\Delta. \quad (49)$$

Note that the number of terms in expansions (44) and (45) was chosen in a physically meaningful way. Based on the relationship characterizing the average behavior of Brownian particles, $R^2 \propto t$, we can estimate the orders of the terms in the expansions as follows:

$$n \propto R^{-1}, \quad n \propto t^{-1/2}, \quad \frac{\partial n}{\partial t} \propto t^{-3/2}, \quad \frac{\partial n}{\partial x} \propto t^{-1},$$

$$\frac{\partial^2 n}{\partial x^2} \propto t^{-3/2}, \quad t \longrightarrow \infty.$$

However, retaining only two terms in each of the expansions (44) and (45) results in a telegraph equation. However, this does not indicate that the telegraph equation is invalid. The reason is that, in this case, the effects of finite propagation velocity of the perturbations come into play.

The integral approach was further developed in papers by Smoluchowski, Chapman, and Kolmogorov [1–5, 35]. A key element in their approach is Markov's postulate—that the length of the jump, Δ, is independent of the prehistory of motion.

8. LEVY–KHINTCHINE DISTRIBUTION

In probability theory, ideas about the form of equation describing random-walk processes have evolved considerably: it is the integral form of the equation which eventually became dominant. Using expansion (44) of functional (43), we can readily obtain the Smoluchowski equation [1–5]

$$\frac{\partial n(x, t)}{\partial t} = \int_{-\infty}^{+\infty} [K(x', x)n(x', t) - K(x, x')n(x, t)]dx'. \quad (50)$$

Here, $K(x, x')dxdx'$ is the probability for a particle at the position x at the time t to pass over to the interval $x' + dx'$ during the time interval dt. We introduce the functional

$$G(x', x) = K(x', x) - \delta(x - x')\int_{-\infty}^{+\infty} K(x, x')dx'. \quad (51)$$

For a homogeneous isotropic medium, we have $G(x' - x) = G(|x - x'|)$. In the simplest case under consideration, this functional has the form

$$\frac{\partial n}{\partial t} = \int_{-\infty}^{+\infty} G(x - x')n(x')dx'. \quad (52)$$

Here, it is more convenient to switch to the Fourier representation for $n(x, t)$ in the variable x. Formal manipulations yield the equation

$$\frac{\partial \tilde{n}_k(t)}{\partial t} = \tilde{G}(k)\tilde{n}_k(t), \quad (53)$$

which indicates that the Fourier harmonics do not exhibit memory effects. Corresponding to the classical diffusion equation is the functional

$$\tilde{G}(k)\tilde{n}_k = -Dk^2\tilde{n}_k. \quad (54)$$

In the case of telegraph equation (22), the memory effects were taken into account [see Eq. (34)]:

$$\frac{\partial \tilde{n}_k(t)}{\partial t} = -k^2\int_0^t \tilde{n}_k(t)M(t - t')\frac{dt'}{\tau} = -k^2 M(t) * \tilde{n}_k(t), \quad (55)$$

where the asterisk indicates the convolution operation.

Applying the Laplace transformation in time, we obtain the following functional for the telegraph equation with memory:

$$\tilde{\tilde{G}}(k, w) = -\frac{Dk^2}{1 - iw\tau}. \quad (56)$$

It is an easy matter to combine the memory and nonlocality effects into a common expression containing a convolution:

$$\frac{\partial \tilde{n}_k(t)}{\partial t} = -k^2\int_0^t \tilde{n}_k(t)\tilde{D}_k(k, t - t')\frac{dt'}{\tau} = -k^2\tilde{D}_k(k, t) * \tilde{n}_k(t).$$

Performing the Laplace transformation in time yields $-Dk^2 \longrightarrow -k^2\tilde{D}_{k,w}(k, w)$. In the theoretical probabilistic approach, however, this heuristic method is unsatisfactory. Below, we will consider this point in more detail.

The approach based on Eq. (53) was developed by Levy and Khintchine [36], who used the approximate equation of the form

$$\frac{\partial \tilde{n}_k(t)}{\partial t} = -k^{\alpha}\tilde{n}_k(t); \quad 0 < \alpha \le 2. \tag{57}$$

It is easy to see that, for $\alpha = 2$, we are dealing with a Gaussian distribution (corresponding to a conventional diffusion equation). Some other analytic distributions are also known. For $\alpha = 1$, we obtain the Cauchy distribution. For $\alpha = 3/2$, we arrive at the familiar Holtsmark distribution [4]. In this context, it is important to note that all the probability densities with $\alpha < 2$ have power-law tails. Another important property is that the second and higher moments of the distributions with $1 \le \alpha < 2$ and all moments of the distributions with $0 < \alpha < 1$ diverge.

9. LEVY DISTRIBUTION FOR TURBULENT DIFFUSION

Monin [9] used the Einstein–Smoluchowski functional given in Eqs. (53) and (57) to describe turbulent diffusion in the atmosphere. That paper anticipated the development of modern ideas of using additional fractional partial derivatives in diffusion equations. Monin was guided by Kolmogorov's ideas about the universal properties of well-developed isotropic turbulence [14]. In the corresponding formulation of the problem, all statistical parameters are determined exclusively by the scale length $l_k \approx \frac{1}{k}$ and the mean energy dissipation rate $\varepsilon = \left[\frac{L^2}{T^3}\right]$. Based on dimensionality considerations, Monin obtained the following expression for the kernel of the nonlocal functional describing turbulent diffusion:

$$\tilde{G}(k) \propto G(\varepsilon, k) = \varepsilon^{1/3}k^{2/3}. \tag{58}$$

This representation is consistent with the results derived in 1926 by Richardson [7] under the assumption that, if $\tilde{G}(k) = -D(k)k^2$, then

$$D(k) \approx \frac{R^2}{t} \propto R^{4/3} \propto k^{-4/3}. \tag{59}$$

Also, in modern terminology [17, 19], the equation

$$\frac{\partial \tilde{n}_k(t)}{\partial t} = -k^{2/3}\tilde{n}_k(t) \tag{60}$$

is one with a fractional derivative with respect to x: $\frac{\partial^{\alpha} n}{\partial x^{\alpha}} \propto \frac{n}{(\Delta x)^{\alpha}} \propto k^{\alpha}n$, where $\alpha = 2/3$ [see formula (58)]. Monin was the first to obtain this equation for the probability density on the basis of physical considerations. He solved this equation and wrote the solution in terms of the Whittaker functions. The solution in question behaves asymptotically as $n(x \longrightarrow \infty) \propto x^{-\frac{11}{13}}$. The problem of the relaxation to a self-similar regime was discussed in detail in [14, 17].

However, Monin was unsatisfied with the above form of the equation. In fact, he derived the following equation with fractional derivatives:

$$\frac{\partial n}{\partial t} = \varepsilon^{1/3}\frac{\partial^{2/3} n}{\partial x^{2/3}}.$$

It is only recently that the idea of using fractional derivatives has come to be recognized [17]. In an effort to derive an equation that would be as clear as the telegraph equation, Monin differentiated his equation twice with respect to time and obtained

$$\frac{\partial^3 n}{\partial t^3} = \varepsilon\frac{\partial^2 n}{\partial x^2}. \tag{61}$$

It is now known that, for many years after the publication of theoretical works of Davydov and Monin, diffusion equations has often been supplemented with different partial derivatives,

$$\frac{\partial^2 n}{\partial t^2}; \quad \frac{\partial^3 n}{\partial t^3}; \quad \frac{\partial^{\alpha} n}{\partial t^{\alpha}}; \quad \frac{\partial^{\beta} n}{\partial x^{\beta}} \tag{62}$$

in order to describe nonlocality and memory effects [17, 19, 37–41]. Moreover, this approach was used not only for diffusion equations in coordinate space but also for those in velocity space.

10. RANDOM-WALK PROCESSES IN CONTINUOUS TIME

As has already been discussed, the Smoluchowski–Chapman–Kolmogorov approach, although fairly general, does not exhibit memory effects [see Eq. (55)]. Montroll and Weiss [42] were the first (1965) to successfully overcome this serious drawback. A careful analysis of the problems of random-walk processes shows that a fundamentally important role is played by the transition probability density. In Markov's approach, the transition probability density is assumed to depend on the spatial variable, $W(\Delta)$, where Δ is a spatial step. Montroll and Weiss used a fundamentally different dependence: they assumed that the transition probability density depends on time, $\Psi(t)$. They also introduced a physically clear quantity: the probability of not undergoing a transition from a point y to any other point during the time t:

$$\Phi_Y(t) = 1 - \int_0^t \Psi_Y(t)dt. \tag{63}$$

The function $\Phi_y(t)$ reflects the relaxation properties of the system. In the simplest case, the function $\Phi_y(t)$ is represented in the form of the Poisson distribution

$$\Phi_y(t) = \exp(-t/\tau), \tag{64}$$

where τ is the mean time between transition events. The function $\Phi_y(t)$ is also being represented in some other forms capable of reflecting the characteristic behavior of relaxing systems:

the Kohlrausch relaxation function

$$\Phi_y(t) = \exp(-\sqrt{\alpha t}), \tag{65}$$

the algebraic relaxation function

$$\Phi_y(t) = (\alpha t)^{-\gamma}, \tag{66}$$

the Montroll function

$$\Phi_y(t) = \exp[-\ln^{\beta}(-t/\tau)]. \tag{67}$$

In the Montroll–Weiss theory, the function $\Phi_y(t)$ plays the governing role. Prior to this, the subscript y in the functions Φ and Ψ served merely to mark an arbitrarily chosen point. The authors of [42] succeeded in writing an elegant chain equation for the probability for a randomly walking particle to occur at the point x at the time t:

$$P(x, t) = \int_0^t R(x, \tau)\Phi_X(t-\tau)d\tau. \tag{68}$$

The functions on the right-hand side of this equation have essentially the same physical meaning as the function Ψ [see definition (63)]. Consider the point x_1 and let the function Ψ_{X_1} be represented as a sum of the probabilities for transitions from the point x_1 to all allowed points x. We then have $\Psi_{X_1}(t) = \sum_{X_1}\Psi(x_1 \longrightarrow x, t)$ and, consequently,

$$R(x, t) = \sum_{X_1}\int_0^t R(x_1, \tau)\Psi(x_1 \longrightarrow x, t-\tau)d\tau + P(x, 0)\delta(t), \tag{69}$$

where $\Psi(x_1 \longrightarrow x, t)$ is the probability density for a transition from the point x_1 to the point x at the time t. Note that the function Ψ depends not only on the time t but also on the relative spatial positions of the points x_1 and x, in which case we have

$$\int_{-\infty}^{\infty} dx \int_{-\infty}^{\infty} \Psi(x_1 \longrightarrow x, t)dt = 1,$$

where $R(x, t)$ is the probability for transitions from other points to the point x during the time interval $(t; t + dt)$. The probability density $P(x, t)$ is related to the particle density by

$$n(x, t) = \frac{NP(x, t)}{\delta V}, \tag{70}$$

where N is the total number of particles and $\delta V = (\delta x)^d$ is a volume element. Applying the Laplace transformation in time and the convolution theorem, we obtain from expressions (68) and (69) the equation

$$s\tilde{P}(x, s) - P(x, 0) = \sum_{X_1}[\tilde{R}(x_1, s) - \tilde{R}(x, s)]\tilde{\Psi}(x_1 \longrightarrow x, s), \tag{71}$$

where, in accordance with expression (68), $\tilde{P}$ and $\tilde{R}$ are related by

$$\tilde{R}(x, s) = \frac{\tilde{P}(x, s)}{\tilde{\Phi}(s)} = \frac{s\tilde{P}(x, s)}{1 - \sum_{X_1}\tilde{\Psi}(x_1 \longrightarrow x, s)}. \tag{72}$$

Then, returning to the physical variables, we arrive at the Montroll–Weiss equation

$$\frac{\partial}{\partial t}P(x, t) = \sum_{X_1}\int_0^t [P(x_1, \tau) - P(x, \tau)]F(x_1 \longrightarrow x, t-\tau)d\tau, \tag{73}$$

where the memory function F is defined in terms of its Laplace transform,

$$\tilde{F}(x_1 \longrightarrow x, s) = \frac{s\tilde{\Psi}(x_1 \longrightarrow x, s)}{1 - \sum_{X_1}\tilde{\Psi}(x_1 \longrightarrow x, s)}. \tag{74}$$

In what follows, we are interested in the functions that depend only on the difference between x and x_1, which corresponds to a homogeneous medium:

$$F(x_1 \longrightarrow x, s) = F(x - x_1, s). \tag{75}$$

Assuming that the variable x takes on continuous values, we can generalize Eq. (73) to a sort of Smoluchowski–Chapman–Kolmogorov equation (52) with memory effects:

$$\frac{\partial}{\partial t}P(x, t) = \int_{-\infty}^{\infty} dx_1 \int_0^t d\tau P(x_1, \tau)F(x - x_1, t-\tau) + Q, \tag{76}$$

where Q is expressed in terms of Laplace transforms as follows:

$$\tilde{Q}(x, s) = P(x, 0) - \tilde{P}(x, s)\tilde{F}(x - x_1, s). \tag{77}$$

The assumption that the memory function is of a multiplicative nature yields

$$F(x-x_1, t-\tau) = G(x-x_1)M(t-\tau). \quad (78)$$

Switching now to Fourier transforms in x and Laplace transforms in t, we arrive at the following equation for the particle density [see relationship (70)]:

$$s\tilde{\tilde{n}}(k, s) - \tilde{n}(k, 0) = -\frac{s\tilde{\Psi}(s)}{1-\tilde{\Psi}(s)}[1-\tilde{G}(k)]\tilde{\tilde{n}}(k, s). \quad (79)$$

It is easy to draw an analogy between this equation and Eq. (53). Obviously, under the conditions

$$M(t) \propto \delta(t), \quad \tilde{M}(s) = \text{const}, \quad (80)$$

the Montroll–Weiss equation is transformed into the Smoluchowski–Chapman–Kolmogorov equation. In fact, choosing the Poisson distribution (64) for the function $\Phi(t)$ ensures the required limiting transition for an equation with memory effects.

In [42–44], telegraph equation (23) was derived for the exponential memory function $M(t) = \exp(-\alpha t)$ and for a Gaussian memory function with $1 - \tilde{G}(k) = -Dk^2$. It is interesting to note that, although the equation considered above and the memory function $M(t)$ both have simple form, the expression for $\Phi(t)$ is fairly complicated in structure [43, 44].

Hence, we see that it is necessary to choose different test functions for different physical situations. In some cases, the choice is conveniently based on the probability functions $\Phi(t)$ and $\Psi(t)$ and, in other cases, it would be worthwhile to choose the memory function $M(t)$.

11. FRACTIONAL DERIVATIVES IN AN EQUATION WITH MEMORY

An important physical quantity in the description of random walk processes with memory is the mean waiting time $\langle t \rangle$ until an event occurs:

$$\langle t \rangle = \int_0^\infty t\Psi(t)dt.$$

This time is an analogue of the mean length of the jump in the theory of Markovian processes. This is not surprising because, in the approach based on memory effects, the transition probability density $\Phi(t)$ is an analogue of the function $W(\Delta)$. For Poisson distribution (64), we have $\langle t \rangle = \tau$.

An important particular case of relaxation functions is represented by those that decrease according to the power law

$$\Phi(t) \propto \frac{1}{(\alpha t)^\gamma}, \quad 0 < \gamma < 1. \quad (81)$$

In this case, the mean waiting time until an event occurs tends to infinity,

$$\langle t \rangle = \int_0^\infty t\Psi(t)dt \longrightarrow \infty. \quad (82)$$

Relaxation functions (81) were found to provide an efficient tool for the analysis of transport processes [43, 44]. For long times t, simple manipulations yield the following expression for $\tilde{M}(s)$:

$$\tilde{M}(s) = \frac{s\tilde{\Phi}(s)}{1-s\tilde{\Phi}(s)} \approx s\Phi(s) = \Gamma(1-\gamma)s^\gamma, \quad (83)$$

where $\Gamma(z)$ is Euler's gamma function. The equation describing memory effects takes the form

$$s\tilde{\Phi}(s)\tilde{\tilde{n}}(k, s) = [1-\tilde{G}(k)]\tilde{\tilde{n}}(k, s) + \tilde{n}(k, 0)\tilde{\Phi}(s). \quad (84)$$

The expression $s\tilde{\Phi}(s)\tilde{\tilde{n}}(k, s) \approx s^\gamma\tilde{\tilde{n}}(k, s)$ can be interpreted as a time derivative of order γ [17]:

$$s\tilde{\Phi}(s)\tilde{\tilde{n}}(k, s) \approx s^\gamma\tilde{\tilde{n}}(k, s) \longrightarrow \frac{\partial^\gamma\tilde{n}(k, t)}{\partial t^\gamma} = \frac{\partial}{\partial t}\int_0^t \frac{\tilde{n}(k, \tau)}{(t-\tau)^\gamma}d\tau. \quad (85)$$

Representing the results in such a manner facilitates interpretation of the scaling relations of the form $R(t) \propto t^{\frac{\gamma}{\alpha}}$, which have found increasingly wider application in the analysis of fractional derivatives

$$\frac{\partial^\gamma n(x, t)}{\partial t^\gamma} = \frac{\partial^\alpha n}{\partial x^\alpha} + F(x, t).$$

The problem of solving equations with fractional derivatives was recently examined in detail in [17, 45], in which the question about the existence of self-similar solutions was also discussed.

To conclude this section, we introduce one more quantity that is often used in the literature to characterize the anomalous nature of transport. Specifically, we define the Herst power index H by the relationship

$$R(t) \propto t^H.$$

For Levy–Khintchine distributions, the Herst power index is equal to $H = \frac{1}{\alpha}$, and, for the telegraph equation, it is equal to $H = 1$.

12. SCALINGS FOR DIFFUSION IN A MEDIUM WITH TRAPS

On the basis of the well-known paper by Balagurov and Vaks [46], we will analyze a particular physical model of diffusion in a medium with traps. Using theoretical probabilistic estimates, we can derive scaling

relations, which can conveniently be interpreted on the basis of relaxation functions. On long time scales, the diffusion of particles in a medium with traps is governed by the fluctuating character of the appearance and disappearance of regions free of traps. We introduce the trapping probability (i.e., the probability for a particle to be captured into a trap) in terms of the Poisson distribution:

$$P_c \propto \exp\left(-\frac{t}{\tau_D}\right). \tag{86}$$

Here, $\tau_D \approx \frac{R^2}{D}$ is the characteristic time scale on which a particle diffuses through a medium until it reaches the boundary of a trap-free region of radius R and D is the local diffusion coefficient. We assume that trap-free regions obeys the Poisson distribution,

$$P_T \propto \exp\left[-\left(\frac{R}{R_0}\right)^d\right], \tag{87}$$

where R_0 is the mean radius of the trap-free regions in a space of dimension d. Now, we can estimate how the radius $R(t)$ of the trap-free region should change in time in order for the survival probability to be the highest:

$$P = P_c P_T \propto \exp\left[-\left(\frac{R}{R_0}\right)^d\right]\exp\left(-\frac{t}{\tau_D}\right). \tag{88}$$

Calculating the time derivative of the argument of the first of the exponential functions in this estimate, we obtain

$$R(t) \propto t^{\frac{1}{2+d}}. \tag{89}$$

For $d > 0$, the diffusion described by this scaling is obviously slower than that described by the classical diffusion scaling

$$R^2(t) \propto t^{\frac{2}{2+d}} \ll t. \tag{90}$$

In the language of fractional derivatives, this indicates that Eq. (84) with a fractional derivative with respect to time can serve as a model equation for describing diffusion in the situation at hand:

$$\frac{\partial^\gamma \tilde{n}(k,t)}{\partial t^\gamma} = \frac{\partial}{\partial t}\int_0^t \frac{\tilde{n}(k,\tau)}{(t-\tau)^\gamma}d\tau, \quad \gamma = \frac{2}{2+d}. \tag{91}$$

Note that the problem about diffusion in a medium with traps is not necessarily related to such issues as condensed states or chemical reactions. The ideas associated with traps are also used in the study of particle trapping by vortices in order to describe the behavior of a passive scalar in a turbulent field [47–50] or in the analysis of the correlation functions of a turbulent field. In what follows, we will consider the problem in which traps in a medium manifest themselves in particle diffusion in a magnetic field with "braided" force lines.

13. KOHLRAUSCH FUNCTION AND LEVY DISTRIBUTION

In the previous section, we considered the model describing slowed particle diffusion. In this model, the estimate of the probability for a particle to survive yields

$$\Phi(t) \propto \exp\left(-t^{\frac{d}{d+2}}\right). \tag{92}$$

For $d = 2$, this formula is the familiar Kohlrausch relaxation law [see formula (65)]. Of particular interest is the fact that the Kohlrausch slowed relaxation law is related to the Laplace transformation of the familiar Levy's law for jumps with the power index $\alpha = 1/2$:

$$\exp(-\sqrt{ws}) = \int_0^\infty \exp(-sx) f_\alpha(x)dx,$$
$$f_\alpha(x) = \frac{1}{2x^{3/2}}\sqrt{\frac{w}{\pi}}\exp\left(-\frac{w}{4x}\right). \tag{93}$$

This simple formula clearly shows a close relationship between the memory and nonlocality effects. Physically, this relationship is not surprising. A particle that stays in a trap in phase space is not involved in events (does not undergo collisions). However, in conventional coordinate space, such a collisionless particle is transported over a large distance during the time it stays within the trap. In this sense, collisionless particles cannot be regarded as being involved in a conventional diffusion process, in contrast to the particles that undergo collisions.

The physical meaning of formal relationship (93) can easily be understood by treating its integral part as an averaging procedure for the Poisson law:

$$\exp(-sx) = \exp(-x/x_0).$$

As an example, let us consider the case $x = V$ and $s = 1/V_0 \approx t/L$, where V is the particle's velocity and L is the size of the region over which the averaging is performed. In this case, we have

$$\exp\left(-\sqrt{\frac{w}{L}}t\right) = \int_0^\infty \exp\left(-\frac{Vt}{L}\right) f(V)dV. \tag{94}$$

As a result, we see that the Kohlrausch relaxation law describes Poisson's probability for a particle not to undergo collision in a region of size L during the time t, averaged by means of a Levy distribution with $\alpha = 1/2$:

$$f_{1/2}(V) \propto \frac{1}{V^{3/2}}\exp\left(-\frac{w}{4V}\right). \tag{95}$$

It should be noted in this context that ideas concerning the use of fractional derivatives are now being actively developed by theoreticians [39, 40]. For strongly nonequilibrium systems in which an important role is played by accelerating and trapping mechanisms, it is clearly necessary to take nondiffusion effects into account in describing the processes in phase space.

14. RETURNS AND SELF-INTERSECTIONS IN DIFFUSION PROBLEMS

In the previous sections, we have often used ideas about the transition probability density that reflect the essential features of the problem of random-walk processes. We have also touched on some questions concerning the relationship between the diffusion coefficient and correlations. Now, we analyze the effect underlying the notion of correlations—return of a randomly moving particle to the initial point. This is best illustrated by considering the problem of one-dimensional random walks at the very beginning of the process. In the problem as formulated, the particle can definitely return to its initial position, thereby providing a clear realistic interpretation of the abstract notion of correlations. Rigorous analysis of returns on complicated spatial grids is necessarily based on the chain equation for the return probability $P_0(t)$. Recall that most of the fundamental problems in the theory of random-walk processes can be formulated in terms of chain equations. However, we restrict ourselves here to estimating the effects of returns.

Simple estimates for these effects can be obtained from the Poisson solution to the equation for the probability density function describing the random walks of a particle. For a space of dimension d, we obtain

$$\rho(x, t) = \frac{1}{(4\pi Dt)^{d/2}}\exp\left(-\frac{x^2}{4Dt}\right), \tag{96}$$

in which case the probability for a particle to return to the point $x = 0$ at the time t has the form

$$P_0(t) \propto \frac{(\delta x)^d}{(4\pi Dt)^{d/2}}. \tag{97}$$

Generally, this simple (although rather efficient) formula, serves merely to obtain estimates [51, 52]. It has the same drawbacks as the simple diffusion model, namely, those associated with the infinite propagation velocity of perturbations and the presence of a δ-shaped particle-source term. The problem can be solved completely by using the chain equation for the probability $P_0(N)$ for a particle to return to the initial point after N random walks. For our purposes, this solution is important because it provides evidence that the dimension of the space, d, which was used above as a formal parameter, plays a more significant role. It turns out [45] that, for grids of dimension $d \le 2$, the particle will inevitably return to its initial position; i.e., the return probability is $P_0(N) = 1$. For grids with $d > 2$, the particle can execute random walks without returning. To be specific, for $d = 3$, we have $P_0(N) \approx 1/3$. We thus see that the case $d = 2$ is intermediate and, as such, attracts much attention among mathematicians.

Along with the return probability P_0, use is made of the number of returns and the number of visited grid points. Usually, the task is to express these numbers as certain scalings and to establish their relationships to other scalings [52].

Using the notion of return, we derive an important scaling relation for particles executing random motion with no self-intersections. We introduce the probability $p(N)$ of self-intersection after N random walks,

$$p(N) \approx \frac{N}{R^d}, \tag{98}$$

where $R^2(N)$ is the root-mean-square displacement, d is the dimension of the space, and $N = t/\tau$ is the number of random walks. In fact, we are assuming that the probability for the particle trajectory to intersect itself is proportional to the number density of visited grid points within the region of random particle motion. The probability for a particle to execute N non-self-intersecting random walks can then be estimated as

$$P_s(N) \approx (1-p)^N\big|_{N\to\infty} \approx \exp(-pN) \approx \exp\left(-\frac{N^2}{R^d}\right). \tag{99}$$

Taking into account the fact that the relationship between the quantities R and N is of a diffusive nature, we can estimate the effective probability of non-self-intersecting random walks by averaging the probability $P_s(N)$:

$$P_F(t) = \int_{-\infty}^{\infty}\exp\left[-\frac{1}{R^d}\left(\frac{t}{\tau}\right)^2\right]\frac{1}{(4\pi Dt)^{d/2}} \times \exp\left(-\frac{R^2}{4Dt}\right)(dR)^d. \tag{100}$$

We assume that the main contribution to the integral comes from the extremum of the integrand,

$$\min\left[\frac{1}{R^d}\left(\frac{t}{\tau}\right)^2 + \frac{R^2}{4Dt}\right], \tag{101}$$

and perform simple manipulations to obtain

$$R_{FL}(t) \propto t^{\frac{3}{2+d}} \gg t^{\frac{1}{2}} \tag{102}$$

for $d \le 3$. Here, we must take into account the fact that, in a space of dimension $d = 1$, non-self-intersecting random walks can occur only for the particles moving in one direction, which indicates that $R \propto t$. We see that estimate (102) satisfies this condition automatically.

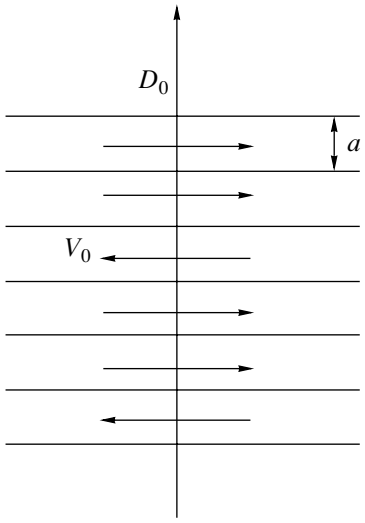

Fig. 1. Dreĭzin–Dykhne model for anisotropic superdiffusion: D_0 is the seed diffusion coefficient, V_0 is the velocity of the transverse pulsations, and a is the transverse dimension of pulsations.

This scaling, which was first obtained in the theory of polymers by Flory [53–55], is very important in describing the properties of turbulent flows. One of the most interesting lines of research on the subject involves analysis of the stochastic properties of an ensemble of vortices. The vortex lines can be considered as self-intersecting trajectories from the model of random-walk processes. We can take into account the contribution of vortex lines to the energy spectrum by using the following scaling, which was derived in the so-called β-model—a fractal model of isotropic turbulence [56]:

$$E(k) \propto k^{-\frac{5}{3}} k^{-\frac{d-d_F}{3}}. \quad (103)$$

Here, the correcting factor for the Kolmogorov–Obukhov spectrum is related to the fractal dimension d_F of the space of random walks of a vortex line. For scaling (102), we have

$$d_F = \frac{2+d}{3},$$

because, by definitions in fractal geometry, the fractal dimension for random walks is determined by the formula $N \propto t/\tau \propto R^{d_F}$. As a result, we arrive at the following estimate for the energy spectrum:

$$E(k) \propto \frac{1}{k^{11/9}} \leq \frac{1}{k}.$$

Turbulence spectra of roughly the same form were analyzed as early as 1950s in the context of the ideas about dissipation spots in a turbulent fluid [14] and interest in them has persisted to the present day [56–62].

15. RETURNS AND SUPERDIFFUSION

In a report on probabilistic problems suggested by turbulence [63], Corrsin formulated several challenging problems. One of them is the problem of how to take returns of the particles diffusing in a turbulent flow into account [52]. At approximately the same time, Dreĭzin and Dykhne published their paper [64], in which they proposed and analyzed a physically clear model for the behavior of a particle that is subject to strongly anisotropic diffusion. Let us consider this model in order to illustrate the efficiency of an approach based on the ideas of returns.

We choose a longitudinal direction (e.g., the direction of the magnetic field) and assume that the particles are subject to a seed longitudinal diffusion with the coefficient D_0. In the transverse direction, diffusing particles are subject to random pulsations generating narrow convective flows with the velocity V_0 and width a (see Fig. 1). Dreĭzin and Dykhne proposed a simple model formula for calculating the transverse diffusion coefficient $D_\perp$:

$$D_\perp \approx \frac{\lambda_\perp^2}{t}, \quad (104)$$

where $\lambda_\perp \approx V_0 t P$. Here, $P = \delta N/N$ is the fraction of uncompensated pulsations, and $N \approx \sqrt{D_0 t}/a$ is the number of flows (each of width a) the particle has crossed. Using Gaussian statistical methods, the authors of [64, 65] obtained the estimate $\delta N \approx \sqrt{N}$ and, as a consequence,

$$D_\perp \approx V_0^2 a \sqrt{\frac{t}{D_0}}. \quad (105)$$

In fact, estimate (105) refers to a superdiffusion regime:

$$\lambda_\perp^2 \approx \frac{V_0^2 a}{\sqrt{D_0}} t^{3/2} \gg t. \quad (106)$$

In order to explain this result, Dreĭzin and Dykhne considered the Euler correlation function

$$C(t_1, t_2) = \int_{-\infty}^{\infty} \langle v(0) v(z) \rangle \Phi(z, t_2 - t_1) dz, \quad (107)$$

where

$$\Phi = \frac{1}{[4\pi D_0 (t_2 - t_1)]^{1/2}} \exp\left[-\frac{z^2}{4D_0(t_2 - t_1)}\right]. \quad (108)$$

This representation agrees exactly with Corrsin's idea about the diffusive nature of correlations [30].

However, the most widely held hypothesis in the description of the anomalous nature of diffusion is that about the significant role of returns [52] in the diffusion model at hand. As a case in point, consider the limit $z \longrightarrow 0$, in which

$$C(t_1, t_2) = C(\tau) \approx \frac{V_0^2 a}{\sqrt{4\pi D_0 \tau}}. \quad (109)$$

We now perform all the necessary manipulations and arrive at result (59):

$$\langle \lambda_\perp^2 \rangle \approx \frac{V_0^2 a}{\sqrt{4\pi D_0}} \int_0^t \int_0^t \frac{dt_1 dt_2}{\sqrt{t_1 - t_2}} \approx \frac{V_0^2 a}{\sqrt{4\pi D_0}} t^{3/2}. \quad (110)$$

The above analysis and calculations permit us to see that the nature of superdiffusion in the Dreĭzin–Dykhne model [64, 65] is associated with the important role of returns, which give rise to correlations between the motions of a diffusing particle in different directions.

Taking into account the results of the above analysis, we can single out the effects of returns:

$$\lambda_\perp^2 \approx \lambda_0^2 N(t), \quad (111)$$

where λ_0 is the displacement of a particle in one flow (see Fig. 1) and $N(t) \approx \sqrt{D_0 t}/a$ is the number of visited flows. With allowance for the number N_B of returns to a given flow, the displacement λ_0 is estimated as $\lambda_0 \approx V_0 \tau_0 N_B(t)$. Finally, setting $\tau_0 \approx \frac{a^2}{2D_0}$ and $N_B(\tau) \approx \frac{\sqrt{4\pi D_0 \tau}}{a}$, we arrive at estimate (110).

At this point, it is expedient to make the following remark about the results obtained in [64]. A closer look at formula (62) shows that it explicitly contains the number of returns for a particle executing random walks along a straight line:

$$N_B(\tau) \approx \frac{\sqrt{D_0 \tau}}{a}. \quad (112)$$

This allows us to try to generalize Dreĭzin and Dykhne's model (109) to a more general topology of flows in a space of dimension $d > 1$:

$$C(\tau) \approx \frac{V_0^2}{N_B(\tau)}. \quad (113)$$

Simple manipulations with this formula make it possible to derive other scalings describing superdiffusion. Thus, for $d \geq 2$, the well-known estimate $N_B \propto t^{2/3}$ [51–55] yields the scaling $x \propto t^{2/3}$, which agrees well with the so-called self-organized criticality model, proposed for describing anomalous transport in plasmas [66–68].

16. SUPERDIFFUSION AND CORRELATIONS

The Dreĭzin–Dykhne model considered in the previous section can be described in terms of the diffusion equation with memory. Applying the ideas of the quasilinear theory, Chukbar [65] averaged the equations describing pulsating flows in the Dreĭzin–Dykhne model in plane geometry:

$$\frac{\partial n}{\partial t} + \mathbf{v}\nabla n = D_0 \Delta n, \quad (114)$$

where D_0 is the seed diffusion coefficient. The set of equations obtained in [65],

$$\frac{\partial n_0}{\partial t} = -\left\langle v_X \frac{\partial n_1}{\partial x} \right\rangle, \quad (115)$$

$$\frac{\partial n_1}{\partial t} = D_0 \frac{\partial^2 n_1}{\partial z^2} - v_X \frac{\partial n_0}{\partial x}, \quad (116)$$

is somewhat analogous to the set of Kadomtsev–Pogutse renormalized equations (37). In fact, in comparison with conventional hyperbolic equation (5), the equation for perturbations contains the diffusive correction term, which has a clear physical meaning. According to the analysis carried out by Dreĭzin and Dykhne, this term describes the diffusive nature of returns, governing the diffusive behavior of the particles. Since the returns occur along the z direction, the diffusive term has the form $D_0 \frac{\partial^2 n_1}{\partial z^2}$.

Applying the Laplace transformation in the time t and the Fourier transformation in the spatial coordinate z, we obtain

$$s\tilde{n}_0(s, x) - n_0(x, 0) = \tilde{D}(s) \frac{\partial^2 \tilde{n}_0}{\partial x^2}. \quad (117)$$

$$\tilde{D}(s) = \lim_{L \to \infty} \frac{1}{2L} \int_{-L}^{L} dz \times \int_{-\infty}^{\infty} dz' \left\{ \frac{\exp[-\sqrt{s/D_0}|z - z'|]}{\sqrt{D_0 s}} v_X(z) v_X(z') \right\}, \quad (118)$$

where the integral is calculated under the condition $z \longrightarrow z'$. We thus arrive at the following equation, which contains fractional derivatives of order $\gamma = 3/2$ and describes the Dreĭzin–Dykhne model:

$$\frac{\partial^2}{\partial t^2} \int_0^t \frac{n_0(t', x)}{\sqrt{\pi(t - t')}} - \frac{V_0^2 a}{\sqrt{2D_0}} \frac{\partial^2 n_0(t, x)}{\partial x^2} = -\frac{n_0(0, x)}{2\sqrt{\pi} t^{3/2}}. \quad (119)$$

The solution to this equation and its self-similar behavior were analyzed in detail in [65]. Note, however, that Eq. (119) does not contain the term accounting for lon-

gitudinal diffusion. In the notation of Chukbar [65], this term should have a nonphysical form, $D_0\frac{\partial^3 n_0}{\partial z^3}$.

It should also be noted that the superdiffusion effect, which is based on the effects of returns, occurs only on spatial scales no longer than the longitudinal correlation length a. This restriction, which was discussed already by Dreĭzin and Dykhne [64] and, later, by Chukbar [65] in analyzing quasi-diffusion in striplike flows, has the form

$$\lambda_\perp^2 \approx \frac{V_0^2 a}{\sqrt{D_0}}\tau_C^{3/2} = a^2, \quad \tau_C \approx \left(\frac{D_0 a^2}{V_0^4}\right)^{\frac{1}{3}}.$$

For time scales $t > \tau_C$, we deal with conventional diffusion, $D_\perp \propto \frac{a^2}{2\tau_C}$.

17. COMPOUND DIFFUSION AND RIPPLED STRUCTURES

One of the first simple scalings in the anisotropic diffusion model has the form [69, 70]

$$R(t) \propto t^{\frac{1}{4}} \ll t^{\frac{1}{2}}. \quad (120)$$

This scaling, which is of the nature of a subdiffusion, was derived based on the following estimate for the magnetic diffusion coefficient D_m:

$$D_m \approx \frac{\Delta_\perp^2}{L_\parallel}, \quad (121)$$

where $\Delta_\perp$ is the transverse displacement of a magnetic field line in moving along a magnetic field with the spatial scale $L_\parallel$. If we assume that the longitudinal motion is also diffusive in nature (the diffusion coefficient being D_0), then, using scaling (120), we obtain

$$\Delta_\perp^2 \approx D_m L_\parallel \approx D_m\sqrt{D_0 t}. \quad (122)$$

The subdiffusion can be avoided by assuming that the motion along the magnetic field is ballistic, $L_\parallel \approx Vt$. In their well-known paper [31], Kadomtsev and Pogutse considered precisely this kind of diffusion in a braided magnetic field. Another way of passing over to the conventional diffusion was proposed by Zybin and Istomin [71], who set $L_\parallel \approx V_0 t$, where V_0 is a certain propagation velocity of perturbations along the field. In such a formulation of the problem, the longitudinal diffusion can be considered using telegraph equation (23), which describes diffusion, $R \propto t$, in the case of perturbations propagating with a finite velocity.

The most efficient mechanism for destroying compound diffusion is associated with the exponential divergence of the neighboring lines of a stochastic magnetic field. This effect was first considered in the abovecited papers by Rechester and Rosenbluth [33, 34]. It is worth noting that the nonstatic nature of a stochastic magnetic field also has a destructive effect on compound diffusion.

Compound diffusion can be examined more carefully. Recall that Dreĭzin and Dykhne's idea about the renormalization of the transverse displacement, $V_0 t \longrightarrow V_0 t\frac{\delta N}{N}$, implies that the returns should be taken into account when considering random walks in the longitudinal direction. Using an analogous approach, we can clarify the physical meaning of the subdiffusive nature of compound diffusion [17]. According to elementary estimates (122), the particle is subject to transverse diffusion for a time shorter than the total diffusion time t. In modern terminology, this is referred to as diffusion in a medium with traps [42–45]. Such situations are described by introducing the notion of the probability $\Phi(\tau)$ of staying in a trap for a time τ. If the probability $\Phi(\tau)$ is represented in the form of scaling,

$$\Phi(\tau) \propto \frac{1}{\tau^\gamma}, \quad (123)$$

then, for $\gamma < 1$, the time interval during which the particle is actually involved in the diffusion process is of the nature of a fractal of dimension $d_F = \gamma$. In fact, we can use Dreĭzin and Dykhne's model and take into account specific relationships from [69, 70] to obtain

$$\Delta_\perp^2 \approx D_\perp t\frac{\delta N}{N}, \quad \text{where} \quad \delta N \propto \left(\frac{t}{\tau_\parallel}\right)^{d_F}, \quad N \propto \frac{t}{\tau_\parallel}, \quad (124)$$

$\tau_\parallel$ is the longitudinal correlation time, and $D_\perp$ is the transverse diffusion coefficient. Then, after substitution, we arrive at

$$\Delta_\perp^2 \approx \frac{D_\perp}{\tau_\parallel^{d_F-1}} t^{d_F}. \quad (125)$$

Turning to the above notation $D_\perp \approx D_m\frac{L_\parallel}{\tau_\perp}$ and $D_0 \approx \frac{L_\parallel^2}{\tau_\parallel}$ and performing all the necessary manipulations, we get

$$\Delta_\perp^2 \approx D_m\frac{\sqrt{D_0\tau_\parallel^3}}{\tau_\perp}\left(\frac{t}{\tau_\parallel}\right)^{d_F}. \quad (126)$$

In the case of compound diffusion, we have $\gamma = d_F = 1/2$, which yields expression (122). The cases in which $d_F = d/2$ are frequently encountered in studies on the subject. Thus, in the percolation models of turbulent diffusion [16], the relative amount of the percolative current lines is estimated in a similar way:

$$\frac{\delta S(a)}{S(a)} \approx \frac{a^{d_F}}{a^2} \approx \frac{1}{a}, \quad d_F = d/2 = 1. \quad (127)$$

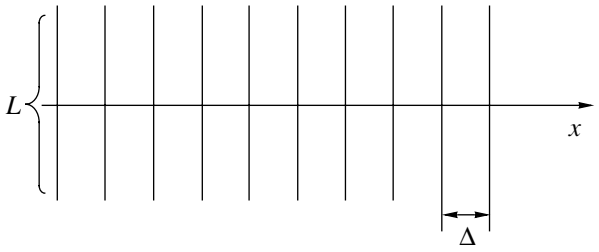

Fig. 2. Rippled structure: L is the length of a ripple and Δ is the distance between the ripples.

The diffusion equation corresponding to a particular fractional value of γ [see relationship (123)] has the form of Eq. (91) with fractional derivatives. Consequently, using the definition of the Herst power index H, we obtain

$$R(t) \propto t^H, \quad H = \gamma/2. \tag{128}$$

The above assumptions concerning the quantity $\Phi(t)$ enable us to use the diffusion approximation for the trap effects:

$$\Phi(\tau) \approx \frac{\sqrt{D_0\tau}}{a}. \tag{129}$$

In fact, we associate the probability for a particle to stay in a trap with the return probability used in the Dreĭzin–Dykhne model. A trap can be regarded as an individual ripple in a rippled structure (see Fig. 2). In the limit in which the length of the ripples approaches infinity, relationship (129) for the function $\Phi(t)$ is quite adequate. The rippled structure model can naturally be generalized to models with ripples of finite length and ripples in the form of fractals.

18. CONCLUSIONS

The significant deviation of transport processes from classical transport necessitates a search for new types of equations. From theoretical probabilistic analysis, it is evident that, in random-walk models, the nonlocality and memory effects can be taken into account by modifying diffusion equations. However, these models should be continuously improved because of the ever-growing number of experimental scalings. Intense development of the theory of renormalizations [14] and correlation-related ideas [62, 68], as well as investigations on Levy distributions [72–75], offer greatly expanded opportunities for future theoretical research on the subject.

ACKNOWLEDGMENTS

I am grateful to V.D. Shafranov, É.I. Yurchenko, and V.I. Ilgisonis for their help and for many useful discussions.

REFERENCES

1. *Brounian Motion*, Ed. by B. I. Davydov (ONTI, Moscow, 1936).
2. N. G. van Kampen, *Stochastic Processes in Physics and Chemistry* (North-Holland, Amsterdam, 1984).
3. Ya. B. Zel'dovich and A. D. Myshkis, *Principles of Mathematical Physics* (Nauka, Moscow, 1973).
4. S. Chandrasekhar, Rev. Mod. Phys. **15** (1), 1 (1943).
5. P. Resibois and M. De Leener, *Classical Kinetic Theory* (Wiley, New York, 1977).
6. A. M. Yaglom, *Correlation Theory of Time-Independent Random Functions* (Gosmeteoizdat, Leningrad, 1981).
7. L. F. Richardson, Proc. R. Soc. London, Ser. A **110**, 709 (1926).
8. B. I. Davydov, Dokl. Akad. Nauk SSSR **2**, 474 (1934).
9. A. S. Monin, Dokl. Akad. Nauk SSSR **105**, 256 (1955).
10. A. A. Vedenov, E. P. Velikhov, and R. Z. Sagdeev, Nucl. Fusion Suppl. **2**, 82 (1962).
11. W. E. Drummond and D. Pines, Nucl. Fusion Suppl. **3**, 1049 (1962).
12. Ya. B. Zel'dovich, S. A. Molchanov, A. A. Ruzmaikin, and D. D. Sokolov, Zh. Éksp. Teor. Fiz. **89**, 2061 (1985) [Sov. Phys. JETP **62**, 1188 (1985)].
13. Ya. B. Zel'dovich, S. A. Molchanov, A. A. Ruzmaikin, and D. D. Sokolov, Usp. Fiz. Nauk **152**, 3 (1987) [Sov. Phys. Usp. **30**, 353 (1987)].
14. A. S. Monin and A. M. Yaglom, *Statistical Fluid Mechanics* (Nauka, Moscow, 1965; MIT Press, Cambridge, MA, 1971, 1975), Vols. 1, 2.
15. *Basic Plasma Physics*, Ed. by A. A. Galeev and R. N. Sudan (Énergoatomizdat, Moscow, 1983, 1984; North-Holland, Amsterdam, 1983, 1984), Vols. 1, 2.
16. M. B. Isichenko, Rev. Mod. Phys. **64**, 961 (1992).
17. K. V. Chukbar, Zh. Éksp. Teor. Fiz. **108**, 1875 (1995) [JETP **81**, 1025 (1995)].
18. G. Falkovich, K. Gawedzki, and M. Vergassola, Rev. Mod. Phys. **73**, 913 (2001).
19. A. J. Majda and P. R. Kramer, Phys. Rep. **314**, 237 (1999).
20. B. B. Kadomtsev, *Collective Phenomena in Plasma* (Nauka, Moscow, 1976).
21. A. S. Kingsep, *Introduction to the Nonlinear Plasma Physics* (Mosk. Fiz.-Tekh. Inst., Moscow, 1996).
22. V. N. Tsytovich, *Theory of Turbulent Plasma* (Atomizdat, Moscow, 1971; Plenum Press, New York, 1974).
23. C. Cattaneo, Atti Semin. Mat. Fis. Univ. Modena **3**, 83 (1948–1949).
24. S. Goldstein and J. Quart, Mech. Appl. Mat. **4** (4), 129 (1951).
25. R. W. Davies, Phys. Rev. **93**, 1169 (1954).
26. A. Tr. Lyapin, Gl. Geofiz. Obs. **19** (81), 175 (1950).
27. H. T. Dupree, Phys. Fluids **9**, 1773 (1966).
28. T. H. Dupree, Phys. Fluids **10**, 1049 (1967).
29. T. H. Dupree, Phys. Fluids **15**, 334 (1972).
30. S. Corrsin, *Atmospheric Diffusion and Air Pollution*, Ed. by F. N. Frenkiel (Academic, New York, 1959).
31. B. B. Kadomtsev and O. P. Pogutse, in *Proceedings of the 7th IAEA International Conference on Plasma Phys-*

ics and Controlled Nuclear Fusion Research, Vienna, 1978, Vol. 1, p. 649.
32. I. Howells, J. Fluid Mech. **9**, 104 (1960).
33. A. B. Rechester and M. N. Rosenbluth, Phys. Rev. Lett. **40**, 38 (1978).
34. A. B. Rechester, M. N. Rosenbluth, and R. B. White, Phys. Rev. Lett. **42**, 1247 (1979).
35. A. N. Kolmogorov, Math. Ann. **104**, 415 (1931).
36. A. Ya. Khintchine and P. Levy, Compt. Rend. **202**, 274 (1936).
37. A. S. Bakai, *Moderate Turbulence* (Nauka, Moscow, 1996).
38. S. A. Reshetnyak and L. A. Shelepin, *Quasi-Steady Distributions in Kinetics* (IPO Avtor, Moscow, 1996).
39. G. M. Zaslavsky, Chaos **4** (1), 111 (1994).
40. A. V. Chechkin and V. Yu. Gonchar, Zh. Éksp. Teor. Fiz. **118**, 730 (2000) [JETP **91**, 635 (2000)].
41. A. A. Vlasov, *Statistical Distribution Functions* (Nauka, Moscow, 1966).
42. E. Montroll and G. Weiss, J. Math. Phys. **6**, 178 (1965).
43. E. Montroll and H. Scher, Phys. Rev., Ser. B **12**, 2455 (1975).
44. R. Metzler and J. Klafter, Phys. Rep. **339**, 1 (2000).
45. J. W. Haus and K. W. Kehr, Phys. Rep. **150**, 263 (1987).
46. B. Ya. Balagurov and V. G. Vaks, Zh. Éksp. Teor. Fiz. **65**, 1939 (1973) [Sov. Phys. JETP **38**, 968 (1974)].
47. R. H. Kraichnan, Phys. Fluids **13**, 22 (1970).
48. V. E. Kravtsov, I. V. Lerner, and V. I. Yudson, Zh. Éksp. Teor. Fiz. **91**, 569 (1986) [Sov. Phys. JETP **64**, 336 (1986)].
49. M. Vlad, F. Spineanu, J. H. Misguich, and R. Balescu, Phys. Rev. E **58**, 7359 (1998).
50. M. Vlad, F. Spineanu, J. H. Misguich, and R. Balescu, Phys. Rev. E **63**, 066304 (2001).
51. J. Feder, *Fractals* (Plenum, New York, 1988).
52. I. I. Sokolov, Usp. Fiz. Nauk **150**, 221 (1986) [Sov. Phys. Usp. **29**, 924 (1986)].
53. J. M. Ziman, *Models of Disorder: The Theoretical Physics of Homogeneously Disordered Systems* (Cambridge Univ. Press, London, 1979).
54. D. Stauffer, Phys. Rep. **2**, 3 (1979).
55. D. Stauffer, *Introduction to Percolation Theory* (Taylor and Francis, London, 1985).
56. U. Frisch, *Turbulence: The Legacy of A. N. Kolmogorov* (Cambridge Univ. Press, Cambridge, 1995).
57. S. I. Vaĭnshteĭn, *Magnetic Fields in Space* (Nauka, Moscow, 1983).
58. B. B. Mandelbrot, J. Fluid Mech. **72**, 401 (1975).
59. B. B. Mandelbrot, *Fractals: Form, Chance, and Dimension* (Freemen, San Francisco, 1977).
60. H. K. Moffatt, J. Fluid Mech. **106**, 27 (1981).
61. H. K. Moffatt, Rep. Prog. Phys. **621**, 3 (1983).
62. V. I. Klyatskin, *Stochastic Equations by the Physicist's Eyes* (Fizmatlit, Moscow, 2001).
63. S. Corrsin, *Random Geometric Problems Suggested by Turbulence* (Johns Hopkins Univ., 1971).
64. Yu. A. Dreĭzin and A. M. Dykhne, Zh. Éksp. Teor. Fiz. **63**, 242 (1972) [Sov. Phys. JETP **36**, 127 (1973)].
65. K. V. Chukbar, Zh. Éksp. Teor. Fiz. **109**, 1335 (1996) [JETP **82**, 719 (1996)].
66. B. A. Carreras, B. Milligen, M. Pedrosa, *et al.*, Phys. Rev. Lett. **80**, 4438 (1998).
67. B. A. Carreras, B. Milligen, R. Balbin, *et al.*, Phys. Rev. Lett. **83**, 3653 (1999).
68. A. J. Krommes and E. M. Ottaviani, Phys. Plasmas **6**, 3731 (1999).
69. G. G. Getmantsev, Astron. Zh. **39**, 607 (1962) [Sov. Astron. **6**, 477 (1962)].
70. T. X. Stix, Nucl. Fusion **18**, 353 (1978).
71. K. P. Zybin and Ya. N. Istomin, Zh. Éksp. Teor. Fiz. **89**, 836 (1985) [Sov. Phys. JETP **62**, 479 (1985)].
72. G. M. Zaslavsky and B. A. Niyazov, Phys. Rep. **283**, 73 (1997).
73. M. F. Shiesinger and G. M. Zaslavsky, *Levy Flights and Related Topics in Physics* (Springer-Verlag, Berlin, 1995).
74. P. Balescu, *Statistical Dynamics* (Imperial College, London, 1997).
75. G. P. Bouchaud and A. Gtorges, Phys. Rep. **195**, 132 (1990).

Translated by O.E. Khadin

Plasma Physics Reports, Vol. 29, No. 11, 2003, pp. 971–977. Translated from Fizika Plazmy, Vol. 29, No. 11, 2003, pp. 1047–1053.

PLASMA DYNAMICS

The Dynamics of and Radiation from a Copper-Wire Corona in a Megaampere Z-Pinch

P. Kubeš*, J. Kravárik*, Yu. L. Bakshaev, P. I. Blinov**, E. M. Gordeev**, S. A. Dan'ko**, D. Klír*, A. V. Korel'skiĭ**, V. D. Korolev**, E. V. Kravchenko**, J. Krása***, E. Krouský***, O. Renner***, G. I. Ustroev**, A. S. Chernenko**, L. Juha***, and A. Yu. Shashkov****

**Czech Technical University, Technicka 2, 166 27 Prague 6, Czech Republic*

***Russian Research Centre Kurchatov Institute, pl. Kurchatova 1, Moscow, 123182 Russia*

****Institute of Physics, Na Slovance 2, 182 21 Prague 8, Czech Republic*

Received April 17, 2003

Abstract—Evolution of the extreme ultraviolet (XUV) and soft X-ray (SXR) emission in the 50- to 2000-eV photon energy range from a plasma corona formed by loading a relatively thick Cu wire (with an initial diameter of 120 μm) was observed in a Z-pinch discharge with a maximum current of 2 MA and current rise time of 100 ns. A diagnostic complex consisting of a five-channel SXR polychromator, a four-frame X-ray pinhole camera, and a mica crystal spectrograph shows that double-humped emission pulses in the XUV and SXR spectral ranges are generated 70–130 ns after the onset of the discharge current. The total energy of the pulses is 5 kJ, and the maximum power is 60 GW. A part of the observed kiloelectronvolt X-ray emission from three to five spots with diameters of 1–2 mm consists of the Cu K- and L-shell lines. © *2003 MAIK "Nauka/Interperiodica".*

1. INTRODUCTION

One of the well-known applications of Z-pinches is the generation of intense X-ray emission. The high intensity and large X-ray yield in a wide spectral range makes Z-pinches unique sources that have various applications in science and technology, including lithography, spectroscopy, and X-ray microscopy. One of the ways of solving the problem of inertial confinement fusion is the use of fast liners generating the radiation needed to ignite a hohlraum-type target, in which a hard X-ray emission is converted into a soft one. At present, a technique that is applied for the generation of relativistic electron beams is widely used in liner-implosion experiments. This technique allows one to carry out experiments at a power level of 10^{13}–10^{14} W [1, 2]. In such experiments, wire arrays made of high-Z materials or annular gas puffs are usually employed. At proper Z-pinch parameters, a plasma with a temperature from a few hundred electronvolts up to 1 keV is produced. The conversion efficiency of the liner kinetic energy into X-ray emission may attain 40–70%, the emission power and the total emission energy being 100 TW and 2 MJ, respectively.

A large number of experiments using the high-current REB generator technique have studied the plasma implosion dynamics. The experiments were carried out at currents of 1 MA that flowed through 10- to 100-μm wires made of high-Z elements ($Z \geq 10$). Interest in those experiments was caused by the fact that the wires turned out to be sources of high-intensity X-ray emission [3–6] in a wide photon energy range. Such sources may be used to produce a plasma with highly-ionized ions that enables one to study X-ray spectra [7, 8]. The high-density plasma corona formed by the wire explosion may be regarded as an active medium for X-ray lasing [9]. An attractive aspect of such investigations is the possibility of obtaining an extreme state of matter due to the high degree of plasma compression after the wire explosion. In those experiments, the plasma parameters in constrictions were almost the same as those obtained in vacuum spark discharges [10]. In addition, the most important features of constriction development—the time instants and positions at which hot spots (HSs) develop [5, 6, 11], the character of the HS motion along the pinch axis [12], the HS fine structure [13], and the spectrum of HS emission [4, 5, 8, 14]—were investigated.

It was shown that, after the wire explosion, a heterogeneous structure is formed that consists of a cold dense core and a hot rarefied corona that contains 3–10% of the wire mass [6] and carries most of the current [15]. An analysis of the experimental data [11] shows that the observed HS generation is related to the compression of the overheated annular structures that form in the corona of the plasma channel. Most of the radiative losses in the ≤1-keV photon energy range are from the hot rarefied corona, whereas the main wire mass is concentrated near the pinch axis and contributes insignificantly to the pinch radiation. In experiments carried out at the Module A5-01 facility [6] at currents of up to

1063-780X/03/2911-0971$24.00

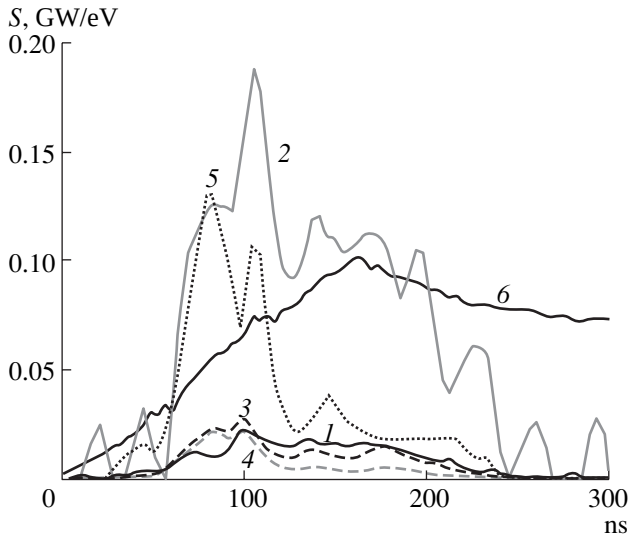

Fig. 1. Waveforms of (*6*) the discharge current and the emission power *S* divided by the bandwidth of the polychromator channel (in eV) for photon energies of (*1*) 60, (*2*) 120, (*3*) 220, (*4*) 340, and (*5*) 600 eV.

500 kA, the soft X-ray (SXR) power attained 10^{11} W and the total SXR energy was 2.5 kJ. Most of the radiation energy was concentrated in the range $E \le 1$ keV, whereas the radiative losses in the range $E > 1$ keV were less than 100 J.

Experiments with megaampere currents revealed new interesting features in the dynamics of the plasma of the exploding wires and in the character of the generation of extreme ultraviolet (XUV) and SXR emission. In [16], the results are presented from XUV diagnostics of the corona formed around a thicker Al wire at the S-300 facility at currents of 2–3 MA. The large wire diameter enables the formation of a wire corona with a higher plasma density. In this case, the wire material at the wire axis remains in a solid state and the plasma evolution occurs primarily in the wire corona. In [9, 17], some interesting features of Z-pinch discharges (such as helical structures, stability and oscillations in the second pinch phase, second pinching, and confinement of the exploding plasma) were interpreted as being associated with the generation of the axial component of the magnetic field. Some important features of the corona evolution are probably, related to the transformation and dissipation of the axial magnetic field. High-energy particles can be accelerated by a strong electric field that is induced due to the fast penetration of the magnetic field into the plasma and its dissipation there. In the experiment performed at the S-300 facility and described in this paper, a relatively thick Cu wire (120 μm in diameter) was used as a load. The corona evolution during the X-ray pulse was investigated using shadowgraphy and X-ray pinhole imaging.

2. EXPERIMENTAL SETUP AND DIAGNOSTIC EQUIPMENT

The high-power pulsed S-300 facility (I = 4 MA, τ = 70 ns), which was designed and built at the RRC Kurchatov Institute, is a convenient tool for performing liner-implosion and wire-explosion experiments with the purpose of developing bright X-ray sources. The current flowing through a wire with a fairly high inductance reaches 2 MA during a rise time of 100 ns. The experiments were performed by loading of a copper wire with a diameter of 120 μm and length of 8 mm.

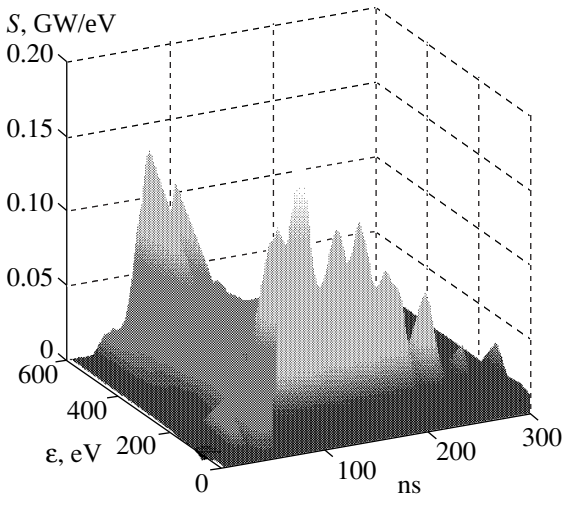

Fig. 2. Emission power *S* divided by the bandwidth of the polychromator channel (in eV) as a function of time and photon energy ε.

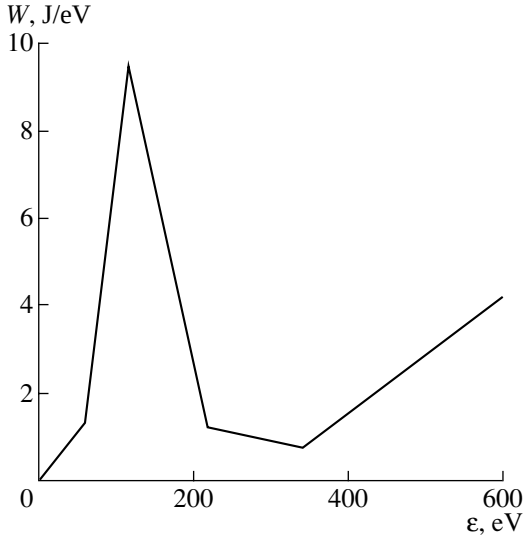

Fig. 3. Emitted energy *W* per 1 eV as a function of the photon energy.

The complex information about the pinch behavior was obtained with the following set of diagnostics arranged in the plane perpendicular to the wire axis:

(i) The temporal evolution of the corona diameter was observed using a visible-light streak camera. The slit of the streak camera was aligned perpendicular to the wire axis, which allowed us to observe the wire region 4-mm distant from the both electrodes. Three frame image converters grabbed plasma images with an exposure time of 3 ns and 10- to 15-ns intervals between the images.

(ii) A microchannel-plate (MCP) detector divided into four frames and providing images with an exposure time of 2 ns and 10-ns intervals between the images was used for SXR photography in the photon energy range higher than 600 eV. 100-μm-diameter pinhole cameras filtered with 10-μm Be foils were used to produce X-ray images at the detector.

(iii) The X-ray spectrum was measured with a convex mica crystal spectrometer with one-dimensional spatial resolution.

(iv) Five-frame shadow imaging with an exposure time of 1 ns and 10-ns intervals between the images was performed using the second harmonic of a neodymium laser ($\lambda = 532$ nm).

(v) The SXR spectrum was measured with a five-channel absolutely calibrated polychromator providing time-resolved measurements of the X-ray intensity in five photon energy ranges with central energies of 60, 120, 220, 340, and 600 eV. X-ray PIN detectors with a time resolution of 1.5–3.0 ns and plane multilayer mirrors were used for the energy separation of photons.

(vi) The dose was measured with filtered thermoluminescent dosimeters.

3. EXPERIMENTAL RESULTS

Experimental results show that the Z-pinch development can differ substantially in different shots. To thoroughly investigate the plasma evolution in each shot, we used a diagnostic facility with a temporal, spatial, and spectral resolution. Figures 1–7 and 9 present a temporally correlated set of plots and images for shot no. 0 204 302.

The results of SXR measurements with the use of a polychromator are presented in Figs. 1–4 and Table 1. Figure 1 shows the waveforms of the discharge current and the spectral power of XUV–SXR emission (the emission power divided by the polychromator channel bandwidth) in five photon energy ranges. The spectral power of XUV–SXR emission as a function of time and photon energy is shown in Fig. 2. The spectral power reaches its maximum (100–200 MW/eV) in the photon energy ranges 75–120 eV and near 600 eV about 80 and 105 ns after the onset of the discharge current. The data presented in Table 1 show a decrease in the full width at half-maximum (FWHM) of the pulse with increasing photon energy. The emission in the 50- to 75-eV range continues from the onset of the current until its maximum, whereas the emission pulse in the kiloelectronvolt range is much shorter (about 15 ns). Figure 3 shows the emitted energy per 1 eV as a function of the

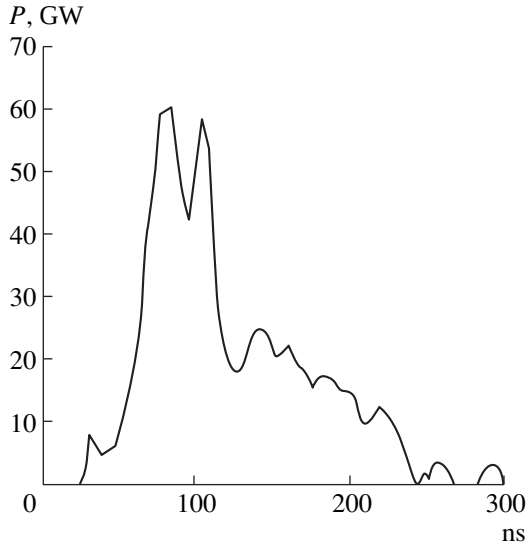

Fig. 4. Time dependence of total emitted power *P*.

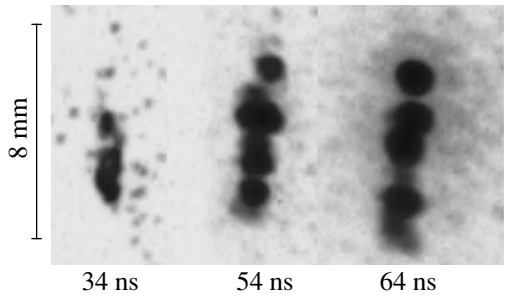

Fig. 5. MCP frames at the instants 34, 54, and 64 ns.

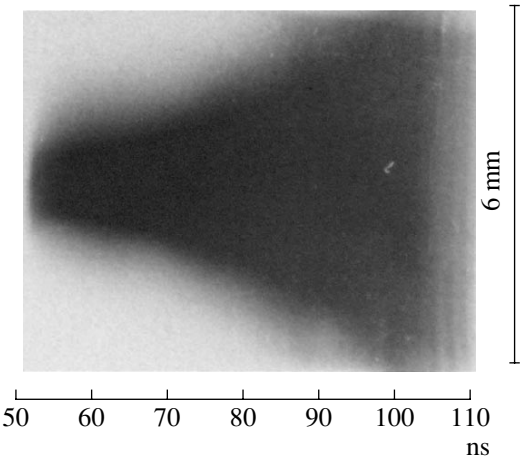

Fig. 6. Visible-light streak image obtained with a slit oriented perpendicular to the wire axis.

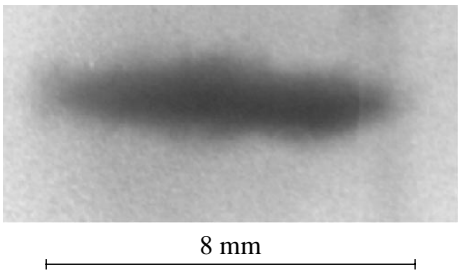

Fig. 7. Visible-light image at the instant 64 ns.

photon energy. The first maximum is higher due to the longer emission time. In Fig. 4, one can see two emission peaks with a power of 50–60 GW in the entire photon energy range (50–900 eV). The total emitted energy in this range is estimated at 3 kJ in the first maximum and 1.5 kJ in the second maximum.

Figure 5 shows three frames obtained with the MCP and pinholes filtered with 10-μm Be foils. One can see the images of an X-ray source emitting in the photon energy range higher than 600 eV during the time interval corresponding to the onset of the first SXR peak (namely, 34, 54, and 64 ns after the onset of the discharge current). The diameter of the spherical emitting spots is 1–2 mm. The number, diameter, and total intensity of these spots increase during the observation time interval (30 ns). It follows from these frames that the typical emission time of one spot is on the order of 10 ns.

The temporal evolution of the wire corona diameter in the visible region can be evaluated from the streak image presented in Fig. 6. The emission arises 50 ns after the onset of the discharge current. At this time, the corona diameter rapidly increases to 1.5 mm. During the next 20 ns (from 50 to 70 ns), the corona diameter increases with a velocity varying from 2×10^6 to 3×10^6 cm/s, whereas during the SXR pulse, the corona expansion velocity reaches 7×10^6 cm/s. Figure 7 shows a visible-light image of the corona at 64 ns, when its diameter is 2–3 mm.

The shadow images presented in Fig. 8 show the surface of the dense corona within the time interval of from 40 to 80 ns after the onset of the discharge current (shot no. 0205292). Here, one can see the onset of instabilities: the ejection of plasma jets (filaments) from the corona surface. Due to the high mass of Cu ions, the velocity of the ejected filaments is relatively low (about 3×10^7 cm/s) and their surface is fairly sharp. It can be seen from first and second frames that the propagation direction of the plasma jets escaping from the corona changes from radial to axial, and, in the third frame, the plasma jets seem to be directed back to the wire.

Figure 9 presents the shadow images of the surface of the dense corona at 57, 67, 87 and 97 ns after the onset of the discharge current (shot no. 0205302). The time dependence of the corona diameter was determined from an image obtained with the visible-light streak camera. The velocity of the corona expansion estimated from this image is 10^6–10^7 cm/s.

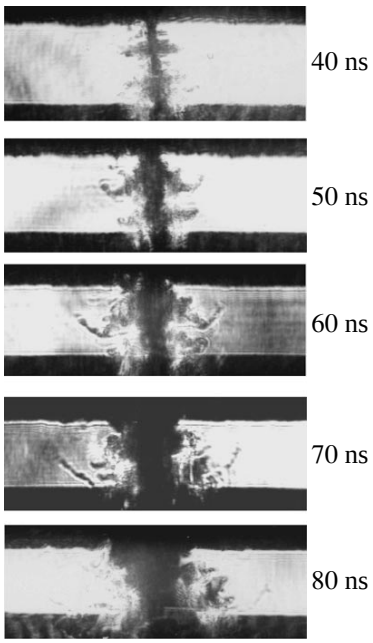

Fig. 8. Shadow images at the instants 40, 50, 60, 70, and 80 ns (shot no. 0205292).

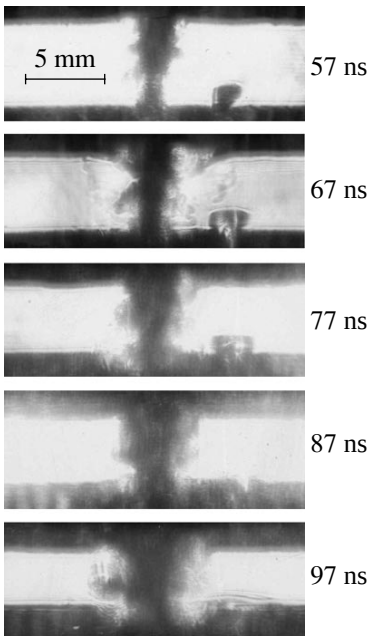

Fig. 9. Shadow images at the instants 57, 67, 77, 87, and 97 ns (shot no. 0205302).

Table 1. FWHMs of SXR pulses in different photon energy ranges

Photon energy, eV	60	120	220	340	600
FWHM, ns	120	100	50	24	20
Energy resolution, %	17	7.8	3.8	3.3	2.0

According to Fig. 10, which shows the X-ray emission spectrum, the lines in the photon energy range 1–2 keV belong to the L shell of Cu ions. This time-integrated spectrum was recorded on a DEF X-ray film. The spectral lines belong to the Cu ions with charge numbers of 23, 21, 20, and 19. The spectral lines listed in Table 2 were identified using the dispersion characteristic of the spectrograph and the tabulated wavelengths [18]. The first, second, third, and fourth resonant lines of the He-like Cu ions correspond to the third and fifth spectroscopic orders, whereas the other lines correspond to the first order.

4. DISCUSSION AND CONCLUSIONS

The evolution of a corona formed around a copper wire differs from the evolution of the aluminum wire corona described in [9]. After the onset of the current, a plasma corona is formed around the wire. The corona expands with an average velocity of 10^6–10^7 cm/s and is characterized by a high plasma density gradient near its surface and by the emission of double-humped pulses in the XUV–SXR spectral range.

The XUV emission arises 40–50 ns after the onset of the discharge current. The maximum photon energy in the two peaks generated at 80 and 120 ns is 120 eV, the maximum emission power is 50 GW, and the total emission energy is 3 kJ. The plasma temperature estimated from the XUV spectrum according to the Plank law turns out to be higher than 40 eV.

The peaks of SXR emission with a maximum photon energy higher than 600 eV are generated at the same instants 80 and 120 ns and have the same maximum power of 50 GW. The total energy of the SXR pulses is 600–800 J; however, the FWHMs of the SXR peaks are smaller (10–20 ns).

The diameter of the simultaneously radiating spherical spots is 1–2 mm, and their lifetime is ~10 ns. The plasma temperature estimated from the SXR spectrum is 150 eV. The K- and L-shell lines of Cu ions are emitted from the spherical spots during the SXR pulse. The plasma temperatures estimated from the emission spectra in the ranges corresponding to the L- and K-shell lines are 400 and 2000 eV, respectively.

In experiments with copper wires, the helical plasma structures that were detected in [9] in both the visible and X-ray spectral ranges were observed during the XUV and SXR pulses. This can be explained as follows. First, in our experiments, the X-ray image converters were equipped with filters that transmit radiation in the photon energy range $h\nu > 600$ eV (in contrast to [9], in which filters that transmit in the range $h\nu > 10$ eV were used), which did not allow us to observe the formation of such structures in the copper wire corona. Second, we used more sensitive visible-light image

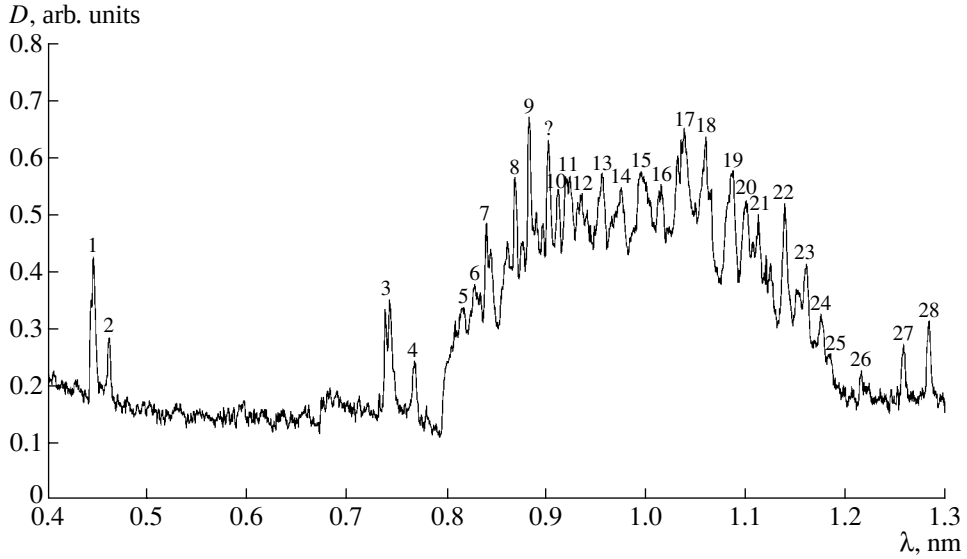

Fig. 10. Photographic blackening D vs. wavelength λ.

Table 2. List of Cu lines from Fig. 10

Peak no.	λ, nm		Charge number	Peak no.	λ, nm		Charge number
	observed	tabulated			observed	tabulated	
1	0.1479	0.1478	27; 3rd order	17	1.0380	1.0392	20
1	0.1486	0.1485	27; 3rd order			1.0400	23
2	0.1540	0.1542	Cu K_α; 3rd order			1.0438	21
3	0.1475	0.1478	27; 5th order	18	1.0592	1.0551	21
3	0.1485	0.1485	27; 5th order			1.0599	19
4	0.1538	0.1542	Cu K_α; 5th order		1.0645	1.0653	19
	0.8080	0.8070	19	19	1.0856	1.0799	21
5	0.8158	0.8158	21			1.0800	20
6	0.8275	0.8275	21			1.0858	20
	0.8334	0.8330	19			1.0893	20
7	0.8395	0.8395	19	20	1.0995	1.0971	20
	0.8440	0.8444	19			1.1002	20
8	0.8687	0.8691	20			1.1014	20
	0.8755	0.8754	20			1.1026	20
9	0.8824	0.8808	20		1.1064	1.1065	20
?	0.9016			21	1.1118	1.1097	20
10	0.9113	0.9102	19			1.1114	20
11	0.9232	0.9233	19			1.1136	20
		0.9233	25		1.1198	1.1198	21
12	0.9345	0.9371	19		1.1239	1.1229	20
13	0.9545	0.9522	19	22	1.1385	1.1386	19
14	0.9745	0.9737	25			1.1416	21
15	0.9979	0.9961	20	23	1.1597	1.1573	21
		0.9982	23			1.1597	19
		1.0057	20	24	1.1750	1.1737	19
16	1.0142	1.0103	23			1.1774	17
		1.0121	20	25	1.1832	1.1830	20
	1.0311	1.0316	20	26	1.2149	1.2140	20
		1.0316	21			1.2165	20
	1.0350	1.0354	20	27	1.2574	1.2573	19
		1.0356	21	28	1.2829	1.2830	19

converters than those in [9]; therefore, we could observe only the outer corona region, which had a diameter much larger than the helical structure diameter.

ACKNOWLEDGMENTS

We are grateful to Prof. A.S. Kingsep for his valuable remarks and to M.I. Ivanov for his help in measuring X-ray spectra. This study was supported by grants from the Ministry of Education, Youth, and Sports of the Czech Republic under contract nos. LA 055, LN 00A100, and J04/98:212300017.

REFERENCES

1. M. V. Bekhtev, V. D. Vikharev, S. V. Zakharov, *et al.*, Zh. Éksp. Teor. Fiz. **95**, 1653 (1989) [Sov. Phys. JETP **68**, 955 (1989)].
2. M. K. Matzen, Phys. Plasmas **4**, 1519 (1997).
3. D. Mosher, S. I. Stephanakis, I. M. Vitkovitsky, *et al.*, Appl. Phys. Lett. **23**, 429 (1973).
4. R. B. Baksht, I. N. Datsko, A. F. Korostelev, *et al.*, Pis'ma Zh. Tekh. Fiz. **6**, 1109 (1980) [Sov. Tech. Phys. Lett. **6**, 474 (1980)].

5. S. M. Zakharov, G. V. Ivanenkov, and A. A. Kolomenskiĭ, Fiz. Plazmy **9**, 469 (1983) [Sov. J. Plasma Phys. **9**, 271 (1983)].
6. L. E. Aranchuk, S. L. Bogolyubskiĭ, G. S. Volkov, *et al.*, Fiz. Plazmy **12**, 1324 (1986) [Sov. J. Plasma Phys. **12**, 765 (1986)].
7. S. M. Zakharov, A. A. Kolomenskiĭ, S. A. Pikuz, *et al.*, Pis'ma Zh. Tekh. Fiz. **6**, 1223 (1980) [Sov. Tech. Phys. Lett. **6**, 523 (1980)].
8. P. G. Burkhalter, C. H. Dozier, and D. J. Nagel, Phys. Rev. A **15**, 700 (1977).
9. P. Kubeš, E. Kravárik, Yu. L. Bakshaev, *et al.*, Fiz. Plazmy **28**, 329 (2002) [Plasma Phys. Rep. **28**, 296 (2002)].
10. V. A. Veretennikov, S. I. Polukhin, O. G. Semenov, and Yu. V. Sidel'nikov, Fiz. Plazmy **7**, 1199 (1981) [Sov. J. Plasma Phys. **7**, 656 (1981)].
11. I. K. Aĭvazov, L. E. Aranchuk, S. L. Bogolyubskiĭ, and G. S. Volkov, Pis'ma Zh. Éksp. Teor. Fiz. **41**, 111 (1985) [JETP Lett. **41**, 135 (1985)].
12. V. I. Afonin, Fiz. Plazmy **21**, 648 (1995) [Plasma Phys. Rep. **21**, 612 (1995)].
13. J. P. Chittenden, R. A. Rossel, S. V. Lebedev, *et al.*, in *Proceedings of the 4th International Conference on Dense Z-Pinches, Vancouver, 1977*, p. 71.
14. L. E. Aranchuk, C. L. Bogolyubskiĭ, and O. V. Tel'kovskaya, Zh. Tekh. Fiz. **55**, 2222 (1985) [Sov. Phys. Tech. Phys. **30**, 1312 (1985)].
15. P. V. Sasorov, Fiz. Plazmy **17**, 1507 (1991) [Sov. J. Plasma Phys. **17**, 874 (1991)].
16. P. Kubeš, J. Kraváric, D. Klír, *et al.*, Fiz. Plazmy **28**, 329 (2002) [Plasma Phys. Rep. **28**, 296 (2002)].
17. P. Kubeš, J. Kravárik, D. Klír, *et al.*, AIP Conf. Proc. **651**, 197 (2002).
18. R. L. Kelly, *Atomic and Ionic UV/VUV Line List*, cfa-www.harvard.edu/amp/data/amdata.html.

Translated by the authors

Plasma Physics Reports, Vol. 29, No. 11, 2003, pp. 978–982. Translated from Fizika Plazmy, Vol. 29, No. 11, 2003, pp. 1054–1058.

PLASMA DIAGNOSTICS

Development of a Collisional Radiative Model for Interpreting the Spectroscopic Measurements of ArII Line Emission

I. V. Moskalenko and D. A. Shuvaev

Russian Research Centre Kurchatov Institute, pl. Kurchatova 1, Moscow, 123182 Russia

Received March 20, 2003

Abstract—A collisional radiative model for an ArII ion is constructed. The populations of the excited states of ArII ions in a plasma of a magnetic confinement system are calculated. It is shown that, in such a plasma, the populations of metastable states are independent of the electron density but, at the same time, are fairly sensitive to the electron temperature. These results allow one to estimate the electron temperature from the measurements of the Doppler profiles of the spectral lines by the laser fluorescence diagnostics. The populations of nonmetastable states calculated as functions of the plasma parameters also make it possible to estimate the electron temperature from passive spectroscopy measurements. © *2003 MAIK "Nauka/Interperiodica".*

1. INTRODUCTION

In recent years, there has been growing interest in the injection of argon (or neon) into high-temperature plasma devices with magnetic thermal insulation in order to achieve "radiatively improved" operating modes in which the line emission redistributes energy fluxes over the vacuum chamber wall in a more uniform fashion [1]. This concept was also adopted for the projected ITER-FEAT tokamak. Another modern-day application of an argon plasma is its use in plasma neutralizers for stripping high-energy D^- ion beams [2]. Measurements of plasma parameters by spectroscopic methods require the development of atomic-kinetics models for different atoms and ions. In the present paper, we begin work in this area by constructing the relevant model for an ArII ion.

The operating conditions of a plasma neutralizer are such that the plasma parameters should be controlled with sufficient precision. The typical values of the plasma parameters correspond to electron densities of 10^{10}–10^{12} cm^{-3} and electron temperatures of 5–30 eV. The spectroscopic diagnostics are based on measurements of the absolute intensities of argon spectral lines in the visible region. The specific feature of the spectral lines of an ArII ion is associated with the presence of metastable energy levels. This is why, even for a plasma with a relatively low electron density, the populations of these levels should be calculated by using a sufficiently comprehensive collisional radiative model for populating the excited states of the ion in question. It should be expected that the populations of the metastable states are weakly sensitive to the electron density because the rates of the processes of their radiative decay are rather low, so that the population and depopulation of these states are governed only by electron–electron collisions.

The accuracy of calculations is restricted by the available data on the oscillator strengths for transitions between different excited states [3]. As for collisional transitions, they will be described by using the data obtained in [4] on the basis of the Born–Coulomb approximation, which has been found to produce fairly realistic results in calculating the rates of collisional transitions in ions. In the case under consideration, it is rather difficult to use approximating formulas because of the complex nature of electron coupling in view of the presence of a large number of equivalent electrons. This is why, in what follows, we choose several basic excited configurations that make the main contribution to the processes under discussion and for which there are fairly reliable spectroscopic data.

2. KINETIC MODEL

The emission intensity at a certain transition frequency ω_{ij} is given by the formula

$$I_{ij} = \hbar\omega_{ij} W(i \longrightarrow j) N(i),$$

where $W(i \longrightarrow j)$ is the probability of a radiative transition from the ith to the jth state and $N(i)$ is the population of the initial state.

The populations of the excited levels satisfy the following balance equations:

$$\frac{dN(i)}{dt} = \sum_j N(j) N_e \langle v\sigma_{j,i} \rangle^{\text{exc}} + \sum_{j>i} N(j) W(j \longrightarrow i)$$

$$+ N^{\text{Ar}^{++}}(1) N_e (\langle v\sigma_i \rangle^{DR} + \langle v\sigma_i \rangle^{RR})$$

$$+ \delta_{1,i} \sum_j N^{\text{Ar}}(j) N_e \langle v\sigma_j \rangle_{\text{Ar}}^{\text{ion}}$$

1063-780X/03/2911-0978$24.00

$$- \sum_{j=1}^{i-1} N(i)W(i \longrightarrow j) - N(i)N_e\langle v\sigma_i\rangle^{\text{ion}},$$

where $\langle v\sigma_{ij}\rangle^{\text{exc}}$ is the excitation rate in collisions with electrons, $\langle v\sigma_i\rangle^{DR}$ is the dielectronic recombination rate, $\langle v\sigma_i\rangle^{RR}$ is the radiative recombination rate, and $\langle v\sigma_i\rangle^{\text{ion}}$ is the collisional ionization rate.

Since the concentration of ArII ions is unknown a priori and is determined by the ionization balance equations, it is natural to eliminate the population of the ground state from the set of model equations and calculate the populations of the excited states relative to that of the ground state, regarding the latter as a population "reservoir." Moreover, since we are considering a steady-state problem, the time derivative of the populations can be set at zero.

Hence, we are using the following population equations with the source q, which describes excitations from the ground state:

$$\sum_{j=1}^{i-1} N(i)W(i \longrightarrow j) + N(i)N_e\langle v\sigma_i\rangle^{\text{ion}}$$

$$- \sum_j N(j)N_e\langle v\sigma_{j,i}\rangle^{\text{exc}} - \sum_{j>i} N(j)W(j \longrightarrow i) = q_i.$$

3. CALCULATION SCHEME

In our calculations, we took into account six excited states corresponding to the sublevels of the fine structure:

(i) $3s^23p^4(^1D)4s\ ^2D\ 3/2\ 18.42655$
(ii) $3s^23p^4(^1D)4s\ ^2D\ 5/2\ 18.45412$
(iii) $3s^23p^4(^1D)3d\ ^2G\ 9/2\ 19.11607$
(iv) $3s^23p^4(^1D)3d\ ^2G\ 7/2\ 19.11886$
(v) $3s^23p^4(^1D)4p\ ^2F\ 5/2\ 21.12704$
(vi) $3s^23p^4(^1D)4p\ ^2F\ 7/2\ 21.14308$

This scheme can be extended substantially to include other excited states (see Fig. 1); however, a serious obstacle to this extension is a lack of reliable information on the lifetimes of the excited states and the excitation cross sections. Below, for the probabilities of radiative transitions, we will use the data from the NIST chemical kinetic database[1] and also the data from [3].

The rates of collisional transitions of electrons with the same spin between the excited states are given by the formulas [4]

$$\langle v\sigma_{a_0a_1}\rangle = 10^{-8}\left(\frac{Ry}{\Delta E}\right)^{3/2}\left(\frac{E_1}{E_0}\right)^{3/2}\frac{Q_{k_{\min}}(a_0, a_1)}{2l_0+1}e^{-\beta}G(\beta),$$

$$\beta = \Delta E/T,$$

$$G(\beta) = A\frac{(\beta+1)\sqrt{\beta}}{\beta+\chi},$$

$$k_{\min} = |l_0 - l_1|.$$

Here, a_0 and a_1 are the configurations of the initial and final states, respectively; l_0 and l_1 are the angular moments of an emitting electron in the initial and final states; and A and χ are the adjusting parameters, which were calculated in [4]. The above formulas also contain the Q factor, which depends on a particular transition and determines the scheme for summing the angular momenta of the initial and final configurations. In our model, we use the following expressions for the Q factor.

(i) For transitions from a shell with equivalent electrons (the excitation from the ground state), we have $a_0 = l_0^m L_0 S$ and $a_1 = l_0^{m-1}[L_pS_p]l_1L_1S$, and the Q factor has the form

$$Q_k(a_0, a_1) = m(G^{L_0S}_{L_pS_p})^2(2l_0+1)(2L_1+1)\left\{\begin{array}{ccc} l_0 & L_0 & L_p \\ L_1 & l_1 & k \end{array}\right\}^2,$$

where the genealogical coefficient $G^{L_0S}_{L_pS_p}$ is equal to $1/\sqrt{3}$ for the ArII ion under consideration.

(ii) For transitions that do not involve equivalent electrons (transitions between the excited states), the Q factor has the form

$$Q_k(a_0, a_1) = (2l_0+1)(2L_1+1)\left\{\begin{array}{ccc} l_0 & L_0 & L_p \\ L_1 & l_1 & k \end{array}\right\}^2.$$

These expressions for the Q factor do not take into account the fine structure. In order to incorporate the fine-structure splitting into J components, it is necessary to use the following additional expression for the Q factor:

$$Q_k(a_0J_0, a_1J_1) = (2L_0+1)(2J_1+1)\left\{\begin{array}{ccc} L_0 & J_0 & S \\ J_1 & L_1 & k \end{array}\right\}^2 Q_k(a_0, a_1),$$

where the 6-j-symbols are calculated from the formulas [5]

$$\left\{\begin{array}{ccc} j_1 & j_2 & j_3 \\ l_1 & l_2 & l_3 \end{array}\right\}$$

$$= \Delta(j_1j_2j_3)\Delta(j_1l_2l_3)\Delta(l_1j_2l_3)\Delta(l_1l_2j_3)w\left\{\begin{array}{ccc} j_1 & j_2 & j_3 \\ l_1 & l_2 & l_3 \end{array}\right\},$$

[1] http://physics.nist.gov/cgi-bin/AtData/lines_form
http://physics. nist.gov/cgi-bin/AtData/levels_form

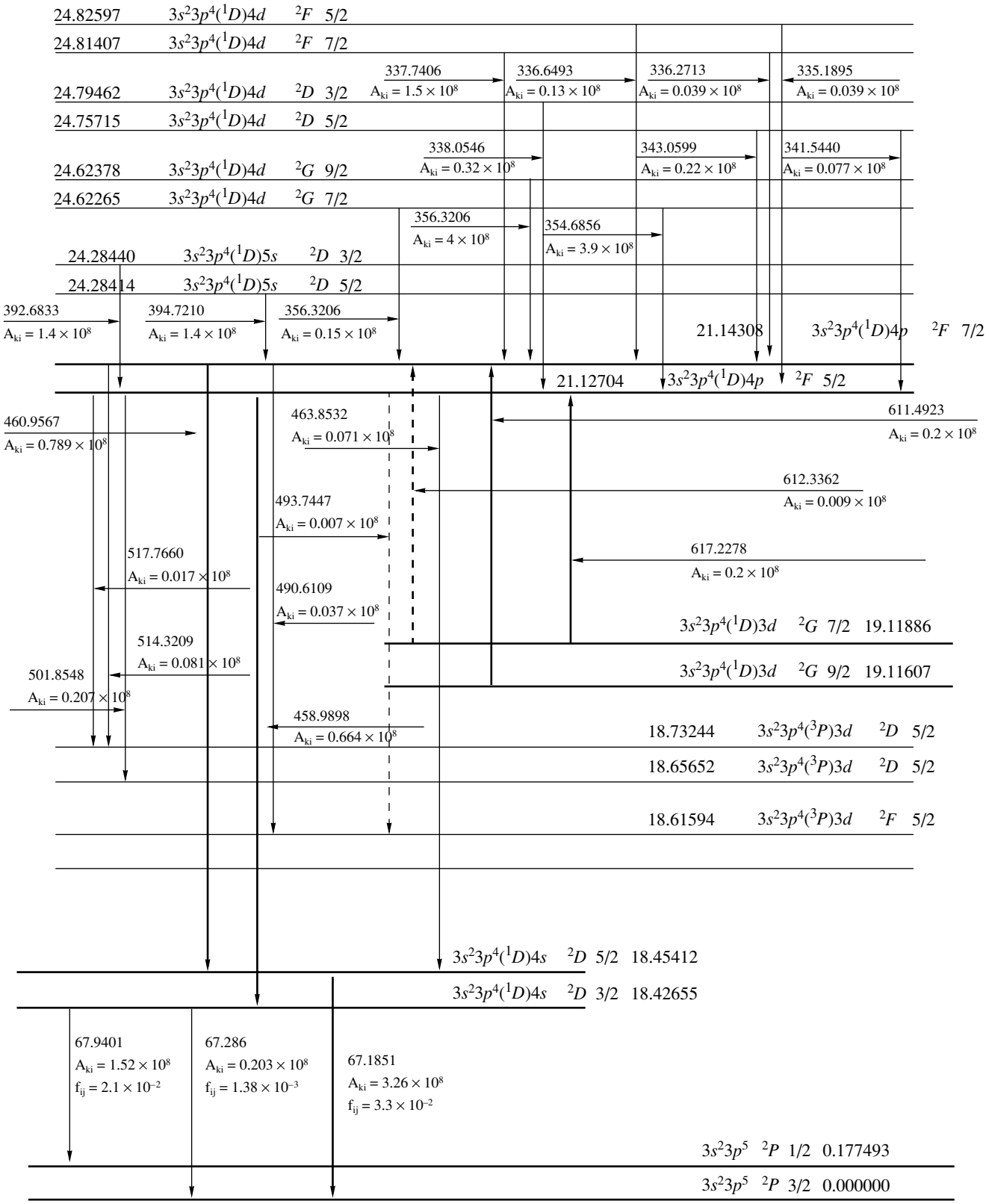

Fig. 1. Full scheme of the levels of an ArII ion. The scheme of levels used in the model is indicated by heavy lines.

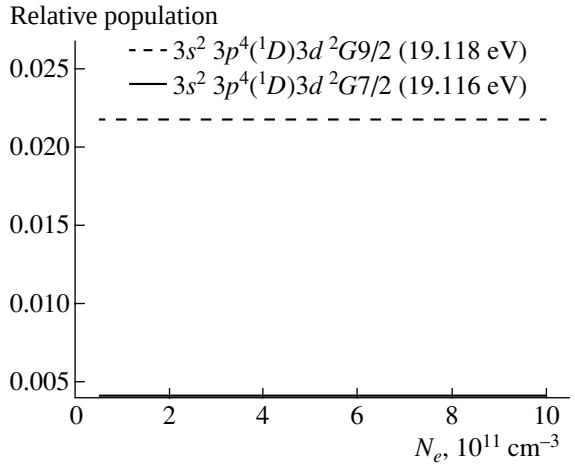

Fig. 2. Dependence of the populations of the metastable states of an ArII ion (relative to the population of the ground state) on the electron density at the electron temperature T = 10 eV.

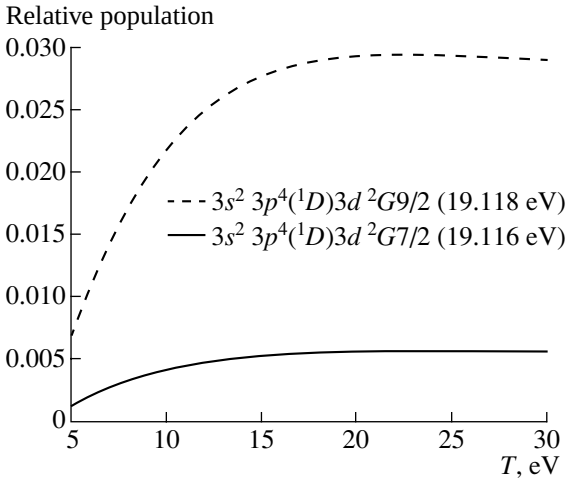

Fig. 3. Dependence of the populations of the metastable states of an ArII ion (relative to the population of the ground state) on the electron temperature at the electron density $N_e = 10^{10}$ cm^{-3}.

$$\Delta(abc) = \left[\frac{(a+b-c)!(a-b+c)!(-a+b+c)!}{(a+b+c+1)!}\right]^{1/2},$$

$$w\left\{\begin{array}{ccc} j_1 & j_2 & j_3 \\ l_1 & l_2 & l_3 \end{array}\right\} = \sum_z (-1)^z (z+1)!$$
$$\times [(z-j_1-j_2-j_3)!(z-j_1-l_2-l_3)!$$
$$\times (z-l_1-j_2-l_3)!(z-l_1-l_2-j_3)!$$
$$\times (j_1+j_2+l_1+l_2-z)!(j_2+j_3+l_2+l_3-z)!$$
$$\times (j_3+j_1+l_3+l_1-z)!\,]^{-1},$$

with summation over the integer values of z at which the arguments of the factorial functions in the denominators are nonnegative.

The deexcitation rate is calculated based on the relationship between the rates of the mutually inverse processes [4]:

$$g_k\langle v\sigma_{ki}\rangle = g_i\langle v\sigma_{ik}\rangle e^{-\beta}, \quad \beta = \Delta E/T,$$

where g is the statistical weight of an excited state.

The ionization rate is calculated from the familiar Lotz formula [4]

$$\langle v\sigma_i\rangle = 6\times 10^{-8}\left(\frac{Ry}{E_z}\right)^{3/2}\beta^{1/2}|\mathrm{Ei}(-\beta)|,$$

where $|\mathrm{Ei}(-\beta)|$ is the integral exponent and $\beta = I/T$ is the parameter containing the ionization potential I of a given state.

4. CALCULATED RESULTS

The results of our calculations of the populations of the excited states as functions of the plasma parameters are shown in Figs. 2–5.

As can be seen from Fig. 2, the populations of the metastable states are almost independent of the electron density in the range of plasma parameters under consideration. As was already mentioned, this is explained by the fact that these states are not depopulated by radiative processes. As a result, the electron density in the numerator of the population source term exactly cancels that in the denominator of the depopulation source term. From Fig. 4, we can see that the population of the nonmetastable state depends linearly on the electron density.

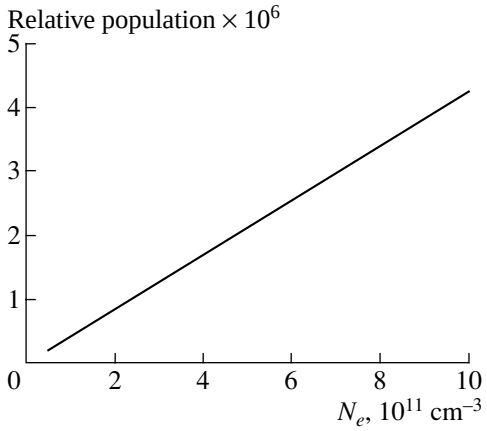

Fig. 4. Dependence of the population of the metastable state $3s^23p^4(^1D)4p\ ^2F$ of an ArII ion (relative to the population of the ground state) on the electron density at the electron temperature T = 10 eV.

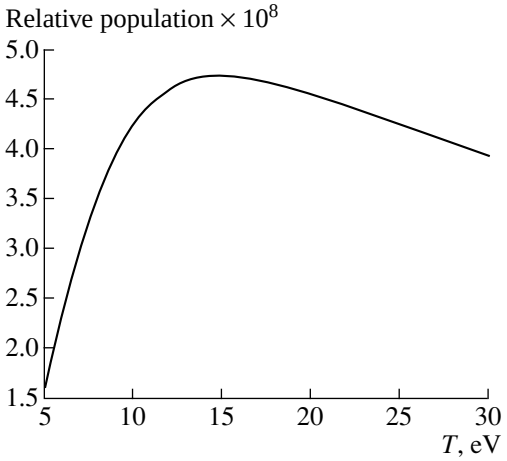

Fig. 5. Dependence of the population of the metastable state $3s^2 3p^4(^1D)4p\ ^2F$ of an ArII ion (relative to the population of the ground state) on the electron temperature at the electron density $N_e = 10^{10}$ cm^{-3}.

In contrast, in the electron temperature range at hand, the populations of metastable states depend sensitively on the electron temperature; this dependence is governed primarily by the excitation function for the atomic states.

5. CONCLUSIONS

We have found that the populations of the metastable states calculated for the range of plasma parameters under consideration are very sensitive to the electron temperature and are almost independent of the electron density. In this situation, the plasma temperature can be determined by measuring the absolute intensities of the spectral lines produced by transitions from the metastable states excited by laser light or electron impacts.

In addition, if the electron temperature near the wall of the device is known, then, under conditions such that the ion density varies insignificantly in the radial direction, the electron temperature at the axis of the plasma column can be determined (or at least estimated) from the data from passive spectroscopy measurements and laser fluorescence diagnostics, in which case it is necessary to take into account the dependence of the populations of the excited states on the electron density.

REFERENCES

1. R. Jaspers, E. Busche, T. Krakor, and B. Unterberg, in *Proceedings of the 24th European Conference on Controlled Fusion and Plasma Physics, Berchtesgarden, 1997*, Contributed Papers, Ed. by M. Schittenhelm, R. Bartiromo, and F. Wagner (Europ. Phys. Soc., Geneva, 1997), Vol. 21A, Part IV, p. 1713.
2. A. A. Skovoroda and V. A. Zhil'tsov, Plasma Phys. Controlled Fusion **43**, 929 (2001).
3. K.-H. Tan and J. W. McConkey, Phys. Rev. A **10**, 1212 (1974).
4. I. I. Sobel'man, L. A. Vaĭnshteĭn, and E. A. Yukov, *Excitation of Atoms and Broadening of Spectral Lines* (Nauka, Moscow, 1979; Springer-Verlag, Berlin, 1981).
5. A. R. Edmonds, in *Deformation of Atomic Nuclei*, Ed. by L. A. Sliv (Inostrannaya Literatura, Moscow, 1958), p. 305.

Translated by G.V. Shepekina

Plasma Physics Reports, Vol. 29, No. 11, 2003, pp. 983–989. Translated from Fizika Plazmy, Vol. 29, No. 11, 2003, pp. 1059–1066.

LOW-TEMPERATURE PLASMA

Determination of the Electron Density and Electric Field in the Plasma of a Low-Pressure Microwave Electrode Discharge in Hydrogen from the Measured Spectral Line Intensities

Yu. A. Lebedev and M. V. Mokeev

Topchiev Institute of Petrochemical Synthesis, Russian Academy of Sciences, Leninskiĭ pr. 29, Moscow, 119991 Russia

Received February 12, 2003

Abstract—The parameters of the plasma of a microwave electrode discharge in hydrogen at pressures of 1–8 torr and incident powers of 20–80 W are measured by the so-called "relative intensity" method. The method allows one to determine the electron density and electric field in plasma by measuring the relative intensities of the H_α, H_β, and 763.5-nm Ar line emission and calculating the electron-impact rate constants from the homogeneous Boltzmann equation. The measurements show that there are regions in the discharge where the electron density is higher (a bright electrode sheath) and lower (a spherical region) than the critical density for the frequency 2.45 GHz ($n_{cr} \sim 7 \times 10^{10}$ cm^{-3}). Inside the spherical region, the electric field varies slightly over the radius and the electron density increases as the discharge boundary is approached. The observed discharge structure can be attributed to the presence of a self-sustained discharge zone (electrode sheath); a non-self-sustained discharge zone (spherical region); and a decaying plasma region, which is separated from the active discharge zone by an electric double layer. © *2003 MAIK "Nauka/Interperiodica"*.

1. INTRODUCTION

Microwave plasma structures arising near the electrode under conditions such that the characteristic plasma dimensions are smaller than the discharge chamber size are a striking example of plasma self-organization. Discharges in molecular gases consist of a thin bright electrode sheath and a surrounding spherical glow, separated from the dark outer space by a sharp boundary [1–4] (Fig. 1). To date, the plasma parameters of such discharges have been poorly studied. The measurements of the electric field and charged particle densities in the active (glowing) discharge region are of special interest because they allow one to determine the mechanisms responsible for the physical processes in a discharge. Since the discharge plasma is nonuniform, these measurements should be spatially resolved. In [1], probe measurements were performed in the discharge chamber outside the glowing part of an electrode hydrogen discharge and the spatial distribution of the microwave electric field was determined from the measured electron temperature by numerically solving the Boltzmann equation. In particular, it was shown that the field decreases exponentially with radius; such behavior corresponds to the surface wave structure. In [5], the parameters of the electron component of nitrogen plasma were determined by the double probe method. It was shown that the electron density is uniform in the active discharge region and drops sharply at the boundary of the glowing region. In [6], an electrode discharge was modeled in the quasistatic approximation.

Microwave electrode discharges have proven to be efficient in plasmachemical technologies (e.g., in diamond film deposition and nanotube production) [7–9]. An advantage of microwave electrode discharges is the

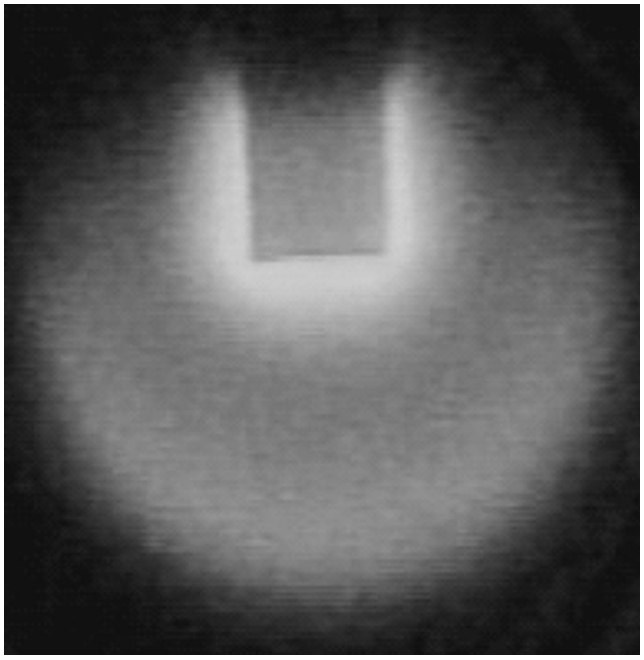

Fig. 1. Photograph of an electrode discharge in hydrogen at a pressure of 1 torr and an incident power of 120 W. The exposure time is 0.25 ms.

1063-780X/03/2911-0983$24.00

absence of electrode erosion, which distinguishes them from discharges operating at lower frequencies.

In our study, a method based on measuring the relative spectral line intensities is employed for noncontact measurements of the electric field and electron density in plasma. The measurements are carried out in the active region of a microwave electrode discharge in hydrogen. The results of spectroscopic measurements are compared with the data from probe measurements and numerical simulations performed in the quasistatic approximation.

2. EXPERIMENTAL SETUP

The measurements were carried out in a hydrogen discharge at a pressure of 1–8 torr and an incident microwave power of 20–80 W, the absorbed power being 2–12 W. A microwave oscillator with a maximum output power of 170 W operated at a frequency of 2.45 GHz. The discharge chamber was a metal cylinder 8.5 cm in diameter (see [1–3] for details). The microwave antenna (a cylindrical stainless-steel tube 6 mm in diameter) was inserted in the chamber through its end via a vacuum joint. The antenna was a part of a coaxial-to-waveguide converter, which was adjusted with the help of a shorting plunger. The experiments were carried out in a gas flow. The gas was supplied through a 3-mm-diameter channel in the upper wall of the discharge chamber and pumped out through a channel in the lower wall. The working gas was hydrogen with a 5% admixture of argon. Argon was added for diagnostic purposes and had practically no effect on the properties of the hydrogen plasma.

The discharge was ignited around the antenna (the exciting electrode). The discharge dimensions were much less than the chamber diameter and the distance from the lower end of the chamber. The discharge emission was output through a window on the side wall of the discharge chamber. The spatial resolution of the measurements was about 0.5 mm. Plasma emission in the spectral range of 400–800 nm was studied using an MDR-23 monochromator. An FEU-79 photomultiplier was used as an emission detector. The optical system was calibrated with the help of an SI-8-200 tungsten band lamp.

3. MEASUREMENT TECHNIQUE

We developed a method for determining the electric field and the plasma density in the discharge from the measured relative intensities of the spectral lines. In [3], it was shown that the degree of dissociation of hydrogen in the discharge under study was low and the hydrogen emission lines H_α and H_β (656.3 and 486.1 nm, respectively) were excited via the dissociative electron-impact excitation of H_2 molecules. The argon line emission (in particular, the 763.5-nm line used in this study) occurs due to the direct electron-impact excitation from the ground state. In this case, we have

$$k_{H_\alpha, H_\beta}[H_2]n_e = I_{H_\alpha, H_\beta}/h\nu_{\alpha,\beta}, \quad (1)$$

$$k_{Ar}[Ar]n_e = I_{Ar}/h\nu_{Ar}, \quad (2)$$

$$\frac{k_{H_\alpha, H_\beta}}{k_{Ar}} = \frac{[H_2]}{[Ar]}\frac{I_{H_\alpha, H_\beta}}{I_{Ar}}\frac{\nu_{Ar}}{\nu_{\alpha,\beta}}, \quad (3)$$

where k_{Ar}, k_{H_α} and k_{H_β} are the rate constants for the direct excitation of argon and the dissociative excitation of the atomic hydrogen states emitting in the H_α and H_β lines, respectively; I_{H_α} and I_{H_β} are the measured emission intensities of the H_α and H_β lines; and ν_{Ar}, $\nu_{\alpha,}$ and ν_β are the frequencies of the characteristic line emission of argon, H_α line, and H_β line, respectively.

From the measured line emission intensities, we determined the ratios of the rate constants for the excitation of the H_α and H_β hydrogen lines to the rate constant for the excitation of an Ar line [see Eq. (3)]. We then found the electric fields E_{H_α} and E_{H_β} corresponding to the obtained ratios k_{H_α}/k_{Ar} and k_{H_β}/k_{Ar} by numerically solving the Boltzmann kinetic equation. Finally, from the obtained values of E_{H_α} and E_{H_β}, we calculated the rate constants for the excitation of the H_α and H_β lines and found the corresponding electron densities by the formula

$$n_{eH_\alpha, H_\beta} = \frac{I_{H_\alpha, H_\beta}}{h\nu_{\alpha,\beta}k_{H_\alpha, H_\beta}[H_2]}. \quad (4)$$

To calculate the microwave electric field, we used a homogeneous Boltzmann equation [10] in which the terms with the electron density gradient and the electric field gradient were neglected. This imposes certain restrictions on the degree of plasma nonuniformity at which the proposed method can be applied. Since the excitation threshold for the H_α line differs from that for the H_β line, a criterion for the applicability of this method could be the coincidence of the densities and fields calculated from the measured H_α and H_β line intensities. In fact, this is a criterion for the applicability of the homogeneous Boltzmann equation.

The error in determining the electric field by the method described is 25–30%, and the error in determining the electron density is as high as a factor of 2. Obviously, such an error in determining the electron density is rather large. However, to gain a general idea of the physical processes in the discharge, it is sufficient to know the ratio between the measured plasma density and the critical electron density. The above accuracy in determining the electron density turned out to be quite sufficient in order to confidently establish that the elec-

tron density in the spherical region of the discharge is lower than the critical density.

4. RESULTS AND DISCUSSION

4.1. Spatial Distribution of the Line Emission in a Hydrogen Discharge

We measured the spatial distributions of the intensities of the H_α 656.3-nm and H_β 486.1-nm lines of the Balmer series of atomic hydrogen (with dissociative excitation thresholds of 17 and 17.66 eV, respectively), the Ar 763.5- and 737.2-nm lines (with thresholds of 13.17 and 14.76 eV, respectively), and the H_2 622.4-nm molecular band (with a threshold of 14.4 eV) of the Q branch of the diagonal band (with the vibrational quantum numbers of the upper and lower states $V' = V'' = 2$) of the Fulcher α system ($d^3\Pi_u \longrightarrow a^3\Sigma_g^+$ transition). The spatial distributions of the intensities of all these lines and bands are similar in shape and coincide with the spatial distribution of the integral intensity of the discharge emission.

Figure 2 presents the radial profiles of the line intensities normalized to their maximum values. It can be seen that the profiles of the relative intensities coincide near their maxima and diverge away from the maxima, being arranged in the order of their line excitation thresholds. Obviously, if these lines are excited by electron impacts from the ground states of a molecule or an atom, then, in the regions where the intensity of the lines with lower thresholds exceeds the intensity of those with higher thresholds, the electric field is lower than that in the region of the maximum line intensity and vice versa in the regions where the intensity of the lines with higher thresholds exceeds the intensity of those with lower thresholds.

Thus, the ratios of the spectral line intensities allow one to gain a general idea of the spatial distribution of the electric field in plasma.

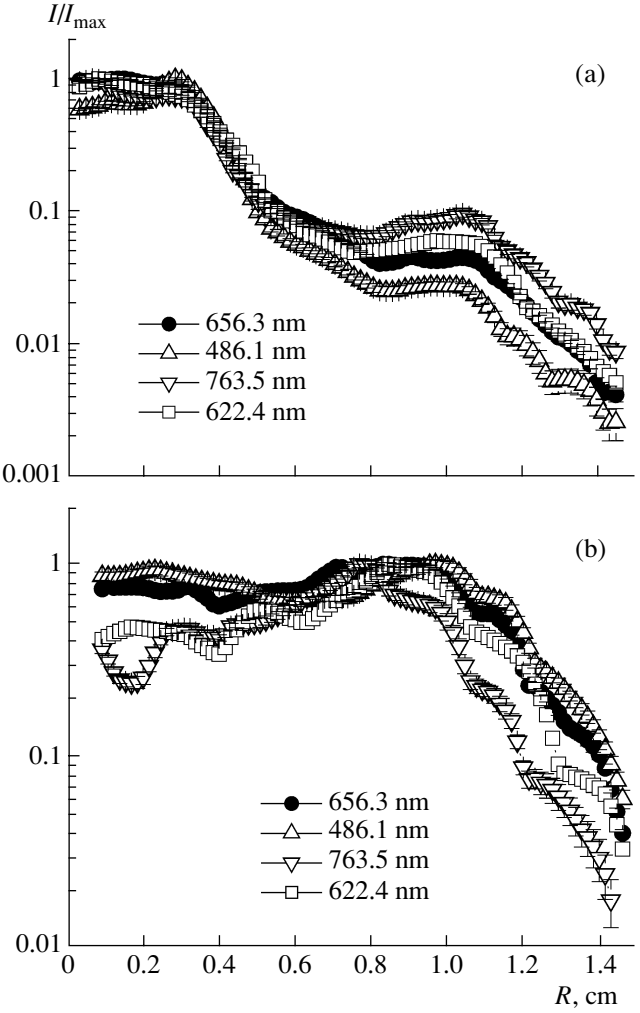

Fig. 2. Radial profiles of the spectral line intensities normalized to their maximum values in the planes located at a distance of (a) 1.4 and (b) 9.2 mm below the edge of the 6-mm-diameter tube electrode for a discharge in the H_2 + 5% Ar mixture at a pressure of 1 torr and an incident power of 80 W.

4.2. Spatial Distributions of the Electric Field and Electron Density in a Discharge

Figure 3 shows the electric field and electron density profiles determined using the method described in Section 3 for a pressure of 1 torr and an incident power of 80 W. Some data are presented in the table. Based on these data, the following conclusions can be drawn:

(i) The values of E_{H_α} and E_{H_β} (as well as n_{H_α} and n_{H_β}) coincide in the spherical region of the discharge and differ in the electrode glow region. This means that the method used for determining the plasma parameters is applicable only in the spherical region surrounding the electrode plasma sheath.

(ii) At a pressure of 1 torr, the electric field in the spherical region is nearly uniform and increases slightly with increasing incident power (from 75–90 V/cm at 20 W to 90–120 V/cm at 80 W).

(iii) The electron density in the spherical region reaches $(2–4) \times 10^{10}$ cm^{-3} at a certain distance from the discharge center, independently of the incident power. On the discharge axis, the electron density is much lower ($n_e = (0.5–2) \times 10^9$ cm^{-3}). This difference is especially pronounced at high powers, when the discharge dimensions are large. The axial depression in the electron density is accompanied by a severalfold decrease in the emission intensity on the discharge axis. In the region surrounding the electrode sheath, the distributions of both the emission intensity and the electron density are in the shape of a sphere. Along the sphere, the electron density is nearly constant. Inside the sphere, the electron density increases monotonically

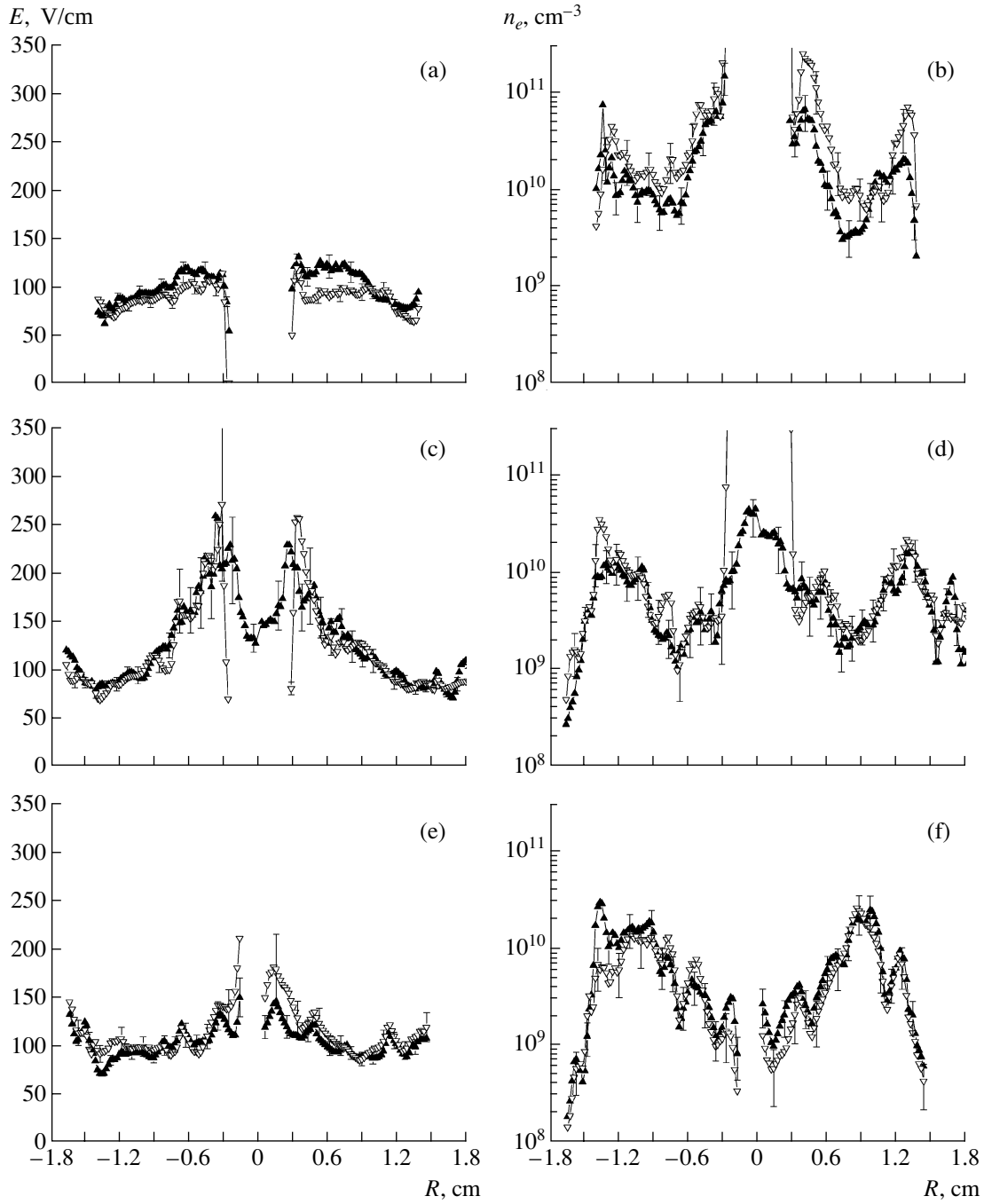

Fig. 3. Radial profiles of the (a, c, e) electric field and (b, d, f) electron density determined from the intensities of the H_α (closed triangles) and H_β (open triangles) lines for different positions of the measurement plane: Z = (a, b) 0.6, (c, d) –1.6, and (e, f) –9.4 mm. The coordinate Z is counted from the edge of the 6-mm-diameter tube electrode (Z = 0) toward the microwave oscillator. The discharge in the H_2 + 5% Ar mixture took place at a pressure of 1 torr and an incident power of 80 W.

with radius. After reaching its maximum at the boundary of the spherical region, the electron density decreases sharply (by one order of magnitude at a distance of 2–3 mm). This decrease is accompanied by an exponential decrease in the emission intensity.

(iv) At a constant incident power (80 W), the electric field in the spherical region increases slightly with pressure (from 90–120 V/cm at 1 torr to 90–140 V/cm at 8 torr), while the electron density varies in the range $(0.5–2) \times 10^{10}$ cm^{-3}.

(v) As the electrode layer is approached, the electric field significantly increases. At an incident power of 80 W and pressures of 1–8 torr, the electric field in the discharge cross section located 1.6 mm below the elec-

trode increases from ≈80 V/cm at the periphery up to at least ≈180 V/cm in the central region (in the applicability region of the method). At lower incident powers and a pressure of 1 torr, the increase in the field is somewhat lower.

(vi) In the electrode sheath, the above method for determining the plasma parameters is generally inapplicable. The calculations according to the intensities of the H_α and H_β lines give different results. This can be related to the presence of the large field gradients in this region, which are not taken into account when solving the homogeneous Boltzmann equation. In this region, various factors that are not taken into consideration can play a significant role (see below).

(vii) In some cases (e.g., at a pressure of 1 torr and an incident power of 80 W 0.6 mm above the electrode edge and 20 W 0.5 mm under the electrode edge), we succeeded in diagnosing the electrode sheath plasma. It turned out that the electron density in the sheath attained $(1–3) \times 10^{11}$ cm^{-3}.

(viii) In the regions where the method concerned is inapplicable, the power and pressure dependences of the maximum electric field in the electrode sheath can be estimated by employing the H_α line only. Such estimates show that, at a constant pressure of 1 torr, the field increases with incident power (from ≈150 V/cm at 20 W to ≈200 V/cm at 80 W) and, at a constant incident power of 80 W, it increases with pressure (from ≈250 V/cm at 1 torr to ≈460 V/cm at 8 torr).

Let us analyze in more detail the problem of the applicability of the method proposed, since it is related to certain physical processes in the discharge (in particular, to the resonance phenomena).

When solving the homogeneous Boltzmann equation in the local approximation, we took into account that the electron energy distribution function (EEDF) was formed due to electron heating in a uniform electric field and the loss of electron energy due to elastic collisions with heavy particles and the excitation of the rotational, vibrational, and electronic states of these particles, as well as their dissociation and ionization. Inside the electron subsystem of the plasma, the energy is redistributed due to electron–electron collisions. In molecular gases, this channel for energy redistribution can be ignored if the degree of ionization is lower than ~10^{-3}. That is why we did not take into account electron–electron collisions when solving the Boltzmann equation.

The nonlocal character of the EEDF manifests itself when the characteristic electron energy relaxation length λ_ε exceeds the characteristic plasma size Λ [11]. In the diffusion-controlled regime of discharge, the relaxation length is $\lambda_\varepsilon \sim (D_a\tau_\varepsilon)^{1/2}$ and $\tau_\varepsilon = 1/\nu_\varepsilon \sim 1/\delta\nu_{ef}$ (these are the conditions that usually occur in experiments). Here, D_a is the coefficient of ambipolar diffusion, δ is the average energy fraction that is lost by an electron in one collision with a heavy particle, and ν_{ef} is the effective frequency of electron collisions with heavy particles. At a pressure of 1 torr, we have $\nu_{ef} \sim 10^9$ s^{-1}, $\delta \geq 10^{-2}$, $D_a \sim 10^4$ cm^2/s, and $\lambda_\varepsilon < 1$ mm. The characteristic radius of the spherical region is $\Lambda \sim 10$ mm; hence, we have $\lambda_\varepsilon \ll \Lambda$. At higher pressures, this condition is satisfied by an even larger margin. This means that, under conditions of our experiments, the nonlocal character of the EEDF can be ignored.

Electric field E and electron density n_e in the non-self-sustained discharge region at different values of the pressure P and incident power W

P, torr	W, W	n_e, 10^{10} cm^{-3}	E, V/cm
1	20	0.5–1	75–90
	40	2–4	85–100
	60	2–3	85–100
	80	1.5–2.5	90–120
2		0.7–1.5	100–110
4	80	~0.7	95–120
8		~1	100–140

The above estimates also show that the EEDF becomes isotropic at distances much shorter than 1 mm. This confirms the applicability of the two-term expansion of the EEDF in spherical harmonics and means that any deviations of the EEDF from being isotropic (e.g., due to the resonance phenomena or plasma inhomogeneity) relax at distances shorter than the spatial resolution of the method employed.

In a quasi-uniform alternating field, an electron acquires energy only in collisions with heavy particles (the so-called Ohmic or Joule heating with $P_{abs} = e^2E_0^2\nu_{tr}/0.707(\omega^2 + \nu_{tr}^2)$). This mechanism is typical of medium- and high-pressure plasmas.

In low-pressure plasmas ($\omega \gg \nu_{tr}$), there are narrow plasma resonance regions (with a characteristic size Δ), in which the electric field can be very high. In such a highly nonuniform field, there is an additional mechanism for accelerating and heating thermal electrons passing through the resonance region (the so-called stochastic heating). This process is characterized by the frequency $\nu^* \approx \bar{v}_e^3/\Delta^3\omega^2$, where $\bar{v}_e$ is the electron thermal velocity. In order to take into account this heating, the electron collision frequency in the formula for the absorbed power must be replaced by the effective frequency $\nu_{ef} = \nu_{tr} + \nu^*$. This process leads to the enrichment of the EEDF with fast electrons in comparison to a uniform plasma. This effect was indeed observed in the experiments. It disappears at pressures higher than 50 mtorr [12, 13].

Thus, under our experimental conditions, the stochastic heating of electrons is of minor importance; accordingly, we took into account only Joule heating.

The role of the resonance phenomena was analyzed in [6], based on the self-consistent simulations of a coaxial plasma system in the quasistatic approximation. It was shown that, at a pressure of 1 torr, the plasma resonance significantly affects the electric field structure and the electron density distribution, whereas at pressures of 3–4 torr, the field structure almost already coincides with that in a system filled with an ordinary dielectric. Hence, at least in the upper range of the pressures under study, the role of plasma resonances is insignificant.

Note that the above criterion for the applicability of the proposed method is, in fact, opposite to that used in finding the self-consistent set of cross sections for electron collisions that are employed when solving a homogeneous Boltzmann equation. Indeed, a set of cross sections is constructed at which the computed electron diffusion coefficient and the first Townsend coefficient match the measured values in a wide range of the parameter E/N. We employed a known set of the cross sections for a homogeneous Boltzmann equation, but checked whether the use of this equation was justified. For this purpose, we used the rate constants for the processes governed by the high-energy part of the EEDF, which is the most sensitive to the effects that lead to the enrichment of the EEDF with fast electrons and that are ignored in our model. On the other hand, it is this part of the EEDF that is of interest for analyzing plasma processes because ionization is, in fact, produced by fast electrons.

Thus, the proposed method for determining the plasma parameters is directly related to the physical processes in the plasma of an electrode discharge. Obviously, the use of an inhomogeneous Boltzmann equation could significantly widen the applicability range of the method. However, this would require the self-consistently determination of the spatial distributions of the plasma parameters, which would make the problem much more difficult to solve and, thus, would reduce to zero the advantages of the method proposed. On the other hand, the experimental evidence of the applicability of the homogeneous Boltzmann equation indicates that the physical processes leading to the EEDF peculiarities (e.g., resonance phenomena) are of minor importance in the plasma region under study. Obviously, these processes can play an important role in the regions where this method is inapplicable. However, these regions are beyond the scope of this study.

4.3. Discussion

As was noted above, the electric field increases sharply when approaching the electrode, whereas it is nearly constant over the radius in the spherical region 6–10 mm below the electrode edge. The electric field distribution is similar to the known field distribution near a biased rod located above a grounded plane [14]. In a plane located near the electrode edge, the field sharply decreases with radius, whereas in a plane located somewhat below the electrode (at a distance of one to one-and-a-half rod diameter), the field is almost constant over the radius.

An analysis of the literature data on the plasmas of self-sustained microwave discharges (see. e.g., [15]) shows that the plasma electron density, as a rule, exceeds the critical density for the field frequencies that are usually used to excite self-sustained microwave discharges. The only exception is the discharge plasma in high-Q cavities, in which the plasma only slightly affects the field distribution [16].

In the spherical region, the electron density (5×10^9–3×10^{10} cm^{-3}) is much lower than the critical density for the given field frequency ($n_{cr} \approx 7 \times 10^{10}$ cm^{-3}), is nearly constant in space, and changes slightly with incident power. The obtained values of the electron density at the plasma boundary quantitatively agree with the results from probe measurements [1].

It is known (see, e.g., [17]) that, in the plasma of a non-self-sustained microwave discharge, the electron density is lower than the critical density. This circumstance allows one to consider the spherical region as a zone of a non-self-sustained discharge. The volume of this region increases with incident power, whereas the values of E and n_e change slightly. Inside the glowing sphere (in the dark space), the electron density decreases severalfold. It follows from the above analysis that the resonance phenomena are of minor importance in this region. At the outer boundary of the spherical region, n_e sharply decreases (by one order of magnitude at a distance of 2–3 mm).

Earlier, based on the measurements of the electron density and the electric field in the plasma of an electrode microwave discharge, it was concluded that the most probable reason for the existence of a sharp outer boundary of the discharge is the presence of an electric double layer [5, 18]. The reason for the origin of the sharp boundary of an electrode microwave discharge, as well as the position and properties of this boundary, requires future study.

5. CONCLUSIONS

A method has been developed for determining the electron density and electric field in plasma by measuring the relative spectral line intensities (the H_α, H_β, and 763.5-nm Ar lines) and calculating the electron-impact rate constants from the homogeneous Boltzmann equation. The method is used to study the spatial distributions of the plasma parameters in a microwave electrode discharge in hydrogen at pressures of 1–8 torr and incident powers of 20–80 W.

The measurements have shown that there are regions in the discharge where the electron density is higher (the bright electrode sheath) and lower (the spherical region) than the critical density for the frequency 2.45 GHz ($n_{cr} \approx 7 \times 10^{10}$ cm^{-3}). Inside the

spherical region, the electric field varies slightly over the radius, and the electron density increases as the discharge boundary is approached.

An analysis of the literature data on microwave discharges allows us to conclude that the observed discharge structure can be attributed to the presence of a self-sustained discharge zone (electrode sheath); a non-self-sustained discharge zone (spherical region); and a decaying plasma region that is separated from the active discharge region by an electric double layer.

ACKNOWLEDGMENTS

This study was supported in part by the Russian Foundation for Basic Research (project no. 02-02-16021) and the Presidium of the Russian Academy of Sciences (under the Fundamental Research Program no. 20).

REFERENCES

1. L. Bardosh and Yu. A. Lebedev, Zh. Tekh. Fiz. **68** (12), 29 (1998) [Tech. Phys. **43**, 1428 (1998)].
2. Yu. A. Lebedev, M. V. Mokeev, and A. V. Tatarinov, Fiz. Plazmy **26**, 293 (2000) [Plasma Phys. Rep. **26**, 272 (2000)].
3. Yu. A. Lebedev and M. V. Mokeev, Fiz. Plazmy **27**, 443 (2001) [Plasma Phys. Rep. **27**, 418 (2001)].
4. Yu. A. Lebedev, M. V. Mokeev, A. V. Tatarinov, and I. L. Epstein, in *Proceedings of the 4th International Workshop on Microwave Discharges: Fundamentals and Applications, Zvenigorod, 2000* (Yanus-K, Moscow, 2001), p. 187.
5. L. Bardos and Yu. A. Lebedev, Teplofiz. Vys. Temp. **38**, 552 (2000) [High. Temp. **38**, 528 (2000)].
6. Yu. A. Lebedev, A. V. Tatarinov, and I. L. Epstein, Plasma Sources Sci. Technol. **11**, 146 (2002).
7. L. Bardos, H. Barankova, Yu. A. Lebedev, *et al.*, Diamond Relat. Mater. **6**, 224 (1997).
8. L. Bardos, H. Barankova, and Yu. A. Lebedev, in *Proceedings of the 42nd Annual Conference of Society of Vacuum Coaters, Chicago, IL, 1999*, Proc. SVC TC, Paper E-7.
9. N. Taniyama, M. Kudo, and O. Matsumoto, Jpn. J. Appl. Phys. **40**, 698 (1995).
10. Yu. A. Lebedev and I. L. Epstein, J. Moscow Phys. Soc. **5** (1), 103 (1995).
11. V. I. Demidov, N. B. Kolokolov, and A. A. Kudryavtsev, *Probe Diagnostics of Low-Temperature Plasma* (Énergoatomizdat, Moscow, 1996).
12. T. A. Grotjohn, in *Proceedings of the 4th International Workshop on Microwave Discharges: Fundamentals and Applications, Zvenigorod, 2000* (Yanus-K, Moscow, 2001), p. 25.
13. J. Kudela, T. Terebessy, and M. Kando, in *Proceedings of the 4th International Workshop on Microwave Discharges: Fundamentals and Applications, Zvenigorod, 2000* (Yanus-K, Mocscow, 2001), p. 63.
14. Yu. P. Raizer, *Gas Discharge Physics* (Nauka, Moscow, 1987; Springer-Verlag, Berlin, 1991).
15. V. M. Batenin, I. I. Klimovskiĭ, G. V. Lysov, and V. N. Troitskiĭ, *Microwave Plasma Generators: Physics, Technology, and Applications* (Énergoatomizdat, Moscow, 1988).
16. S. Krasik, D. Alpert, and A. O. MacCoubrey, Phys. Rev. **76**, 722 (1949).
17. A. S. Zarin, A. A. Kuzovnikov, and V. M. Shibkov, *Freely Localized Microwave Dischardge in Air* (Neft' i Gaz, Moscow, 1996), p. 204.
18. Yu. A. Lebedev and M. V. Mokeev, Teplofiz. Vys. Temp. **38**, 381 (2000) [High Temp. **38**, 338 (2000)].

Translated by N.N. Ustinovskiĭ

Plasma Physics Reports, Vol. 29, No. 11, 2003, pp. 990–992. Translated from Fizika Plazmy, Vol. 29, No. 11, 2003, pp. 1067–1069.

BRIEF COMMUNICATIONS

Controlling the Characteristics of a Repetitive Volume Discharge in CFC-12 and Its Mixtures with Argon

A. K. Shuaibov, A. I. Dashchenko, and I. V. Shevera

Uzhhorod National University, vul. Pidgirna 46, Uzhhorod, 88000 Ukraine

Received November 26, 2002; in final form, March 27, 2003

Abstract—The parameters of a repetitive volume discharge in CF_2Cl_2 (CFC-12) and its mixtures with argon at pressures of $P(CF_2Cl_2) \le 0.4$ kPa and $P(Ar) \le 1.2$ kPa are studied. The discharge was ignited in an electrode system consisting of a spherical anode and a plane cathode by applying a dc voltage $U_{ch} \le 1$ kV to the anode. The electrical and optical characteristics of a volume discharge (such as the current–voltage characteristics; the plasma emission spectra; and the waveforms of the discharge voltage, the discharge current, and the total intensity of plasma emission) are investigated. It is found that, by shunting the discharge gap with a pulsed capacitor with a capacitance of $C_0 \le 3.5$ nF, it is possible to control the amplitude and duration of the discharge current pulses, as well as the characteristics of the pulsed plasma emission. The increase in the capacitance C_0 from 20 to 3500 pF leads to a significant increase in the amplitude and duration of the discharge current pulses, whereas the pulse repetition rate decreases from 70 to 3 kHz. The glow discharge exists in the form of a domain with a height of up to 3 cm and diameter of 0.5–3.0 cm. The results obtained can be used to design an untriggered repetitive germicidal lamp emitting in the Cl_2(257/200 nm) and ArCl (175 nm) molecular bands and to develop plasmachemical methods for depositing amorphous fluorocarbon and chlorocarbon films. © *2003 MAIK "Nauka/Interperiodica".*

Repetitive volume discharges in fluorocarbons and chlorocarbons (CCl_4, CF_4, etc.), as well as in pure chlorine, are efficient sources of short-wavelength radiation (λ = 190–280 nm) [1–3], which is of significant interest for the sterilization of medical instrumentation, air disinfection, surface activation, and other applications in high-energy chemistry and microelectronics. At present, plasmas of the chlorofluorocarbon (CFC) decomposition products are considered to be a promising means for depositing thin amorphous carbon-containing insulating films in VLSICs [4]. Because of the high electronegativity of CFCs, the excitation of spatially homogeneous discharges in them encounters difficulties, some of which can be overcome by operating with nanosecond volume discharges [5]. However, the ignition of such discharges requires the application of high-voltage modulators. Hence, it is of interest to develop a method for obtaining a low-pressure volume discharge in CFC-12 with a dc power supply, such that the repetitive operation mode is enabled by the onset of discharge instability. Numerical simulations of a low-pressure glow discharge in a model electronegative gas [6] showed that, due to the redistribution of the electric field along the discharge gap, the discharge operates in a repetitive mode ($f \le 10$ kHz). In [7], we experimentally observed and studied this operational mode of a low-pressure glow discharge in a Kr/Cl_2 mixture. The possibility of controlling the parameters of such a discharge in CF_2Cl_2 and its mixtures with rare gases has not yet been examined. In [8], it was shown that, based on a volume discharge with a dc power supply in a grid–plate electrode system, it is possible to create a planar Xe/Cl lamp operating with Xe/Cl_2(HCl) mixtures at pressures of $P \le 2$ kPa; however, neither the parameters of this type of a pulsed discharge nor the possibility of controlling them have been considered.

In this paper, we study the characteristics of a repetitive volume discharge in CFC-12 and its mixtures with argon.

The discharge operated in an electrode system consisting of a spherical anode and a plane cathode with an interelectrode distance of 3 cm. A dc voltage was applied to the anode through a ballast resistance of 20 kΩ. The average discharge current was in the range 2–50 mA. The partial pressures of CFC-12 and Ar were varied in the ranges 50–300 Pa and 100–1200 Pa, respectively. The electrode system was mounted in a 10-l buffer chamber. A description of the experimental facility is given in [2, 7]. In order to control the discharge parameters, a set of KVI-3 and KVI-2 pulsed capacitors with a total capacitance of 200–3500 pF was connected in parallel to the discharge gap, whose intrinsic capacitance (together with the parasitic wiring capacitance) was ≤10–20 pF.

The volume discharge had the shape of a truncated cone. The small (upper) base of the plasma domain was adjacent to the anode, whereas its lower base was spherical in shape and was separated from the cathode by a 1- to 7-mm dark space. The diameters of the lower and upper bases of the plasma domain was as high as 3.0 and ≤2.0 cm, respectively. As the pressure of CFC-

1063-780X/03/2911-0990$24.00 © 2003 MAIK "Nauka/Interperiodica"

12 or the Ar/CF_2Cl_2 mixture increased, the transverse size of the plasma decreased by a factor of 3 to 5.

The static current–voltage characteristic of the discharge corresponded to the normal mode of discharge ignition. The average voltage at the anode did not exceed 1 kV. The initial part of the dynamic current–voltage characteristic corresponded to the abnormal stage of a glow discharge [9]. The discharge current then reached its maximum and began to decrease (although the discharge voltage kept increasing), which resulted in the formation of a negative-slope branch of the current–voltage characteristic.

An analysis of the plasma emission spectra showed that the main fraction of the total emission intensity (≥70%) was concentrated in the 150- to 300-nm spectral range. The emission spectrum from a discharge in pure CFC-12 consisted of broad overlapping bands with maxima at 257 and 200 nm. This emission can be attributed to the emission bands of Cl_2 molecules ($D' - A'$ and $(\Sigma - \Sigma)$ transitions) and CCl* radicals.

Figure 1 presents the waveforms of the discharge voltage and current and the total emission intensity from a discharge in pure CFC-12 for different CFC-12 pressures; average discharge currents; and capacitances C_0, shunting the discharge gap. At the minimum capacitance, the total duration and amplitude of the discharge current pulses were minimum ($\Delta t \le 50$ ns and $I_{max} \le 1.5$ A, respectively). Pulsed emission with a duration of ~300 ns occurred in the early afterglow of discharge current. The pulse amplitude decreased with increasing average current. As the capacitance C_0 increased to 900 pF, the current pulse duration increased twofold and the current amplitude increased to 25 A. The current reached its maximum value at the leading edge of the discharge voltage pulse. At low CFC-12 pressures, the discharge current and the emission intensity reached their maxima simultaneously. Within the time interval t = 100–200 ns, the current flowed against the applied voltage. This was related to the instability of the cathode sheath of a short-lived glow discharge, which is similar in nature to a Trichel pulse [10, 11]. The duration of the emission pulse attained 500 ns. Under these conditions, the diameters of the plasma domain were 1.5 cm near the anode and 2.0 cm near the cathode, and the discharge was homogeneous. As $P(CF_2Cl_2)$ increased to 0.4 kPa, the domain remained homogeneous only in the anode part with a diameter of 0.5 cm, whereas its cathode part acquired a form of a bundle of thin streamer channels with a total diameter of 2.0 cm. In this case, the emission pulse had two maxima and its duration increased by a factor of 2.0–2.5. The first of these maxima occurred at the leading edge of the current pulse, and the second one occurred at the trailing edge. The shape of the voltage pulse changed only slightly.

Figure 2 shows the waveforms of the current and the emission intensity from a volume discharge in Ar/CF_2Cl_2 mixtures for different partial argon pressures

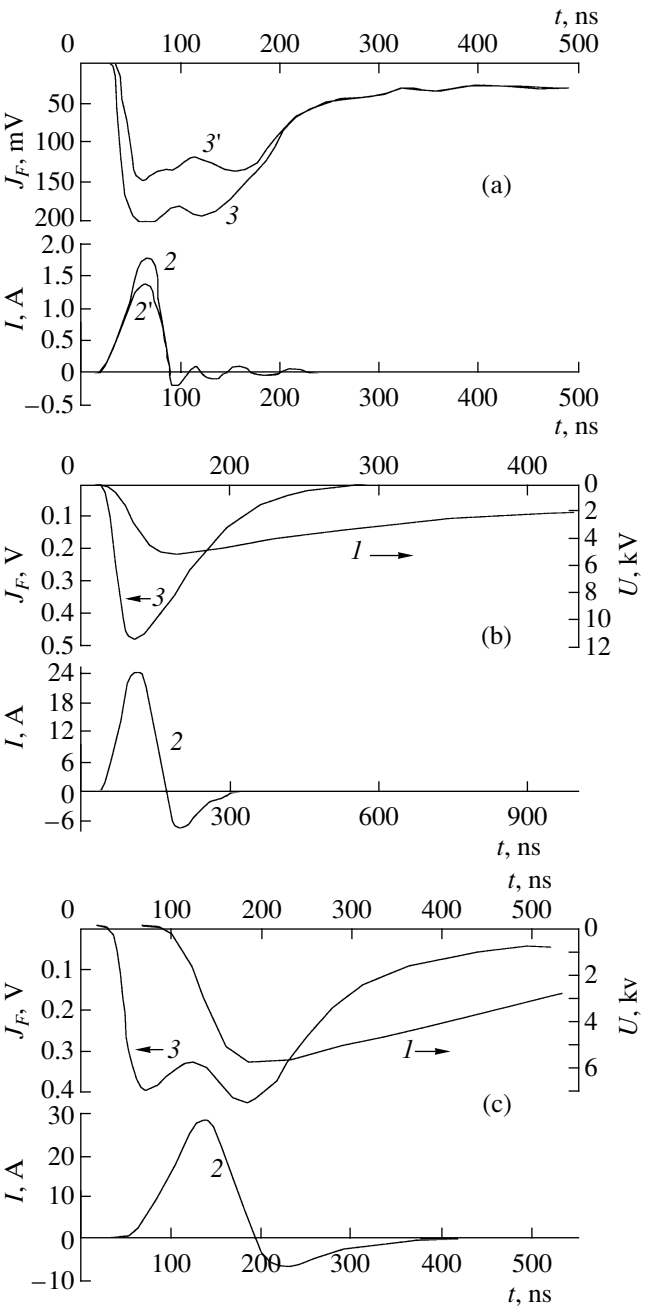

Fig. 1. Waveforms of the (*1*) discharge voltage, (*2*) discharge current, and (*3*) emission intensity from a volume discharge in CFC-12 for (a) $P(CF_2Cl_2)$ = 160 Pa, C_0 = 20 pF, and I_{ch} = (*2*, *3*) 10 and (*2*', *3*') 30 mA; (b) $P(CF_2Cl_2)$ = 80 Pa, C_0 = 900 pF, and I_{ch} = 30 mA; and (c) $P(CF_2Cl_2)$ = 400 Pa, C_0 = 900 pF, and I_{ch} = (*1*, *3*) 6 and (*2*', *3*') 30 mA.

and average discharge currents. For Ar/CF_2Cl_2 mixtures with a low partial argon pressure, the emission intensity was maximum at low average discharge currents. As I_{ch} increased, the current pulse duration decreased. The increase in P(Ar) to 1.33 kPa led to an increase in the current pulse duration and a decrease in

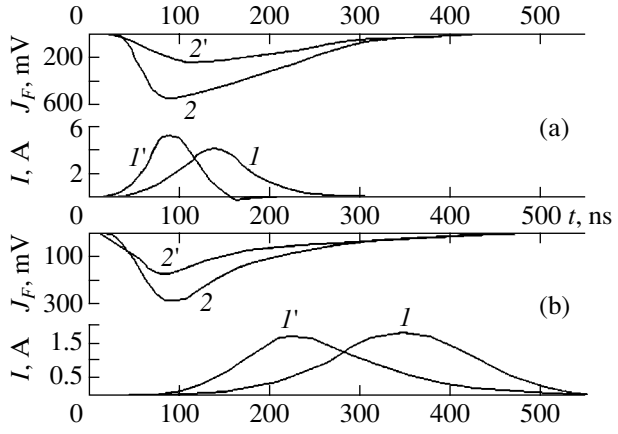

Fig. 2. Waveforms of the (*1*) discharge current of and (*2*) total emission intensity from a volume discharge in Ar/CF_2Cl_2 mixtures for (a) $P(Ar)/P(CF_2Cl_2)$ = 160 Pa/120 Pa and I_{ch} = (*1*, *2*) 6 and (*1*', *2*') 30 mA and (b) $P(Ar)/P(CF_2Cl_2)$ = 1330 Pa/120 Pa and I_{ch} = (*1*, *2*) 6 and (*1*', *2*') 30 mA.

the amplitude and duration of the emission pulse. In this case, the integral emission pulse shifted in time toward the leading edge of the discharge current pulse.

The estimated total power of UV–XUV emission from the entire surface of the radiation source attained 1–2 W, the efficiency being ≤5%.

Thus, we have studied the parameters of a short-lived glow discharge in CFC-12 and its mixtures with argon at pressures of $P \le 1.33$ kPa. The discharge was fed from a dc power supply and was not confined by dielectric walls. It has been found that such a discharge operates in a repetitive mode and acts as a selective source of UV–XUV radiation from the transitions of Cl_2 and ArCl* molecules. Shunting the discharge gap with a capacitance ($C_0 \le 2$–3 nF) allows one to control the parameters of the repetitive discharge. The shunting capacitance acts as an energy storage bank, whereas the discharge itself is self-induced. This type of a glow discharge can be used to design a simple repetitive low-pressure germicidal lamp and to develop new methods for depositing amorphous carbon-containing films.

REFERENCES

1. L. M. Vasilyak, S. V. Kostyuchenko, A. V. Krasnochub, and M. E. Kuz'menko, Zh. Prikl. Spektrosk. **65**, 302 (1998).
2. A. K. Shuaibov, L. L. Shimon, I. V. Shevera, and A. I. Dashchenko, Fiz. Plazmy **25**, 640 (1999) [Plasma Phys. Rep. **25**, 585 (1999)].
3. A. K. Shuaibov, A. I. Dashchenko, and I. V. Shevera, Pis'ma Zh. Tekh. Fiz. **28** (8), 48 (2002) [Tech. Phys. Lett. **28**, 330 (2002)].
4. V. V. Ivanov, K. S. Klopovskiĭ, D. V. Lopaev, *et al.*, Fiz. Plazmy **28**, 272 (2002) [Plasma Phys. Rep. **28**, 243 (2002)].
5. Yu. D. Korolev, G. A. Mesyats, and A. M. Yarosh, Khim. Vys. Énerg. **21**, 464 (1987).
6. I. Peres and L. C. Pitchford, J. Appl. Phys. **78**, 774 (1995).
7. A. K. Shuaibov, A. I. Dashchenko, L. L. Shimon, and I. V. Shevera, Pis'ma Zh. Tekh. Fiz. **28** (16), 85 (2002).
8. É. A. Sosnin and V. F. Tarasenko, Zh. Tekh. Fiz. **67** (12), 43 (1997) [Tech. Phys. **42**, 1411 (1997)].
9. Yu. P. Raizer, *Gas Discharge Physics* (Nauka, Moscow, 1987; Springer-Verlag, Berlin, 1991).
10. V. I. Chigin', Ukr. Fiz. Zh. **47**, 350 (2002).
11. Yu. S. Akishev, I. V. Kochetov, A. I. Loboĭko, and A P. Napartovich, Fiz. Plazmy **28**, 1136 (2002) [Plasma Phys. Rep. **28**, 1049 (2002)].

Translated by N.N. Ustinovskiĭ

Plasma Physics Reports, Vol. 29, No. 11, 2003, pp. 993–995. Translated from Fizika Plazmy, Vol. 29, No. 11, 2003, pp. 1070–1072.

Derek Robinson and Historical Experiment in Magnetic Fusion Research

It has been one year since Prof. Derek Robinson, prominent fusion research scientist, a leading figure in the UK Fusion Research Program, and Director of the UKAEA Culham Science Centre, died at the age of 61. He was a key person in the historical experiment on local measurement of the electron temperature by the Thompson scattering technique in the T-3 tokamak (Kurchatov Institute) in the second half of 1969. This experiment convinced the international fusion community of the validity of information presented 35 years ago at the 3rd IAEA Conference (Novosibirsk) by Academician L.A. Artsimovich, the leader of the Soviet fusion research program, who reported that a quasi-steady plasma with an unprecedented (for that time) temperature of about 1 keV had been obtained in the T-3 tokamak. This implied that enhanced (Bohm) plasma diffusion, which had been observed in Princeton stellarators and which did not allow one to increase the plasma temperature at a given heating power, was not a universal phenomenon and, therefore, was not an insuperable obstacle in creating a fusion reactor. The majority of participants at the Novosibirsk conference listened to Artsimovich's report skeptically. One of those who took the report seriously was Prof. R.S. Pease, the Director of the Harwell Plasma Labortatory. He was the first Western scientist to recognize the critical mind and physical intuition of Artsimovich a few years before the Novosibirsk conference, after he had found in Artsimovich's book *Controlled Thermonuclear Reactions*, published in 1961, a valid interpretation of the results of the Livermore experiment (performed in late 1960) on repeated plasma compression in an open confinement system (later, the authors of the experiment corrected their interpretation of the results obtained). Aware of the importance of increasing the plasma temperature in fusion devices, Prof. Pease agreed with Artsimovich's proposal on the necessity of independently checking the T-3 plasma parameters. At that time, Dr. Robinson and his colleagues were involved in investigations of the relation between plasma turbulence and the profiles of the magnetic field and electron temperature in the ZETA device. To measure the distribution of the plasma electron temperature, a diagnostic technique based on the Thomson scattering of a ruby laser had been created. A group of English physicists headed by N.J. Peacock arrived at the Kurchatov Institute with this apparatus. At the height of the Cold War, it was no easy matter to organize such a visit of British scientists and technicians, equipped with an experimental facility with a total mass of 5 t. Like Soviet scientists travelling abroad, their British colleagues would also obey certain requirements. In particular, as Prof. Pease remembered, the visit of Dr. Robinson to the USSR would have been impossible had he not gotten married a year before.

Derek Robinson was born on May 27, 1941, in Douglas, on the Isle of Man. In 1965, he graduated from Manchester University and, as a talented student, was sent to work at the Atomic Centre in Harwell. There, he investigated plasma turbulence in the ZETA toroidal device, in which large-scale plasma instabilities related to the toroidal electrical current were stabilized (in contrast to tokamaks) by a relatively weak toroidal magnetic field, decreasing practically to zero at the plasma edge. Dr. Robinson found that small-scale plasma turbulence was suppressed (the so-called "quiescent" regime) when the direction of the toroidal magnetic field outside of the main current channel was reversed, whereas the total toroidal magnetic flux was conserved due to the high electric conductivity of the vacuum vessel. Systems of this type were called reversed field pinches (RFPs). Such systems are a remarkable example of plasma self-organization: the macroscopic stability of the plasma in an RFP is provided by supplying power to maintain the current pulse continuously gen-

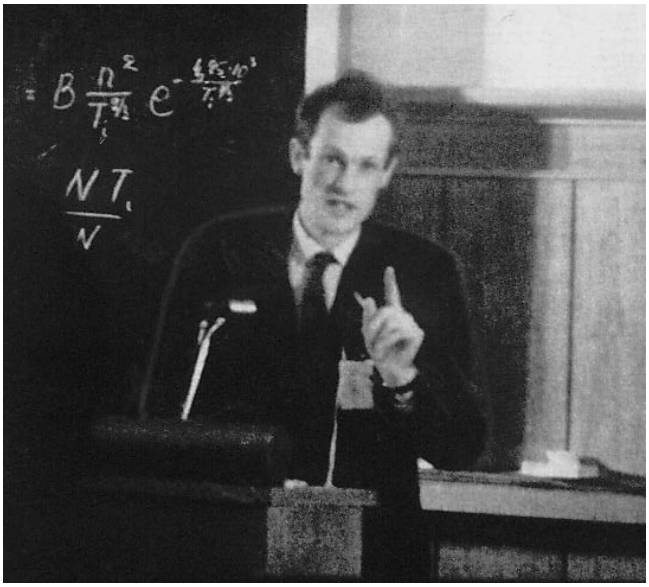

Fig. 1. Derek Robinson. Report at the Dubna workshop, 1969.

1063-780X/03/2911-0993$24.00

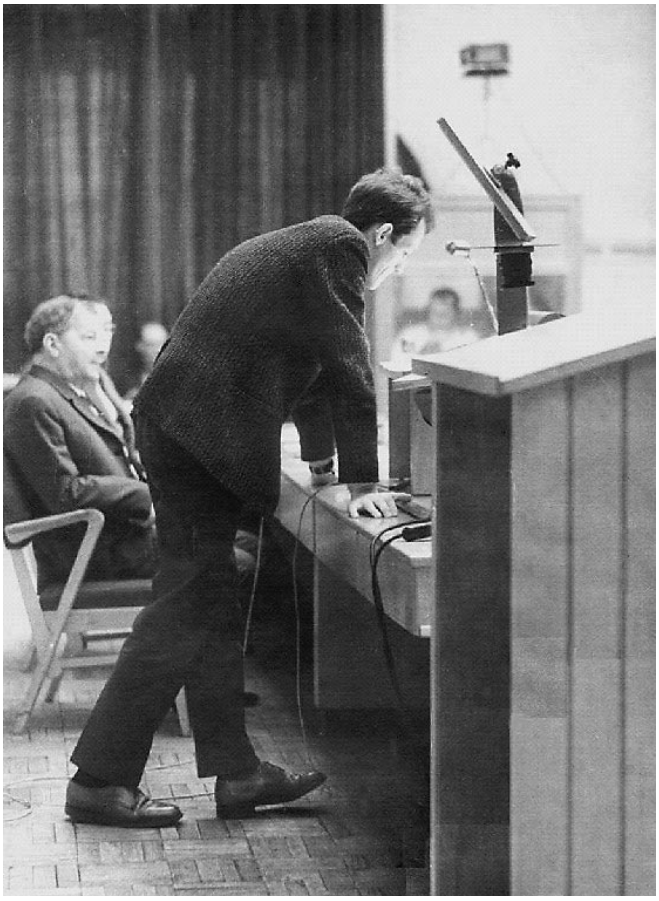

Fig. 2. During Dr. Robinson's historical report. The person on the left is L.A. Artsimovich, the chairman of the session.

Fig. 3. After the report by Dr. Robinson. The person on the right is L.A. Artsimovich; at the center is V.V. Sannikov, the Soviet participant of the joint experiment.

erating a toroidal magnetic field with the radial profile that is necessary for macroscopic plasma stability. In addition to experimental investigations, Dr. Robinson performed a number of theoretical studies on plasma stability in ZETA-type systems. In particular, he calculated the maximum possible ratio of the plasma pressure to the magnetic field pressure and the plasma density profiles stable against ideal magnetohydrodynamic perturbations. In experiment, he was the first to implement a technique for measuring the electron temperature by Thomson scattering. It is this technique with which the British scientists performed the above experiment to determine the electron temperature in the T-3 tokamak. As V.V. Sannikov, a Soviet participant of this experiment, remembered, his British colleagues first used a ruby laser in the free-generation mode with a pulse duration of Δt = 1 ms and a pulse energy of E = 50 J. The use of such pulses seemed to be attractive due to their large energy, since, in this case, the number of scattered photons was expected to be fairly large. However, the amount of radiation emitted by the plasma itself over a time of 1 ms also turned out to be very large. Since the cross section for the scattering by electrons is very small, $\sigma \cong 6.6 \times 10^{-25}$ cm^2, the integral signal from spontaneous plasma emission exceeded that from the scattered laser radiation. For this reason, Dr. Robinson employed a Q-switched laser generating a giant pulse with a duration of $\Delta t \approx 10^{-9}$ s and an energy of $E \approx 3$ J; i.e., the integration time was decreased by a factor of 10^5. Although, in this case, the laser energy decreased by more than one order of magnitude, the signal-to-noise ratio increased to about 10. This made it possible to record the scattered signals with an accuracy of 7–10%.

The results of this joint Soviet–British experiment were reported by Dr. Robinson at the Second International Workshop on Toroidal Systems, held in Dubna, near Moscow, in 1969 (the first workshop was held at Princeton in 1965), and were then published in *Nature* (1969, vol. 224, p. 488).

This experiment convinced the international fusion community of the fact that an electron temperature one order of magnitude higher than in other contemporary devices had indeed been achieved in a tokamak. For this reason, in the 1970s, studies on magnetic plasma confinement all over the world began to switch over to tokamaks. The subsequent continuous progress in increasing the plasma parameters showed that the turbulent processes in a tokamak plasma aggravate plasma

thermal insulation to a lesser extent than in RFPs, which are conceptually rather similar to tokamaks. This convinced scientists of the possibility of achieving the plasma parameters required for a fusion reactor. In fact, the a transition from tokamaks with a small plasma radius of $a = 0.15$ m to those with a radius of $a \cong 0.4$ m, and then with $a \cong 1$ m, resulted in experiments with plasma parameters at which the power released in D-T thermonuclear reactions was comparable to the input power. The continuous progress in increasing the plasma parameters in these devices has finally led to the elaboration of an international project: the International Thermonuclear Experimental Reactor (ITER).

Dr. Robinson contributed greatly to all stages of this progress toward his final goal. He actively participated in the JET (the largest all-European tokamak) and ITER programs and gave lectures on controlled fusion research in a number of developing countries. In addition to his participation in designing large devices, he continued searching for alternative approaches to magnetic plasma confinement. Thus, he was the first to implement the model of a conceptually new, extremely compact tokamak with an aspect ratio R/a only slightly larger than unity.

The name of Derek Robinson, a remarkable scientist and a highly intelligent, considerate, and kind man, will remain forever in the history of controlled fusion research.

V. D. Shafranov